QATAR UNIVERSITY

COLLEGE OF ENGINEERING

DEVELOPMENT OF BIFUNCTIONAL OXYGEN ELECTROCATALYSTS USING SOLUTION COMBUSTION SYNTHESIS FOR FUEL CELL APPLICATIONS

BY

ANCHU ASHOK

A Dissertation Submitted to

the Faculty of the College of Engineering

in Partial Fulfillment of the Requirements for the Degree of

Doctorate of Philosophy in Materials Science and Engineering

[June] 2019

COMMITTEE PAGE

The members of the Committee approve the Dissertation of

Anchu Ashok defended on 17/04/2019.

Prof. Faris Tarlochan

_____

Dissertation Supervisor

Dr. Anand Kumar

_____

Dissertation Co-Supervisor

Dr. Rahul R Bhosale

_____

Dissertation Co-Supervisor

Dr. Anwarul Hasan

_____

Committee Member

Approved:

_____

Abdel Magid Hamouda , Dean, College of Engineering

ABSTRACT

ASHOK, ANCHU., Doctorate: [June]: [2019], Doctorate of Philosophy in Materials Science and Engineering

Title: Development of Bifunctional Oxygen Electrocatalyst Using Solution Combustion Synthesis for Fuel Cell Application.

Supervisor of Dissertation: Prof. Faris Tarlochan.

Advanced energy storage and conversion systems such as fuel cells and metal air batteries achieved wide attention. Oxygen reduction reaction (ORR) and Oxygen evolution reaction (OER) are the prominent reactions that govern the charging and discharging capability of batteries as well as fuel cells. The bifunctional electrocatalyst that can be used to activate both the reactions (ORR and OER) are demanding and still challenging. Platinum (Pt) group metals are found to be the most efficient electrocatalyst, but their high cost and limited availability restrains large scale commercialization. Intensive research focused on developing highly active, cost-effective and earth abundant materials for bifunctional oxygen electrocatalyst for next generation energy sources.

In this work, we mainly focused on the solution combustion synthesis (SCS) method for preparing nanoparticles and studying their bifunctional electrocatalytic performance in alkaline medium. The structure, physio-chemical nature and composition of the material can be tuned by the synthesis condition that enables us to correlate them with the catalytic performance for oxygen reactions.

In SCS technique, the fuel to oxidizer ratio (φ) is identified as a critical parameter affecting the properties of the synthesized nanoparticles. In the first part of this study, we prepare cobalt nanoparticles with different fuel ratio (φ = 0.5, 1 and 1.5). Then we

synthesized bimetallic Ag-M (Cu and Co) using three different modes of SCS. The phase distribution of the catalyst after stability shows a clear phase de-alloying and segregation of elements that reduces the performance.

Thereafter, we focused on perovskite materials $LaMO_3$ (M = Cr, Mn, Fe, Co, Ni) with stable and homogeneous perovskite phases. $LaMnO_3$ shows the maximum current density for ORR, whereas $LaCoO_3$ shows best performance for OER. Finally, we focused on enhancing the surface area of perovskite by incorporating a leachable salt (e.g. KCl) during combustion that breaks down the three-dimensional crystalline structure to restrict post combustion agglomeration and sintering, which in-turn translates into better electrocatalytic performance. Based on these results, we conclude that the salt assisted SCS has the potential for preparing highly efficient and durable bifunctional electrocatalyst suitable for fuel cells and metal air batteries.

DEDICATION

TO MY LITTLE ISHANI AND SHIVA

ACKNOWLEDGMENTS

I would like to express my sincere gratitude towards the *God Almighty* for all the blessing and mercy for the successful completion of this thesis.

I am grateful to my lead supervisor Prof. Faris Tarlochan and co-supervisors Dr. Anand Kumar and Dr. Rahul R Bhosale for their wonderful support, patient guidance, valuable advice, positive appreciation and constructive criticism throughout the degree which led to the successful completion of the research work.

I greatly appreciate and acknowledge the support receive from center laboratory unit (CLU) , gas processing center (GPC), center of advanced material (CAM) and Qatar energy and environmental research center (QEERI) for various catalyst characterizations such as XRD, SEM, TEM and XPS. I am especially thankful to Dr. Said Mansour, Director of Core Labs at the Qatar Environment and Energy Research Institute (QEERI) for their help in providing HR-TEM and EDS analysis. I am equally thankful to Mr. Sivaprasad and Mr. Saeed Gad in chemical engineering department for their technical support during the entire period of my research. I would also like to extend my sincere thanks to Dr. Abdul Matin for his valuable time for sharing the knowledge that was very helpful for design the experiments during the initial time of research.

Special thanks to all my lab mates and colleagues for who have all contributed to the progress I have made. Finally, I would like to express to my deepest gratitude to my family and friends for all the supports and encouragement to achieve this degree.

Especially to my husband, who has given me extra care, strength, motivation and without you I would not be who I am today. I would like to say a big thank to my

Ishani, for being as the best daughter in the world. You are there with me from the starting of the PhD and never complaint me on my busy and late-night works. Thank you so much for both of you for standing beside me with your unconditional love, care and patience without that I never be able make my dream come true. Words can never express how I am thankful to the little one Shiva, who needs me more this time. Thanks once again for the support and motivation.

TABLE OF CONTENTS

LIST OF TABLES

LIST OF FIGURES

LIST OF ABBREVIATIONS

Abbreviation	Definition
ORR	Oxygen Reduction Reaction
OER	Oxygen Evolution Reaction
EIA	Energy Information Administration
CNT	Carbon Nano Tubes
TMO	Transition Metal Oxide
DFT	Density Functional Theory
RGO	Reduced Graphene Oxide
RHE	Reverse Hydrogen Electrode
BSCF	Barium Strontium Cobalt Iron
Wt%	Weight Percentage
N-RMGO	Nitrogen Doped Reduced Graphene Oxide
HRGOS	Hollow Reduced Graphene Oxide Spheres
CS	Combustion Synthesis
SCS	Solution Combustion Synthesis
VCS	Volume Combustion Synthesis
SWCS	Second Wave Combustion Synthesis
SHS	Self- Propagating High Temperature Synthesis
SA-SCS	Salt Assisted Solution Combustion Synthesis
PVA	Poly Vinyl Alcohol
DIW	De-Ionized Water
XRD	X-Ray Diffraction
SEM	Scanning Electron Microscopy
TEM	Transmission Electron Microscopy
EDS	Energy Dispersive X-Ray Spectroscopy
XPS	X-Ray Photoelectron Spectroscopy
FTIR	Fourier-Transform Infrared Spectroscopy
UV-VIS	Ultraviolet–Visible Spectroscopy
BET	Brunauer–Emmett–Teller

CV	Cyclic Voltammetry
LSV	Linear Sweep Voltammetry
CA	Chronoamperometry
RDE	Rotating Disk Electrode
RRDE	Rotating Ring Disk Electrode
KL	Koutecky-Levich

LIST OF NOMENCLATURE

Symbol	Meaning	Unit
φ	Fuel to metal oxidizer ratio	-
ν	Metal valency	-
λ	Wavelength of X-Ray	nm
d	Lattice spacing	nm
θ	Diffraction maximum	degree
R	Gas constant (8.314)	J mol^{-1} K^{-1}
T	Temperature	K
F	Faraday constant (96485)	C mol^{-1}
C_0	Bulk O_2 concentration (7.8×10^{-7})	mol-cm^{-3}
v	Kinematic viscosity (0.01)	cm^2 s^{-1}
D_0	O_2 diffusion coefficient (1.9×10^{-5})	cm^2 s^{-1}
k	Electron-transfer rate constant	-
J	Measured current densities	mA cm^{-1}
J_L	Diffusion-limited current	mA cm^{-1}
J_k	Kinetic current densities	mA cm^{-1}
I_D	Disc current	mA
I_R	Ring current	mA
N	Collection efficiency (0.25)	-
n	Number of electron transfer	-
b_{low}	Low tafel slope	mV $decade^{-1}$
b_{high}	High tafel slope	mV $decade^{-1}$
J_{ex}	Exchange current density	mA cm^{-1}

CHAPTER 1: INTRODUCTION

1.1. Introduction

Increasing energy consumption, rising greenhouse gas emission from fossil fuel combustion and its adverse effect on environment stimulated intense research work to develop renewable and alternative energy sources such as solar, wind, wave powers and some modern energy storage and delivering systems such as batteries and fuel cells [1-3]. To date, combustion of fossil fuels is used as a major energy source to meet highly demanding applications in industry and transportation. Researchers and scientist are still searching for alternative energy system with low cost, high efficiency, environmentally friendly and highly abundant in nature. In 2017, US Energy Information Administration (EIA) reported an increase in demand of consumable energy by the mid-21st century worldwide [4] (Figure 1.a).

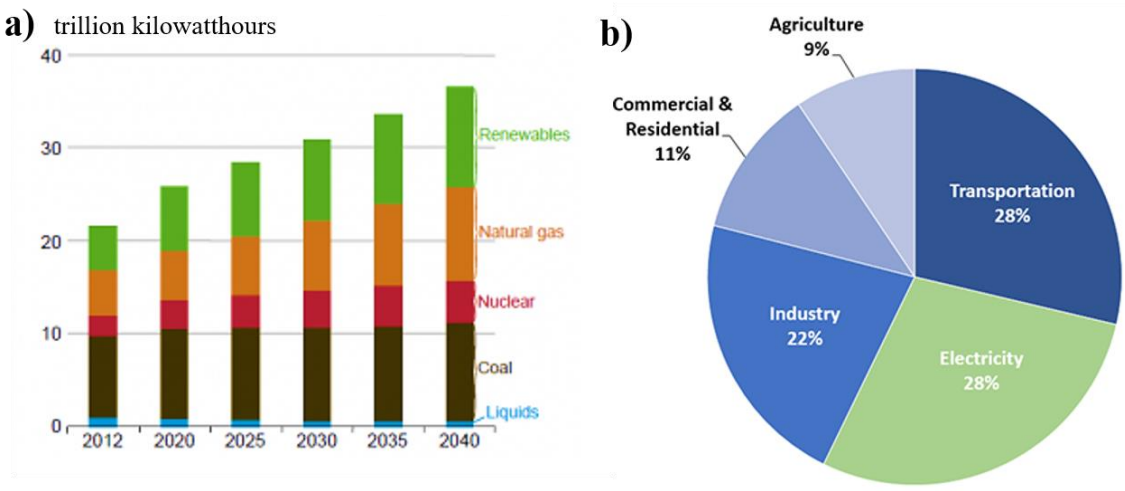

Figure 1. a) World net energy generation (trillion kilowatt hours) by different energy source through (2012-2040) b) Greenhouse gas emission in US (2016) from different economic sector [4].

The consumption of fossil fuel to generate electricity keeps increasing every year and it is anticipated that approximately 57 % of the total electricity by 2040 will depend on the fossil fuel energy (natural gas and coal). Inventory of U.S. Greenhouse Gas Emissions and Sinks in 2016 published the estimation of total greenhouse gas emission from different public sectors in US is shown in Figure 1.b. The largest share of greenhouse gas was shared by transportation (28%) and electricity (28%) through the burning of fossil fuels such as coal, natural gas, gasoline and diesel [2]. These studies alerted the importance of reducing fossil fuels in future and thereby minimizing the emission of greenhouse gases to save the nature.

More environmentally friendly and greener technologies have gained great attention among researchers, and fuel cell-based technology is one of the most interesting owing

to its high efficiency, unlimited resources, environmentally safe and noise less system when compared to conventional energy distribution system [5,6]. Fuel cells generate heat and electricity during the electrochemical reaction between the hydrogen and oxygen to form water. Unlike batteries, it does not require recharging as long as fuel and oxidants are continuously supplied. When compared to thermal engine, fuel cells are environmentally friendly, highly efficient and surplus source of reactants make fuel cell a better candidate for energy in coming generations [7,8]. Due to its efficient performance and technology they are widespread in the commercial areas of portable and stationary power generation, space shuttles and transportation and thus reduce the global issues of energy requirement and clean environment [9].

In 2014, Toyota Mirai launched the first fuel cell car with hydrogen fuel cell as main energy source. Later in 2016, Hyundai and Honda developed their own fuel technology and commercialized it as Tucson fuel cell and Honda clarity fuel cell car respectively. EasyJet, the second largest airline network in Europe is developing a new hydrogen fuel cell system as the power source for the planes. Fuel cell technology is not limited to automotive applications, it can also be implemented on many of our energy consumable devices. MyFc, a leading manufacturer of chargers for many portable devices such as smartphone and tablets, introduced new fuel cell mobile charger that uses only salt and water for charging. Main issue in the commercialization of fuel cell technology is its low performance and the stability of the electrode material for long term applications [9].

The main reaction mechanism in fuel cells is oxygen reduction reaction (ORR) and for batteries it requires both oxygen reduction reaction (ORR) and oxygen evolution reaction (OER) during its discharging and charging process respectively [10]. It is highly desirable

to develop bifunctional catalysts that are suitable for both fuel cells and metal air batteries [11-15]. Many chemical and physical attributes such as composition, structure, phases, valence, morphology, size, surface area, and electronic conductivity can affect the catalytic performances of material driving electrochemical reactions in fuel cells and batteries [16,17].

1.2. Motivation

The research is still going on to find out a suitable catalyst with good kinetics and performance of nanoparticles. Highly dispersed Platinum (Pt) and Iridium (Ir) material on carbon black are considered as the best material for ORR and OER performance that promote the electron transport in the overall reaction [18-23]. The Pt loading at anode should be 0.05 mg cm^{-2} for the oxidation of hydrogen, while in cathode, for sluggish reaction kinetics of ORR the Pt loading should be minimum of 0.4 mg cm^{-2} for better reduction [16] .Commercially, only Pt is reported to be used for fuel cells, particularly for ORR reaction, but their limited availability (only South Africa and Russia are the major supplier) and high cost are the key factors in limiting their large scale catalytic applications[24] . Also, Ir is thermodynamically unstable and causes agglomeration and reduces the electrochemical activity of OER [25]. So, it is desired to replace Pt and Ir with some more abundant and cheaper material with high activity and stability. To address these issues, advanced catalysts with bi-functional performance towards both ORR and OER, and excellent electrochemical durability must be developed [12,26]. Once such advanced catalysts are developed, they can be used as cost-effective bi-functional catalysts for fuel cells and batteries as well.

Recent development in this field shows various strategies adopted to decrease Pt loading by replacing Pt with alloys of Pt group metals (PGM), developing core-shell structures, utilizing transition metal oxide (TMO), carbon-based nonmetals such as CNT, graphite, reduced graphene oxides to enhance ORR and OER performance [27-29]. Bimetallic transition metals (and metal oxides), due to their high activity and long-term stability are seen as a possible alternative for replacing the precious metals. The synergy between the metals increases the sluggish kinetics and achieves better stability. Also, perovskite with ABO_3 structure are also a promising candidate for the cost-effective bi-functional catalyst for ORR and OER reactions in alkaline medium [30-34]. The substitution of one element with a transition metal changes the oxidation state and thereby increases the catalytic activity of the material itself.

Synthesis of catalyst is the main money consuming step during any catalytic applications [35]. Here we propose to employ an efficient, fast, simple and economical way of synthesis procedure, i.e; solution combustion synthesis. Using solution combustion synthesis (SCS), it can synthesize variety compounds with different composition with homogeneous morphology. This forms the basis of the proposed research, to synthesize bifunctional catalyst for ORR and OER using solution combustion synthesis.

In this work, controlling the surface alloying of the material through three different modes of combustion synthesis and its effect in electrochemical catalytic performance for ORR and OER are investigated. The stability of the catalyst was also studied using the long-term electrochemical run and understand the final composition of the material after the stability test was also analyzed.

1.3. Research questions

Developing bi-functional catalyst in a cost-efficient manner for ORR and OER applications with improved performance and durability is still challenging. The main four research questions that motivate me to carry out this work are:

Developing a bifunctional catalyst using solution combustion synthesis for ORR and OER applications.

Probing the effect of combustion-controlled surface alloying and understanding its effect on its activity and stability.

Synthesis of uniform perovskite materials using solution combustion synthesis and understanding the activity towards ORR and OER.

Study the effect of salt assisted SCS on agglomeration, surface area of nanomaterials and their electrochemical performance.

1.4 Research objective

The objective of this research is to study the synthesis condition of combustion synthesis on the structural properties of the catalyst and correlating synthesis conditions with electrocatalytic performance of catalysts for ORR and OER reactions. The below tasks need to be completed to achieve the research objective:

Proposing different mode of solution combustion synthesis and investigating their characteristics and catalytic performance towards ORR and OER.

Understanding the stability and phase separation of silver and its alloy for long term stability run.

Proposing an effective and simple method of synthesizing single-phase Lanthanum based

perovskites and compare the catalytic activity for fuel cell and battery application

Identifying the effect of salt assisted solution combustion synthesis and compare its activity with conventional solution combustion synthesis.

1.5 Outline of thesis

This thesis consists of 8 main chapters. The details of each chapter are as following:

Chapter 1 introduces the present context and motivation of the research.

Chapter 2 detailed the reaction mechanism in ORR and OER and the current state of art of oxygen electro catalyst.

Chapter 3 provides the description of synthesis procedure, tools and techniques for material characterization and the electrochemical set up for catalyst testing

Chapter 4 explains the influence of fuel ratio on the performance of combustion synthesized bifunctional catalysts for ORR and OER.

Chapter 5 provides the detailed explanation on probing the effect of combustion-controlled surface alloying and explains its effect on ORR and OER.

Chapter 6 detailed on the synthesis of perovskites using solution combustion synthesis and their performance as an oxygen electrocatalyst.

Chapter 7 introduces the effect of salt assisted combustion synthesis on electrochemical performance of perovskites.

Chapter 8 presents the conclusion of the overall current research work and recommends some future work for the improving the efficiency of the catalysts.

CHAPTER 2: LITERATURE REVIEW

2.1. Fuel cells and Batteries

Renewable electric energy resources such as solar and wind power are promising candidate for clean and sustainable energy source that require efficient energy storage devices such as fuel cells, batteries and capacitors. In particular, smart gird energy storage and electric vehicle propulsion demand for highly efficient, durable and inexpensive rechargeable electric storage devices such as reversible fuel cells and rechargeable batteries [17].

Electrochemical process such as oxygen reduction reaction (ORR) and oxygen evolution reaction (OER) is considered to be the heart of various renewable energy generation systems such as regenerative fuel cells and rechargeable batteries, where ORR and OER are opposite reactions [14,15].

In electrically rechargeable metal-air batteries, the two fundamental electrochemical reactions, ORR and OER are responsible for the charging and discharging process respectively and illustrated in Figure 2 [36]. Development of bifunctional ORR and OER catalysts is a long-standing challenge in the field of electrochemistry [14]. The recent advance on the field of electrochemistry aims the design of functionally active single catalyst for ORR and OER suitable for the development of durable and highly active electrically rechargeable metal-air batteries [37-42]. Electrically rechargeable metal air batteries consist of an anode, made of pure metal and an external cathode that uses ambient air where charging and discharging occurs simultaneously, and aqueous electrolyte as conducting medium.

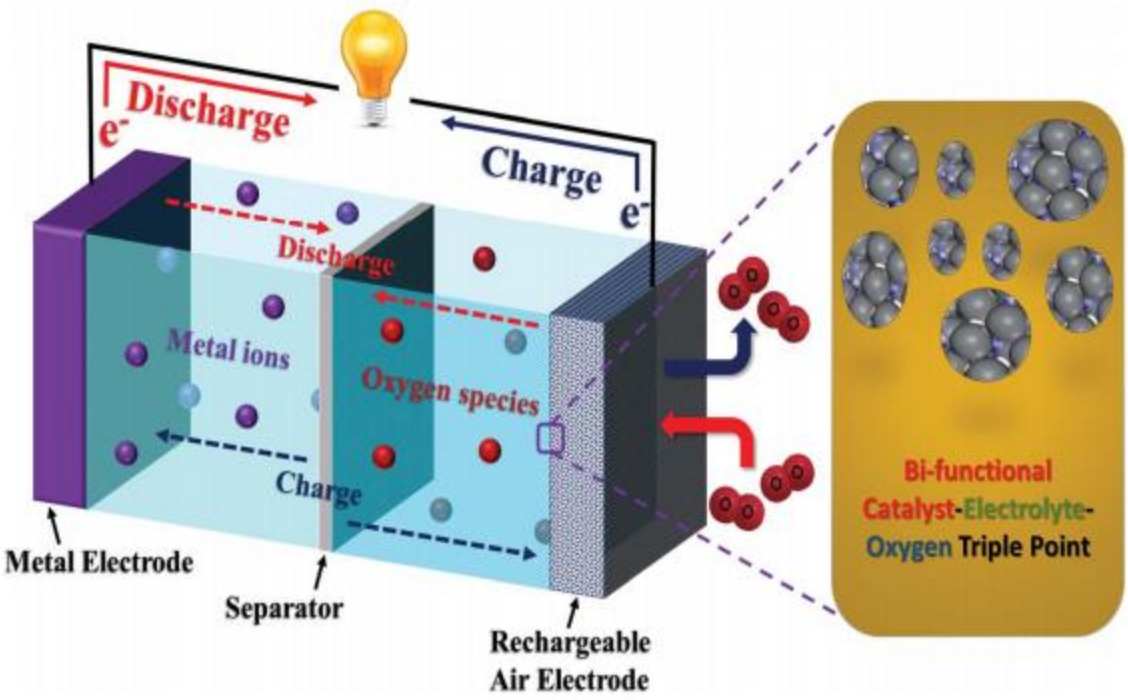

Figure 2. Illustration on the operating principle of rechargeable metal air batteries catalyzed using bifunctional oxygen electrocatalyst [36].

Metals such as Al, Zn, Fe and Mg are commonly used anodes, which improve the stability over aqueous medium through passivating the surface with the corresponding oxides and hydroxides [43]. During discharging, the metal anode gets oxidized and the ORR reaction takes place on the porous catalytic sites of cathode in presence of ambient air, and can be represented as:

Anode: $M \leftrightarrow M^{n+} + ne^-$ (M: metal and n: oxidation number of metal ion)

Cathode: $O_2 + ne^- + 2H_2O \leftrightarrow 4OH^-$

During charging, the above electrochemical reaction can be reversed with oxygen

evolution OER on the cathode surface. The ORR in the air cathode of metal air batteries are similar to ORR in hydrogen fuel cells and are explained in the following section. The ORR in air cathode takes place on the triple phase boundary (Solid-Liquid-Gas) of solid porous catalyst in contact with liquid aqueous electrolyte and gaseous O_2 [43].

Fuel cells generate heat and electricity during the electrochemical reaction between the hydrogen and oxygen to form water. Unlike batteries it does not require recharging as long as fuel and oxidants are continuously supplied [44]. When compared to thermal engine, fuel cells are environmentally friendly, highly efficient and surplus source of reactants make fuel cell a better candidate for energy in coming generations. Due to its efficient performance and technology they are widespread in the commercial areas of portable and stationary power generation, space shuttles and transportation; thus reduce the global issues of energy requirement and clean environment [45]. Many chemical and physical attributes such as composition, structure, phases, valence, morphology, size, surface area, and electronic conductivity can affect the catalytic performances of material driving electrochemical reactions in fuel cells.

The basic operation of fuel cell consists of water-based solution of potassium hydroxide (KOH) as the alkaline electrolyte, negatively charged anode and positively charged cathode from an external supply. The negative hydroxyl ion present in the solution allows the movement ions from anode to cathode and release water as byproduct [46] (Figure 3). At anode, 2 hydrogen molecules combine with 4 hydroxyl ions from the electrolyte to produce 4 water molecules along with 4 electrons.

Anode: $$2H_2 + 4OH^- \rightarrow 4H_2O + 4e^-$$

The electron thus released reaches the cathode through external circuit and react with

water and O_2 to form hydroxyl ions.

Cathode: $O_2 + 2H_2O + 4e^- \rightarrow 4OH^-$

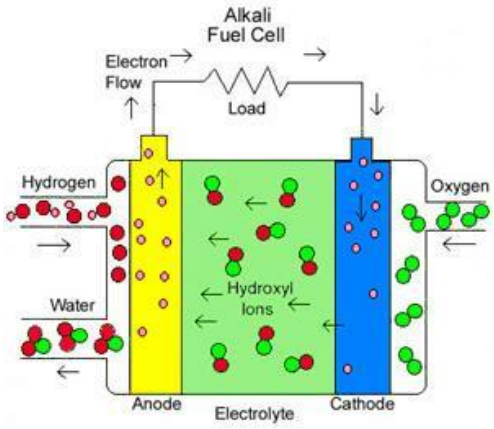

Figure 3. Basic working principle of fuel cells [46].

The anode and cathode are made of highly dispersed conductive active material that promotes the electron transport in the overall reaction. In this chapter we discuss the mechanism of ORR and OER in alkaline medium and the recent advances and development of oxygen electrocatalyst.

2.2. Current perspective

Most of the catalyst development research have focused on either ORR or OER that are applicable for fuel cells and water splitting technologies respectively [26]. Rechargeable air electrode is fabricated with the catalysts that work for both ORR and OER mechanism. Incorporating two catalysts in a single structure increases the system cost and manufacturing complexities. Therefore, it is highly desirable to develop a single active material that is functional for both ORR and OER [47].

During past decade, development of bifunctional oxygen electrocatalyst primarily

focused on reducing the material cost, either through adding some conductive material support and minimize the precious metal loading or by introducing some nonprecious catalyst / metal free catalysts. Recently, new catalyst research efforts are taken for optimizing the bifunctional ORR/OER activity that are comparable with ideal Pt and Ir based catalysts. Great breakthrough have been made to design and prepare various transition metal-based catalysts including spinel structures, perovskite oxides, transition metal alloys, doped metal oxides as well as the nitrides, sulfides, hydroxides and carbides of metals [14].

Metal free carbon-based catalyst are another category of oxygen catalyst that gained great attention due to the great electrical conductivity that offers excellent charge transport during electrochemical reactions. These include hetero atom doped CNTs, graphene layers added to non-precious metals also improves the performance [48,49]. However, it causes the surface degradation due to corrosion of carbon atoms at higher potential during OER [50]. Much more efforts gained attention to develop a composite or hybrid non-precious metal oxygen electrocatalyst. The hybrid catalysts with carbon based materials and expensive components of La, Co, Sr, and Ni show excellent performance without sacrificing the bifunctionality [30,51]. The synergetic effect of metal oxide and carbon improves the ionic conductivity and reduces the overpotential of OER that in turn improves the durability and reduced the degradation during OER. Due to the development of active and durable bifunctional catalyst, overall cost of lithium air batteries reduced to $ 300 per kW per hour that was initially $ 1000 per kW per hour.

2.3. ORR and OER Mechanism in Alkaline medium

Rechargeable metal air batteries and fuel cells operate on the basic electrochemical processes such as ORR and OER. Catalyzing both ORR and OER is critically important due to the intrinsically sluggish kinetics of the two reactions. ORR proceeds through a diffusion followed by absorption of oxygen species, where the electron from the catalyst is transferred to the adsorbed oxygen in order to weaken or break the double bonded oxygen molecule. The resulted hydroxide ion is removed from the catalysts surface into the alkaline solution [52]. While OER is multi step electron transfer process with more difficult and complex electrochemical reactions [53]. Most of the research on bifunctional oxygen electrocatalyst has been conducted in alkaline medium; either potassium hydroxide (KOH) or sodium hydroxide (NaOH), due to less corrosive nature compared to acidic medium. The reaction kinetics is faster in alkaline electrolytes than acidic electrolytes. Also, the exchange current density of ORR and OER is higher in alkaline electrolyte.

The mechanism of ORR and OER in alkaline medium is described in the following section.

2.3.1. Oxygen reduction reaction

The ORR is catalyzed mainly on metals and metal oxides and its mechanism has been extensively studied [11,12,15]. Based on the type of absorbed oxygen, metal based catalysts such as Pt, Au and Ag proceeds through either four electron pathway or two electron pathways [54,55]. The oxygen adsorption can be of bidentate O_2, where two oxygen atoms are coordinated with the metal surface, or it can proceed via end-on O_2

adsorption, where a single oxygen atom is coordinated perpendicularly to the surface of metal. The former adsorption mechanism is known to favor four electron pathway and the latter one proceeds via two electron pathways respectively [43].

The bidentate O_2 adsorption reaction can be expressed as:

$$O_2 + 2H_2O + 2e^- \rightarrow 2OH_{ads} + 2OH^-$$

$$2OH_{ads} + 2e^- \rightarrow 2OH^-$$

Overall reaction: $O_2 + 2H_2O + 4e^- \rightarrow 4OH^-$ (direct $4e^-$ reduction to OH^-)

The end-on O_2 adsorption can be expressed as:

$$O_2 + H_2O + e^- \rightarrow HO_{2,ads} + OH^-$$

$$HO_{2,ads} + e^- \rightarrow HO_2^-$$

Overall reaction: $O_2 + H_2O + 2e^- \rightarrow HO_2^- + OH^-$ ($2e^-$ pathway)

The two-electron end on adsorption can further be processed with either a two-electron peroxide reduction or peroxide disproportionation as follows:

Two electron peroxide reduction: $HO_2^- + H_2O + 2e^- \rightarrow 3OH^-$

Peroxide disproportionation: $2HO_2^- \rightarrow 2OH^- + O_2$

These two ORR reactions may consist of several elementary steps. The oxygen molecule adsorption is further explained using two reaction mechanism; inner-sphere electron transfer mechanism and outer-sphere electron transfer mechanism. During inner-sphere electron transfer mechanism, the undissolved oxygen molecules are directly adsorbed on the active sites of the catalyst to form adsorbed O_2 (O_2^* , where * indicates the active site of catalyst) [56]. However in outer-sphere electron transfer mechanism the hydroxide ions and dissolved oxygen species from the aqueous electrolyte is adsorbed onto the active sites. In the outer-sphere electron transfer mechanism the oxygen species cannot

directly bond to the active sites. In alkaline medium, both the reactions may occur simultaneously, while in acidic medium inner-sphere electron transfer mechanism is predominant due to the insufficient hydroxide ions in the medium. In alkaline medium, the active sites immediately adsorb the hydroxide ions and the outer-sphere electron transfer mechanism is followed with the inner-sphere electron transfer mechanism. The solvated oxygen molecule $[O_2^-.(H_2O)_n]$ is connected to the adsorbed hydroxyl species(OH_{ads}) through a hydrogen bond between H atom in (OH_{ads}) and O atom from water molecule. Thus after de-solvation, $O_{2,ads}^-$ is formed over the surface of the active sites of the catalysts [57].

M-OH + $[O_2^-.(H_2O)_n]$ +e^- → M-OH + $[O_2^-.(H_2O)_n]$

$[O_2^-.(H_2O)_n] \rightarrow O_{2,ads}^-$ + nH_2O

The further reduction of adsorbed molecular oxygen O_2^* proceeds with three predominant mechanisms explained as follows:

Dissociation pathway: These are direct reaction mechanism, where the O-O bond directly breaks to form two O^* intermediates and is further reduced separately into OH^* species.

Associative pathway: instead of breaking O-O bond directly into O^* intermediate, a protonation of O_2^* become a dominant pathway that form OOH^* and is followed through the cleavage of O-O bond to form two O^* intermediates and is further reduced separately into OH^* species.

Peroxide pathway (or 2nd associative): OOH^* intermediate is formed via protonation step of O_2^* and is further reduced into HO_2^- through $2e^-$ reaction pathway.

The ORR mechanism over the metal oxide catalyst follows the same basic principle of

pure metal as discussed above, but the charge distribution might be different due to the incomplete coordination of the surface cations of the stoichiometric oxide with the adsorbed oxygen atom. The mechanism and reaction pathway varies depending on the catalyst's electronics structure and properties. The anion coordination is completed from the oxygen from the water molecule of the aqueous electrolyte. For transition metal oxides (TMO), dominant ORR mechanism is through the associative $2e^-$ + $2e^-$ pathway [58]. Based on associative pathway, O-O bond is converted into O^* with OOH^* intermediates and meantime, electron would transfer from metal cation into O^* intermediates to form $M^{(m+1)} - O^{2-}$ [59]. The ORR pathway on TMO can be described as either inner-sphere electron transfer mechanism or outer-sphere electron transfer mechanism as explained below:

Inner-sphere electron transfer mechanism:

Direct $4e^-$ reaction pathway:

$$2M^{(m+1)} - O^{2-} + H_2O + e^- \rightarrow M^{(m)+} - OH^- + OH^-$$

$$O_2 + e^- \rightarrow O_{2,ads}^-$$

$$M^{(m)+} - OH^- + O_{2,ads}^- \rightarrow M^{(m+1)-} - O - O^{2-} + OH^-$$

$$M^{(m+1)-} - O - O^{2-} + H_2O + e^- \rightarrow M^{(m)+} - O - OH^- + OH^-$$

$$M^{(m)+} - O - OH^- \rightarrow M^{(m+1)-} - O^{2-} + OH^-$$

$2e^-$ reaction process:

$$M^{(m+1)-} - O - O^{2-} + H_2O + e^- \rightarrow M^{(m)+} - OH^- + HO_2^-$$

Outer-sphere electron transfer mechanism:

$$\text{M-OH} + [O_2^-.(H_2O)_n] + e^- \rightarrow \text{M-}OH^- + [O_2^-.(H_2O)_n]$$

$$[O_2^-.(H_2O)_n] \rightarrow O_{2,ads}^- + nH_2O$$

$$\text{M-}OH^- + O_{2,ads}^- \rightarrow M^{(m+1)-} - O - O^{2-} + OH^-$$

$$M^{(m+1)-} - O - O^{2-} + H_2O + e^- \rightarrow M^{(m)+} - O - OH^- + OH^-$$

$$M^{(m)+} - O - OH^- \rightarrow M^{(m+1)-} - O^{2-} + OH^-$$

$2e^-$ reaction process:

$$M^{(m+1)-} - O - O^{2-} + H_2O + e^- \rightarrow M^{(m)+} - OH^- + HO_2^-$$

The rate determining step of ORR on the surface of the catalyst is the competition between $O_2^{2-}/2OH^-$ displacement or the regeneration of OH^- that in turn determined by the degree of σ^* orbital and covalence of metal oxide. Thus high-performance catalyst can be obtained through proper tuning of the electronic structure of metal oxide [32]. The ORR reaction takes place on the triple site of catalyst-electrolyte-oxygen and it is critically important to increase the number of active sites shared in the interface of solid-liquid-gas phase system.

2.3.2 Oxygen Evolution Reaction

The mechanism and pathway for oxygen evolution reaction is complex and is difficult to describe. As the name says, the oxygen is evolved from the metal oxide sites, rather than a pure metal [14]. So the mechanism and electron transfer pathway may vary from each catalyst depending on the geometry of the metal cation. The transition metal ions with multi-valences are highly favorable for OER because the reaction proceeds through the interaction of oxygen intermediates and metal ions that ends with bond formation and

change in valence state. The rate determining factor of the OER is the geometric arrangement of metal cation site that changes the absorption energy of the oxygenated species. The OER mechanism of the transition metal oxide in alkaline electrolyte can be represented as follow:

$$2M^{m+} - O^{2-} + OH^{-} \rightarrow M^{(m-1)+}\text{-O-}OH^{-} + e^{-}$$

$$M^{(m-1)+}\text{-O-}OH^{-} + OH^{-} \rightarrow M^{m+} - O - O^{2-} + H_2O + e^{-}$$

$$2M^{m+} - O - O^{2-} \rightarrow 2M^{m+} - O^{2-} + O_2$$

Owing to low redox potential and high electronic conductivity, RuO_2 and IrO_2 are highly active for oxygen evolution reaction. However, the high cost and sluggish kinetics for ORR limits their application as bifunctional oxygen electrocatalysts [36].

2.4. Electrocatalyst for ORR and OER

Based on the literatures, bifunctional oxygen electrocatalyst are classified as four broad groups; noble metals, non-precious metals, carbon-based materials, and hybrid materials. Noble metals are ruthenium (Ru), rhodium (Rh), palladium (Pd), silver (Ag), osmium (Os), iridium (Ir), platinum (Pt), and gold (Au) that prevent the corrosion and oxidation when exposed to air [14]. The cost of these materials is comparatively higher. Non-precious metals are commonly transition metal oxides (TMOs) and different forms of transition metals such as oxides, nitrides, sulfides and carbide with different crystal structures such as spinel, pyrochlores and perovskites. Carbon based materials that have been found to be efficient for ORR and OER includes carbon black, CNTs and graphene. Finally, the hybrid

catalysts consist of non-precious materials incorporated with carbon-based materials that improve the electrical conductivity of the materials [28]. Next section discusses some of recently reported electrocatalyst for ORR and OER reactions, including the bifunctional catalysts.

2.4.1. Noble metal catalysts

Platinum : Platinum (Pt) and Pt-alloys are the most active catalysts for ORR, but they do not show any catalytic activity for OER due to the formation of oxide film over the surface at higher potential [60-65]. The ORR activity of low index Pt surface have been widely studied and the performance increases in the order of Pt (100) <<Pt(111)~Pt (110) [66]. Felix and coworkers extensively investigated the structural effect of high indexed Pt surface and interpret that the ORR activity is greatly dependent on the existence of terraces and steps on the Pt surfaces. The activity is higher for increased terrace density and for ones with lower terrace width on high index planes of n (hkl)-(mno) where n indicates the number of atomic row terraces , (hkl) is the terrace structure and (mno) represents the structure of steps [67,68]. Similar to the activity effect on high index planes, several studies have been conducted to understand the shape controlled effect on ORR activity. Octahedral Pt(111) nanoparticles are tested to be more active than cubic Pt(100). Tetrahexahedron (hk0) trisoctahedron (hhk) and trapezohedron (hkk) and nanoparticles with at least one Miller index larger than unity were found to be more active than (100) or (111) facets [69-71]. The reason for this activity improvement is due to the presence of high density of low-coordinated atoms present on the steps, kinks and edges [72]. The challenge in using shape-controlled Pt is the stability of nanoparticles under ORR, as they tend to change to thermodynamically equilibrium shapes during the reaction

in alkaline medium [73].

Size of Pt particle also affects the ORR activity; the particle size reduced from 5 nm to 1nm shows a decrease in the ORR activity. This could be due to a drastic decrease in (111) and (100) facets, and the existence of more low coordinated edges and kinks on the surface sites that cause stronger oxygen bonding. Owing to this effect, the specific activity of the Pt nanoparticles with size less than 3 nm shows a drastic decrease in activities, and the peak mass activity is observed at 3nm that decreases for higher and lower sized Pt nanoparticles [74]. For particles smaller than 3 nm, the rate determining step is O-O bond breaking due to the higher binding energy of oxygen; and for larger particles, it is the first protonation and electron transfer reaction [75].

Fabbri and coworkers studied the influence of Pt dispersion on conductive carbon support that greatly reduced H_2O_2 through decreasing the interparticle distance and extending an electric double layer between nearby Pt atoms [76] . Pt alloys with superior ORR activity can be explained by various reasons that include the compressive strain-stress due to the smaller Pt-Pt bond, increased surface roughness due to the dissolution of transition metal oxides and finally the strain and ligand effect that causes the downshifting of Pt d-band center [77,78]. The activity enhancement of PtM alloy originates from M site transition metals where M = Co, Ni, Fe, Cu, Ag, Au, Pd, Cr, Mo, Mn, Al), out of these Pt alloyed with Co, Ni and Fe are widely considered due to their superior ORR activity. Han and his team found that the ORR activity and stability is highly influenced by the dissolution potential of the alloyed element [79]. The ORR activity of as-sputtered polycrystalline film shows the performance trend as Pt_3Co~ Pt_3Fe > Pt_3Ni > Pt_3V> Pt_3Ti> Pt [78]. However, Pt skeleton and skin type surface prepared after proper thermal annealing

shows a different trend in the specific activity that follows the order of Pt_3Co > Pt_3Ni > Pt_3Fe> Pt_3V> Pt_3Ti> Pt. These results show the significance of post thermal treatment of PtM alloys on engineering the ORR activity and surface structure [80]. Alloying Pt with some early transition metals (Y, Sc, Hf, La, Ce, Ga and Gd) also has some pronounced effect on the ORR activity and stability. Sung *et al* studied ORR activity on PtM films (M = Y, Zr, Ni, Co and Ti), and the results show an increasing order of Pt_3Ti < Pt < Pt_3Zr < Pt_3Co< Pt_3Ni < Pt_3Y. A similar study was conducted by Stephens *et al*, who found that Pt_5M shows much higher activity than Pt_3M alloys as shown in Figure 4**.**

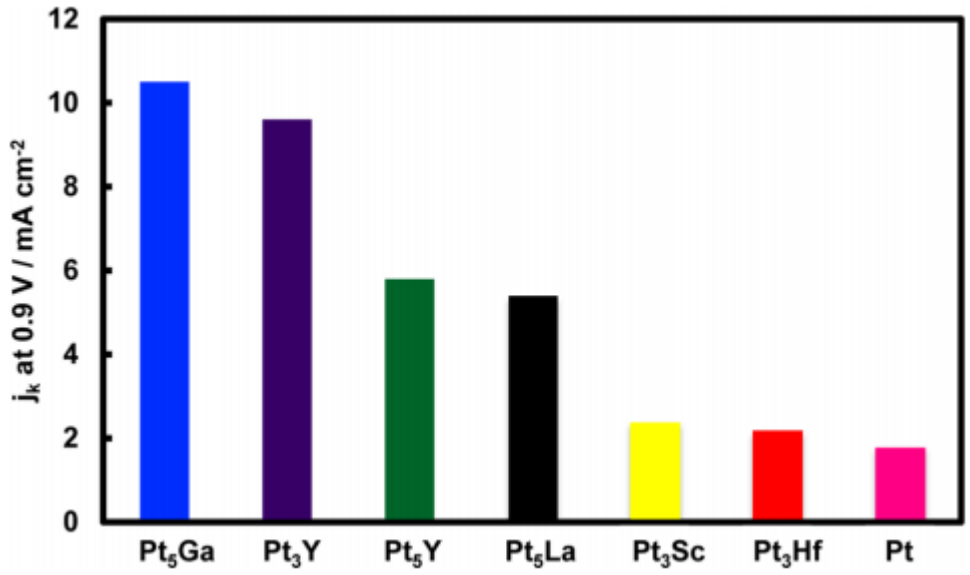

Figure 4. Kinetic current density comparison of various thin fil, Pt_3M and Pt_5M alloys at 0.9 V [81].

The activity of Pt alloys is highly influenced on the crystalline orientations, where Pt_3Ni (111) are more active than Pt_3Ni (110) and Pt_3Ni (100) [81]. Choi *et al* studied the nature

of ORR activity on octahedral Pt-Ni alloy (edge length 9 nm) with its effect on atomic % of Ni on the total alloy as shown in Figure 5 . It was found that $Pt_{2.5}Ni$ shows much more activity than $Pt_{1.4}Ni$, Pt_2Ni, $Pt_{3.2}Ni$ and $Pt_{3.7}Ni$. In case of too low Ni content, binding energy of oxygen is too high that slows down the reduction of the adsorbed oxygenated species. On other hand, too high Ni content resulted in low binding energy for breaking O-O bond and facilitates further charge transfer. $Pt_{2.5}Ni$ have neither too weak nor too strong oxygen binding energy that showed significantly highest ORR activity [82].

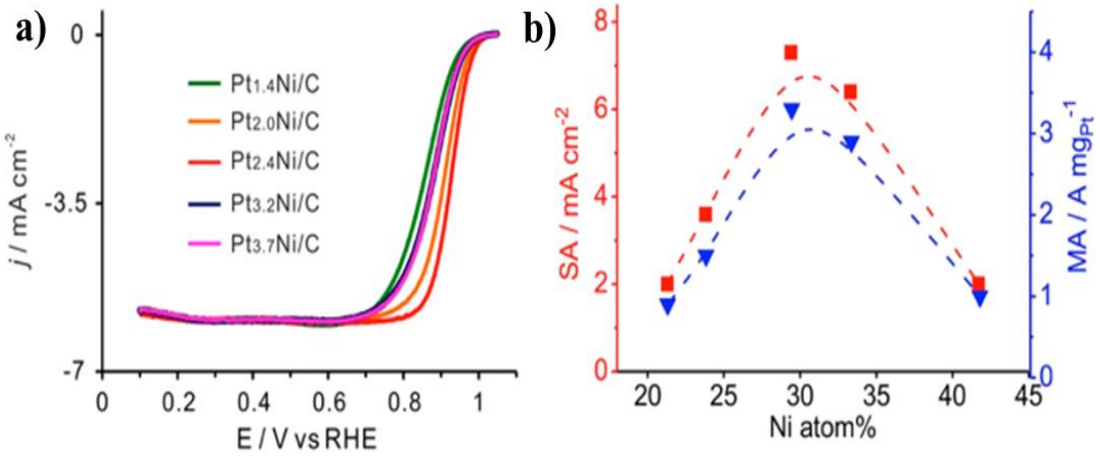

Figure 5. ORR polarization curve of Pt-Ni/C with different Ni atomic composssssssition in O_2 saturated 0.1 M $HClO_4$ at a scan rate of 10 mVs^{-1} with rotor speed 1600 rpm b) Mass activity and specific activity as a function of Ni atom % of octahedral Pt-Ni/C at 0.9 V [82].

Palladium:

Palladium (Pd) belongs to Pt group that shares similar electronic properties but shows ORR activity 5 times lower than Platinum. The reactivity of Pd is much higher than Pt

and facilitates strong bonding of oxygen, which in turn gets oxidized at more negative potential. Kondo and coworkers studied the effect of low index planes of Pd structure on ORR activity and conducted a comparative study with Pt [83]. The higher index facets Pt(110) and Pt (111) exhibits higher ORR activity than Pt (100) in $HClO_4$ solution, while Pd (100) shows highest activity among them when used in the same solution as represented in Figure 6.a**.** Shao *et al.* studied the structural dependence of Pd towards ORR and found that cubic Pd/C shows a specific activity 10 times higher than octahedral Pd/C at 0.9 V in acidic solution as in Figure 6.b [84]. The higher activity of cubic Pd/C is attributed to the low oxygen coverage that provides more reactive site than octahedral Pd/C and conventional Pd nanoparticle. Moreover, the DFT analysis shows that the oxygen binding energy of Pd(100) is comparatively lower than Pd(111), that improves the ORR kinetic [85] Cubic Pd with an average particle size of 27 nm shows higher activity than spherical particles [86]. The main challenge in using Pd cube is its extremely low stability and potential cycling converts the regular cube to irregular morphology.

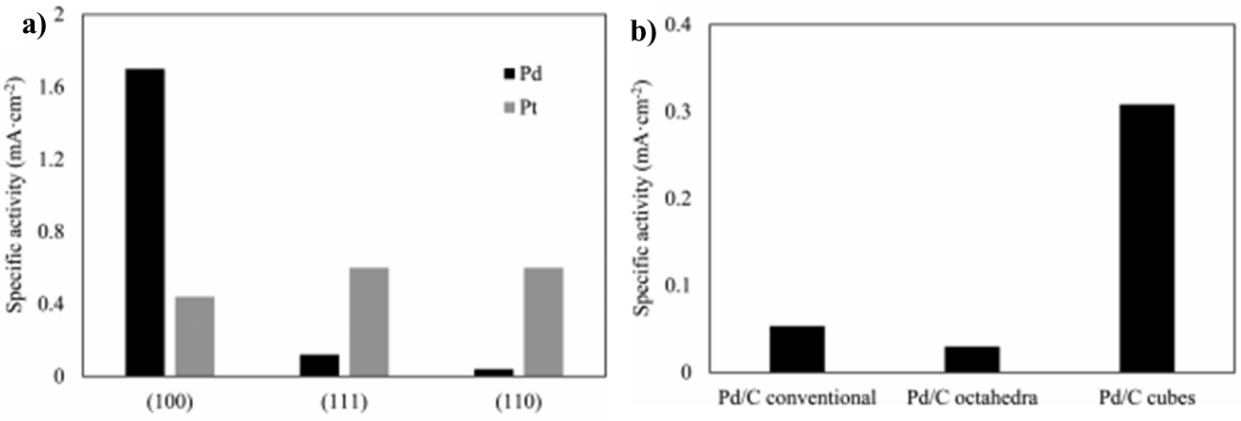

Figure 6. ORR specific activity a) on low facets of single crystal Pt and Pd and b) nanostructured Pt and Pd at 0.9 V in HClO4 solution [84].

Pd nanorods synthesized via electrodeposition process exhibits an ORR activity 10 times higher than Pd nanoparticles [87]. Alloying Pd with other metals Pd-M (M= Fe, Ni, Co, Cr, Ti, Mn, V, Sn, Cu, Ir, Ag, Au, Rh, Pt) shows much higher ORR activity that are comparable with Pt. Zhou *et al*. experimentally analyzed the ORR activity of $Pd_3Fe(111)$ and found that the activity and kinetics are greatly improved than the conventional Pd and are comparable to Pt [88].

Different nanoalloys of Pd with various morphologies such as sponges (PdAu) [89], nanodendrites(Pd-Rh) [90], nano cubes, octahedral etc. has widely been explored for ORR. Metal carbides and oxides are widely used supports for Pd alloys to improve the activity and stability towards ORR mechanism. Pd-Au supported over nanocrystalline tungsten carbide shows excellent ORR activity with a positive potential shift of 70 mV when compared to Pt/C [91]. The onset potential of Pd_3Co alloy was shifted to 100 mV in positive direction, through the addition of Ce as an efficient metal support during the

synthesis. The addition of Ce shows a Pd enrichment on the alloy surface and promotes the interaction between PdCo and Ce oxide that improves the overall electronic conductivity. Similar study carried out by Kwon et al, observed the synergetic effect of CeO_2 and PdCo causes a positive onset potential shift of 50 mV [92] . Durability of Pd and Pd based catalysts is still challenging for practical applications.

Ruthenium and Iridium:

Ruthenium (Ru) and Iridium (Ir) is found to be the top catalyst on the volcano activity plot of OER Thermochemical density functional theory (DFT) [93]. Neyerlin *et al* studied the effect of alloying Ru and Ir with transition metals that shows the improvement in OER activity [94]. Amorphous RuO_x showed prolonged activity than crystalline Ru oxide owing to its structural flexibility, but the durability was the main concern [95]. Sun *et al* reported the synthesis of Ruthenium nanocrystals supported over carbon black using surfactant assisting method as an efficient catalyst for ORR and OER that shows excellent performance in Li-ion batteries with high reversible capacity, low charge-discharge overpotential and good cyclic performance up to 150 continuous cycles [96]. Ruthenium supported over graphene materials shows excellent bifunctional electrochemical characteristics, has been extensively studied [ref]. Jian *et al* reported the synthesis of core shell RuO_2 that was coated on the core CNTs shows excellent performance in rechargeable Li-O_2 batteries [40]. These hybrid core-shells RuO_2/CNT shows improved catalytic activity and cyclic performance. Kwak and coworkers developed carbon free catalyst with Ru and RuO_2 foam as binders as electrocatalyst using electrodeposition technique *via* a hydrogen bubble template. The prepared particle with dendritic bracken-like structure is divided into thin branches that exhibit excellent oxygen efficiency and

low charge/discharge overpotential in Li-ion batteries. Nanosized Mn-Ru binary oxide that contains γ-MnO_2 and hydrous RuO_2 with fusiform nanorods and nanoparticle morphologies exhibits remarkable electrocatalytic activity towards ORR and OER with excellent cyclic stability for Li-ion batteries [97] . A spool like Ru-Ni nanocrystals with Ni concentrated in pillars and Ru as hexagonal rings in sandwich form are successfully synthesized that shows excellent electrocatalytic activity in alkaline medium with low overpotential and tafel slope with excellent durability [98].

Reier and team studied the OER activity and stability of Ru, Ir and Pt nanoparticles supported over carbon black and compare the activity corresponding to bulk material [99] . In contrast, Ir in nanoparticle and bulk phase shows comparable OER activity than Ru and Pt. Moreover, the Ru nanoparticle exhibits strong corrosion at higher potential of OER, which affects the stability to sustain the reaction. Highly interconnected nanoporous Ir-Pd alloy supported on carbon black shows remarkable ORR and OER performance with excellent stability in alkaline medium. Pd (111) facet promotes the oxygen reduction reaction, while Ir particles are responsible for the oxygen evolution. The study on the atomic percentage of Ir and Pd shows that, Ir:Pd with a ratio of 0.23:0.77 is found to be the optimum ratio for high activity, performance and stability [100]. Recently, Yang *et al* reported the synthesis of free-standing 3D porous Ir-Ni-Co alloy ($Ir_{70}Ni_{15}Co_{15}$) using dealloying strategy that shows significant improvement in the electrocatalytic activity in acidic medium [101].

Silver based metal catalyst:

Silver (Ag) shows high activity, better tolerance, stability and longer performance for ORR mechanism [102,103]. Silver is one of the best HO^{2-} eliminating catalysts and the

Ag single phase crystal and Ag nanoparticles follows pseudo 4 e^- pathway [104-106]. It was reported that the Ag with larger particle size of 174 nm proceeded by direct 4 e^- pathway while that of Ag with 4.1 nm size follows two step $2e^- + 2e^-$ electron process. The more defective surface on the bulk Ag provide a strong absorption of OH^- ions that hinders the two-site O_2 chemisorption that was the main criteria for $4e^-$ reaction pathway [107]. The activity of single facet Ag crystal increases in the order of Ag(100) ≤ Ag(111) ≤ Ag(110) [108]. In Ag (110) the absorption of hydroxide species and the activation energy that enables more active sites for the oxygen species.

The weaker Ag-O_2 interaction makes stronger O-O bonding that causes difficult to break the bond in electrolyte. So, Ag-O interaction must be stronger to enhance the electrochemical activity of the catalyst and consequently increases the kinetics of ORR. Also, due to its cost ORR activity of pure Ag is not good enough for commercial applications [38,109,110]. To increase the catalytic activity of silver, doping with some other transition metal is needed. So, it is required to modify the Ag with some elements that are cheaper and abundant. This can be achieved by incorporating the cheaper metals along with Ag. Cobalt is a better option due to the low cost, electrical resistance and being corrosion free in basic medium. An active Co^{3+} site in Co_3O_4 shows great performance in ORR. The high interaction of adsorbed oxygen with Ag in the Ag-Co/C particle increases the ORR activity by rupturing O-O bond. Also, the adsorption of oxygen to Ag from the well oxidized Co_3O_4 results in increase in the oxygen transport rate. Lin *et al* reported that the presence of cobalt in Au-Co for ORR changes the electronic structure of the gold [111]. Y. Wang *et al*. reported on the hydrothermal method of synthesis of Ag-C, Co_3O_4-C and Ag/Co_3O_4-C and compared the mono metal and bimetal effect in the catalytic

activity [112].

Cu is highly abundant in earth crust and has been used for various electrocatalytic reactions. So, we choose copper (Cu) and silver (Ag) as elements for making the electrode. Silver composites with cobalt, copper, palladium, nickel and manganese were reported elsewhere and show good improvement in the ORR activity through the synergetic coupling effect between silver and the metals incorporated [103,113,114]. These silver alloys exhibit lower overpotential and higher limiting current density along with high stability. The alloying of Ag and Cu has been reported to be an active electrocatalyst for fuel cell and zinc-air batteries, with $Ag_{75}Cu_{25}$ showing better electrocatalytic performance for ORR reaction as compared to silver alloys with Co, In and Fe having similar composition [115,116]. DFT calculations indicate the existence of strong adsorption energy and low activation energy barrier in bimetallic silver-copper [117].

Ag (40 % wt)/ CNT is reported as the best composition of Ag/CNT for oxygen electrocatalyst [118]. Graphene with two dimensional (2D) and three-dimensional (3D) framework loaded over Ag catalyst were reported recently and Ag/GO linked by thiols, Ag/rGO linked by deoxyribonucleic acid (DNA), and 3D GO/carbon supported Ag composite (Ag/GO/C) are the most significant ones [119-121]. The onset potential (E_{onset}) and half wave potential ($E_{1/2}$) of these silver/ nanocarbon catalysts are 50-100 mV lower than the commercial Pt/C.

Gold based metal catalysts:

Gold based metal catalysts are of considerable importance and are achieved wide attention due to their good conductivity, better biocompatibility, tunable electronics and

optical characteristics, higher catalytic activity. Au (100) is the most active single crystalline facet for ORR applications. The over potential for OER on Au (100) at 0.34 V in 0.1 M NaOH electrolyte is lower than that of Pt (100) in 0.1 M $HClO_4$ [122,123]. Bulk Au in polycrystalline state is relatively inert and at nanoscale Au exhibits good catalytic activity. Incorporating cheaper noble metals such as Ag or other transition metals reduces the overall cost of the oxygen electrocatalyst. Hu *et al.* reported a volcano plot on the composition effect of AuAg catalyst in the size range of 3 to 5 nm on the activity, where 36 at.% of Au is the best composition that gave best performance [124]. AgAu Janus particles were synthesized using a combination of Langmuir−Blodgett method and galvanic exchange method, with a minimum loading of Au, the specific activity and mass activity of the catalysts was found to be 6 to 7 times higher than Ag nanoparticles [125]. Gengtao and team, first time reported the highly rigid and flexible 3D porous nickel-manganese oxide (Ni_6MnO_8) coupled with 1D ultrathin Au nanowires (Au-NWs) as an efficient catalysts for bifunctional ORR/OER reactions [126]. The Au nanowire act as a flexible conductive electronic network that promote ORR, while nickel-manganese oxide is robust carbon free support highly stable on alkaline environment that are prominent for OER. The coupling of both structures together effectively shows a complementary role through overcoming their deficiencies and promoting both (ORR and OER) oxygen electrocatalytic reaction. The structural advantage of hybrid Ni_6MnO_8/ Au-NWs as the oxygen electrocatalyst are shown in Figure 7 . The Ni_6MnO_8/ Au-NWs shows significantly improved activity in terms of more positive onset potential, half wave potential, number of electrons and least yield of HO_2^-. Gold-Iridium composite over carbon support (Au-Ir/C) synthesized using facile one-step

process is reported as an efficient bifunctional catalyst with excellent ORR/OER characteristics and catalytic stability [127]. Self-supporting nanoporous gold prepared using dealloying method and precious palladium over layer was successfully deposited by epitaxial layer by layer growth was found to be a promising catalyst for ORR and OER that are applicable for fuel cells and metal air batteries [128]. Zhang *et al* followed facile one step hydrothermal process for the synthesis of molybdenum disulfide nanosheets that are decorated with gold nanoparticles were reported as effective catalyst for ORR and OER for rechargeable Li–O_2 batteries [129].

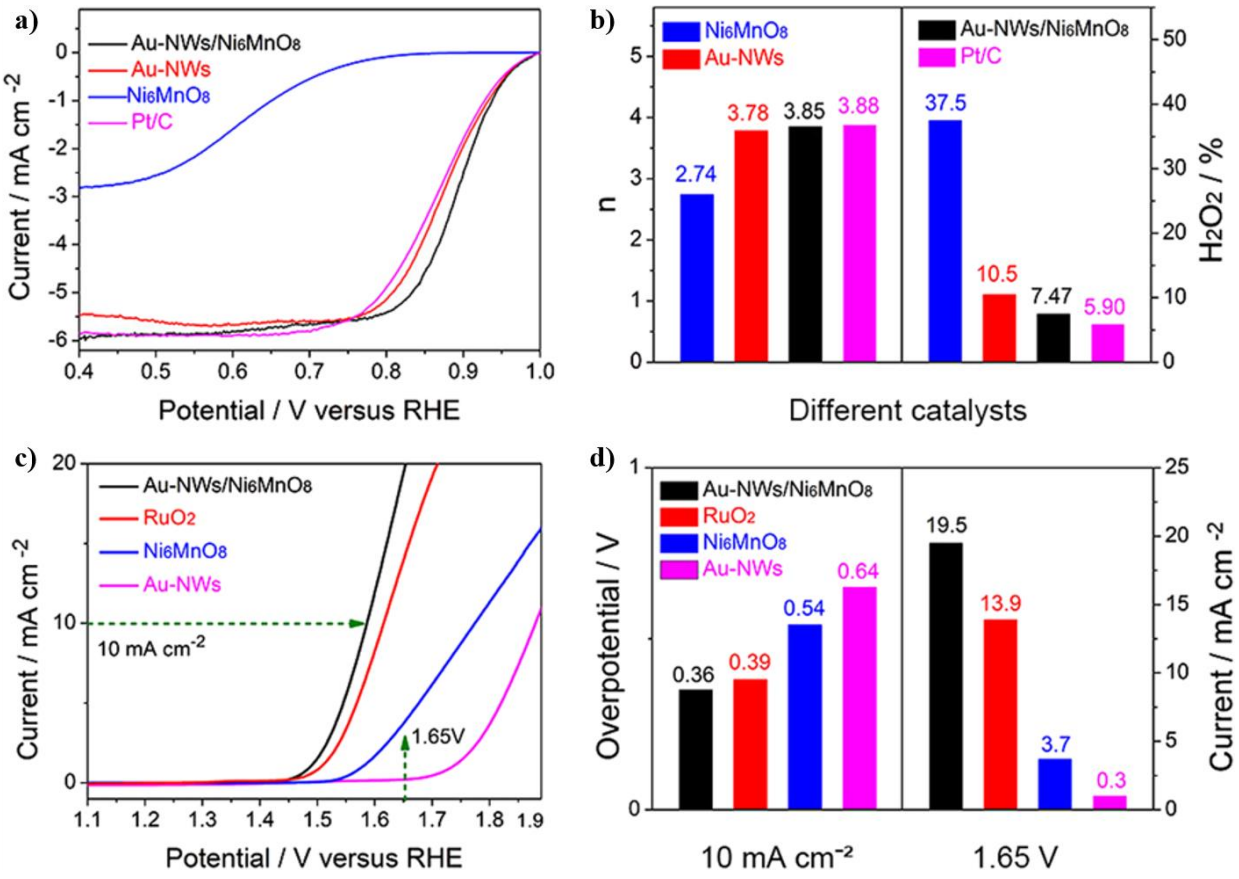

Figure 7. a) LSV plot of the catalysts in 1 M KOH saturated with O_2 at a rotation speed

of 1600 rpm and 5 mVs^{-1} b) representation of hydrogen peroxide and number of electron transfer (n) c) OER polarization curve d) bar plot on overpotential, onset and halfwave [127].

Nanosized Au supported over Graphene is more stable and active than supported over conventional Vulcan carbon [130]. Au/reduced graphene oxide (rGO) reported three times higher the specific activity than Au nanoparticles [131].

Non-Noble metal catalysts

Transition metal oxides (TMOs): TMO gain great importance in the field of catalysis due to its abundance, low cost and stability [132]. Even though, they are less stable in acidic medium, they are reasonably stable in alkaline solution. Manganese oxides are the first transition metal oxide to act as a catalyst in ORR [133]. Mao *et al* noticed first the dependence of oxidation states in Mn for the electrocatalytic reaction with activity in the order of Mn_5O_8 < Mn_3O_4 < Mn_2O_3 < MnOOH [134]. Later on Cheng *et al* [135] found the activity of MnO_2 phases α- > β- > γ-MnO due the conductivity and tunneling effect of electrons is shown in Figure 8.

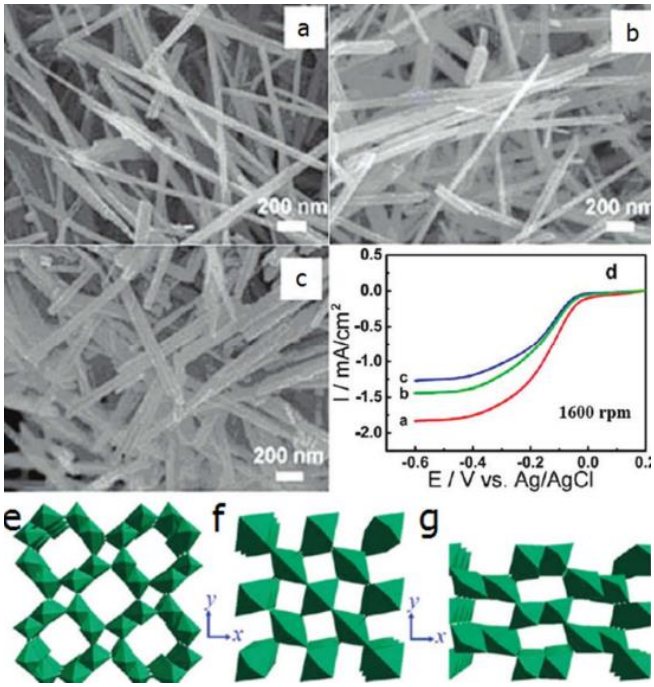

Figure 8. α-MnO_2, β MnO_2 , γ MnO_2 (a-c) SEM images (e-g) crystal structure (d) LSV of . α-MnO_2 (red), β MnO_2 (green), γ MnO_2 (blue) at 1600 rpm in O_2 saturated 0.1 M KOH at scan rate of 1 mVs^{-1} [135].

α-MnO_2 with enlarged surface area enhances the catalytic performance of the electrode material. Similar study was conducted by Meng *et al.* on the synthesis if MnO_2 with different morphology such as nanoparticles, nanowires and nanoflakes with different crystallographic structures as shown in Figure 9.a-g (α-MnO_2, β MnO_2 , γ MnO_2, amorphous MnO_2) on bi-functional electrocatalytic activity [136]. The electrochemical activity of these structures follow in the order of α-MnO_2 > amorphous MnO_2 > β MnO_2 > γ MnO_2 towards ORR and OER activities as in Figure 9.h-i.

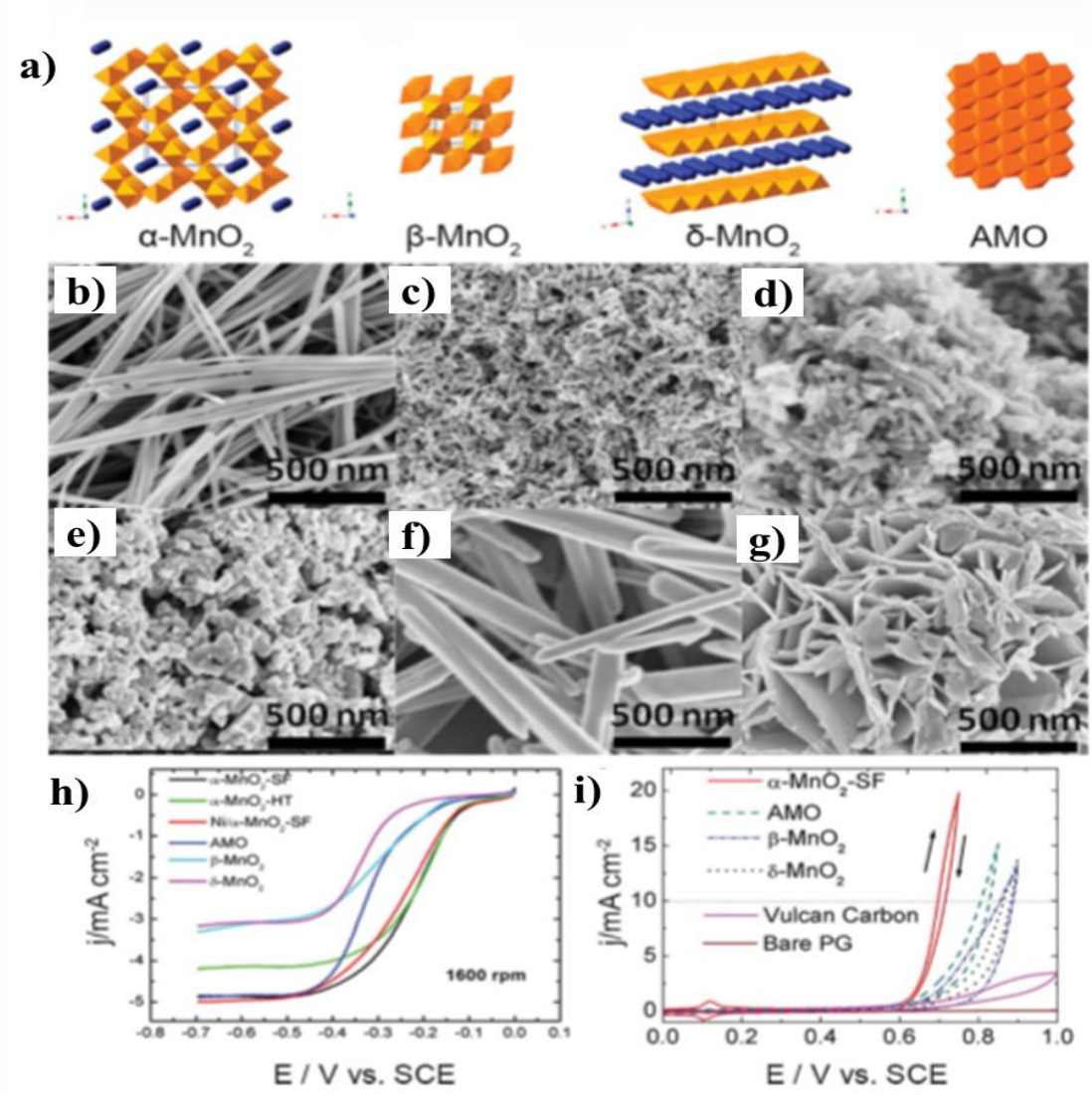

Figure 9. a) Different crystallographic structures of MnO_2 b) α-MnO_2 (Hydrothermal) c) α-MnO_2 (solvothermal) d) Ni/ α-MnO_2 (solvent free synthesis) e) amorphous α-MnO_2 f) β MnO_2 g) γ MnO_2 h and i) ORR and OER polarization curves of various crystal phases of MnO [136].

While MnO_x with low valency metals such as Ni (II) or Mg (II) improve the selectivity and stability of the catalyst through the direct four electron pathway [137,138]. Hybrid

oxides with choral, spinel, perovskites, layered structure with other transition metals with variety of oxidation states give more freedom to tune the physical and chemical property of the materials [139,140]. Zhu *et al* synthesized a group of compounds $M_xFe_{3-x}O_4$ (M=Mn, Fe, Co and Cu) with ferrate spinel structure [141]. Among this $MnFe_2O_4$ shows better performance comparable to commercial Pt/C. The activity of perovskites depends on the availability of σ* -orbital and the oxygen covalence [142]. Low conductivity is one of the reasons hindering the performance of transition metal oxides. To overcome this effect, high quantity of carbon material was added to the catalyst only for improving conductivity. In effect the dead weight of the total material loaded to the electrode increases and thus reduces the interfacial contact

Cobalt exists in different valance states with donor-acceptor chemisorption sites for the absorption or desorption of oxygen are suitable as bifunctional oxygen electrocatalyst [143,144]. Spinel Co_3O_4 with Co^{I} and Co^{II} oxidation states consist of tetrahedral and octahedral sites respectively. The tetrahedral occupied sites are active for ORR, while octahedral Co^{II} form Co-O that favors OER mechanism [145]. In Co_3O_4, replacing Co^{III} ions with manganese reduces the intrinsic OER activity [146]. Another study reported that, decreasing Co^{III} ions on octahedral sites reduces the OER performance, while doping Mn on octahedral and tetrahedral site shows favorable ORR mechanism [147].

Trasatti *et al.* reported the dependence of OER activity on the enthalpy requirement for the transition from lower to higher oxidation states [148]. Menezes *et al* prepared nano-chains of Co_3O_4 s from cobalt oxalate precursor micelles that are found to be more stable and active for OER than solvothermal Co_3O_4 nanorods are shown in Figure 10 [149].

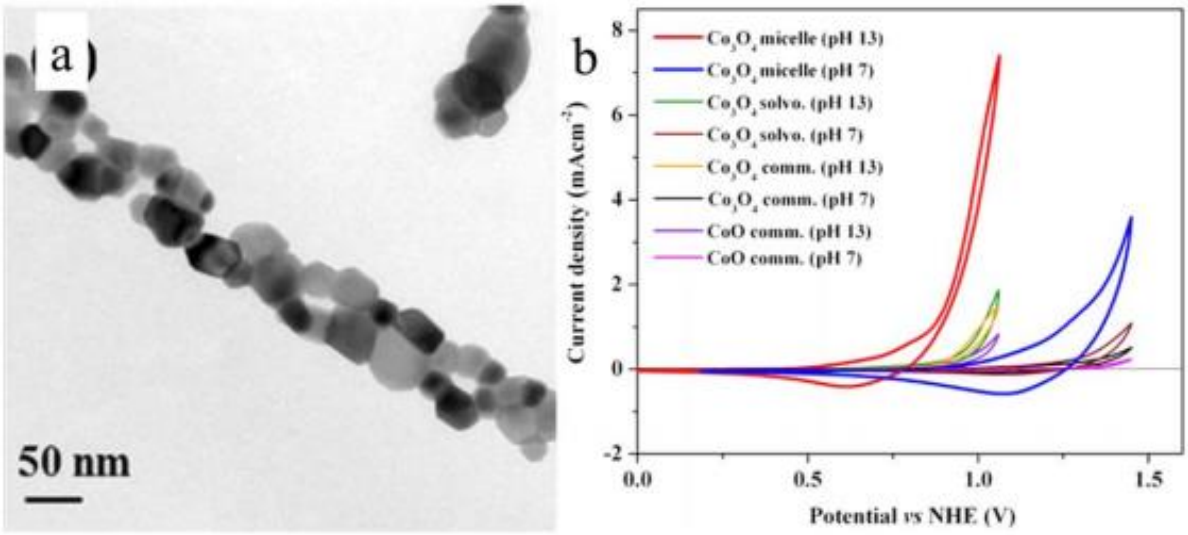

Figure 10. (a) TEM image of Co_3O_4 nanorods (b) cyclic voltammetry of Co_3O_4 prepared from micellar (nanochains) and solvothermal (nanorods) synthesis and compared with commercial cobalt oxides [149].

Li et al reported the preparation of NixCo3-xO4 nanowire arrays with self- standing mesoporous structure with Ni doped into Co3O4, increases the overall roughness factor, conductivity, current density and electrochemical performance [150]. The current density of NiCo3O4 was 7 times higher than Co3O4. Prabhu and coworkers developed 1D NiCo2O4 spinel oxide using electrospinning technique and tune the surface morphology into porous tubes and rods through adjusting the synthesis parameters. The onset potential for nanotubes and nanorods was found to be 0.78 V and 1.62 V (vs. RHE) with an OER potential difference of 0.84 V. This overpotential gap is smaller than the other reported precious metals such as Pt/C, Ru/C and Ir/C [151]. In another study, a ternary metal oxide of CuxMn0.9−xCo2.1O4 (x= 0, 0.3, 0.6, and 0.9) with 4 nm particle size exhibits excellent ORR and OER activity in 1 M KOH medium. The potential difference between

the half wave potential of CuxMn0.9−xCo2.1O4 and commercial Pt/C was measured to be only 50 mV. Also, the onset potential of OER for CuxMn0.9−xCo2.1O4 is 100 mV negative than commercial Pt/C shows the possibility of replacing the precious Pt with these ternary oxides [152].

Perovskites: Recently perovskite oxides received wide attention due to the flexibility and tunability of the physico-chemical and catalytic properties. These classes of materials possess exceptional thermochemical stability, ionic conductivity and electrochemical behavior to make them promising candidates for industrial and academic research [153,154]. Figure 11 showing the perovskite oxides with ABO3 crystal structure, with A site being a rare earth metal (Lanthanides e.g. La, Gd, Pr or alkaline earth metals) and B sites a transition metal (e.g. Mn, Cr, Fe, Ni, Co), are the best choice for efficient bifunctional ORR/OER catalyst because of high activity and low cost [155-157]. The crystal lattice of perovskites (A or B) can be occupied by a variety of metals influencing their catalytic properties. In an ideal case the crystal sites of A and B will occupy equal number of cations (A/B=1) and any change in this equivalency is likely to result in the stabilization of the unstable oxidation state of the transition cations in B sites causing a change in the electronic structure and the catalytic performance [158,159].

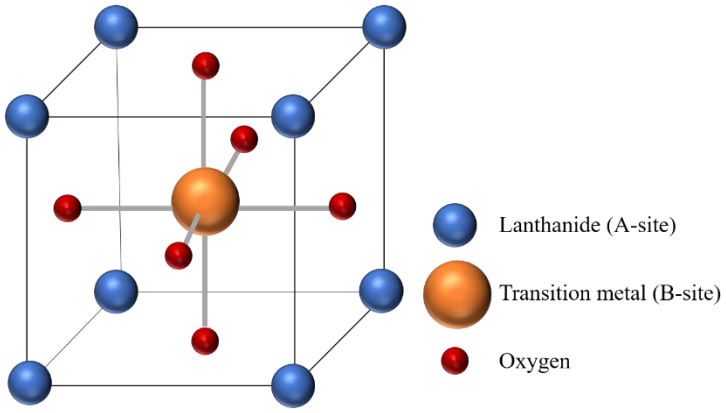

Figure 11. Unit cell ABO_3 perovskite structure.

Catalytic properties can be controlled by manipulating the bond strength between B-site species and attached oxygenated species. According to crystal field theory (CFT), the d-orbital of transition metals are affected by the octahedral arrangement of six negative charges around it [160,161]. The d orbital degenerates by splitting into two high energy (e_g) and three lower energy orbitals (t_{2g}) while maintaining the same average energy level. The magnitude of energy splitting determines the electronic configuration of d orbital. If the splitting energy is lower than spin-pair energy the configuration follows high spin, and with higher splitting energy results low spin state. It is important to identify the electronic structure of the transition metal oxide that controls the catalytic activity towards ORR and OER [162]. Figure 12 shows the possible 3d orbital electronic configuration of B site transition metal cations in $LaMO_3$ (M=Cr, Mn, Fe, Co and Ni) for different spin states. The Cr^{3+} at low spin state, Co^{3+} at intermediate state and other transition metals at high spin are found to be stable spin state configurations [162-169]. Suntivich *et al*. proposed that the rate determining step in the ORR/OER reaction is based on the e_g orbital filling of B site transition metal cations [170,171]. If the d-electrons are

less, the valence state goes up and the e_g orbital filling is low resulting in strong adsorption of oxygenated species on the B site (strong B-OH bond). This strong bonding limits the overall reaction rate by the slow desorption of OH and its derivatives during ORR/OER. Similarly, too high e_g filling causes weak adsorption of oxygenated species that limits the reaction through the slow adsorption of reactants. Therefore, to enhance the activity of ORR/OER reaction it is required to balance the adsorption and desorption of reactants and the intermediate respectively. The better way is to optimize the e_g orbital filling to be nearly 1 (e_g =1).

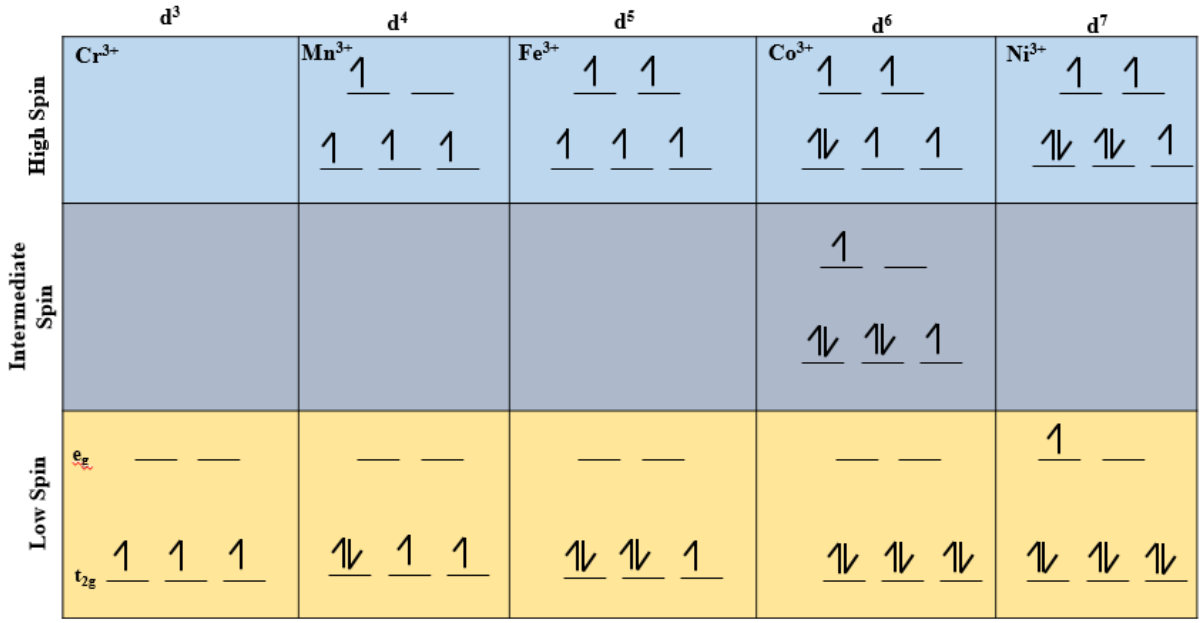

Figure 12. The possible 3d orbital electronic configuration for LaMO (M=Cr, Mn ,Fe, Co and Ni) for different spin states

The reported mechanism for ORR/OER on perovskite oxide catalysts is summarized in

Figure 13. The main four reactions involved in ORR are surface hydroxide replacement (Step 1), surface peroxide formation (Step 2), surface oxide formation (Step 3), and surface hydroxide regeneration (Step 4).

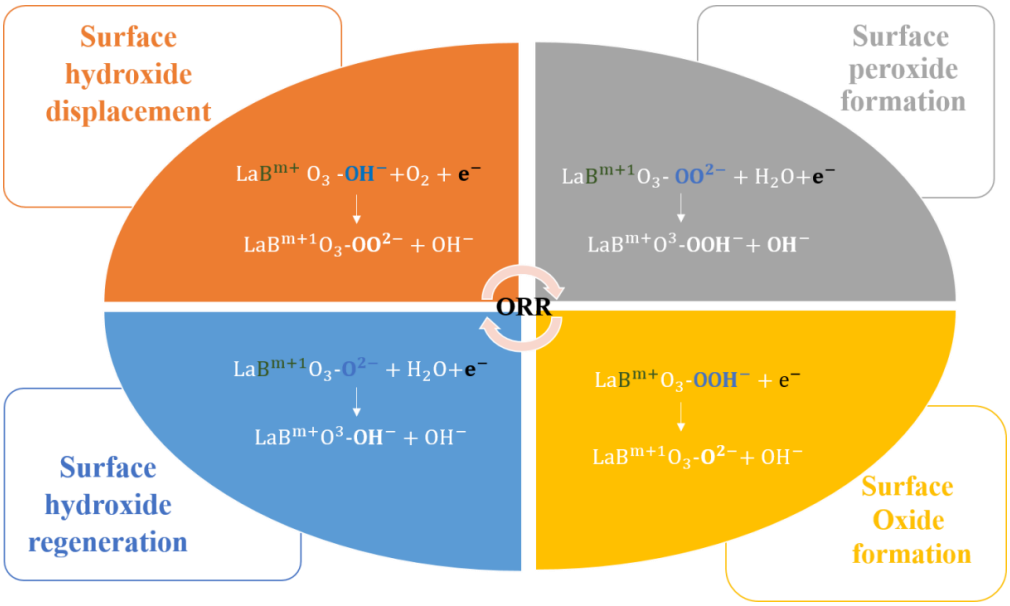

Figure 13. Proposed four electron ORR mechanism on perovskite surface .

The rate determining reaction for ORR perovskite catalyst are step 1 (OO^{2-}/OH displacement) and step-4 (OH^- regeneration). The e_g electrons in B site transition-metal cation is attached with OH^- ions from the electrolyte. In surface hydroxide replacement step the unstable B-OH^- is stabilized to B-OO^{2-} form by removing an electron from B-OH^- through $O_2 + e^-$ reaction. If the e_g value is less than 1, the bonding is very strong and the energy is not sufficient for the replacement and vice versa for high e_g values. The surface peroxide formation in perovskite structures is mainly through the reaction: $O_2^{2-} + H_2O + e^- \rightarrow OH^- + OOH^-$. Then the hydroxide intermediate is converted to

surface oxide in the transition-metal cation surface by changing the oxidation state +(m) to +(m+1). The final step in ORR is the surface hydroxide regeneration that is the reverse reaction of step 1 where O^{2-} is displaced as OH^- on the B site with m+ oxidation state. The rate of ORR reaction is determined by the response of O_2^{2-}/OH displacement that is indirectly related to the e_g orbital filling of B site transition-metal cation. The overall process following four-electron reaction pathway for ORR can be expressed as:

$$O_2 + H_2O + 4e^- \rightarrow 4OH^-$$

The reaction sequence for OER is depicted in Figure 14. Like ORR, the binding of OER intermediates to oxide surface is governed by the e_g filling of transition metal cations in B site and thus the catalytic activity. The rate-determining steps in oxygen evolution reaction (OER) are O-O bond formation (Step 2) and proton extraction of oxyhydroxide group (Step 3). The transition metal cations with e_g occupancy close to unity facilitate these two RDS efficiently and lead to highest OER activity. The proposed overall OER mechanism can be represented as:

$$4OH^- \rightarrow 2H_2O + O_2 + 4e^-$$

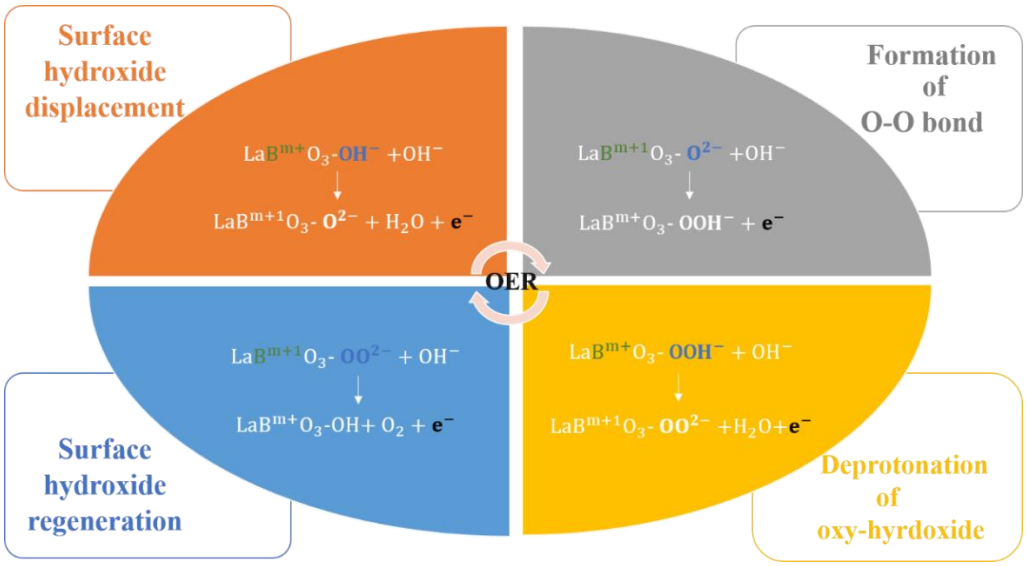

Figure 14. Proposed four electron OER mechanism on perovskite surface.

In 1975, Matsumoto *et al* first reported $LaNiO_3$ perovskite for oxygen electrocatalysis [172,173]. Bockris and coworkers investigated 18 perovskite structures of $La_{1-x}Sr_xTO_3$ (T= Ni, Co, Mn, Fe, Cr, and V) and they corelated the catalytic activity with highly occupied antibonding σ^* orbital of transition metal – OH bond and proposed a volcano plot based on the catalytic activity and bond strength of transition metal – OH bond [174]. Among $LnMnO_3$ (Ln = rare earth metals) perovskite, La is found to be the best for ORR/OER reaction and the activity trend is in the order of La > Pr > Nd > Sm > Gd > Y > Dy > Yb [175] . Sunarso *et al* studied the intrinsic ORR activity of La based transition metal oxide $LaTO_3$ (T = Ni, Co, Fe, Mn, and Cr) without adding any conductive material such as carbon black and found the activity in the increasing order of $LaCrO_3$ < $LaFeO_3$ < $LaNiO_3$ $LaMnO_3$ < $LaCoO_3$ with least formation of HO_2^- (1.5%) that confirms the pseudo 4 electron transfer pathway[176]. Also, they investigated the equal incorporation of transition metals along with Ni based La perovskites $LaNi_{0.5}M_{0.5}O_3$ (M= Fe, Co, Cr,

Mn) and the catalytic activity is in the order of $LaNi_{0.5}Fe_{0.5}O_3$ < $LaNi_{0.5}$ $Co_{0.5}O_3$ < $LaNi_{0.5}Cr_{0.5}O_3$ < $LaNi_{0.5}Mn_{0.5}O_3$. Shao-Horn and team conducted several studies in powdered perovskite catalyst and detailed investigation was conducted on epitaxially oriented $La_{1-x}Sr_xM_nO_3$ surfaces on Nb-doped $SrTiO_3$ substrates for ORR. $La_{0.67}Sr_{0.33}$ MnO_3 with (110) and (111) orientation is found to be the optimum one when compared with (001)[51]. The same group reported the effect of adding some conducting agents such as carbon black into the low conducting perovskite structures in order to improve the electron transfer to the catalyst surface during ORR/OER mechanism. $LaNiO_3$ with 17 wt % of acetylene black exhibits higher specific area and mass activity than $La_{0.75}Ca_{0.25}FeO_3$ and $LaCu_{0.5}Mn_{0.5}O_3$ [177]. The volcano plot proposed by Shao horn *et al* shows the better understanding on the ORR activity of various perovskite oxide added with carbon black and the activity is in the order of : $LaMnO_{3+\delta}$ > $LaNiO_3$ > $La_{0.5}Ca_{0.5}MnO_3$ > $LaMnO_3$ > $LaMn_{0.5}Ni_{0.5}O_3$ > $La_{0.5}Ca_{0.5}CoO_{3-\delta}$ > $La_{1-x}Ca_xFeO_3$ > $La_{1-x}Ca_xCrO_3$ as shown in Figure 15 [178]. The e_g electron filling ~ 1 and the increased covalence between O 2p orbital and 3d transition metal is the main principle behind the ORR activity of the perovskite oxides. Bare $LaCoO_3$ shows 50 % higher formation of HO_2^-, when compared to $LaCoO_3$ mixed with conductive carbon black and shows a pseudo 4 e^- pathway in ORR [179]. A $2e^-$+ $2e^-$ electron pathway was identified for $La_{0.6}$ $Ca_{0.4}CoO_3$ supported with carbon black in 1 M KOH electrolyte with a 3% HO_2^- production during ORR [180].

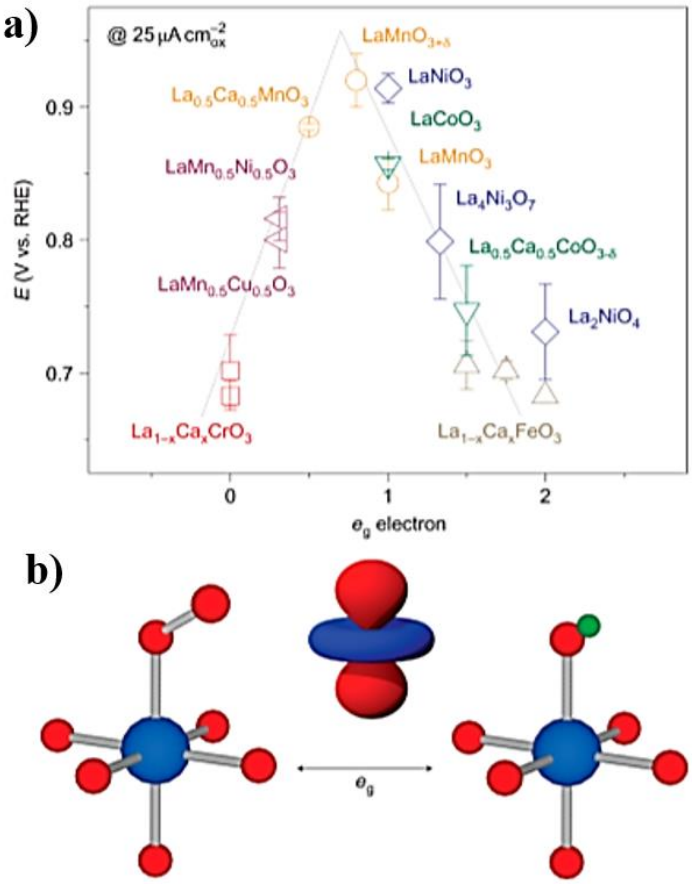

Figure 15. Significance of eg electron of perovskites on the ORR activity a) volcano plot of perovskite oxide as a function of eg orbital b) eg orbital structure of perovskite towards the surface O atom and its role on the exchange of O_2^{2-}/OH^- ions. B ions (Red) [178].

Bare barium strontium cobalt iron perovskite oxides (BSCF) show the formation of 50 to

70 % of HO_2^- during ORR. The mixing of acetylene black exhibits improvement in E_{onset} and reduced the formation of HO_2^- and the optimum wt % of the catalyst BSCF(78 wt %)/AB with 28% HO_2^- formation and overall number of electron transfer of 3.43 during reaction mechanism [181]. These studies confirmed the reduction peroxide yield after the mixing of carbon black into the perovskite oxides, even though they are not solely efficient for ORR. The HO_2^- formed is chemically stable over the conductive carbon and is further reduced or decomposed over the active site of perovskite oxides. The pseudo 4 e^- pathway ($2e^- + 2e^-$) proceeds through the initial reduction of OH^- to HO_2^- over the carbon black and the resulted HO_2^- is further reduced into H_2O over the perovskite sites [182].

$LaFe_{0.95}Pd_{0.05}O_3$ (LFP0.05) and $LaFe_{0.9}Pd_{0.1}O_3$ (LFP0.1) perovskites were synthesized using sol gel method with citrate- EDTA- metal nitrate combined precursors. The post thermal treatment under different environment controls the oxidation state of the Pd. The presence of a reducing environment yield Pd^0 (LFP0.05R) and in presence of air it produces Pd^{2+} ((LFP0.05RO). XPS analysis in Figure 16.a shows the existence of mixed oxidation states of Pd^{3+} and Pd^{4+} on the surface of LFP0.05. The ORR activity shown in Figure 16.b increases in the order of $LaFeO_3$ (LF) < LFP0.05R< LFP0.05RO < LFP0.05 is attributed to the presence of Pd with higher oxidation state. The ORR activity of the catalyst was further improved by increasing the Pd ratio on the catalyst as shown in Figure 16.c. In Figure 16.d LFP0.1 shows more kinetic current and higher mass activity than commercial Pt. The presence of one or more B site cations shows some synergic effect on the perovskite active sites to achieve favorable ORR kinetics. The B site cations was replaced with 4d transition metals such as palladium was studied before through the

tuning of the oxidation state of Pd [183].

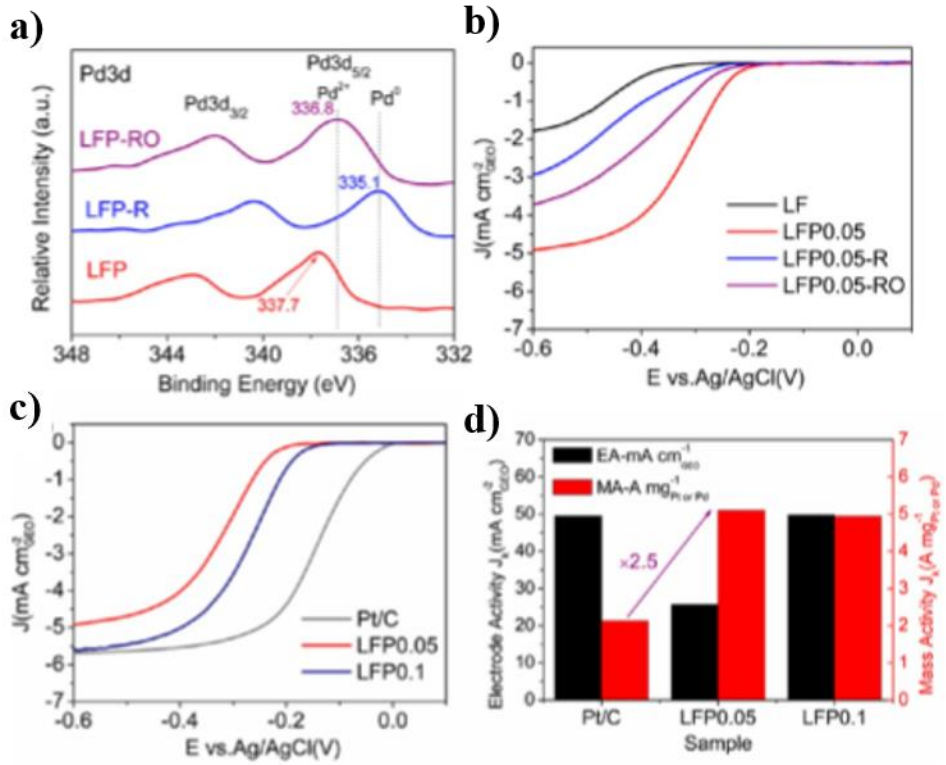

Figure 16. a) XPS spectrum of Palladium for LFP0.05, LFP0.05R and LFP0.05RO b) LSV polarization curve for LF, LFP0.05,LFP0.05R, LFP0.05RO. c) RDE polarization curve for Commercial 20 wt % Pt/C, LFP0.05, and LFP0.1 in 0.1 M KOH at 1600 rpm [183].

In 1980s, $LaNiO_3$ was developed due to their intriguing activity toward OER in alkaline medium [184]. Later on Yang *et al.*, introduced a design aspect of the catalyst towards OER and its molecular orbital concepts in the alkaline medium [ref]. The OER activity of $LaCoO_3$ and $La_{0.5}Ca_{0.5}$ $CoO_{3-\delta}$ was systematically investigated and introduce many

more perovskite OER catalysts as shown in Figure 17.a and its volcano shape relationship of the activity with the e_g filling of B site transition metal oxide as represented in Figure 17.b [185].

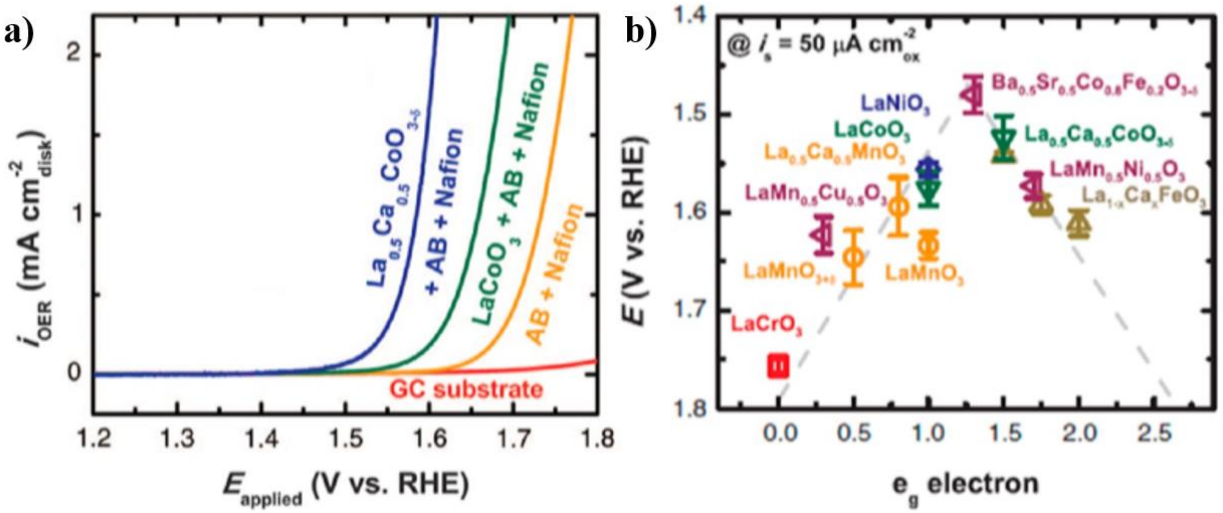

Figure 17. a) OER activity curve of bare $LaCoO_3$ and $La_{0.5}Ca_{0.5}CoO_{3-\delta}$, also after adding it with acetylene black (AB) b) Volcano plot shows the relationship of overpotential and e_g orbital filling of B site cations [185].

Zhao *et al.* developed highly porous perovskite structures of $La_{0.5}Sr_{0.5}CoO_{3-\delta}$ (LSCO) nanowire with high oxygen mobility that are synthesized using multistep micro emulsion of the metal precursors in alkaline medium. These hierarchical with high specific surface area are found to be more suitable of ORR and OER mechanism and are applicable for non-aqueous Li−air batteries [186]. Takeguchi and his team synthesized double layer perovskite oxide of $LaSr_3Fe_3O_{10}$ as bifunctional electrocatalysts for ORR/OER reaction. $LaSr_3Fe_3O_{10}$ reversible air electrode catalysts can easily remove the oxygen from the surface and with an equilibrium potential of 1.23 V [37]. Jin el al prepared

$Ba_{0.5}Sr_{0.5}Co_{0.8}Fe_{0.2}O_3$ (BSCF) perovskite oxides and tested its bifunctionality of the catalysts towards ORR and OER in alkaline medium. BSCF catalyst follows direct four-electron pathway with maximum limiting current density of 6.25 $mAcm^{-2}$ at 2500 rpm that are comparable to commercial 20 % Pt/C. The onset potential of the synthesized catalysts shows a positive shift of 0.12 V in ORR and the onset potential lowers to 0.2 V in the OER reaction when compared to pure carbon black shows the excellent bifunctionality of BSCF [187].

Graphene based metal catalyst: Graphene supported with transition metal oxides gained great attention in research due to the stability and activity. The electrocatalytic activity of this supported catalyst on ORR/OER was well studied using both theoretical and experimental way [188,189]. Synergic coupling of graphene and transition metal oxide through the proper embedding of achieve a stable ORR and OER activity at cathode and anode respectively [190]. Along with the transition metal oxides incorporated over the graphene structure, other functional groups (nitrogen, carboxyl and hydroxyl) can be doped over it to increase the performance and stability [191].

Cobalt oxide coupled on graphene with 2D and 3D morphology shows excellent catalytic activity for ORR in alkaline electrolyte [49,192,193] . The schematic representation of the synthesis of Co_3O_4/rGO hybrid is shown in Figure 18.a. Co^{2+} ions are functionalized with the negative oxygen ions in the graphene sheet through coordination. During hydrothermal process, the Co^{2+} ions present in the graphene sheet was oxidized into Co^{3+} and form Co_3O_4 rods that deposited on reduced graphene oxides (rGO) through in-situ thermal reduction. SEM image in Figure 18.b indicates the presence of Co_3O_4 nanorods dispersed uniformly over the rGO substrate. EDX confirms the presence of Co, O and C

with Co to O ratio of 3: 4 is represented in Figure 18.c.

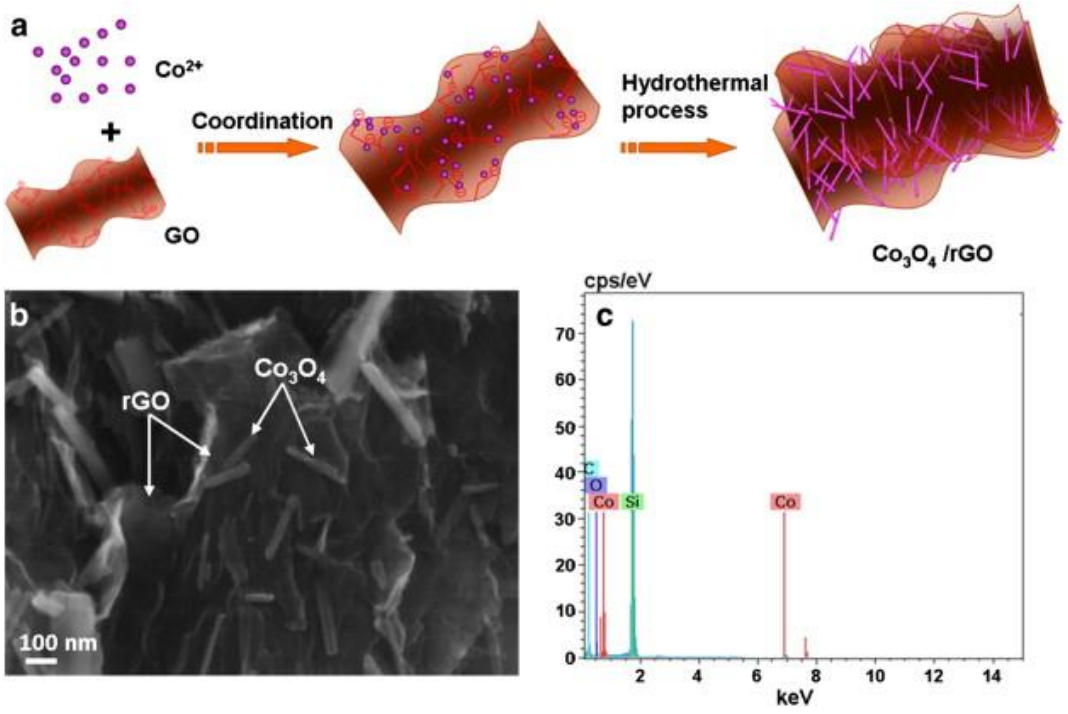

Figure 18. a) Illustration of the synthesis of Co_3O_4/rGO hybrid (b) SEM image c) EDS spectrum of the nanocomposite [192].

The ORR performance of Co_3O_4/rGO in ORR is measured with LSV plot shown in Figure 19.a. [193]. The onset potential of Co_3O_4/rGO is more positive than Co_3O_4 and rGO, is very close to commercial Pt/C indicates the improvement in ORR activity of Co_3O_4 coupled with rGO. Nyquist plot shown in Figure 19.b indicates the electron transfer kinetics of nanohybrids. The diameter of the Co_3O_4/rGO in Nyquist plot is much smaller than Co_3O_4, but similar to rGO. This shows that by embedding material in rGO enhances the electron transfer in its composite that influences the ORR activity of Co_3O_4/rGO. The LSV curve of Co_3O_4/rGO at different speed is shown in Figure 19.c results the number of electron transfer calculation of 3.5 from KL plot. Therefore,

Co_3O_4/rGO favors $4e^-$ transport in the electrolyte and electrode. Chronoamperometric curve shown in Figure 19.d shows the stability of catalyst over time. Co_3O_4/rGO is stable over 6000s while in Std Pt/C after 2000s there shows a slight degradation. This reveals that Co_3O_4/rGO is more catalytic stable and active in 0.1 M KOH solution.

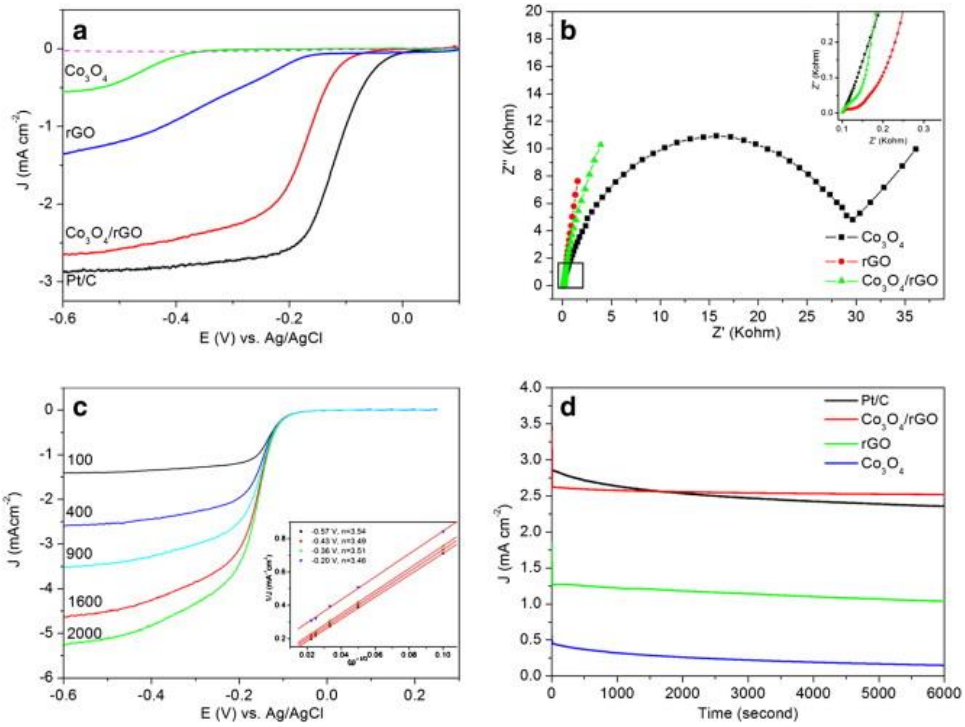

Figure 19. a) Rotating disk electrogram on Co_3O_4, rGO, Co_3O_4/rGO and commercial Pt/C in O_2 saturated 0.1 M KOH solution b) Open potential Nyquist plots of Co_3O_4, rGO and Co_3O_4/rGO c) LSV curve of ORR for Co3O4/rGO at different rotation speed d) Chronoamperometric analysis [193].

Liang *et al.* prepared Co_3O_4/N-rmGO (nitrogen doped reduced graphene oxide) and proven the activity for both ORR and oxygen evolution reaction (OER) in 1 M KOH as well as 6 M KOH with comparable performance with commercial Pt/C [48]. The OER

performance of Co_3O_4/N-rmGO is found to be higher than Co_3O_4 and Co_3O_4/rmGO with very smaller overpotential of 0.31 V at 10 $mAcm^{-2}$. Chen and coworkers synthesized mesoporous spinel $NiCo_2O_4$ nanoplatelets anchored over graphene sheets that improve the overall surface area and facilitate the transport of the reactants during the ORR/OER reactions. The insertion of Ni cation into the octahedron sites of spinel structure improves the electrical conductivity and rapid charge transport over the catalyst [194]. In the work reported by Yan *et al*, spinel $FeCo_2O_4$ attached onto hollow reduced graphene oxide spheres (HrGOS) were synthesized using an electrostatic method with SiO_2 spheres as templates that demonstrate highly enhanced bifunctional activity due to the synergetic effect of $FeCo_2O_4$ and hollow graphene spheres. The ORR activities of FeCo2O4/HrGOS are surpassed to that of Pt/C and OER performance is comparable to that of RuO_2/C [195]. Dai *et al.* synthesized bimetallic nanoparticles embedded on graphene that are $MnCo_2O_4$ on graphene nanosheets [196]. The presence of cubic phase and the shifting of peaks to lower degree in $MnCo_2O_4$/N-rmGO could be due to the substitution of Mn cations over it. The activity of $MnCo_2O_4$/N-rmGO composite was calculated using LSV of ORR as shown in Figure 20.

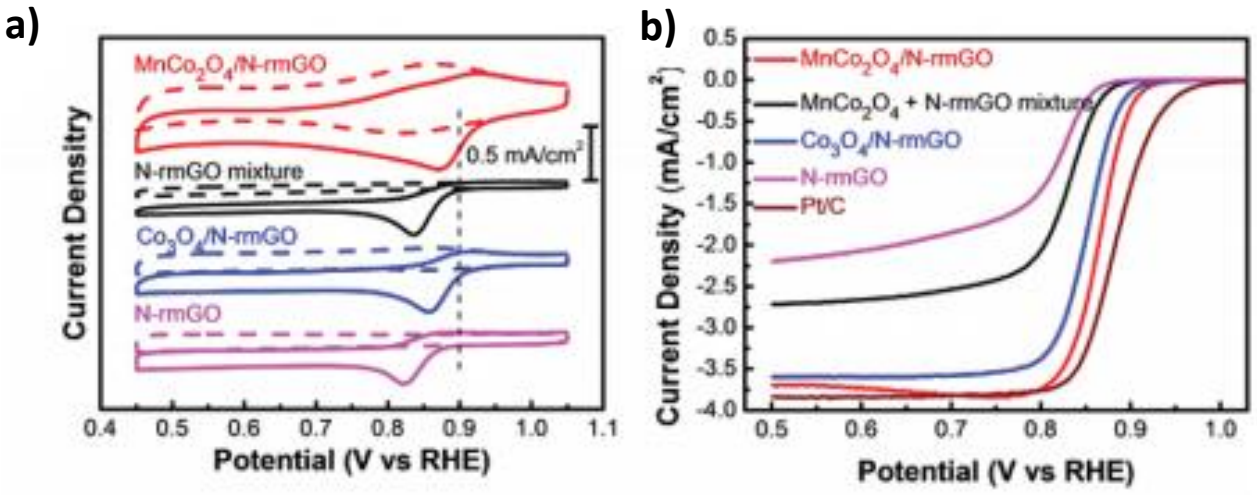

Figure 20. a) Cyclic voltagram for $MnCo_2O_4$/N-rmGO hybrid, $MnCo_2O_4$ + N-rmGO mixture, Co_3O_4/N-rmGO hybrid, and N-rmGO in 1M KOH with O_2 saturated(solid) and N_2 saturated(dashed) solution b) steady state polarization curve of $MnCo_2O_4$/N-rmGO hybrid, $MnCo_2O_4$ + N-rmGO [195].

The positive shifting of onset potential in $MnCo_2O_4$/N-rmGO at 0.88 V than Co_3O_4/N-rmGO (0.86 V) in Figure 20.a possess prominent electrocatalytic activity with excellent performance. This study suggests the addition of Mn over cobalt based graphene enhances the electrocatalytic activity. The LSV at 1600 rpm in Figure 20.b shows higher limiting current density in $MnCo_2O_4$/N-rmGO (~ 3.8 mA/cm^{-2}) than Co_3O_4/N-rmGO (3.62 mA/cm^{-2}). Thus $MnCo_2O_4$/N-rmGO can be considered as a good ORR accelerator which has comparable performance with commercial Pt/C. The OER performance of $MnCo_2O_4$/N-rmGO is found to be lower than Co_3O_4/N-rmGO could be due to the substitution of Mn^{3+} into the active sites of Co^{3+} that are considered as the most suitable sites for OER. Apart from Mn-Co, researchers pointed there interest in synthesizing some

other series of nano bimetallic composite like Co-NiO_x/GNs [197], Co- FeO_x/GNs [198] with high activity and longer durability in alkaline electrolyte.

Recently, Rebeca Marcilla [199] and co-workers successfully synthesized $NiCoMnO_4$/N-rGO as highly efficient bifunctional catalyst for both oxygen reduction and oxygen evolution reaction (ORR and OER). Ni, Co and Mn in its elemental state were anchored over the nitrogen doped graphene nanosheets. The synthesis step is illustrated as shown in Figure 21.

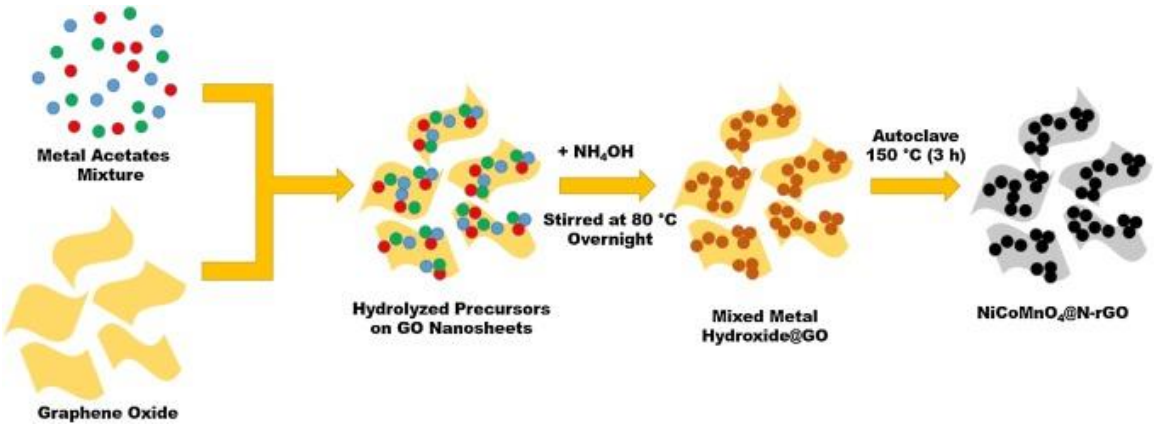

Figure 21. Schematics for the synthesis of $NiCoMnO_4$/N-rGO material [199].

$NiCoMnO_4$ shows higher number of electron transfer and greater kinetic reaction rate than all other prepared material during ORR. $NiCoMnO_4$/N-Rgo shows higher limiting current density than Pt/C as shown in Figure 22. At lower over potential, the tafel slope of $NiCoMnO_4$/N-rGO is much lower than other materials under study indicates the superior catalytic performance with high stability and durability.

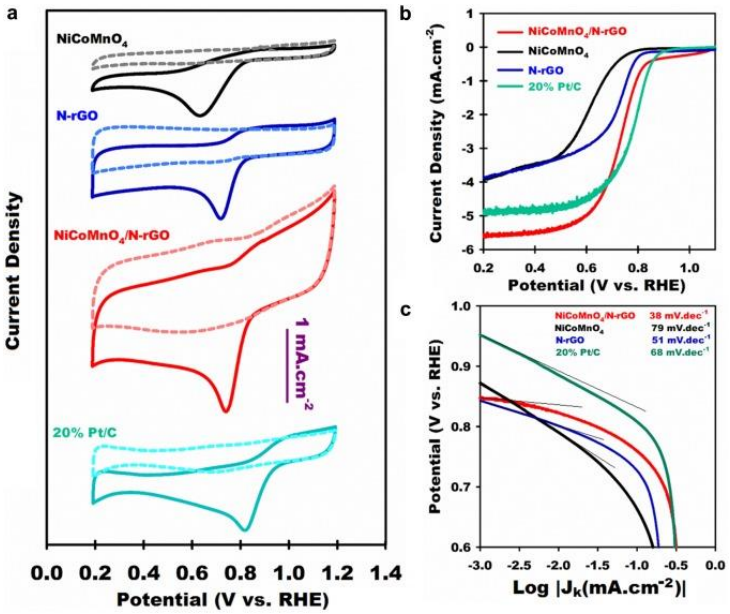

Figure 22. a) CV of $NiCoMnO_4$, N-rGO, $NiCoMnO_4$/N-rGO, and commercial Pt/C 20% in O2 and N_2 saturated 0.1M KOH with sweep rate of $20mVs^{-1}$ b)rotating disk LSV of $NiCoMnO_4$, N-rGO, $NiCoMnO_4$/N-rGO, and commercial Pt/C in O_2 saturated 0.1 M KOH [199].

Shaojun, et al. in 2012 conducted another study on cobalt based graphene nanomaterial for ORR, in which Co nanoparticles with a layer of CoO were anchored successfully to graphene sheets (Co-CoO/GNs). Co and CoO was synthesized through ultra-sonication and achieved a core-shell. Thus synthesized core-shell structure of Co/CoO in graphene with diameter 10 nm shows better half wave potential than standard commercial Pt/C and triggered 4 electron flow at -0.5 V was calculated using K-L plot. . Moreover, these electrocatalyst shows long term stability and durability than Pt/C was demonstrated in the stability test using chronoamperometric method [200].

Wu et al. prepared Co3O4/CNT hybrid catalyst with activity and stability because of the enhanced active surface area, effective catalytic coupling and stabilized dispersion [201]

.

2.5. Limitation of existing PGM and Non-Noble metal catalyst towards ORR/OER

High energy density technologies of fuel cell and metal air batteries are among the recent sources for energy conversion and storage systems being investigated to meet the energy requirement of future decades. These technologies are greatly dependent on a pair of sluggish electrochemical reactions such as ORR and OER [202-209]. Both reactions require high cost metals to enhance its activity and stability, but their availability and cost limit their worldwide application in electrochemical technologies. Platinum (Pt) and Pt-alloys are the most active catalysts for ORR, but they do not show any catalytic activity for OER due to the formation of its oxide film over the surface at higher potential [60-65] whereas on the contrary RhO_2 and IrO_2 are reported to be most active catalysts for OER without much activity for ORR [210-216]. Moreover, the catalytic activity of Pt and IrO_2 reduces with time because of deactivation caused by agglomeration at the atomic scale.

The Pt loading at anode should be 0.05 mg cm^{-2} for the oxidation of hydrogen, while in cathode, for sluggish reaction kinetics of ORR the Pt loading should be minimum of 0.4 mg cm^{-2} for better reduction [132,217]. Commercially, only Pt is reported to be used for fuel cells, particularly for ORR reaction, but their limited availability (only South Africa

and Russia are the major supplier) and high cost are the key factors in limiting their large-scale catalytic applications [218].

It is still challenging to develop a non-precious and readily available bifunctional catalyst suitable of simultaneously activating the ORR and OER. Design and synthesis of the heterogeneous bifunctional catalysts includes metal hydroxides, carbon materials and sulfides recently received great attention. Also, it is reported that these materials shows excellent activity and stability during ORR and get easily oxidized for OER at higher over potential. While, the transition metal oxides are likely to be more stable for OER at relatively higher oxidizing environment. Synthesis of perovskite at high temperature causes structural agglomeration, while their excellent tunable electronic structure gives them an advantage in oxygen electrocatalysis. Many challenges in the graphene-based composites for electrochemical reaction are remaining. The reaction mechanism over the graphene-based nanocomposites and their surface composition and the defective sites influence on ORR activity is not yet well defined. The electron interaction and the active site sharing of metal oxide and graphene is still not clear.

CHAPTER 3: EXPERIMENTAL METHODS

3.1. Catalysts synthesis

During the past decade, considerable attention has been paid on the synthesis of nanomaterial in the size range of 1-100 nm with superior chemical and physical properties [219-222]. The properties of nano-sized particle differ from the bulk due to the confinement in size, surface area and large surface to volume ratio that enables the most active sites on the surface of the particles [223,224]. Owing to these features the nanoparticles gained great demand both for research and industrial applications. Generally, there are two main approaches for the nanoparticle preparation: top-down and bottom-up. In top-down approach, the coarse structures are converted into fine nanoparticles through physical or chemical techniques. While the bottom-up synthesis allows atomic level arrangement of subunits through chemical processes to form nanoparticle of desired size and shape with improved surface characters. In this work we followed mainly solution combustion synthesis with three different modes and salt assisted synthesis to improve the structural characteristics.

3.2. Combustion synthesis for catalyst preparation

3.2.1. Introduction

Combustion synthesis (CS) method is the most widely used bottom-up approach that is simple, economical, fast and feasible way to synthesize nanoparticles requiring only normally used laboratory facilities such as beakers, hot plate heaters etc. [225-232]. This mode of synthesis allows the preparation of wide variety of nanomaterials including metals, binary and complex oxides, ceramics, alloys and composites with high purity and

homogeneity [233].Traditionally CS has been used in solid-solid reactive medium where the reactant powders are pressed together to form pellets that are heated with a heat source either locally or uniformly all over the volume. Based on the mode of ignition CS has been classified in two groups as shown in Figure 23; self- propagating high temperature synthesis (SHS) [234-236] or volume combustion synthesis (VCS) [237-240]. In the former case, the reactive pellet is ignited locally at one end and the self-sustained combustion propagates from one end to other end in a controlled manner. The latter case deals with an even heating and ignition in the entire sample that leads to combustion reaction taking place throughout the volume abruptly in an un-controlled way. The solid-solid CS products have heterogeneity and particle size of the same order as that of reactive powders, though this heterogeneity can be controlled to a great extent by manipulating the green density and void space in the reactive pellet, nonetheless it is difficult to get nanoscale materials. To improve the limitations in solid combustion synthesis and produce nanoparticles with uniform properties, solution combustion synthesis (SCS) was developed.

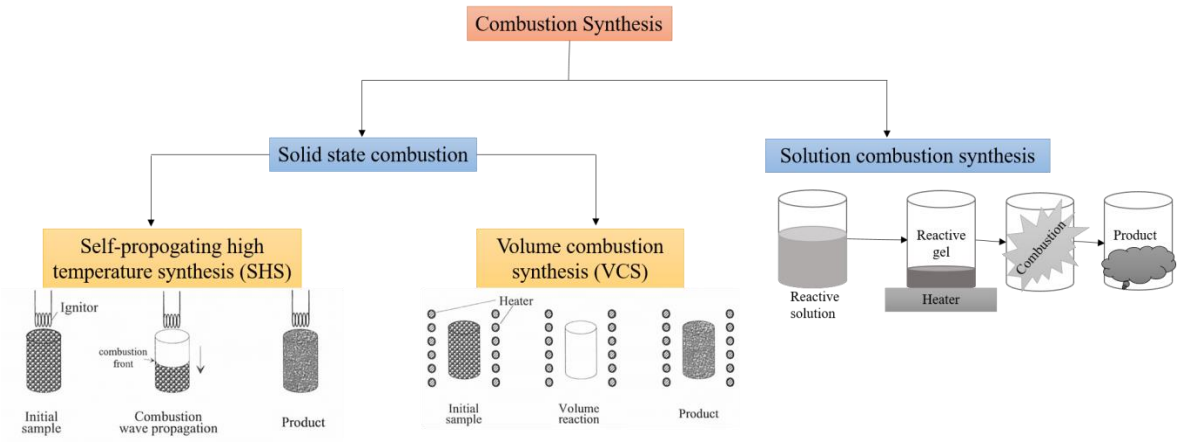

Figure 23. Classification of combustion synthesis and its schematic representation.

In SCS mode, water-soluble metal precursors, e.g. metal nitrates (oxidizer) and fuel are homogeneously mixed to form a reactive aqueous solution. Metal-nitrates being water soluble and efficient oxidizer are the natural choice as metal precursor, while the fuel is selected based on the presence of carboxylic, amine and other reactive groups, suitable to act as reducing agents. Glycine, urea, glucose, citric acid, hydrazine, poly vinyl alcohol (PVA) are the primarily reported fuels in the literature, where the choice of fuel and their relative amount does influence the properties of synthesized materials [241-250]. A mechanistic study of SCS between metal nitrate and glycine as fuel reveals that the energy required for the self-sustained reaction at higher temperature is provided by the reaction between NH_3 and HNO_3 that are released as the decomposition products from metal nitrate and glycine respectively. The released energy during this exothermic reaction is sufficient for the crystallization and purification of nanomaterials without any post synthesis thermal treatment and purification. The stoichiometric equation (1) is commonly used to represent the combustion reaction between a metal nitrate and glycine

[251-253]:

$$M^{\nu}(NO_3)_{\nu} + \left(\frac{10}{9}\,\varphi\right) NH_2CH_2COOH + \frac{10}{4}\,(\varphi - 1)O_2$$

$$\downarrow \qquad (1)$$

$$M^{\nu}O_{\frac{\nu}{2}}(s) + \left(\frac{20}{9}\varphi\right) CO_2(g) + \frac{25}{9}\varphi H_2O(g) + \left(\frac{5\varphi + 9}{9}\right) N_2(g)$$

Where ν be the metal valency and φ be the fuel to metal oxidizer ratio defined in a way such that φ =1 represents stoichiometric condition requiring no external oxygen for complete combustion, whereas φ > 1 represents fuel rich and φ < 1 as fuel lean conditions. The nature of fuel and the fuel to oxidizer ratio (φ) are the critical parameters that greatly influence the characteristics of the synthesized nanopowders. The φ value governs the maximum combustion temperature that in turns tunes the particle size, porosity, surface area, level of agglomeration and number of gaseous products. The excess gaseous product evolved during the combustion reaction help in decreasing the combustion temperature as they take away considerable energy from the system while escaping, and during this process they form aligned channels generating porosity in the nanomaterials. These phenomena lead to smaller particle size, less agglomeration and large porosity. The single step combustion synthesis process involves following key distinct features making them attractive for many applications:

- Liquid phase reactive media provides the homogenous mixing of reactant at the molecular level.
- High combustion temperature ensures high crystallinity and high purity.

- Short reaction period and the large amount to gaseous products favor smaller crystallite size and high porosity.
- Highly exothermic reaction ensures minimum external energy requirement for synthesis.

3.2.2. Synthesis procedure

Metal nanoparticles were prepared by mixing a measured quantity of metal nitrate and glycine with stoichiometric fuel to oxidizer ratio (ϕ). The quantity of metal nitrates and glycine was calculated based on the stoichiometric equation 1. The precursors were dissolved in 25 ml of deionized water (DIW) and stirred continuously for 1 hr to obtain a homogeneous mixture and thereafter it was placed over the hot plate at 300°C until all the water evaporates, and the solution becomes thick with honey like consistency. Once the solution reaches its ignition temperature, combustion starts locally at one point and spreads to other parts of the beaker leaving nanopowder in the beaker. The schematic of the synthesis procedure is shown in Figure 24**.** The samples were collected as synthesized, hand-ground using mortar-pestle and sieved with 75μm size sieve to obtain nanoparticles with size < 75μm size. These materials were further used for material characterization and electrochemical testing.

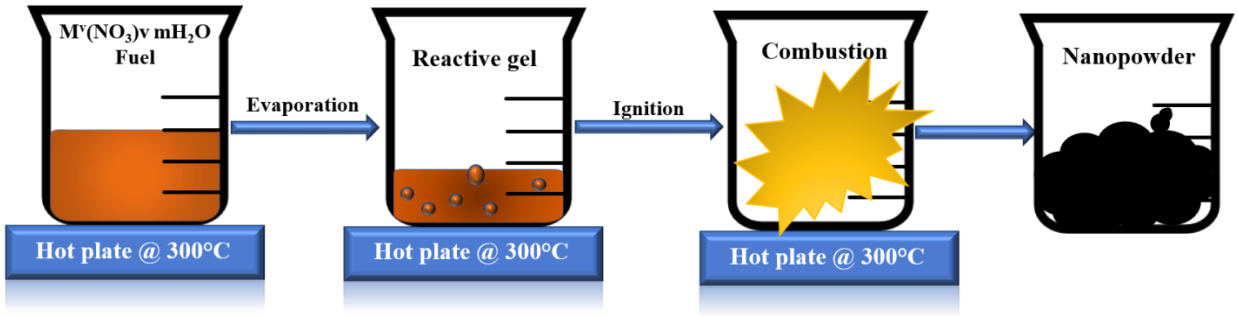

Figure 24. Stepwise synthesis of nanoparticles using solution combustion technique

3.3. Salt assisted combustion synthesis

3.3.1. Introduction

Self-propagating solution combustion synthesis faces mainly two issues in controlling the level of agglomeration and promoting phase formation. In the past decade, many researches were conducted for inhibiting the agglomeration, phase formation, crystalline size, surface area and morphology through choosing different fuels and adjusting the fuel to oxidizer ratio [254-257]. Nevertheless, none of these techniques was a permanent solution for the agglomeration in the solution combustion synthesis. In 2006, Weifang Chen and co-workers reported an alternative strategy to inhibiting agglomeration in solution combustion synthesis by introducing soluble inert salt to the redox mixture of metal nitrate and fuel solution [258]. While using these diluents (KCl or NaCl), adiabatic temperature and wave velocity of the combustion wave can be decreased and thus reduce the rate of agglomeration and the growth rate of particle size. The salt inclusion act as a template to inhibit the agglomeration by binding the particles from growing further and breaks up the three-dimensional porous structure that enhances the total surface area. X. Zhang *et al*. proposed the possible mechanism of formation of well-dispersed $CoFe_2O_4$

nanoparticle using salt assisted solution combustion synthesis [259]. It has been proved that, the hardness, abrasive wear resistance and binding strength of the particles increases with the decrease in particle and thereby increases the performance characteristics [260]. These inorganic salts are much cheaper, highly soluble in water, thermally stable at high temperature, unreactive to the redox mixture, easily removed from the product mixture through washing and great recyclability when compared to other organic salts.

3.3.2. Synthesis Procedure

The synthesis procedure is same as conventional solution combustion synthesis. Initially, metal nanoparticles were prepared by mixing a measured quantity of metal nitrate and glycine with stoichiometric fuel to oxidizer ratio (ϕ). The quantity of metal nitrates and glycine was calculated based on the stoichiometric equation 1. The precursors were dissolved in 25 ml of deionized water (DIW) and stirred continuously for 1 hr to obtain a homogeneous mixture. Secondly, KCl to metal ion ratio of 2/3 was used to measure the amount of KCl added to the solution and the mixture was placed in a heater at 300°C until all the water evaporates. Once the combustion happens, the product was dispersed over DI water and boiled it for several times to remove the extra salt residuals. The resulted paste was dried over the oven at 70 °C for 3 h. The sequence of salt-assisted solution combustion synthesis is shown in Figure 25.

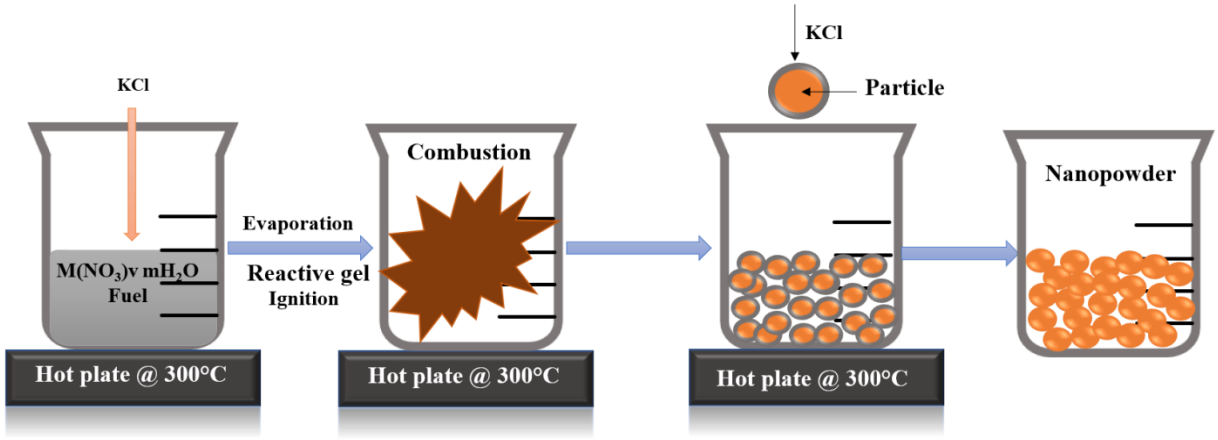

Figure 25. Stepwise synthesis of salt-assisted solution combustion synthesis (SCS).

3.4. Catalyst characterization

3.4.1. X-Ray Diffraction (XRD)

X-Ray Diffraction (XRD) is a rapid analytical tool to identify the structure, physical property and phase identification of crystallite materials. A constructive interference of monochromatic X-rays and a crystalline sample that obeys Braggs law is the working principle of XRD (Figure 26). The Braggs law can be represented as:

$$n\lambda = 2d\sin\theta \qquad (2)$$

where n (any integer), λ, d and θ be the order of reflection, wavelength of X-Ray, spacing between the crystal lattice planes that produces constructive interference and the angle of incidence of X-rays respectively. This law relates the wavelength of electromagnetic radiation to the diffraction angle and the lattice spacing in a crystalline sample.

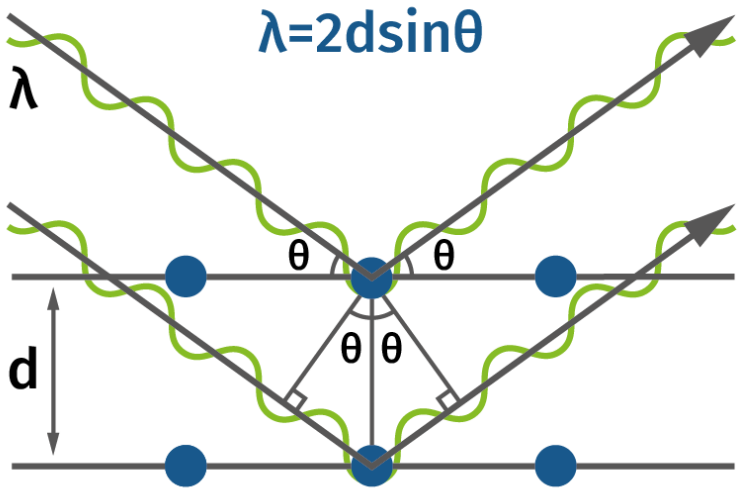

Figure 26. Schematics of the incident X-Rays with atoms in the crystal plane.

The XRD pattern obtained is the unique "fingerprint" of the crystal structure and by interpreting it properly using the theoretical diffraction patterns of crystal structures in the database (e.g. JCPDS card) identifies the crystalline form of the sample. In this work, we used Rigaku MiniFlexII Desktop X-ray powder diffractometer with a wavelength of Cu-Kα radiation and 10-80° scan range to identify the crystallinity of the catalyst synthesized.

3.4.2. Scanning Electron Microscopy (SEM)

Scanning Electron Microscopy is a type of electron microscopy that images the sample through the surface scanning using focused electrons. The morphological characterization of the sample down to 50 nm size can be resolved using SEM. The electron gun with Tungsten filament cathode generate electrons beam with energy of 0.2 eV to 4.0 eV is focused to a spot of 0.4- 5 nm diameter through one or two condenser lenses as in Figure 27.

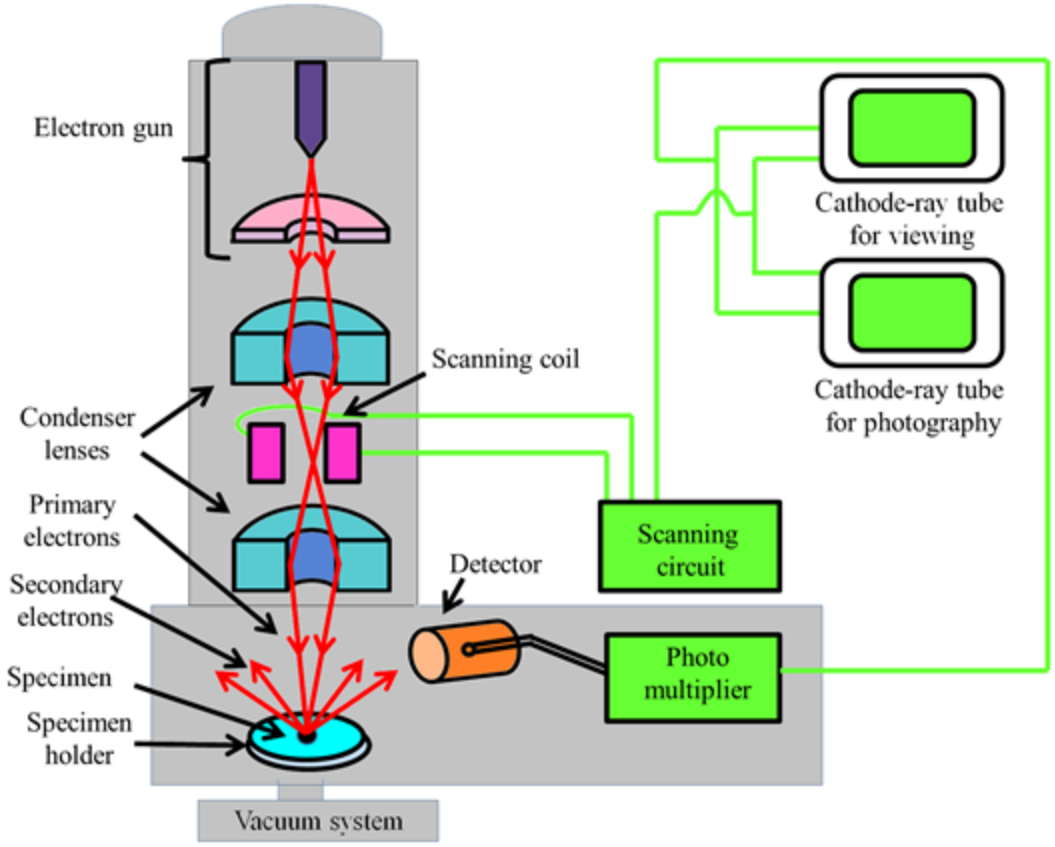

Figure 27. Schematic diagram of scanning electron microscopy (SEM)

The electrons that interact with the atoms in the sample stimulate the emission of low-energy secondary electrons and high-energy back scattered electrons. The detected secondary electrons varied its intensity depending on the morphology and topography of the sample and the back-scattered electrons helps for the rapid phase discrimination through the contrast in the composition of sample and provide with a three-dimensional image. In this study, we used SEM, Nova Nano 450, FEI was used to identify the surface morphology of the samples.

3.4.3. Transmission Electron Microscopy (TEM)

Transmission Electron Microscopy (TEM) is another technique in which beam of electron is transmitted through the sample to generate two-dimensional image. In TEM, thermionic emission gun is to generate electron beam and are focused anywhere between 40 – 200 kV potential. The thickness of the specimen should be less than 100 nm in order to transmit the electron beam through the sample. TEM is often used to identify the internal structure of the specimen even as small as a column of atoms with ultra-high resolution. FEI Talos F200X TEM coupled with EDS (FEI SuperX EDS system) was used to identify the particle size and elemental mapping is used in the whole work.

3.4.4. Energy dispersive x-ray spectroscopy (EDS)

Energy dispersive x-ray spectroscopy (EDS) is a surface analytical technique that allows identifying the elemental composition and its relative atomic concentration (%). The electron beam (or x-ray beam) that hit on the surface of the specimen generates some X-Rays that provide the elemental information of the sample. During the electron bombardment, the electron from the inner shell was ejected by leaving a hole where the electron was misplaced. The electron from the higher energy state tends to move to the lower energy vacant level by leaving some energy in the form of X-Rays. The generated X-Rays have energy intensity equal to the difference in energy between lower energy shell and higher energy shell. The released x-rays were detected by counting the number and intensity of the signal using an energy dispersive spectrometer. Depends on the signal intensity it is possible to map the corresponding elemental with different contrast and thus

identify the individual elements using visual inspection of the image. FEI SuperX EDS system coupled with TEM is used for the elemental mapping in this work.

3.4.5. X-Ray Photoelectron Spectroscopy (XPS)

X-Ray Photoelectron Spectroscopy (XPS) is a surface sensitive quantitative tool to measure the chemical composition, electronic structure and chemical bonding state (or oxidation state) of the specimen surface. XPS measurement is taken by probing the rays into the depth of 5 nm over the sample surface. The surface scanned using mono-energetic Al kα x-rays triggers the formation of photoelectrons from the sample. The energy of the emitted photoelectron was measured using electron energy analyzer that is incorporated with the detector. The detector identifies the intensity of the emitted photoelectron and the binding energy, that in turns analyzed the surface elemental composition, chemical state and electronic structure (Figure 28).

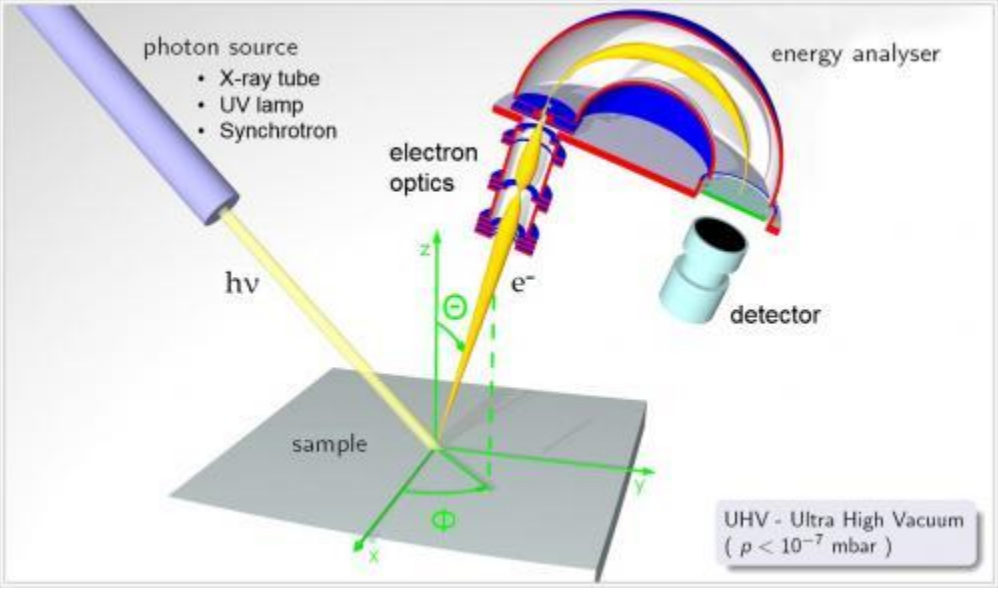

Figure 28. Schematics of X-ray photoelectron spectroscopy.

In our work, the role of xps is to identify the chemical and electronic state of bimetallic catalyst and the bonding configuration of monometals in solid bimetallic solution. The bonding configuration and elemental analysis on the surface of bimetallic materials were identified using X-Ray Photoelectron Spectroscopy XPS, Kratos AXIS Ultra DLD.

3.4.6. Fourier-transform infrared spectroscopy (FTIR)

Fourier-transform infrared spectroscopy (FTIR) is a commonly used technique for the quantitative and qualitative analysis of organic substances to understand the molecular structure and chemical bonding of the molecules in it. The IR signal from the source passes through the sample through interferometer and received by the detector. The received signal is processed through an amplifier and analog to digital converter respectively. The output signal provides the information of how much of the beam is absorbed and that represents the molecular fingerprint of the sample and also detailed the structural insights. Thermo Nicolet FTIR 6700 in the range of 400 to 1800 cm^{-1} is used to understand the chemical bonding on the surface of catalyst.

3.4.7. Ultraviolet–visible spectroscopy (UV–Vis)

Ultraviolet–visible spectroscopy (UV–Vis) is a popular analytical technique that uses specific wavelength of light in the range of UV (190-400 nm) and visible (400 to 800 nm) spectrum. The sample is shined with light in wavelength of UV-Vis spectrum; it absorbs some of the light and transmits the rest of the light. The transmitted light was detected and quantitatively analyzed the absorbance profile of the sample. The ratio of intensity of

light pass through the sample (I) and the light intensity before passing through the sample (I_0) is the Transmittance and can be expressed in terms of absorbance as

$$A = log\frac{I_0}{I} \qquad (3)$$

The principle behind UV-Vis spectroscopy is based on the excitation of electron. When a photon of particular energy hits in atoms and molecules the electrons is excited form lower energy state to higher energy state with an energy difference called “band gap”. The band gap of a material is influenced by its chemical structure and can be calculated using Tauc equation:

$$\alpha h\nu = A(h\nu - E_g)^n \qquad (4)$$

where h be the Planck's constant, ν be the frequency of the vibration, A is the absorption coefficient, E_g is the band gap of the semiconductor and n is a constant, which is 1/2 for a direct transition or 2 for an indirect transition. Optical properties of the synthesized catalysts in this work were studied using Thermo scientific Evolution 300 UV-Visible spectroscopy.

3.4.8. Brunauer–Emmett–Teller (BET) surface area

Brunauer–Emmett–Teller (BET) theory is based on the physical adsorption of gas molecule on the solid surface that measures the specific surface area and pore size distribution of the material. BET theory applies on the multilayer system where the adsorbent gases are chemically inert to the sample surface. BET, the multilayer adsorption system works as an extension of Langmuir isotherm where the adsorbed gas over monolayer was calculated. Physical absorption between the adsorbate molecule and adsorbent surface area carried out in liquid nitrogen environment is through relatively

weak van der Waal force. Continuous flow or volumetric flow procedure is used to measure the amount of adsorbed gas molecule. Outgassing is the most important pre-treatment procedure that remove all the gasses and contaminants that are already present in the sample surfaces and pores, thus make the surface pores empty and allow the total adsorption of adsorbent gases to improve the accuracy.

Adsorption-desorption isotherms of all synthesized materials were recorded on a Micromeritics ASAP 2420 Surface area analyzer at liquid nitrogen temperature. From the adsorption desorption isotherms, specific surface area was calculated using BET method. Following are the conditions for Degassing and Analysis:

Degas Conditions:

1. Evacuation

Temp ramp rate: 10 ^{o}C/min

Target Temp: 90 ^{o}C/min

Evacuation rate: 5.0 mmHg/s

Evacuation time: 60 min

2. Heating Phase

Temp: 120 ^{o}C/min

Temp ramp rate: 10 ^{o}C/min

Time: 240 min

Analysis Condition:

Method: Silica Alumina, N_2@ 77 K

3.5. Electrochemical performance

In order to conduct the electrochemical measurements, the synthesized nanoparticles added with conductive carbon black were used for the cathodic reaction of the electrochemical cell. A 30 mg of catalyst was mixed with 3.5 ml of DIW and sonicated for 1 hr. Then a 70 mg of carbon black was measured and added slowly over the well-dispersed nanoparticles and again sonicated for 3 hr. The ink thus prepared was dried on a hot plate at 110°C overnight. The working electrode was prepared by dispersing 10 mg of Catalyst/C in 2.5 ml DIW and sonicating for 1 hr. A 20 µL of the dispersed solution was deposited over the working electrode (5mm dia. glassy carbon disc) and kept for drying in open environment. Once dried, a 20 µL Nafion solution (0.1 wt%) was dropped slowly to bind the catalyst over the electrode and kept for drying overnight. The catalyst loaded over the glassy carbon is 122.4 $\mu g cm^{-2}$ .The following techniques were used to understand the electrochemical performance of the catalyst.

3.5.1. Cyclic voltammetry (CV)

Cyclic voltammetry (CV) is a potentiodynamic electrochemical technique that measure the current develops in an electrochemical cell with a backward and forward potential sweep that provides more information on electrochemical reaction rate and redox potentials [261]. During this potential cycling, corresponding current was measured from the working electrode and plotted with respect to applied potential gives the cyclic voltammogram trace. The electrochemical characterization of an analyte in the solution or the property of the material adsorbed on the working electrode can be measured using cyclic voltammetry. Figure 29 shows the cyclic potential ramp and a typical voltammogram correspond to it. The rate of potential sweep over time during each cyclic

run of the experiment is its scan rate (V/s). The generated current was measured between the working electrode and counter electrode, while the potential is measured between working electrode and reference electrode.

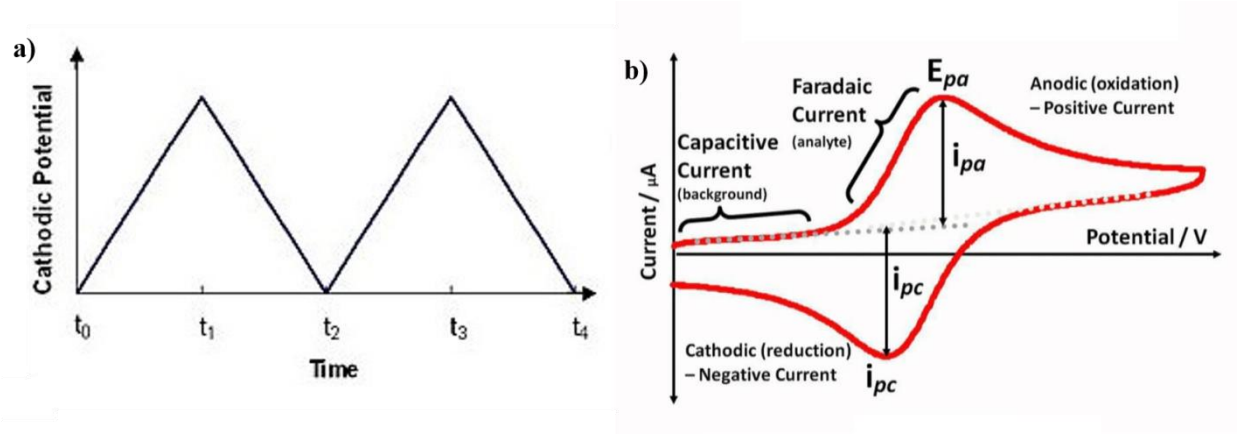

Figure 29. a) Cyclic voltammetry potential waveform b) Typical cyclic voltammogram for a reversible reaction.

The potential sweep from t_0 to t_1 in Figure 29.b increases the cathodic potential and thus increases the cathodic current (I_{pc}) through the reduction of analyte on the system. The potential depletion from t_1 to t_2, cause the re-oxidation of the reduced analyte, if the redox couple is reversible and increases the current value in the anodic reaction (I_{pa}) [261]. If the reversibility of the redox couple is high, the peak current curve of anodic and cathodic reaction looks similar. This single electron redox reaction can be represented as:

$$M^+ + e^- \leftrightarrow M \qquad (5)$$

The speed of the scanning potential is controlled by the scan rate and faster the scan rate, more will be the electron transfer in the working electrode and current generated will be the limited by the diffusion of analyte species to the surface of electrode. The measured

current value is proportional to the square root of the scan rate. Faster the scan rate, size of the diffusion layer decreases and increases the quantity of current measured.

3.5.2. Linear sweep voltammetry (LSV)

Linear sweep voltammetry (LSV) is an electroanalytical method to measure the current at working electrode through the linear sweep of voltage from its lower limit to higher limit. LSV is an irreversible electrochemical reaction with the potential sweep only in one direction [261]. Consider the electrochemical reduction of Fe^{3+} to Fe^{2+} and a thermodynamic equilibrium was established over the electrode surface as mentioned using Nernst equation:

$$E = E^0 + \frac{RT}{nF} log \frac{Fe^{3+}}{Fe^{2+}} \quad (6)$$

Where E is the applied potential difference and E^0 be the standard potential of electrode used.

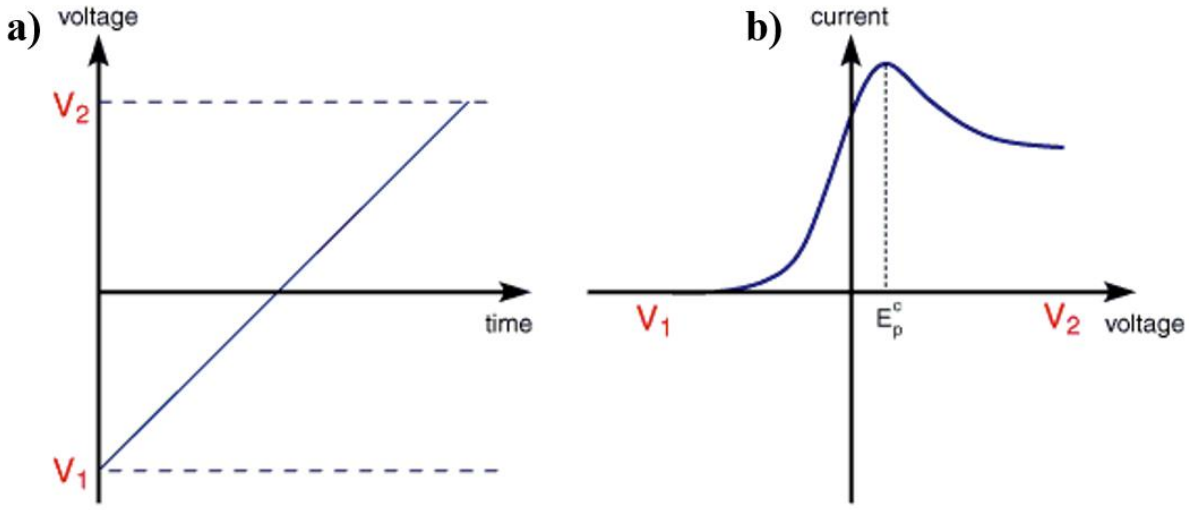

Figure 30. a) Direction of linear potential sweep b) corresponding current-voltage profile.

While increasing the potential from the equilibrium potential V_1 to V_2, the surface of the working electrode changes and starts to flow current by converting more reactants as in the following equation.

$$
\begin{aligned}
Fe^{3+} + e^- &\longleftarrow Fe^{2+} \\
Fe^{3+} + e^- &\leftharpoons Fe^{2+} \\
Fe^{3+} + e^- &\rightleftharpoons Fe^{2+} \\
Fe^{3+} + e^- &\rightleftharpoons Fe^{2+} \\
Fe^{3+} + e^- &\longrightarrow Fe^{2+}
\end{aligned}
\qquad (7)
$$

At some particular potential, a thick diffusion layer formed over the surface of the electrode that slows down the transfer of reactant flux to the electrode to satisfy the Nernst equation (6) and current value drops from its maximum. The size of the diffusion layer is

related to the voltage scan rate. For low scan rate, higher will be the thickness of diffusion layer over the electrode and thus reduces the measured current and vice versa. LSV identifies the unknown species over the electrode and calculate the solution concentration.

3.5.3. Chronoamperometry (CA)

Chronoamperometry (CA) or potential step amperometric is an electrochemical technique in which the potential between the working electrode and reference electrode is stepped and the resulted current with respect to time was measured. When the potential difference between the reference electrode and working electrode is zero, there is no redox reaction takes place and the net current value is zero. When a potential that enough to induce a redox reaction is applied over the working electrode (at t_0), the reactants get reduced through the depletion of the oxidants (Figure 31**)**. Through density gradient process, more reactants move away from the electrode and the flow of oxidants increases towards the surface of working electrode. These moving charges are termed as diffusion current. In this work, we used CA to understand the durability of the catalysts and identified the degradation mechanism.

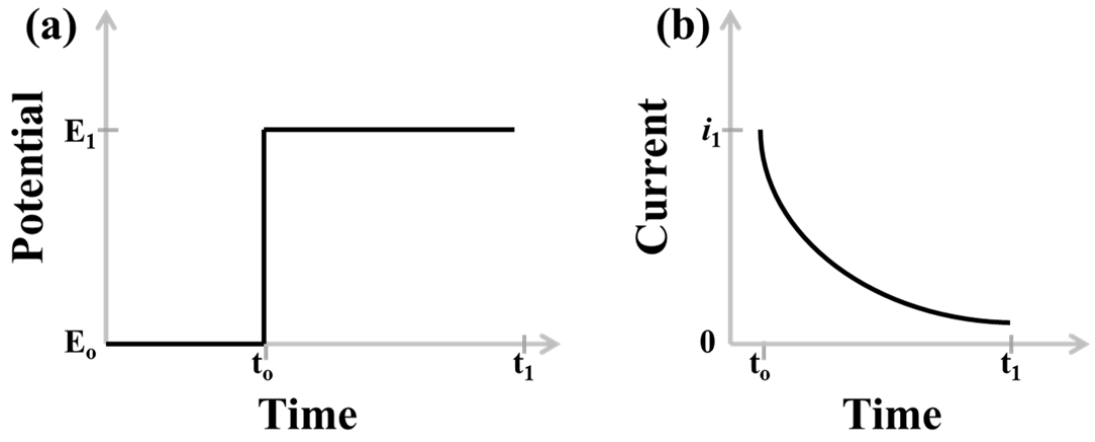

Figure 31. a) Potential waveform for chronoamperometry b) current signal associated

with the potential step.

3.5.4. Rotating disk electrode (RDE) and rotating ring disk electrode (RRDE) measurement

A Rotating disk electrode (RDE) is a hydrodynamic electroanalytical technique that induces a flux of analyte to the electrode that reduces the diffusion layer thickness. The electrode can rotate between 400 rpm to 3000 rpm in its vertical axis. The rotation of electrode induces a high rate of steady-state mass transport through convection. The RDE electrochemical setup is used to analyze the reaction mechanism related to a chemical phenomenon. Rotating disk electrode system consist of a conductive disk such as Pt, Ni, Cu, Au, Fe, Si, CdS, glassy carbon and graphite, surrounded with an inert non-conductive polymer or teflon attached to an electric motor that controls the rotation of the electrode as shown in Figure 32.a. The rotating disc drags the solution near to the surface and causes a momentum in the direction of tangent that pushes the electrolyte towards the exterior side, ie to the direction perpendicular to the working electrode (Figure 32.b). Thus, the rotation causes the pushing of the liquid electrolyte towards it and enables the kinetic study of the electrochemical reaction involved.

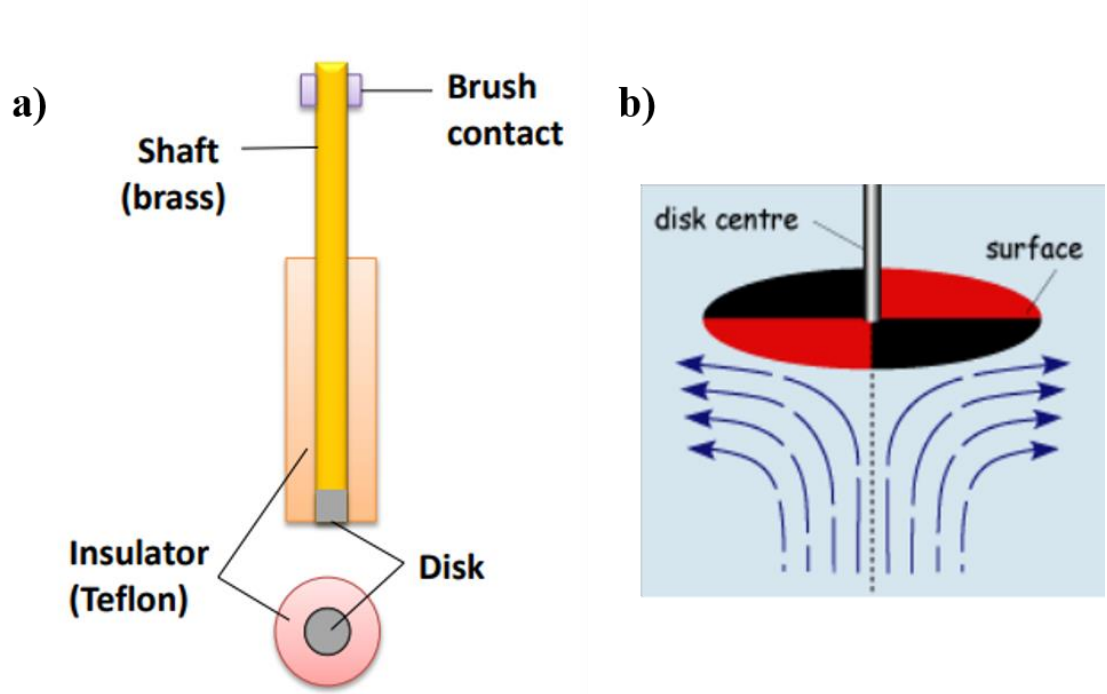

Figure 32. a) schematic diagram of RDE b) motion of electrolyte in the RDE configuration.

RDE measurements for ORR in KOH involves three regions with diffusion limiting current value, half wave potential and onset potential that governs the catalytic activity as in Figure 33. First region is kinetic control region including on-set potential which is trigger potential for a desired reaction, second region is kinetic and diffusion mixed control region including the half wave potential and third region is diffusion control region including diffusion controlled current.

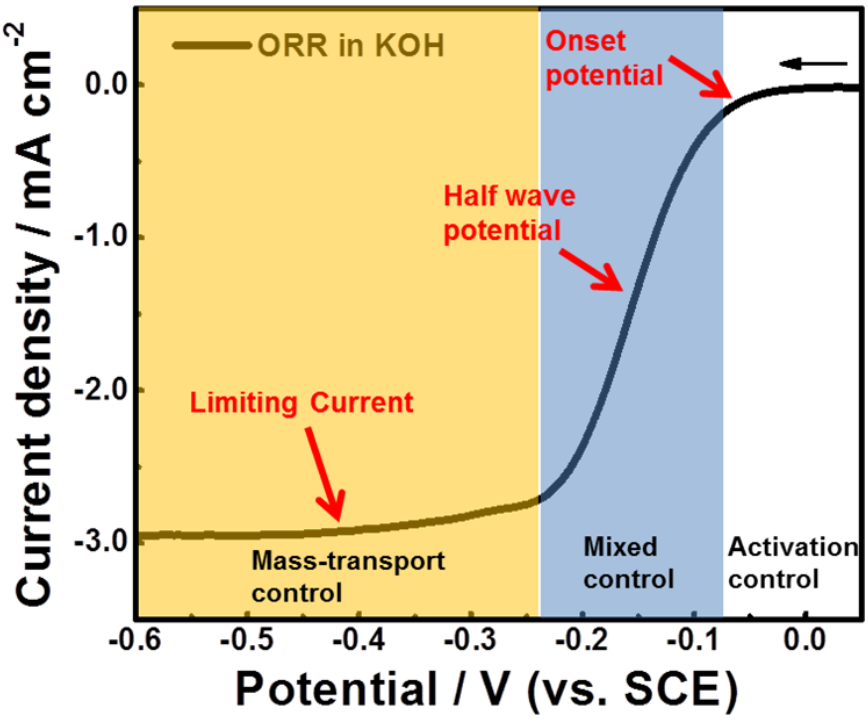

Figure 33. I-V profile of ORR in KOH.

Koutecky-Levich (KL) plot was used to calculate the number of electrons transferred in the overall reaction from the slope of the best fit on the linear slope on the basis of KL equation:

$$\frac{1}{J} = \frac{1}{J_L} + \frac{1}{J_K} = \frac{1}{B\omega^{1/2}} + \frac{1}{J_K} \qquad (8)$$

$$B = 0.62nFC_0(D_0)^{2/3}v^{-1/6} \qquad (9)$$

$$J_k = nFkC_o \qquad (10)$$

Where J, J_L, and J_K are measured current densities, diffusion-limited current and kinetic current densities owing to transport, and the kinetic current densities related to charge transfer, respectively. ω is the electrode angular rotation, n is the overall electron transfer, F is the Faraday constant (96485C mol^{-1}), C_0 is the bulk concentration of O_2 dissolved in

the electrolyte (7.8×10^{-7} mol-cm^{-3} for 1 M KOH electrolyte), v be the kinematic viscosity of electrolyte (0.01 cm^2 s^{-1}), D_0 is the O_2 diffusion coefficient (1.9×10^{-5} cm^2 s^{-1}) and k is the electron-transfer rate constant.

Rotating ring disk electrode (RRDE) is also a hydrodynamic voltammetry that consist of two working electrodes. The main difference between the RDE and RRDE is the secondary ring working electrode around the main central working electrode. RRDE is commonly used to understand the mechanism of the reaction and measure the intermediate products. As explained in Chapter 2, ORR can follow either direct four electron pathway or two electron pathways with two intermediate reactions. The intermediate hydrogen peroxide can be detected through the Pt ring over the RRDE and thus calculate the number of electron transfer as the following equation:

The number of electron transfer (n) and H_2O_2 yield ($H_2O_2^-$ %) per oxygen molecule was calculated using below equation:

$$n = \frac{4\times I_D}{I_D + I_R/N} \qquad (11)$$

$$H_2O_2\ \% = \frac{200\times I_R/N}{I_D + I_R/N} \qquad (12)$$

where I_D, I_R and N are the disc current, ring current and collection efficiency (N= 0.25) respectively.

In our work, a standard three cell electrode with an aqueous solution of 1M KOH as an electrolyte and a PINE instrument bipotentiostat (WaveDriver 20) were used at room temperature to measure the electrochemical activities. A glassy carbon disc of 5 mm diameter attached to a Teflon RDE housing (PINE Instruments) and connected with a rotator (maximum speed of 3600 rpm) was used as a working electrode. A platinum coil

and Ag/AgCl (in a 4M KCl solution) single junction were used as the counter electrode and the reference electrode respectively. Before conducting CV analysis, the working electrode was pretreated electrochemically for 100 cycle with a scan rate of 500 mVs^{-1} in the potential range between -0.9 V to 0.4 V. To start the CV analysis a 100 ml KOH electrolyte was bubbled with high purity N_2 gas for 1 hr and the CV data was collected between -0.9 V to 0.4 V with a scan rate of 50 mVs^{-1} for 10 cycle. The oxygen (reduction and evolution) reactions were studied by purging O_2 for 1 hr and conducting a CV analysis in the above-mentioned potential range. The linear sweep voltammetry was performed in the potential of -0.9 V to 0.7 V at a scan rate of 5 mVs^{-1} with a rotation speed ranging from 400 rpm to 1600 rpm.

Rotating ring disk electrode (RRDE) measurement was carried out in same electrochemical workstation with working electrode is 5mm glassy carbon electrode with platinum ring of 7.50 mm outer diameter and 6.5 mm inner diameter where the ring potential was set to be +0.6 V. A platinum coil be used as counter electrode and Ag/AgCl (in a 4M KCl solution) single junction as reference electrode. The measurement was conducted in 1 M KOH electrolyte solution saturated with O_2 prior to the experiment.

CHAPTER 4: INFLUENCE OF FUEL RATIO ON THE PERFORMANCE OF COMBUSTION SYNTHESIZED BIFUNCTIONAL CATALYSTS FOR ORR AND OER

4.1. Introduction

Solution combustion synthesis (SCS) is fast, simple, economical way of synthesizing nanomaterials by fast heating rate (up to 10^6 K/s). The energy required for the synthesis was meet from the heat of reaction during the process. The combustion temperature in SCS is high enough to avoid the post treatment methods (e.g.: calcination). The typical SCS involves the exothermic reaction between the metal nitrates and oxygen containing fuel (e.g. hydrazine, glucose, urea, glycine). Depending on the type and ratio (φ) of fuel used, the physical and chemical nature of the nanoparticle varied. Particle size, porosity, surface area, nature of oxide carbon content and morphology can be tuned with the fuel ratio (φ). Cobalt nanoparticles synthesized using SCS modes were reported before in our previous work. Here we are reporting the electrochemical behavior of cobalt nanoparticles synthesized using SCS with different fuel ratio (φ=0.5,1,1.75)

4.2. Experimental

Aqueous solution of cobalt nitrate ($Co(NO_3)_2 \cdot 6H_2O$) and glycine ($C_2H_5NO_2$) were used for the synthesis of cobalt nanoparticles. The quantity of nitrate and fuel were calculated to obtain 1.5 g of product in the output whereas the amount of glycine varies with the fuel ratio (φ=0.5, 1, 1.75). The measured precursors were dissolved in 25 ml deionized (DI) water and kept for 1 hour at room temperature to obtain a homogeneous solution that was placed over the hot plate heater at 250°C to heat the entire solution until combustion takes

place and nanoparticles are formed. The obtained nanoparticles were crushed using a hand mortar and sieved using < 75 µm sieve to achieve uniformity in the particle size. The prepared cobalt nanoparticles were mixed with carbon black to ensure the conductivity in the electrochemical reaction. A 30 mg of cobalt nanoparticle was dispersed well in 0.2 ml of DI water and sonicated for 1 hr followed by a slow addition of 70 mg of carbon black to prepare the ink for electrocatalytic experiments. The ink thus formed was dried on the hot plate at 110°C until all water evaporated and sample dried. The dried sample was again crushed and sieved to be used as a functional catalyst for electrochemical experiments. The working electrode was prepared by dispersing 10 mg of Co/C in 2.5 ml DI water and sonicate for 1 hr. A 20 µl of that solution was slowly deposited over a glassy carbon disc (5mm dia) and allowed to dry overnight. A 20 µl of 0.01% nafion solution was added to bind the catalyst over the surface.

4.3. Result and discussion

4.3.1. Catalysts characterization

XRD pattern of cobalt nanoparticles shown in Figure 34 indicates the phase change of cobalt at different fuel ratios utilized during synthesis. At lower fuel ratio, φ= 0.5, the cobalt is present as Co_3O_4, and by increasing fuel content to φ= 1.75, Co_3O_4 partially reduces to form a mixture of CoO and Co_3O_4. Scherrer's equation was used to calculate the crystallite size of particles from XRD pattern [262]. While changing the reduction condition from fuel lean (φ=0.5) to stoichiometry, the crystallite size increases from 10.1 nm to 18.23 nm and for the fuel rich state (φ= 1.75) the size increases to 20.2 nm. It is common to observe an increase in the crystallite size and a decrease in BET surface area

as the fuel content is increased during synthesis [263].

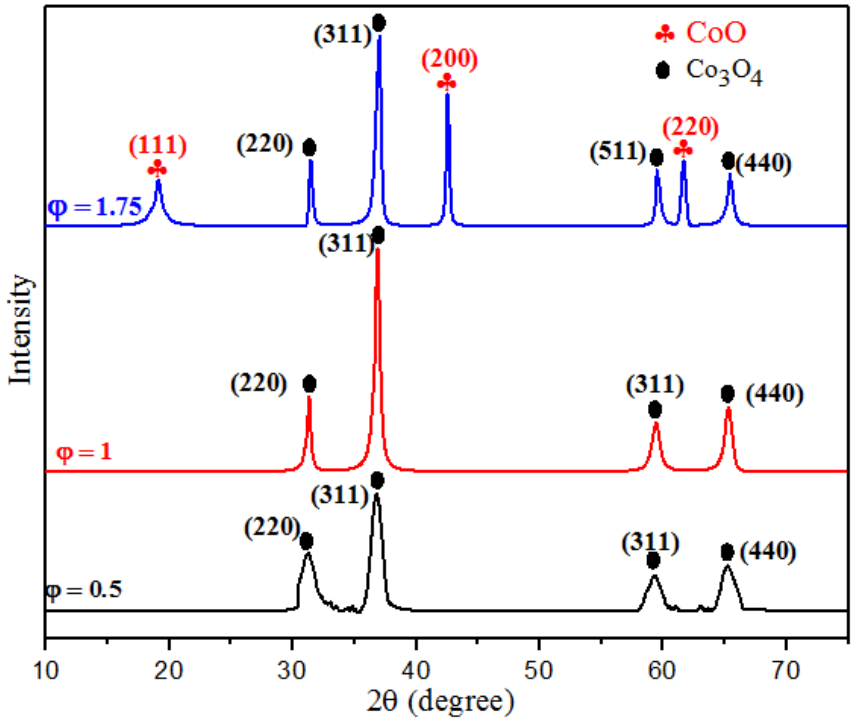

Figure 34. XRD profile of cobalt nanoparticles synthesized using SCS method at different fuel ratio.

The SEM morphology and the elemental composition of the synthesized cobalt oxide are shown in Figure 35. SEM images of cobalt nanoparticles synthesized using SCS technique with a) 0.5 b) 1 c) 1.75 fuel ratio (scale- 10 µm). The table shows the atomic concentration of different element obtained from EDX analysis of the corresponding SEM images, clearly indicates porous nature of material formed due to evolution of gaseous products during combustion. In congruence with surface area, porosity is also affected by the amount of fuel used during synthesis; nonetheless pore size distribution is not very uniform. The elemental composition indicates the presence of more carbon

content with higher fuel ratio (8.87 % for φ=0.5 as compared to 12.87 % for φ=1.75), possibly due to an increase in the carbon coming from the fuel used. The diminishing oxygen concentration from 53.82 % (φ=0.5) to 38.76 % (φ=1.74) is an indication of the reducing environment created by using excess fuel that partially converts the Co_3O_4 to CoO as indicated by the XRD results.

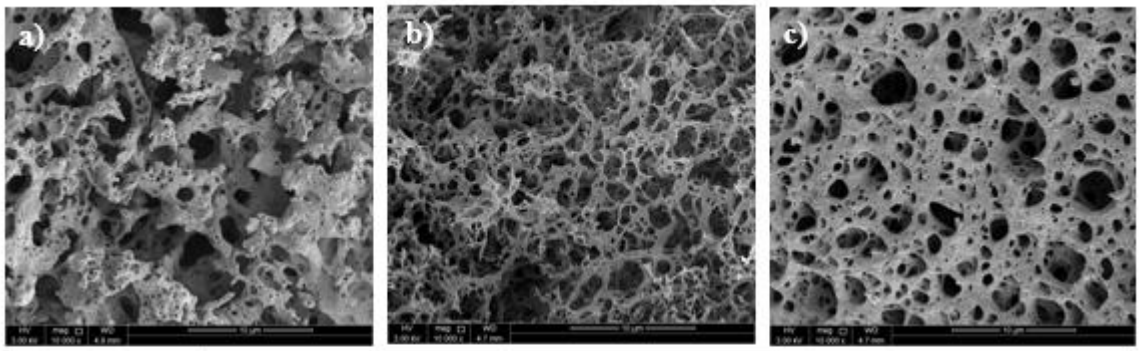

Element	at.% @ ϕ = 0.5	at.% @ ϕ = 1	at.% @ ϕ = 1.75
Cobalt	37.31	41.60	48.37
Oxygen	53.82	47.58	38.76
Carbon	8.87	10.82	12.87

Figure 35. SEM images of cobalt nanoparticles synthesized using SCS technique with a) 0.5 b) 1 c) 1.75 fuel ratio (scale- 10 µm). The table shows the atomic concentration of different element obtained from EDX analysis of the corresponding SEM images.

Figure 36 shows the TEM images of catalysts synthesized at different fuel ratio. Low magnification images of catalyst for φ = 0.5, 1 and 1.75 (Figure 36**.** a, d and g) show an increase in the particle size along with increase in the level of agglomeration. The particle size in the fuel lean catalyst, φ = 0.5, is 8-12 nm whereas the size appears to increase at

higher fuel ratio though exact size estimation through visual inspection is difficult due to agglomeration. Figure 36 (b, g and h) illustrate the HRTEM of individual particles. Well-resolved lattice fringes with inter-planar distance of 0.25 nm and 0.28 nm corresponding to (311) and (220) planes for spinel structured Co_3O_4 [264] can be clearly identified. The FFT square spots shown in Figure 36**c** suggests Co_3O_4 single crystal features, in a good agreement with the XRD phases identified in Figure 34. The lattice point at (222) with lattice spacing of 0.23 nm is well indexed for spinel Co_3O_4 [265]. The lattice spacing of 0.475 nm and 0.205 nm confirms the set of planes (111) and (200) which corresponds to the CoO as in the XRD peaks for $\varphi = 1.75$.

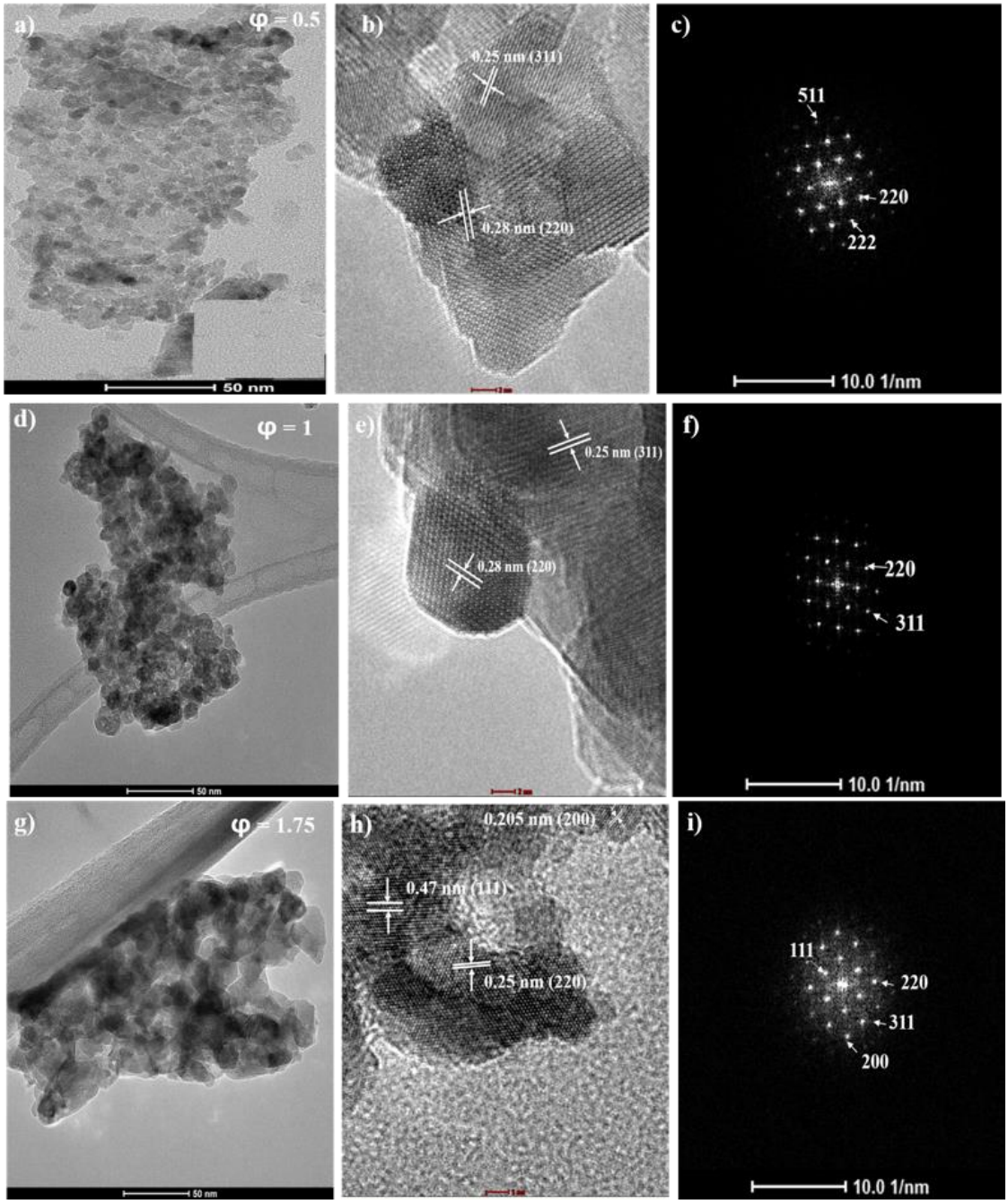

Figure 36. TEM, HRTEM and SAED images of synthesized catalysts (a-c) φ = 0.5 (d-f) φ = 1 (g-i) φ = 1.75.

The elemental mapping of the corresponding TEM images in Figure 36 is shown in Figure 37. The STEM images of synthesized catalyst at φ = 0.5, 1 and 1.75 are shown in Figure 37(a, e and i). The elemental mapping confirms the uniform presence of Co and O throughout the catalyst. The decrease in brightness of the O spectrum represents the decrease in the oxides of cobalt.

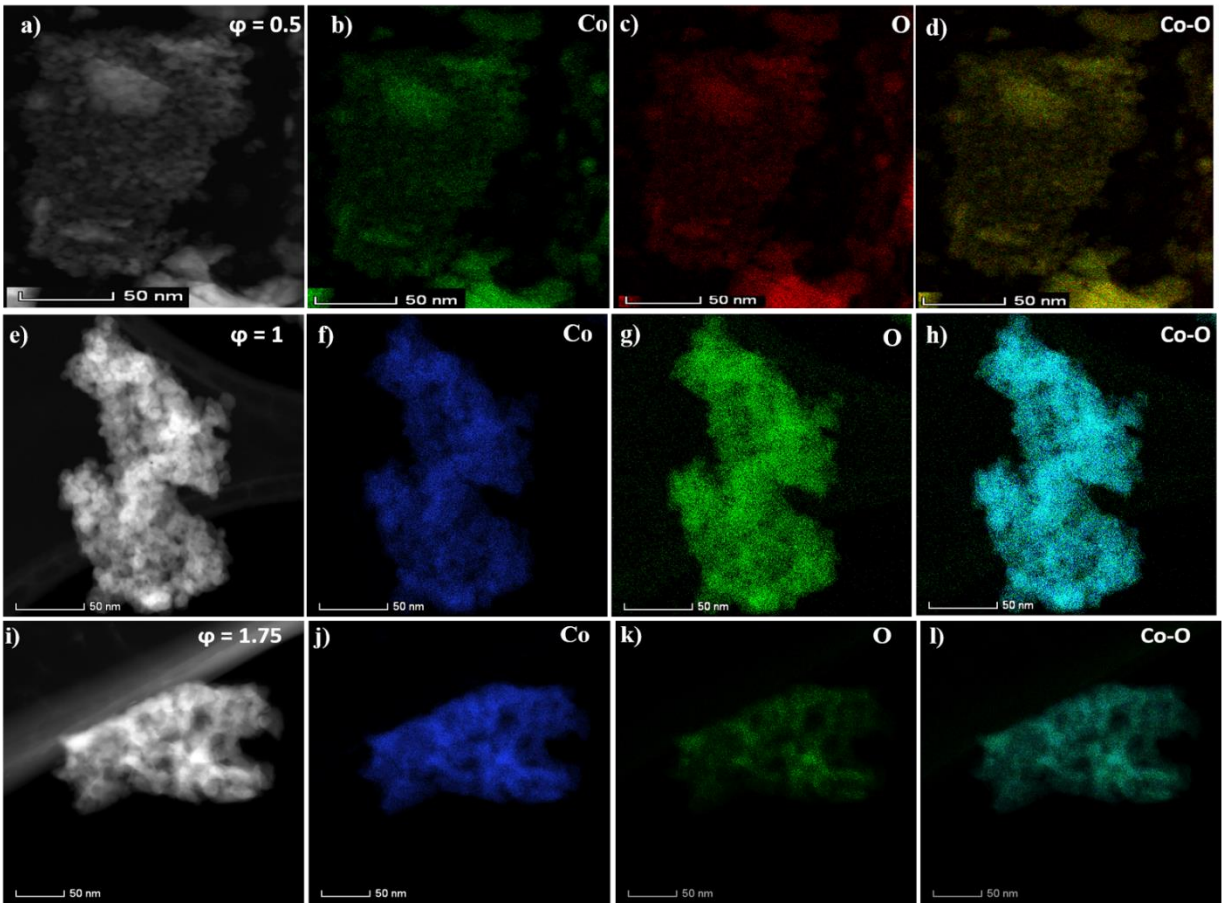

Figure 37. Elemental mapping by high-angle annular dark-field scanning transmission electron microscopy (HAADF-STEM) for synthesized catalysts at different fuel ratio.

The optical behavior of the three catalysts were studied using UV-Vis spectra as shown in Figure 38. The optical absorption spectrum in Figure 38**(**a-c**)** shows two bands corresponding to the two ligands to metal charge transfer transition normally occurring in the spinel Co_3O_4. The lower band peaks associates with φ =0.5, 1 and 1.75 are at 445 nm, 525 nm 540 nm and that of higher band wavelength are 785 nm, 795 nm and 800 nm. The red shift of the peaks towards fuel lean condition shows the tendency of decrease in particle size. The absorption peak centered at lower band is associated with O^{-2} to Co^{+2} and higher band corresponds to O^{-2} to Co^{+3} transition [266-269]. The optical band gap energies can be determined using the Tauc plot with hν in x- axis and $(\alpha h\nu)^{1/r}$ in y-axis where r = ½ for direct band gap materials and α is the absorption coefficient as shown in Figure 38(d-e). The extrapolation of the hν value to α = 0 at the linear portion of the curve gives the band energies. There are two linear portions intersecting at x axis at E_{g2} and E_{g1} holding values of 2.2 eV and 0.91 eV for φ = 0.5, 2 eV and 0.92 eV for φ = 1, and 1.95 eV and 1.1 eV for φ = 1.75. The optical band gap ($E_g = E_{g2} - E_{g1}$) of three catalysts synthesized at φ = 0.5, 1 and 1.75 are 1.29 eV, 1.08 eV and 0.88 eV respectively. The relation between band gap energies and particle size are inversely proportional and indicates a decrease in particle size with increase in band gap. Based on this statement, the particle size increases with increase in fuel ratio with highest particle size for φ =1.75 and lowest for φ =0.5, showing good consistency with the XRD and TEM results.

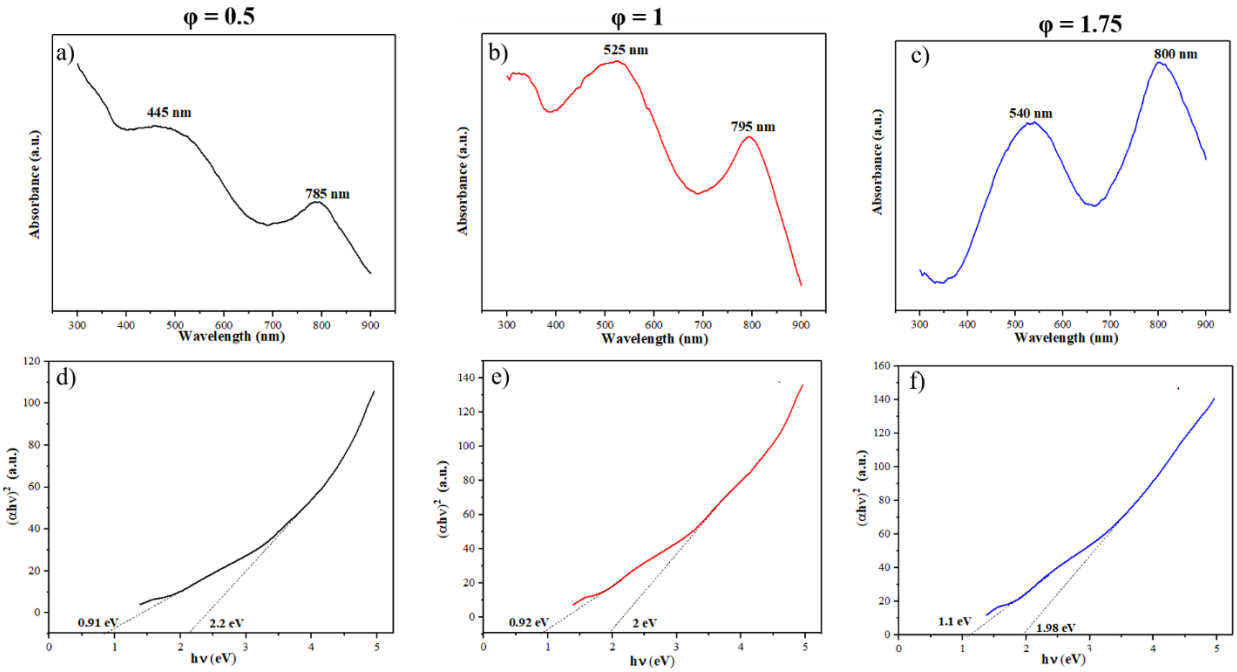

Figure 38. UV-absorption spectrum (a-c) and corresponding tauc plot to obtain bandgap by extrapolation to $\alpha = 0$ for all the catalyst at $\varphi = 0.5$, 1 and 1.75.

4.3.2. Electrochemical analysis and characterization

Figure 39 displays the cyclic voltammogram (CV) of the three cobalt catalysts in an O_2 saturated 1M KOH solution. The anodic peak (a_1) at positive current density and cathodic peaks (c_1 and c_2) at negative current density corresponds to the oxidation and reduction reactions. Number of cobalt oxide phase with different oxidation states are confirmed with the multiple peaks in the CV. The redox behavior of cobalt oxide in alkaline medium can be described as following [269,270]:

Oxidation / Anodic scan :

$$3Co(OH)_2 + 2OH^- \rightarrow Co_3O_4 + 4H_2O + 2e^-$$

$$Co_3O_4 + OH^- + H_2O \rightarrow 3\,CoOOH + e^-$$

$$CoOOH + OH^- \rightarrow CoO_2 + H_2O + e^-$$

Reduction / Cathodic scan :

$$CoO_2 + H_2O + e^- \rightarrow CoOOH + OH^-$$

$$3\,CoOOH + e^- \rightarrow Co_3O_4 + OH^- + H_2O$$

$$Co_3O_4 + 4H_2O + 2e^- \rightarrow 3Co(OH)_2 + 2OH^-$$

The further increase in positive current density after a_1 peak is associated with the oxidation reaction known as oxygen evolution reaction:

$$4OH^- \rightarrow O_2 + 2H_2O + 4e^-$$

The CV characterized by an anodic peak (a_1) and cathodic peak (c_1) is due to the quasi-reversible redox couple $CoO_2 / CoOOH$ in the reaction. The oxygen reduction peak (C_2) at φ =0.5 has a positive shift compared to other two catalysts and reflects the better activity for oxygen reduction reaction. The catalyst synthesized at higher fuel value has lower activity, possibly due to the high residual carbon decreasing the active metal content, in addition to large crystallite size and smaller surface area.

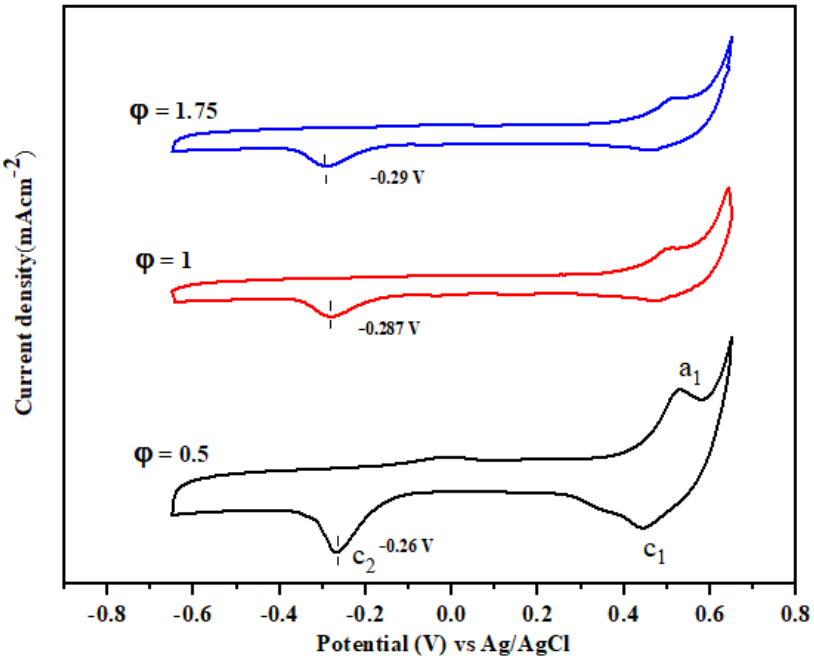

Figure 39. CV curves of cobalt nanoparticles synthesized using SCS mode at different fuel ratios in O_2 saturated 1M KOH solution at a scan rate of 50 mVs^{-1}

The LSV curves shown in Figure 40.a confirm the bifunctional activity of the catalyst for ORR and OER. The ORR activity in 1M KOH alkaline medium with 1600 rpm rotation speed at a scan rate of 5 mVs^{-1} shown in Figure 40.b indicate the maximum diffusion limiting current density for Co with φ=0.5, whereas the curves are almost overlapping for φ=1 and φ=1.75. There is a clear positive shift in the onset potential for φ=0.5 at -0.165 V which indicates the better catalytic activity on φ=0.5 than on φ=1 or φ=1.75. The catalytic activity for OER in O_2 saturated 1M KOH solution in the potential window of -0.12 V to 0.8 V shown in Figure 40**c** displays the highest anodic current for φ=0.5 compared to the other two catalysts. The OER current densities of φ=0.5, 1 and 1.75 at 0.8 V are 90.49, 49.5 and 44. 4 $mAcm^{-2}$ respectively. The anodic current density of

φ=0.5 is nearly double to that of the other two catalysts. RDE polarization curves at various rotation speeds from 400rpm to 1600rpm were used to understand the kinetics of ORR on φ=0.5 catalyst, and the results are presented in Figure 40.d. The limiting current densities increases by changing the rotation from 400 rpm to 1600 rpm by shortening the O_2 diffusion distance to the catalysts surface.

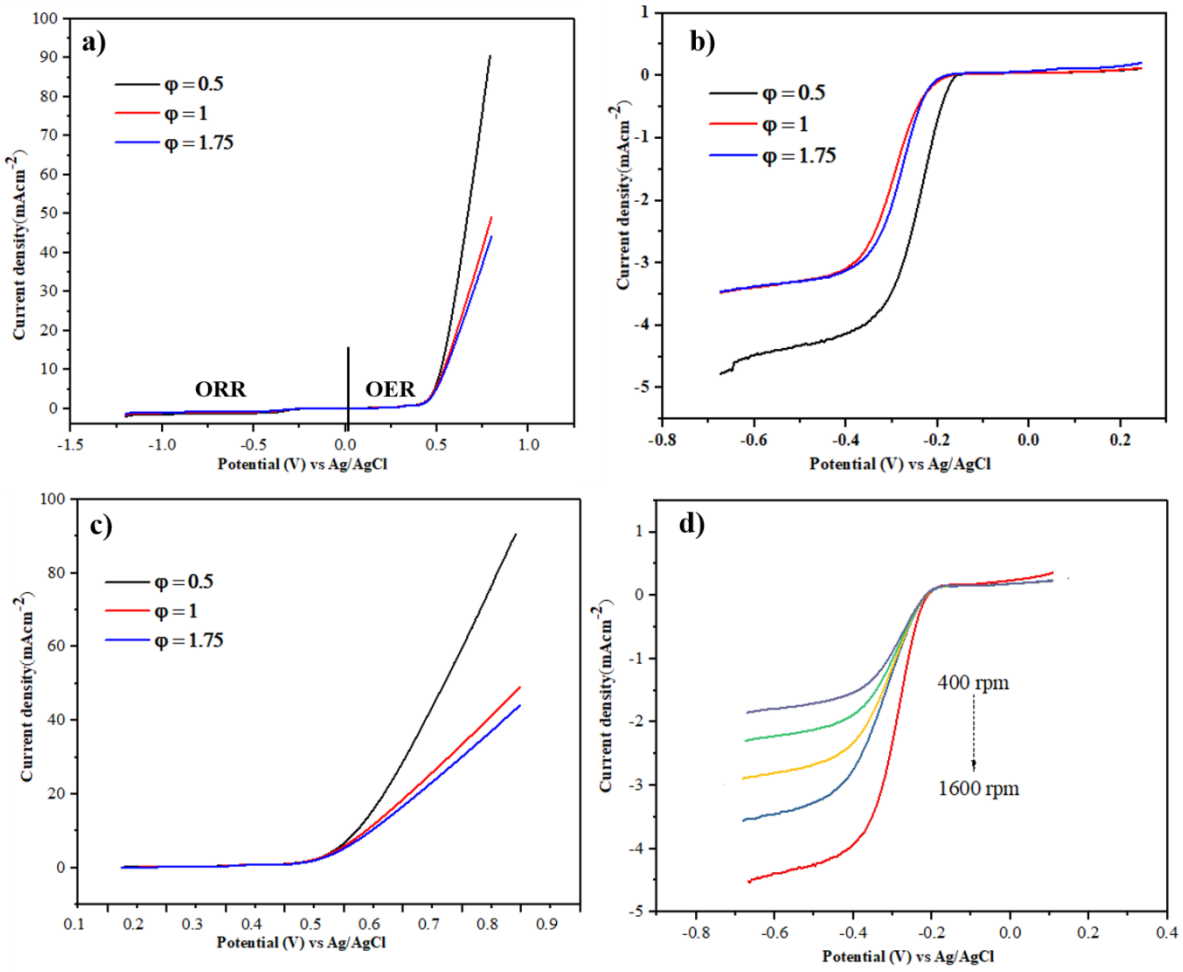

Figure 40. a) Rotating disk electro voltammogram of cobalt catalyst at different fuel ratio in O2 saturated 1M KOH solution with a rotation speed of 1600 rpm at a scan are of 5 mVs-1 in the potential range of -1.2 V to 0.8 V b) ORR region of LSV curve between 0.7 V and 0.2 V c) OER plot in the region of -0.12 V to 0.8 V d) steady state polarization curve of Co @ ϕ=0.5 at different rotation rate in 1 M KOH electrolyte.

The overall number of electron transfer during oxygen reduction reaction is used as a criterion to determine the efficiency of a catalyst that can be obtained by using equation (9), and graphically represented in KL plots as shown in Figure 41.a. The KL plot at -

0.45V follows a linear behavior that indicates the first order kinetics towards the dissolved oxygen reduction. The number of electron exchanged per oxygen molecule for the ORR are calculated to be 3.2, 2.99 and 2.9 for φ=0.5, φ=1 and φ=1.75 respectively. Kinetic current density shown in Figure 41.b follows a decrease in its intensity with increase in the fuel ratio. The electrocatalytic activity of the bifunctional catalyst towards ORR and OER can be more adequately specified in terms of Tafel plots shown in Figure 41.c-d. The Tafel plots are obtained by plotting J_k corresponding to the potential (V), where J_k is the kinetic current density obtained from Koutecky–Levich equation (8). The two slopes marked (at a high and a low potential) in the Tafel plot correspond to Temkin isotherm and Langmuir isotherm. The most suitable catalyst will have the lowest slope value at Langmuir isotherm and highest slope value at Temkin isotherm. Table 1 shows the Tafel slope for each region at ORR and OER. Co with φ=0.5 achieves the most appropriate conditions with a slope value of 48 mV/dec at Langmuir isotherm and 88 mV/dec at Temkin isotherm. In the OER activity region, all of the catalysts exhibit good performance with the highest activity observed for φ=0.5.

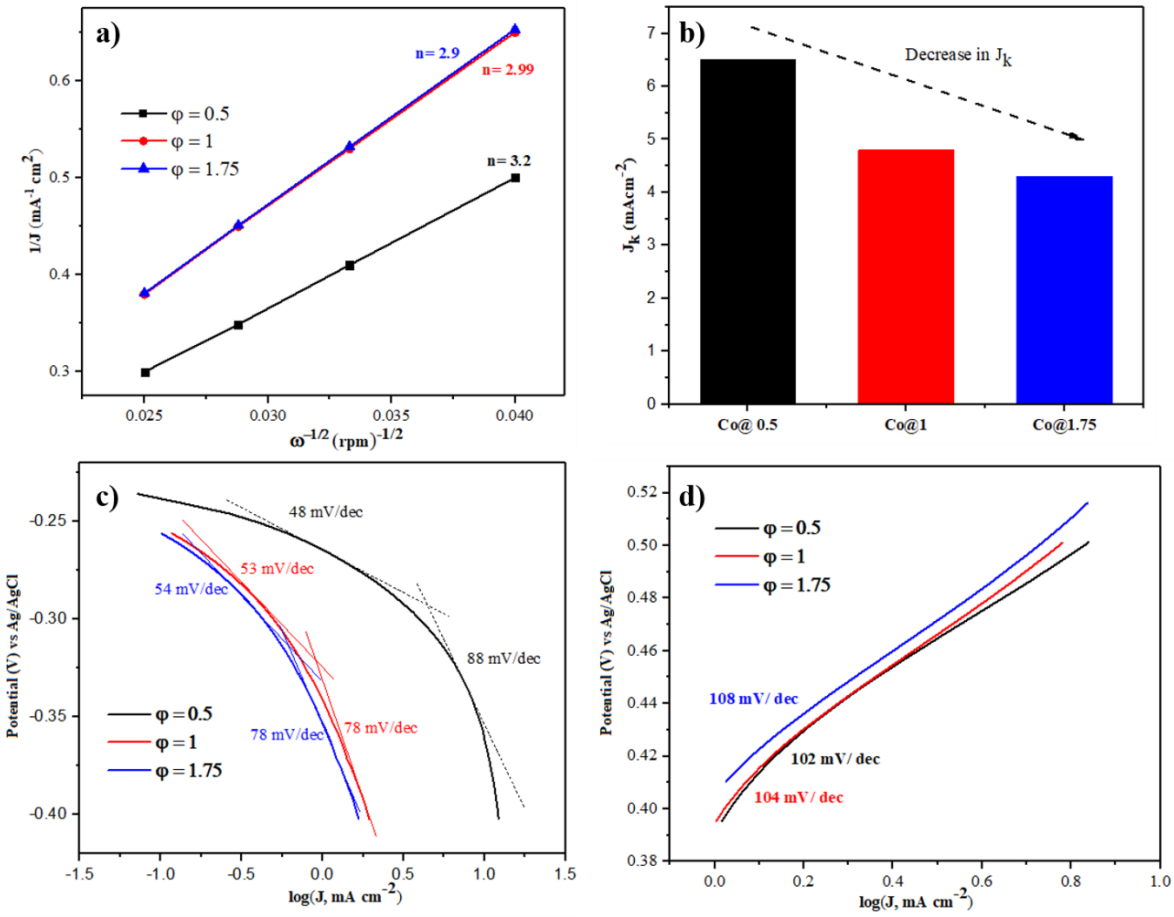

Figure 41. a) Koutechy - Levich plot for the ORR at -0.45 V, b) kinetic current density for all the catalysts, c) Tafel slope for ORR region, d) Tafel slope OER region in O2 saturated 1M KOH electrolyte at a rotor speed of 1600 rpm.

The observed differences in the electrocatalytic performance could be due to the differences in physio-chemical properties of the synthesized materials. The catalyst prepared with fuel-rich (φ=1.75) solution have low activity due to the lower surface area, larger crystallite size and high amount of carbon. The level of amorphous carbon at high fuel ratio hinders the activity of the catalysts. The cobalt nanoparticles in Co_3O_4 phase

follow high activity and four electron pathway when compared to other phase, CoO, which is anticipated to follow 2 electron pathway due to the intermediate formation of HO_2^- reducing the activity.

Table 1. Tafel Performance Parameters for ORR and OER

	ORR Tafel slope		OER Tafel slope
Catalyst	b_{low} (mV dec^{-1})	b_{high} (mV dec^{-1})	(mV dec^{-1})
0.5	48	88	102
1	53	78	104
1.75	54	78	108

4.4. Conclusion

Cobalt nanoparticles with different fuel ratios (φ = 0.5, 1, and 1.75) were synthesized using solution combustion synthesis. At lower fuel values (φ=0.5), the particles were in Co_3O_4 phase and by increasing the fuel ratio, a partial reduction is observed, displaying a mixture of CoO and Co_3O_4 phases at φ=1.75. The elemental composition from EDX study indicates an increase in carbon content and a decrease in oxygen content when increasing the fuel ratio. Based on the CV results, the ORR potential peaks for Co (φ=0.5) showing a positive shift from the potential observed for other two catalysts synthesized at higher fuel ratio. LSV results show a positive shift in the onset potential for Co (φ=0.5) exhibiting the highest limiting current density. The OER current density follows a similar trend with maximum value observed for Co (φ=0.5). A comparison of Tafel plots, on account of lower slope at Langmuir isotherm and higher slope at Temkin isotherm, also

confirms an improvement in the electrocatalytic performance of Co ($\varphi = 0.5$) in relation to other two catalysts. The observed differences in the electrocatalytic behavior of the three catalysts could be due to the nanoparticle size, surface area, porosity in addition to the oxidation state of Co found after synthesis. The fuel lean condition ($\varphi = 0.5$) is associated with the synthesis of smaller nanoparticles with higher surface area, possibly being dominant factor in improving its activity for ORR and OER reaction.

Outcome of the chapter published in journal: Ashok, A., Kumar, A., Bhosale, R. R., Almomani, F., Saad, M. A. H. S., Suslov, S., & Tarlochan, F. (2019). Influence of fuel ratio on the performance of combustion synthesized bifunctional cobalt oxide catalysts for fuel cell application. *International Journal of Hydrogen Energy*, 44(1), 436-445.

CHAPTER 5- PROBING THE EFFECT OF COMBUSTION-CONTROLLED SURFACE ALLOYING AND STUDY THE EFFECT ON ORR AND OER.

5.1. Introduction

Bimetallic nanoparticles have received great attention due to their multi functionalities, selectivity and activity over monometallic particles and their increasing applications to various areas including electronics, optical, catalytic and magnetic [271-276]. Bimetallic nanoparticles with different structures like crown-jewel, hollow, heterostructure, core—shell, alloys and porous structure has been synthesized using various techniques such as chemical methods, hydrothermal, impregnation, sol–gel, spray pyrolysis, and precipitation methods [277-281]. This structural diversity is due to the atomic distribution of the individual metals in bimetals. The significance of bimetals due to their chemical and physical properties is derived from the synergetic factors of two constituent metals in the bimetals [282-284].

5.2. Synthesis of Ag-Co_3O_4 alloys using SCS

Bimetallic Silver-Cobalt (Ag-Co) gained a wide attention in different branches of science and industry including catalysis [285,286], biotechnologies [287], energy storage and conversion devices such as fuel cells, batteries etc. [288-290]. Different techniques have been used for the preparation of bimetallic AgCo including hydrothermal reduction, sol-gel, intermatrix synthesis, co-precipitation and so on [285,287,291]. Erdogan *et al* synthesized bimetallic AgCo using co-precipitation method and studied the catalytic oxidation of carbon monoxide [291]. Alonso and co-workers tested the bacterial disinfection property of fibrous polymer Ag/Co composites and compared the

bactericidal activity of monometals of Ag and Co [287]. Lima *et al* designed bimetallic silver-cobalt particles with different molar ratio for oxygen reduction reaction in alkaline medium [290]. In this chapter, we used solution combustion synthesis for nanoparticle preparation and studied the effect of synthesis conditions on surface and bulk structures that shows good ORR and OER response in basic medium.

The bimetallic silver-cobalt was synthesized using three different modes of solution combustion synthesis with 1:1 weight ratio. The synthesis process is schematically represented in Figure 42**.** It should be noted that three synthesis modes are termed as AgCo-11, AgCo-12 and AgCo-21 for the sake of convenience and not necessarily represent the metallic form of Ag and Co. As it will be clear in subsequent sections, in most cases cobalt is present in oxidized states.

Mode 1- AgCo-11:

A homogeneous aqueous solution of silver nitrate ($AgNO_3$), cobalt nitrate $Co(NO_3)_2 \cdot 6H_2O$ and glycine ($C_2H_5NO_2$) with fuel to oxidizer ratio (φ) of 1.75 was prepared by mixing desired molar ratio of precursors in 25 ml of water. The amount of precursors were measured based on the preparation of 1.5 g of products using stoichiometric values as shown in equation (1). The dissolved precursors were heated over a hot plate at 250°C until the water evaporates, and the reactive gel reaches to its auto-ignition temperature. Thereafter, the self-sustained combustion wave propagates from one end to other end of the beaker by converting the precursors to metal/oxides nanopowder.

Mode 2- AgCo-12:

During this mode, the silver nitrate ($AgNO_3$) and glycine ($C_2H_5NO_2$) with fuel to oxidizer

ratio (φ) of 1.75 was combusted in a single step in Figure 42 shows Mode 2 to produce silver nanoparticles. A solution of cobalt nitrate $Co(NO_3)_2 \cdot 6H_2O$) and glycine ($C_2H_5NO_2$) were mixed with the synthesized silver nanoparticles in the next step. This solution was mixed thoroughly by dispersing the nanopowder completely; thereupon this mixture was combusted over the hot plate heater. This combustion mode is termed as second wave combustion synthesis (SWCS) and usually involves two stages consisting of solution combustion synthesis. In this mode, the cobalt/cobalt-oxide particles are expected to be on the top of the silver nanoparticles that synthesized in the first stage of combustion.

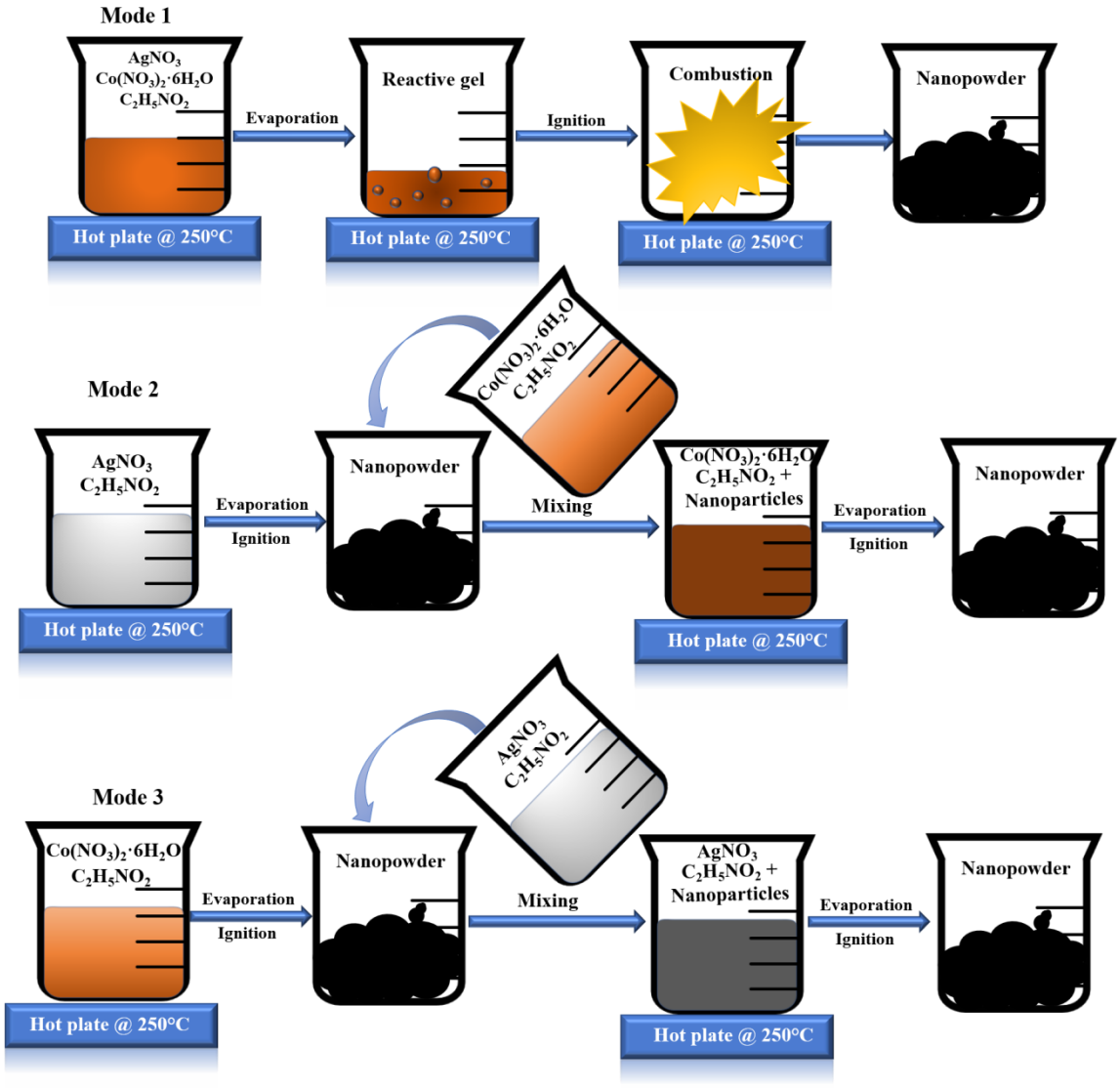

Figure 42. Schematic representation of three different modes of solution combustion synthesis.

Mode 3- AgCo-21:

In mode 3, cobalt nitrate $Co(NO_3)_2 \cdot 6H_2O$) and glycine ($C_2H_5NO_2$) solution was combusted to synthesize cobalt/cobalt-oxide nanoparticles initially. These nanopowders are mixed with silver nitrate ($AgNO_3$) and glycine ($C_2H_5NO_2$) solution followed by

second wave combustion. Here silver particles are expected to be on the surface possibly covering cobalt nanoparticles. The obtained nanopowders from three modes were crushed using hand motor and sieved to obtain particles < 75μm. These particles were characterized using different techniques to identify the structure and composition of the synthesized nanopowders.

5.3. Results and Discussion

5.3.1. Catalysts characterization

Detailed thermodynamic analysis of all the expected way of combustion is illustrated in Figure 43. Silver at φ =1.75 gives an adiabatic combustion temperature of 1676 K with silver in liquid phase. The melting point of Ag is 1234 K and any temperature higher than this value causes conversion of solid phase to liquid form. The adiabatic combustion temperature of Co is 1469 K and AgCo-11 is 889.85 K respectively. The cobalt nitrate-glycine mixture at φ =1.75 yields pure metallic cobalt, and silver nitrate-cobalt nitrate-glycine (AgCo) system gives metallic Ag crystals and cobalt in Co_3O_4 phase. In AgCo-12, cobalt nitrate-glycine combustion takes place in presence of silver nanoparticles that was prepared during the first stage of combustion, and the whole system reaches an overall combustion temperature of 1424 K and the output phases at the adiabatic combustion temperature are liquid Ag with solid metallic cobalt. While in AgCo-21, there are three possibilities with the Co, CoO and Co_3O_4 during the second phase of combustion. AgCo-21 with Co reaches the combustion temperature at 1423 K with Ag liquid phase and metallic cobalt form. When using CoO as the input in second stage, the output product distribution is a mixture of Ag (liquid), CoO and Co at 1394 K. The partial

reduction of CoO to Co was possibly achieved during the combustion of silver-glycine system due reducing environment created by product gases. Similarly, Ag (NO_3)-$C_2H_5NO_2$ combustion in presence of Co_3O_4 gives metallic silver at 1069 K along with the conversion of 88 % of Co_3O_4 to CoO. During the second wave combustion, there is a possibility of gaseous mixture creating reducing environment that reduces the existing oxides formed during the first stage of combustion.

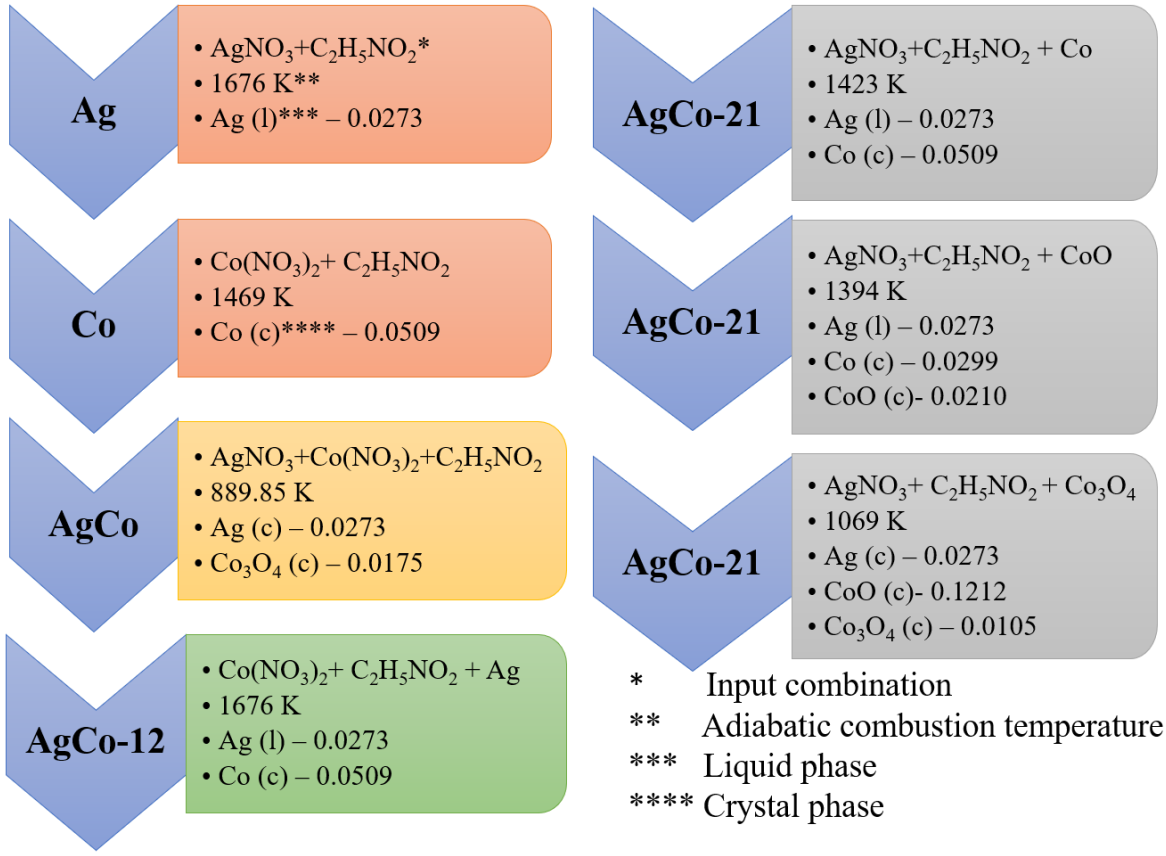

Figure 43. Adiabatic combustion temperature and the output products in the three modes of combustion.

The sequence of reaction in bimetallic combustion can be explained in terms of the decomposition temperature of silver nitrate and cobalt nitrate obtained from literature and are in the order of 473 K and 448 K respectively [292,293]. Once the temperature of the cobalt nitrate-silver nitrate-glycine mixture reaches to 448 K, cobalt nitrate starts to decompose possibly leading to exothermic combustion reaction that increases the temperature and subsequently starts the combustion of silver-nitrate-glycine. In this sequence, Ag is anticipated to be on the surface of cobalt/cobalt-oxide even though it involves a single step combustion synthesis. This sequence is similar to the steps involved in AgCo-21 that is accomplished in two stages. The silver nitrate- glycine combustion is performed in presence of cobalt oxide that have been synthesized earlier. Based on the order in which combustion reaction takes place in AgCo system, some similarities in properties of AgCo-11 and AgCo-21 are anticipated.

Figure 44 shows the XRD pattern of Ag-Co nanoparticles prepared via three different modes of solution combustion synthesis. The phase identification indicates the presence of metallic Ag and oxides of cobalt in +2 and +3 oxidation states. The presence of peak in all the three cases at 38.2°, 44.3°, 64.6° and 77.6° corresponds to the Ag (111), Ag (200), Ag (220) and Ag (331) respectively. The diffraction pattern of cubic Co_3O_4 displays four characteristic bands at 31.28°, 36.6°, 59.21° and 65.32° that were confirmed with PDF#43-1003. In AgCo-12 and AgCo-21, the Co_3O_4 phase was partially reduce to CoO through the second phase of combustion that produces a reducing atmosphere for further reduction. The presence of CoO in AgCo-12 and AgCo-21 indicates the weak diffraction pattern at 43.54°. This result seems inconsistent with the thermodynamic analysis discussed earlier, however, it should be noted that thermodynamic calculations

were performed assuming adiabatic and inert conditions, whereas actual combustion experiments were conducted in a beaker placed on a hot plate heater and open to atmospheric air. A close look at the peaks shown in Figure 44.b indicates a slight shift in 2θ of Ag (111) and Co_3O_4 (311) planes to higher value could be due to either the existence of lattice strain or by the change in chemical composition owing to solid solution formation. The doping of one atom to other causes the rearrangement of the atom periodicity and thus changes cell parameters causing a shift of diffraction peaks. AgCo-12 shows greater displacement that promotes the better incorporation of Ag and Co atoms together to form alloys acting as transition zones leading to bimetal formation [294-296].

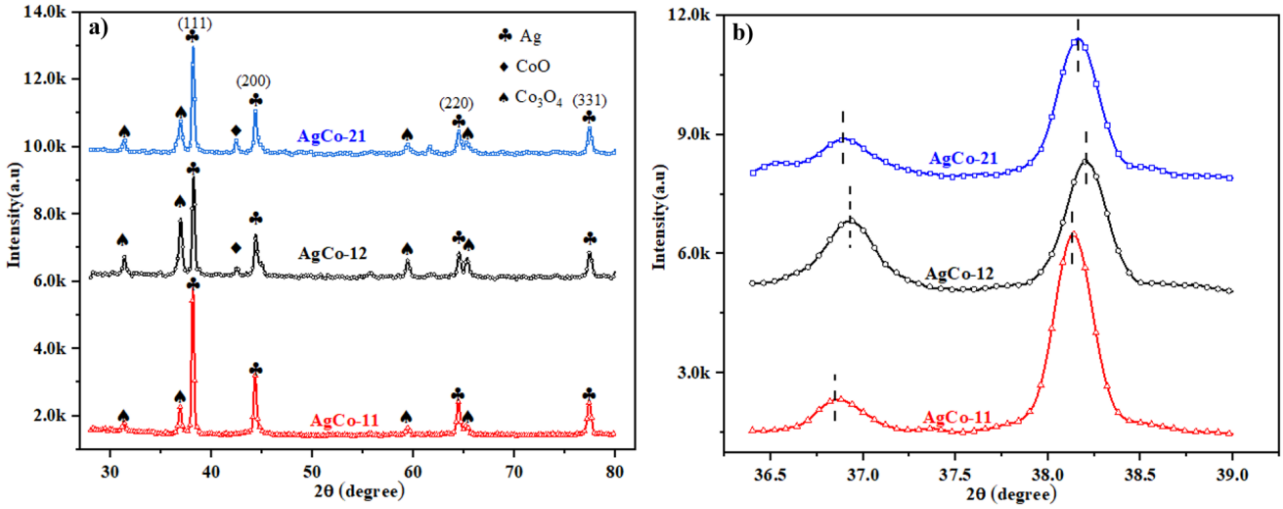

Figure 44. a) XRD pattern of bimetallic AgCo synthesized using different modes of combustion synthesis b) selected 2θ region of XRD pattern.

FTIR spectrum in Figure 45 indicates the chemical bonding and functional groups attached to the surface of as-prepared AgCo nanopowders. The spectrum of AgCo

compounds were compared with monometals of combustion synthesized Ag and Co, prepared with the same fuel ratio. The absorption band between 400 to 655 cm^{-1} is related to the metal-oxygen bond on the catalyst surface. In that case, Ag does not display any absorption peak either due to the presence of Ag in pure metallic phase or due to the local sintering at higher value of fuel ratio that weakens the bonding vibrations [297,298]. The absorption at 652 and 549 cm^{-1} in cobalt are attributed to the stretching vibration of cobalt-oxygen bond and confirms the presence of spinel Co_3O_4. The vibration spectrum at 652 cm^{-1} is related to tetrahedrally coordinated Co^{2+}($3d^7$), and 549 cm^{-1} band confirms the octahedrally coordinated Co^{3+}($3d^6$) [242,299]. The presence of unburned carbonyl impurities from the incomplete combustion was affirmed from the weak absorption peak at 835 cm^{-1} [300]. The absorption spectrum of monometallic cobalt and AgCo-12 has close resemblance that indicates the presence of predominantly cobalt on the surface of AgCo-12. Moreover, the absorption peak of AgCo-21 tends to merge the peak to a flat band confirming the pre-dominant elemental phase of metallic silver on the surface. The existence of peaks related to spinel Co_3O_4 in AgCo-21 is possibly due to a higher molar ratio of cobalt in the overall composition.

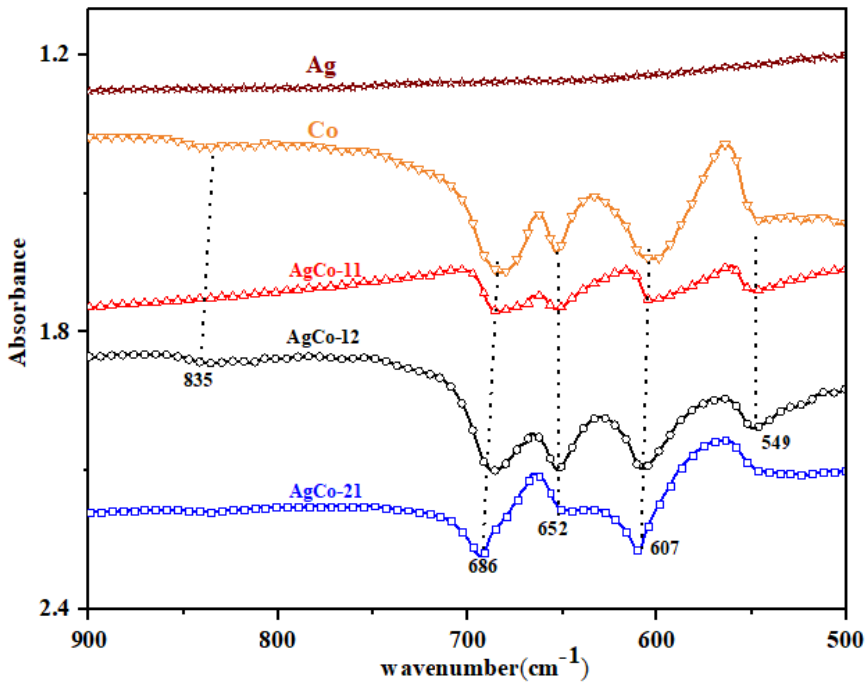

Figure 45. FTIR spectrum of as-prepared bimetals of Ag-Co and its monometals synthesized using different modes of SCS.

The optical absorbance spectrum of all the synthesized catalysts is shown in Figure 46**.** The surface plasmon resonance band of silver nanoparticle show a single absorption peak at 470 nm, and that for cobalt nanoparticle there are two absorption bands at 540 nm and 800 nm. The lower band at 540 nm can be related to the O^{-2} to Co^{+2} charge transfer, whereas the higher band at 800 nm is associated with the O^{-2} to Co^{+3} charge transfer [268,269]. In silver-cobalt systems, the optical absorption band showing only single surface plasmon resonance peak on the lower band spectrum confirms the alloying between silver and cobalt [301]. The resonance peak of silver at 470 nm and lower band spectrum cobalt at 540 nm merges together while alloying. The lower band in AgCo-12 shifted to left side (blue shift) when compared to other two bimetals, which could be due

to the quantum confinement of the nanoparticles with decrease in dimension [302]. The absorption band gaps for all the samples as shown in Figure 46.b were determined using Tauc equation (4) [303,304]:

The two-band gap values in cobalt are due to the presence of two absorption peaks that points the inter-band transition in spinel Co_3O_4. The lower band gap corresponds to the transition between O^{2-} and Co^{3+}, and higher band is associated with O^{2-} and Co^{3+} charge transfer [305,306]. The Co^{3+} forms an intermediate band inside the energy gap of spinal Co_3O_4. The optical band gap of AgCo-12 was found to be higher when compared to other compounds that could be due to the quantum confinement effect with decrease in crystallite size of particles.

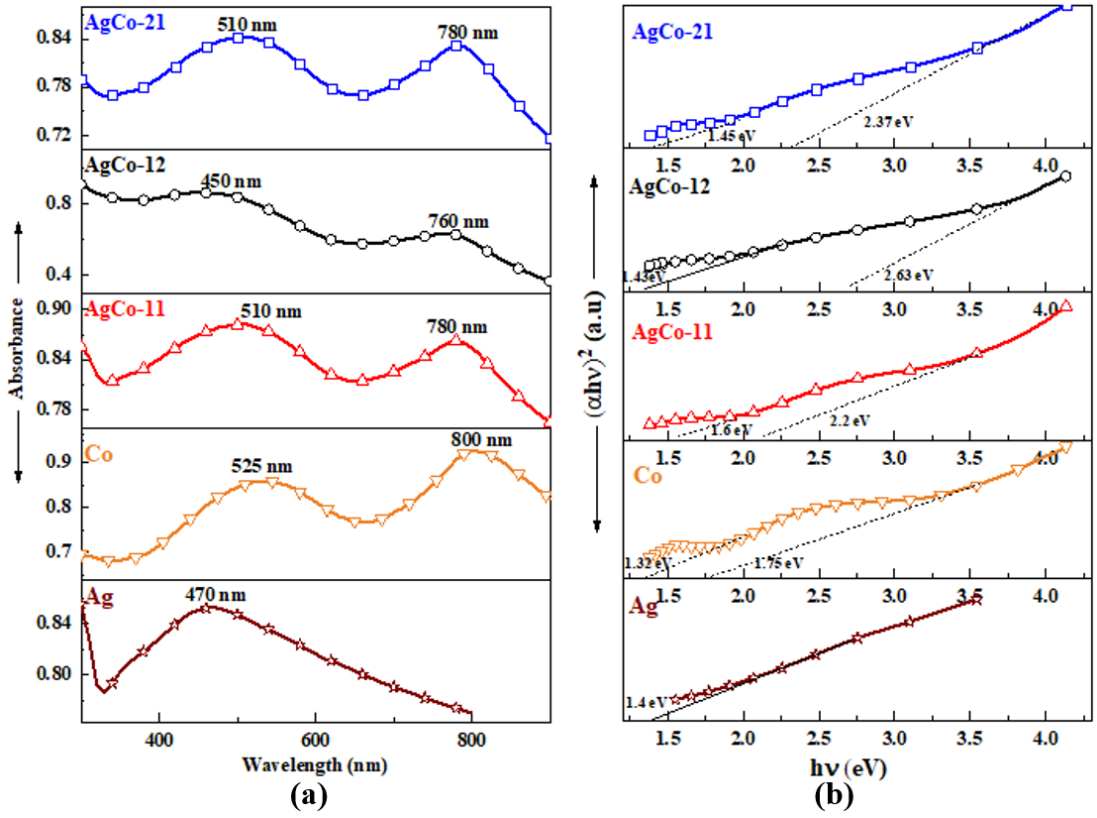

Figure 46. (a) UV-Vis absorption spectrum of monometals of Ag and Co, and alloyed AgCo compounds in aqueous solution, and (b) their corresponding Tauc plot.

SEM micrograph of the AgCo alloys synthesized using three different modes of solution combustion synthesis is shown in Figure 47. The synthesis mode plays an important role in tuning the morphology and structure of the nanoparticles. A detailed discussion on the effect of combustion synthesis parameters on the morphology and structure can be found earlier reports [263,307]. It can be seen that all the nanopowder show porous network, which is predominantly due to the channels formed by escaping gases that are released during the combustion process. AgCo-11 shows a broad distribution of smaller particles on larger clusters. AgCo-12 indicates the presence of larger clusters of fine particles.

Moreover, AgCo-21 gives wider distribution of relatively uniform sized smaller particles that agglomerate to form lumps. The identification of Ag and Co is difficult from visual inspection and requires TEM along with phase mapping for better understanding.

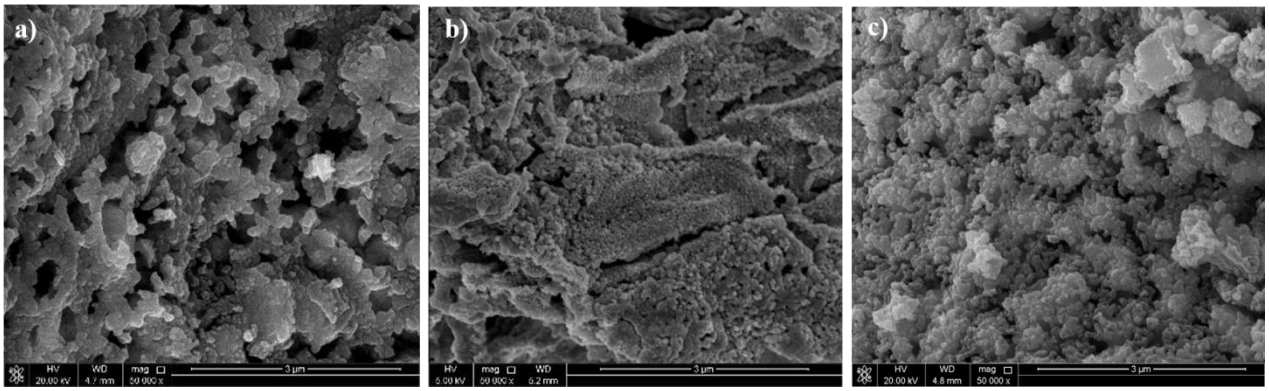

Figure 47. SEM of as-prepared AgCo alloys using different modes of SCS, (a) AgCo-11, (b) AgCo-12, and (c) AgCo-21.

TEM images of three Ag-Co NPs are presented in Figure 48. Based on their phase contrast, the silver NPs (Ag atomic weight = 107.8682) are expected to appear darker as compared to cobalt (Co atomic weight = 58.933). NPs are found to be agglomerated in all the three samples nonetheless Ag NPs seem to be well dispersed in AgCo-11 (Figure 48.a & d) and AgCo-21 (Figure 48.c & f) sample as compared to AgCo-12 (Figure 48.b & e). Agglomeration is reported to be a common challenge in SCS synthesized samples [263,307,308], and in case of bimetallic Ag-Co, Ag NPs seem to be relatively less affected as compared to cobalt, possibly due to being smaller in size and anchored to cobalt NPs. For AgCo-11, as it can be seen in Figure 48.a, isolated silver particles in the range of 8 – 15 nm size are distributed over the larger cobalt oxide particles. In the case

of AgCo-12, Ag particles are expected to be partially/fully covered by Co particles that are synthesized in the second combustion wave as shown in Figure 48.b whereas in case of AgCo-21 (Figure 48.c), Co particles are synthesized first, and Ag particles are deposited on Co surface. A size distribution study indicates that Ag NPs are in the range of 7 – 14 nm.

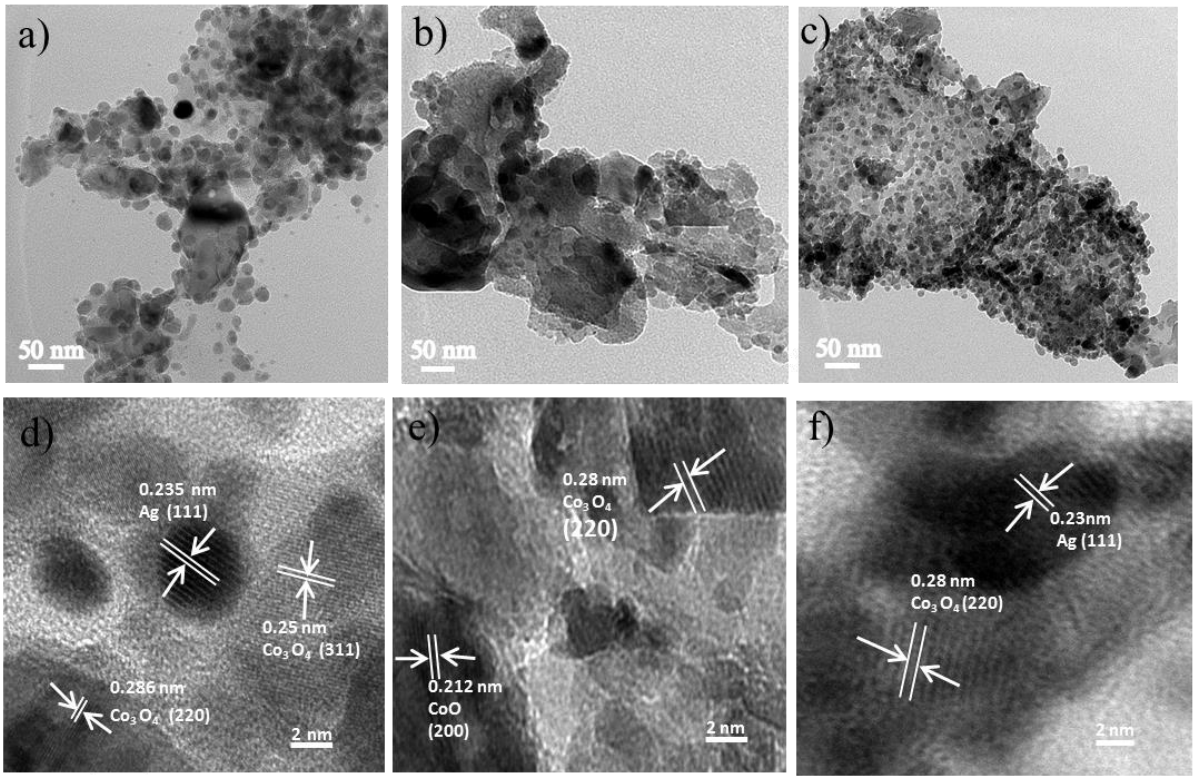

Figure 48. TEM images of as synthesized NPs and its corresponding lattice fringes at high magnification for (a and d) AgCo-11 (b and e) AgCo-12 (c and f). AgCo-21.

High resolution TEM images indicating lattice fringes are shown in Figure 48.d–f and confirm that NPs are highly crystalline in nature. FFT analysis of Ag NPs in AgCo-11

samples (Figure 48.d) indicates an atomic plane spacing of 0.235 nm correlating with (111) lattice planes of Ag crystals that is in good agreement with XRD data (Figure 44). This indicates the presence of Ag (111) planes having face-centered cubic (fcc) structures [309]. FFT analysis on Co crystals indicates the presence of Co_3O_4 with lattice spacing of 0.286nm and 0.25nm corresponding to (220) and (311) crystal planes. In Figure 48.e it is difficult to analyze the lattice spacing of silver NPs nonetheless Co-oxide crystals plane spacing of 0.28 nm and 0.212 nm corresponding to Co_3O_4 (220) and CoO (200) planes are seen [310], and found in the phases as detected by XRD. AgCo-21 in Figure 48f shows the presence of Ag (111) and Co_3O_4 (220) crystal planes [311].

The elemental phase mapping of the synthesized AgCo nanoparticles using three different modes of SCS shown in Figure 49 gives a better understanding of alloying and elemental composition. The elemental mapping confirms the presence of Ag and Co throughout the catalyst. The increase in brightness of STEM image in AgCo-21 could be due to the presence of more silver on the surface of cobalt and that gives a higher contrast image. As apparent from the TEM image, AgCo-12 have higher cobalt particle on the surface and size confined particles are lying below the cobalt. It also shows a better control in alloying for AgCo-12 that is evident from the XRD peak shifting when compared to the other two samples. The surface elemental composition is further evaluated using XPS analysis to confirm the findings from TEM and SEM images.

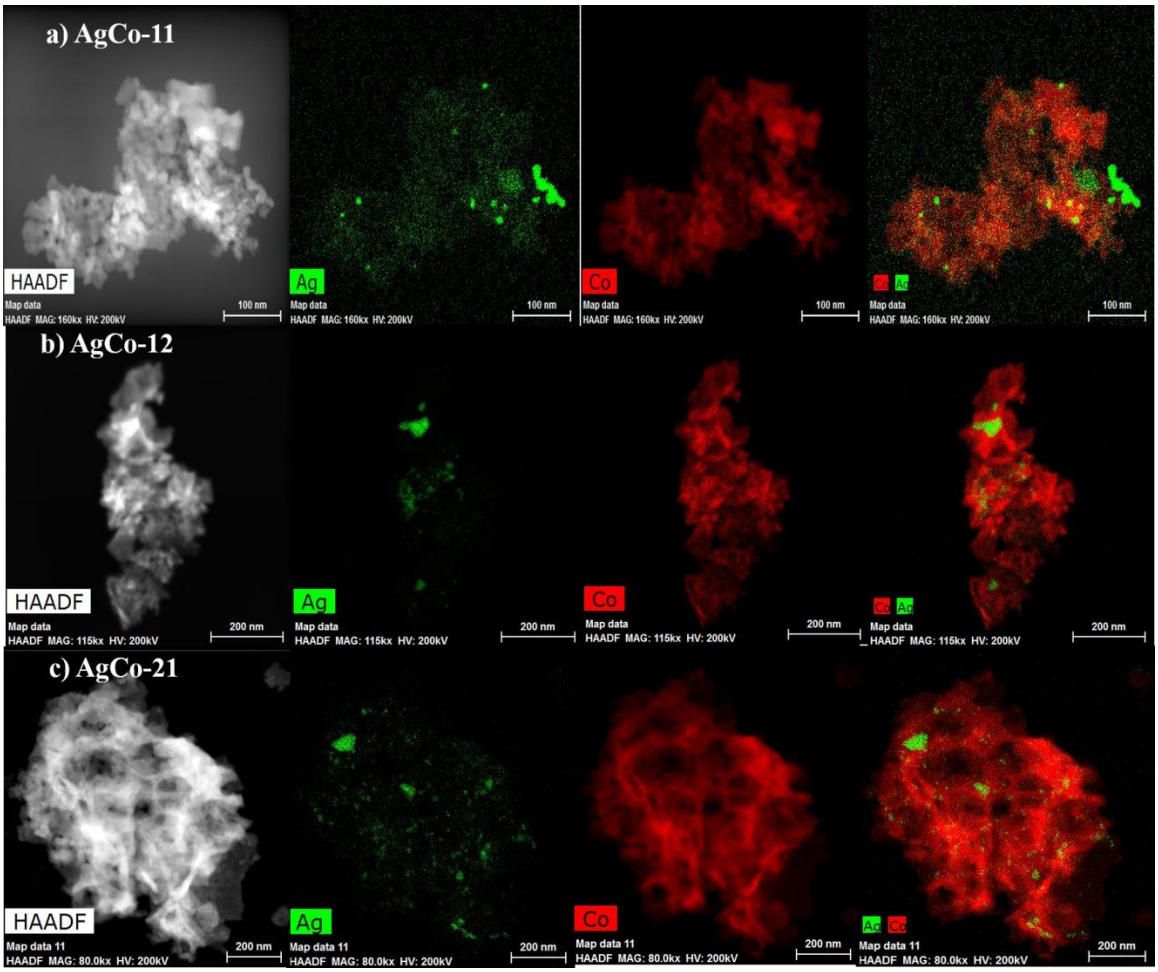

Figure 49. Elemental phase mapping by HAADF-STEM for the synthesized Ag-Co nanopowders.

Figure 50 shows the xps surface analysis of as-prepared silver-cobalt alloys. The xps spectrum in Figure 50.a gives the maximum intensity of Ag3d for AgCo-11 and AgCo-21 than AgCo-12. It shows two strong peaks at 368.4 eV and 374.4 eV with a splitting of 6 eV that are attributed to the Ag 3d5/2 and Ag 3d3/2 orbitals of metallic Ag [312,313]. The position of Ag 3d5/2 and Ag 3d3/2 and its corresponding areas are shown in the Table 2**.** It should be noted that the areas of Ag 3d peaks for the three AgCo samples show

dramatic distinction. The peak area is a function of the number of Ag atoms on the surface. Highly dispersed Ag atoms on the surface cause an increase in the intensity of Ag3d spectrum lines. With this aspect, the amount of Ag3d in the surface is decreasing in the order of AgCo-21>AgCo-11>AgCo-12. This could be due to the synthesized silver in the first stage of combustion being covered with cobalt synthesized later. This sequence of combustion reduces the surface Ag content in AgCo-12 than other two cases.

Table 2. Measured XPS Spectrum for Ag3d and the Quantitative Analysis.

	Ag 3d5/2			Ag 3d3/2		
	B.E (eV)	Area	%Area	B.E (eV)	Area	%Area
AgCo-11	368.2	4743.26	34.51	374.2	3387	24.64
AgCo-12	368.02	4552.08	39.90	374.0	2974	26.07
AgCo-21	368.27	5488.33	44.73	374.2	3448	28.13

Each Ag 3d level can be de-convoluted by splitting the peaks on the basis of Gaussian function to calculate the amount of various oxidation states. The deconvolution was able to detect two additional peaks at ~ 366 eV (~ 372 eV) and ~ 369 eV (~ 375 eV) indicating the presence of Ag_2O (Ag^I) and AgO (Ag^{II}) along with metallic Ag, which is the major phase as shown in Figure 50.b-d [314,315]. The existence of this oxidized form can also be correlated with the cobalt on the scanning surface. The ratio of Ag^I and Ag^{II} is higher in AgCo-12 than AgCo-21, which could be due to the better adhesion of oxygen from Co_3O_4 on the surface of Ag. The absence of Ag^I in the AgCo-21 sample may be due to

the presence of more Ag on the surface and that hinders the oxygen coupling from cobalt species that are lying beneath it.

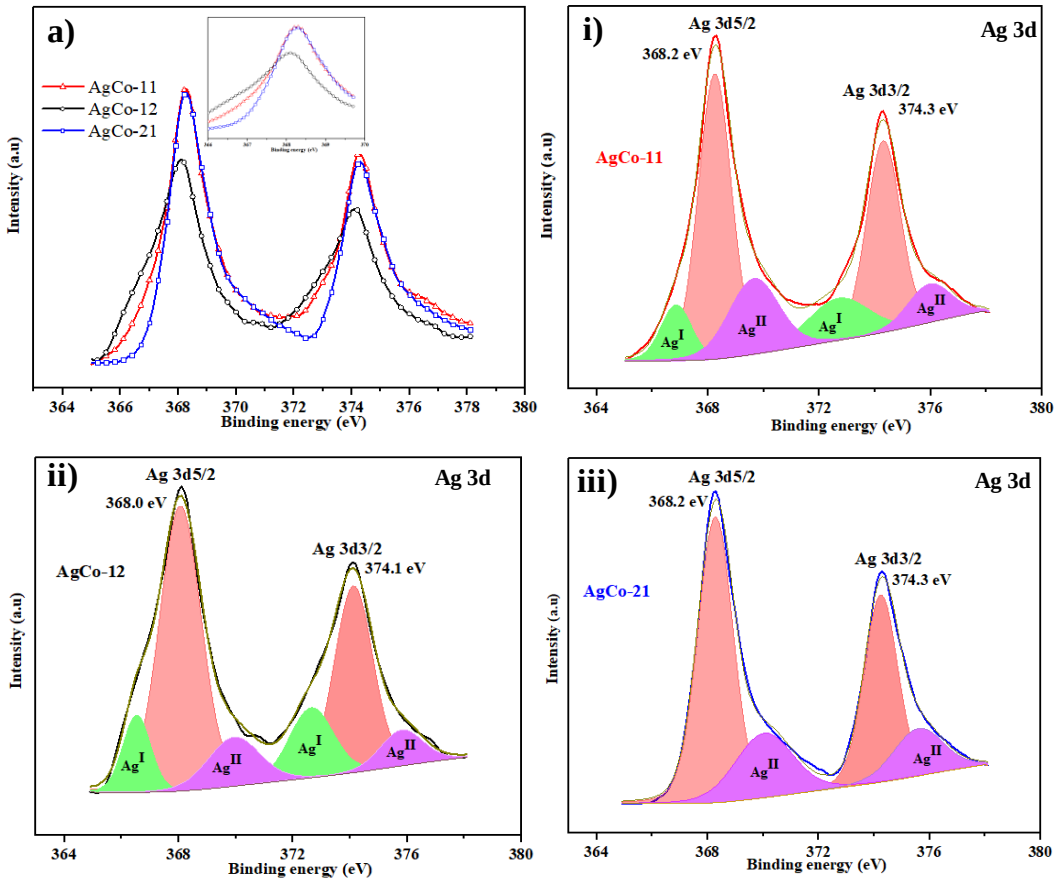

Figure 50. XPS spectrum of Ag 3d of AgCo of (a) peak intensity spectrum of Ag 3d and (i-iii) de-convoluted spectrum of each Ag 3d.

It is clear from the Co2p spectrum in Figure 51.a that the Co concentration on the surface increases in the order of AgCo-11< AgCo-21 <AgCo-12. The highest content of Co on the surface of AgCo-12 is from the second wave combustion when cobalt is synthesized on the surface of previously formed silver. The inset in Figure 51.a of Ag3d in AgCo-12

has shifted to a lower binding energy and Co2p in AgCo-12 was shifted to higher energy value relative to AgCo-11 and AgCo-21. This shift indicates that electron was transferred from Co to Ag in the alloys and there exist a strong electronic interaction between the metals in AgCo-12 [316]. The Co2p curve fitting in Figure 51.i-iii confirms the existence of two spin orbital doublets (Co^{3+} and Co^{2+}) and two shake up satellite peaks. The Co2p spectrum in has two distinct sharp peaks at 780.2 ± 0.6 and 795.6 ± 0.6 eV that correspond to Co2p3/2 and Co2p1/2 with a spin orbital splitting of ~ 15.4 eV [317]. The deconvolution of each Co 2p peak indicates the co-existence of Co^{3+} and Co^{2+} at lower and higher binding energies. The peak area of AgCo-12 shows higher value and the AgCo-11 be the least one. The surface ratio Co^{2+}/Co^{3+} of AgCo-12 (0.81) was similar to that of AgCo-21 (0.76), but much higher than of AgCo-11 (0.54). Some of Co_3O_4 formed initially is reduced to CoO (Co^{3+} to Co^{2+}) through the second wave combustion as evident in XRD and thermodynamic calculations is the reason of this trend in surface composition of Co^{2+}/Co^{3} [318]. The same reasoning can be extended to the change in area of shakeup satellite peaks at 789.5 eV and 804.5 eV. These shakeup satellite peaks are the characteristics of Co_3O_4 and the peak is higher for AgCo-11 and least for AgCo-21 could be the reason for no reduction of Co_3O_4 to CoO in former case and there is a chance of higher reduction in later case through the second wave combustion.

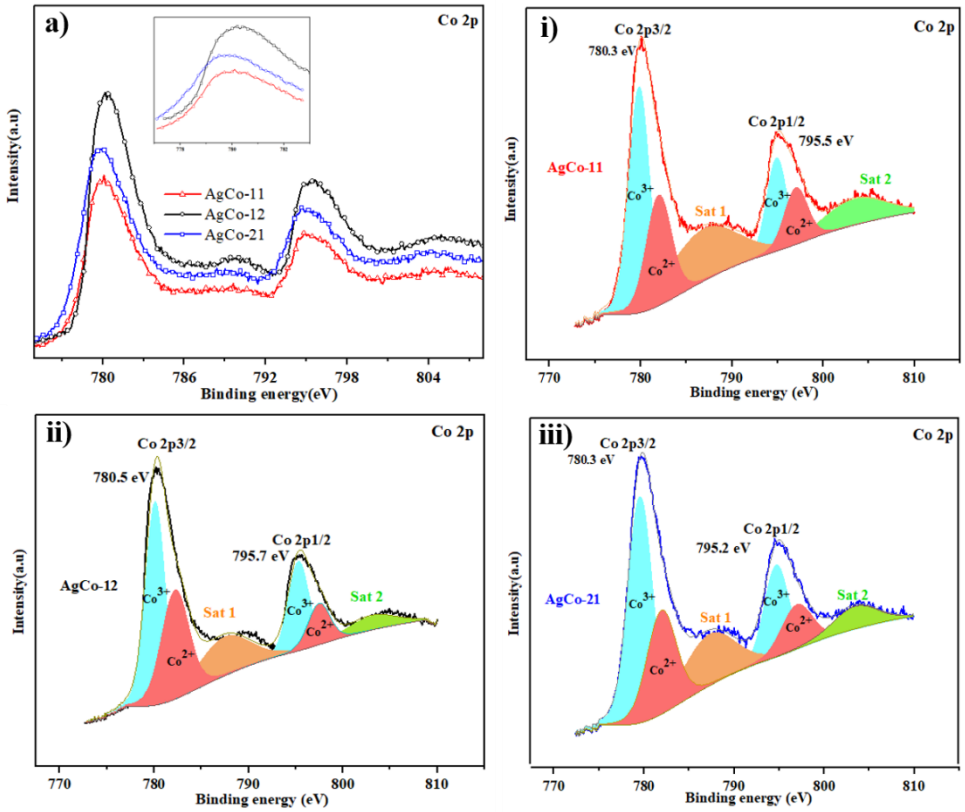

Figure 51. XPS spectrum of Co 2p of bimetallic Ag-Co of (a) peak intensity spectrum of Ag 2p and (i-ii) de-convoluted spectrum of each Ag 3d.

The XPS of O 1s spectrum in the inset Figure 52.a shows a characteristic peak at 529.6 eV (O_L) corresponded to the oxygen of the metal crystal lattice (M- O bond) and a noticeable shoulder peak at higher binding energy suggested the presence of absorbed oxygen on the surface [319,320]. The quantitative analysis of O1s (Figure 52.a) in the three modes samples give maximum intensity of oxygen for AgCo-12, whereas AgCo-11 and AgCo-21 hold same amount of oxygen. The existence of more O 1s content on AgCo-12 could be from the oxygen bounded to the cobalt (Co_3O_4) where AgCo-12 carries more cobalt on the surface as discussed above.

The de-convoluted xps peak of C 1s core level of sample is illustrated in the inset of Figure 52.b. The sharp peak at 284.6 eV indicating the presence of sp^3 C-C bond and smaller shoulder peaks at ~ 286 eV and ~ 288 eV show the bonding configuration of C-O-C and O-C=O respectively. The combined spectrum of all the AgCo samples signifies the existence of higher atomic configuration of carbon in AgCo-11 and decreases in the order of AgCo-11 > AgCo-21 > AgCo-12. The decrease in carbon content on AgCo-12 (16.93 %) and AgCo-21 (17.93 %) when compared AgCo-11(29.98 %) is due to the combustion of extra carbon in the second wave of synthesis in SWCS mode that reduces the overall C 1s composition. During second wave combustion, there is a subsequent rearrangement of elements on the surface and the higher content of carbon in AgCo-11 causes the reduction of overall metallic/oxide content of Ag and Co on the surface. This gives more prominent evidence for the presence of approximately equal proportion of silver on AgCo-11 and AgCo-21 whereas AgCo-21 gives more atomic concentration of cobalt on the surface than AgCo-11 sample. To summarize, it is clear from the result and discussion that the synthesis sequence plays a great role in the surface composition and final structure of the nanocompound. Moreover, through SWCS there is a better control in alloying and reduction in the carbon content, which is relatively high in conventional solution combustion synthesis. The nanoparticles synthesized using this modified technique can be used in various field of catalytic application owing to the upgraded surface science and better control in structure.

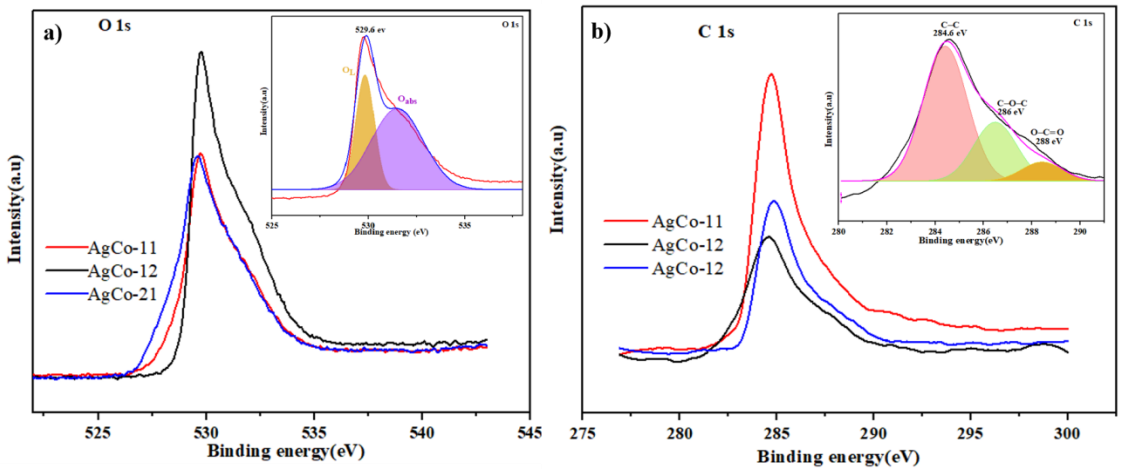

Figure 52. XPS spectrum of a) O 1s b) C 1s of three samples of Ag-Co. Inset shows the corresponding deconvolution spectrum.

5.3.2. Electrochemical analysis and characterization

The electrocatalytic activity of Ag-Co bimetallic catalyst synthesized via different schemes has been examined with CV to test the bi-functionality in N2- (Figure 53.a)/O2-saturated (Figure 53.b) 1.0 M KOH electrolyte at a scan rate of 50 mVs-1. ORR activity was assessed by comparing the two CVs in O2-saturated electrolytes. The complete electrocatalytic activity of Ag-Co (ORR and OER) includes the redox reaction that involves the oxidation of Ag and reduction of silver oxides. The redox reaction peaks in Figure 53.a at A2 and C2 is due to the formation and reduction of AgO [321] , respectively that can be represented as follows

$$Ag_2O + 2OH^- \leftrightarrow 2AgO + H_2O + 2e^-$$

The second pair of redox reaction peaks at A_1 and C_1 at 0.7-0.75V and around 0.5-0.6 V is attributed to the formation and reduction of Ag_2O [322] as represented below:

$$2Ag + 2OH^- \leftrightarrow Ag_2O + H_2O + 2e^-$$

The redox reactions A_2 and C_2 are same for all the three types of catalysts, while A_1 and C_1 are different. A clear shift of C_1 in the cathodic direction is visible towards a negative potential in the order of 0.58, 0.54 and 0.51V for AgCo-21/C, AgCo-11/C and AgCo-12/C is due to the strong interaction of the absorbed oxygenated species and highest for AgCo-12 when compared to other catalysts could be due to the presence of more Co-species over the surface[290]. The extra reduction peak of C_3 in O_2-saturated 1.0 M KOH electrolyte (Figure 53.b) is due to the oxygen reduction reaction. The cathodic reaction on AgCo-12/C is positively shifted by 0.208 in comparison with AgCo-11/C and AgCo-21/C. As reported before, the electrochemical activity has been enhanced through the ligand mechanism of charge transfer between the catalyst metals where the Co particles that perturbs the active sites of Ag NP[13,289].

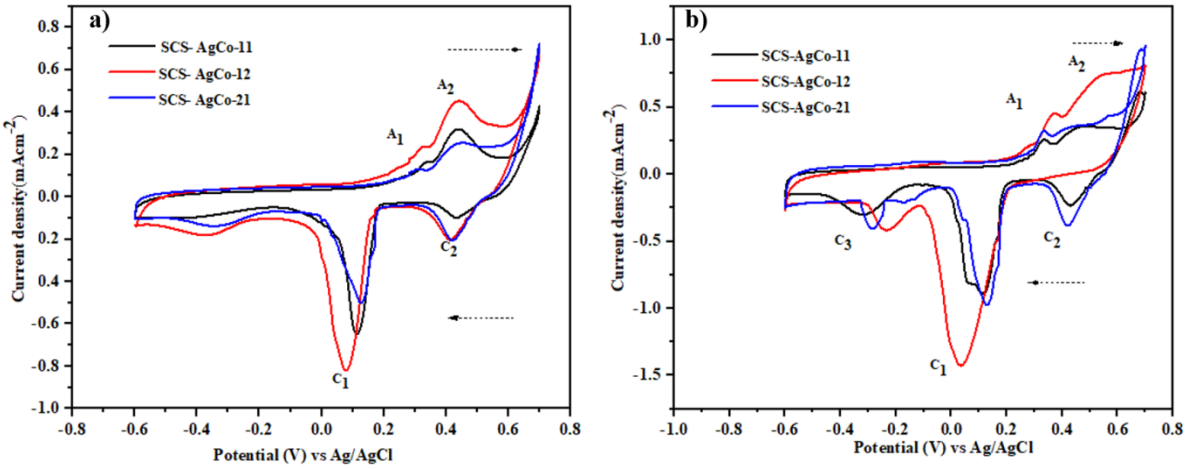

Figure 53. Cyclic voltammetry for AgCo-11 /C, AgCo-12/C, AgCo-21/C catalyst in a) N_2 saturated b) O_2 saturated 1M KOH electrolyte at $0.05Vs^{-1}$ in a wide potential range to demonstrate the ORR and OER performance. Arrow indicates the scan direction

The catalytic activity of all the samples was obtained using the LSV measurement at a speed range from 400 rpm to 1600 rpm in O_2-saturated of 1.0 M KOH solution is shown in Figure 54.a. The activity of the catalyst was determined by the half-wave potential of ORR curve. The positive shift on the onset potential is more on AgCo-12/C in comparison with AgCo-11/C and AgCo-21/C and the calculated limiting current density on AgCo-12/C is greater than other two Ag-Co catalysts but lower than standard Pt/C. AgCo-12/C shows comparable kinetics with Pt/C. The limiting diffusion current density in the disk increases with the increase in rotation speed for AgCo-12/C catalyst (Figure 54.b). This expected trend is due to the decrease in diffusion barrier that enables an easy pathway for the passage of electrons at high speed.

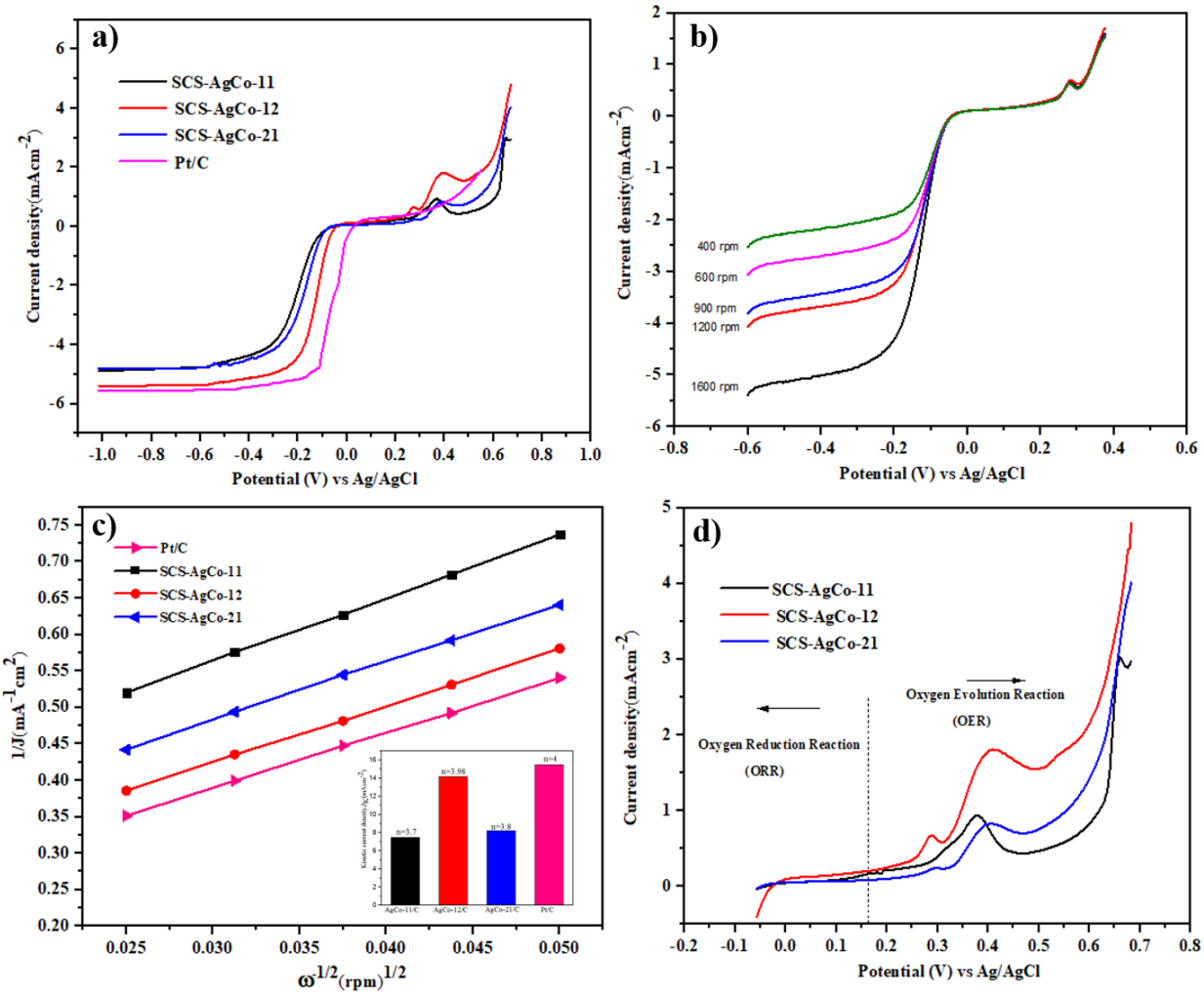

Figure 54. a) Rotating Disk electrode I-V polarization curve in O_2 saturated 1M KOH at 1600 rpm for different Ag-Co alloy synthesized with SCS at a scan rate of 5 mVs^{-1} b) LSV performance of AgCo-12 /C at different rotation rate from 1600 rpm to 400 rpm c) K-L plot for ORR at 0.15 V (Inset- bar plot shows the kinetic current density and the number of electron transfer in each catalysts) d) Bifunctional ORR and OER performance of different catalysts.

Levich plot in Figure 54.c shows the electron transfer that occurs in the overall ORR. The

number of electrons transferred is independent on the rotation speed, but they are greatly influenced by the catalytic material used and the reaction environment. The number of electron transfer (n) calculated from the Levich line slope of the catalyst by Equ (3.9) is explained earlier. It is observed that AgCo-12/C results in the transfer of 3.9 electrons whereas AgCo-11/C and AgCo-21/C involved in 3.7 and 3.8 electron exchange at a potential of 0.15 V. The inset bar plot shows the kinetic current density in which AgCo-12/C has the value very close to standard Pt/C. The bi-functionality of Ag-Co catalyst shows the anodic current (OER) and cathodic current (ORR) for RDE-LSV experiment at 1600 rpm (Figure 54.d). In OER, AgCo-12/C has higher anodic current than other two catalysts. This suggests the rapid transfer of electrons between electrolyte and the catalyst. An increase in the catalytic activity of the electrochemical reaction for AgCo-12/C is evident from all the above results. The presence of Co_3O_4 and CoO in the sample as mentioned in the XRD (Figure 44) and TEM (Figure 48) analysis respectively. Cobalt oxide network formed over Ag particles increases the binding energy to the oxygen adsorbed and facilitates the O–O bond splitting [290]. Also, the oxygen adsorbed on Co_3O_4 is transferred to the adjacent Ag particles and get reduced there. Likewise, if the rate of oxygen transport to the Ag is higher in AgCo-12/C it will increase the activity in the ORR and OER reaction.

Tafel plot has proved another way to analyses the mechanism of ORR. Mass transfer corrected Tafel plot is obtained from the $\log(J_k)$ vs V where J_k is the kinetic current density calculated from modified Koutecky–Levich Equ (3.8). Two different linear Tafel slopes were noticed at low and higher over potentials in each catalyst. Lower slope at lower potential and with larger values of slope at higher overpotential corresponding to Temkin

isotherm and Langmuir isotherm is preferred for better reduction mechanism [323]. Tafel slopes in Figure 55.a for AgCo-11/C, AgCo-12/C and AgCo-21/C are in the order of 35mVdec^{-1}, 29 mVdec^{-1}and 30 mVdec^{-1}, respectively for higher potential; and 79 mVdec^{-1}, 85 mVdec^{-1}, 81 mV dec^{-1} for lower potential. Lower Tafel slope for AgCo-12/C when compared with other catalyst indicates the fast transport of electrons between the catalyst and electrolyte. The catalytic efficiency was identified by calculating the exchange current density[324]. The exchange current density J_{ex} for AgCo-11 /C, AgCo-12/C and AgCo-21/C are 2.7×10^{-5}A/cm^{-2} (5.5×10^{-4}A/cm^{-2}), 1.06×10^{-4}A/cm^{-2} (4.2×10^{-3}A/cm^{-2}) and 4.4×10^{-5}A/cm^{-2} (1.3×10^{-3}A/cm^{-2}) for high over potentials (low over potential). J_{ex} is a strong evidence to show that AgCo-12/C is more sensible for the electric current response with the potential and a promising catalyst for the ORR reaction. Tafel plot in Figure 55.b for OER corresponding to the three Ag-Co catalysts with smallest slope for AgCo-12/C displaying better catalytic performance for the water electrolysis reaction (OER) to generate oxygen. Overall, the AgCo-12/C catalyst shows the best performance for OER and ORR among the three catalysts tested. This high activity could be ascribed to its synergic coupling between the mono-metals and a fast charge transport in it.

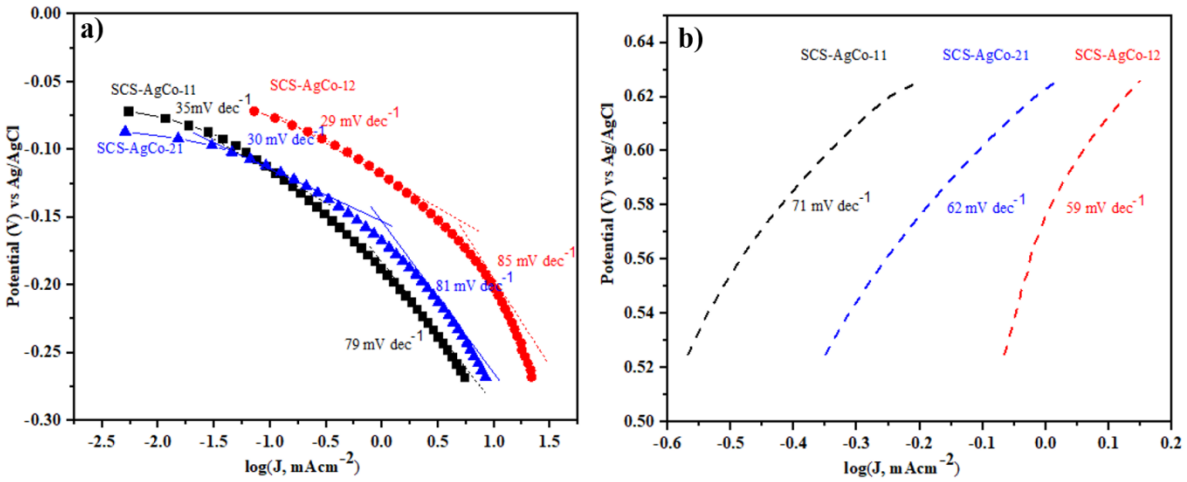

Figure 55. Mass-transport corrected tafel plot for a) ORR and b) OER of various catalysts in 1M KOH solution corresponding to 1600 rpm LSV plot

The catalytic activity of AgCo-12/C for ORR was confirmed with low Tafel slope and lower exchange current density at high potential, and high exchange density and larger Tafel slope at lower potentials. So, it can be concluded that AgCo-12/C is a promising catalyst for the application of fuel cell and water electrolysis owing to the presence of more Co atoms on the surface that promote the transfer of oxygen to Ag where it is reduced by releasing electrons.

5.4. Synthesis of Ag-CuO alloys using SCS

The alloying of Ag and Cu has been reported to be an active electrocatalyst for fuel cell and zinc-air batteries [115], with $Ag_{75}Cu_{25}$ showing better electrocatalytic performance for ORR reaction as compared to silver alloys with Co, In and Fe having similar composition. DFT calculations indicate the existence of strong adsorption energy and low

activation energy barrier in bimetallic silver-copper [117]. In this section, we report the application of solution combustion synthesis (SCS) to prepare high surface area Ag-Cu nanomaterials and access their performance for ORR and OER.

Synthesis of mono-metals of silver and copper (SCS Ag & SCS Cu): Silver nanoparticles were prepared by mixing a measured quantity of silver nitrate and glycine with stoichiometric fuel to oxidizer ratio (φ). The quantity of metal nitrates and glycine was calculated based on the stoichiometric Equation (1) [263,307]. The precursors were dissolved in 25 ml of deionized water (DIW) and stirred continuously for 1 hr to obtain a homogeneous mixture, and thereafter it was placed over the hot plate at 300°C until all the water evaporates. Once the solution reaches its ignition temperature, combustion starts locally at one point and gradually spreads throughout the synthesis medium leaving nanopowder inside the beaker. Similarly, copper nanoparticles were synthesized using copper nitrate and glycine with φ = 0.5 to obtain maximum yield. Using a higher amount of fuel, as in case of φ = 1, results in a highly vigorous combustion forming a dense fume dispersing the copper nanoparticles in air with only small quantity remaining inside the beaker.

Mode 1 - AgCu-11: In this mode of synthesis, bimetallic Ag-Cu were synthesized in a single step by adding silver nitrate and copper nitrate together with glycine (φ = 0.5) by keeping the molar ratio Ag:Cu at 1:1. The procedure followed for synthesis was same as that mentioned in above section.

SCS AgCu-12: This is a two-step synthesis technique termed as second wave combustion synthesis (SWCS) in which silver nanoparticles was synthesized in the first step using a mixture of silver nitrate and glycine as explained before. In the second step, the

synthesized Ag nanoparticles were mixed with the homogeneous solution of copper nitrate-glycine and heated again over the hotplate to allow it for a second combustion. The prepared sample is expected to be bi-metallic Ag-Cu nanoparticles with different surface composition than SCS AgCu-11, with higher amount of Cu on the surface.

Mode 3 AgCu-21: In this mode of synthesis, the copper nanoparticles were synthesized first using copper nitrate-glycine solution. The resulted nanoparticles were mixed with the silver nitrate - glycine solution for the second wave combustion synthesis. The SWCS AgCu-21 is expected to have higher Ag content on the surface as compared to SCS AgCu-11.

5.5. Results and discussion

5.5.1. Catalysts characterization

The XRD results of the silver-copper nanoparticles synthesized in different modes of SCS are shown in Figure 56. In silver nanoparticles, four peaks of metallic silver (JCPDS card no. 65-2871) at 38.11° (111), 44.31° (200), 64.41° (220) and 77.41° (311) are clearly observed. The copper sample is presented as mixed oxides of CuO (JCPDS 48-1548) and Cu_2O (JCPDS 78-2076). The bimetallic AgCu-11 and AgCu-12 samples indicate the presence of Ag and CuO, whereas the AgCu-21 does not show any peaks associated with oxides of copper. The absence of copper oxides in AgCu-21 sample could be due to the possible reduction of CuO to Cu in the second wave of combustion.

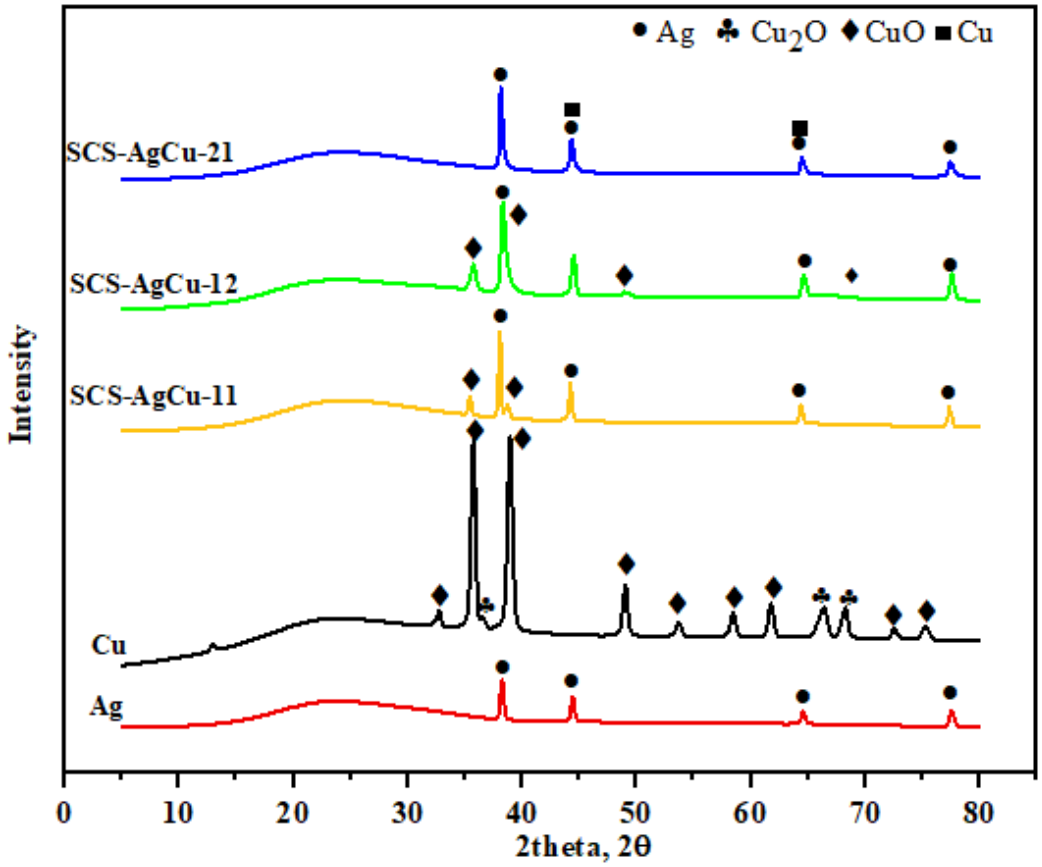

Figure 56. XRD pattern of synthesized silver-copper using different modes of combustion synthesis

The SEM micrographs of the SCS silver-copper in different modes of combustion

synthesis are shown in Figure 57. The agglomeration of nanoparticles is clear in all the SEM images [263,307,308]. The silver nanoparticles formed in Figure 57.a are in micron level as clusters of nanoparticles. Copper nanoparticles are also agglomerated but show high porosity. The AgCu-11 microstructure looks similar to that of AgCu-21 showing plate like structures resembling with metallic Ag microstructure obtained in Figure 57.a. This indicates the surface could be mainly composed of Ag particles. In the case of AgCu-21, the two-step SWCS would result in silver particles being formed on already synthesized copper particles. As evident from the metal nitrate decomposition temperature pattern (copper-nitrate glycine system would have a lower ignition temperature than the silver-nitrate glycine system) the AgCu-11 may have experienced the synthesis of copper particles followed by the synthesis of silver particles, thus silver being mainly formed on the surface of copper particles. This analysis of combustion synthesis pattern is consistent with the SEM microstructures and easily explains the similarity in the microstructure of AgCu-12 and copper particles in Figure 57.d and Figure 57.b respectively that are different as compared to Figure 57.a,c,e. In AgCu-12, the silver particles are synthesized first and copper in the second stage of combustion. This combustion sequence results in copper combustion on the surface of already synthesized silver particles and thus having higher surface composition.

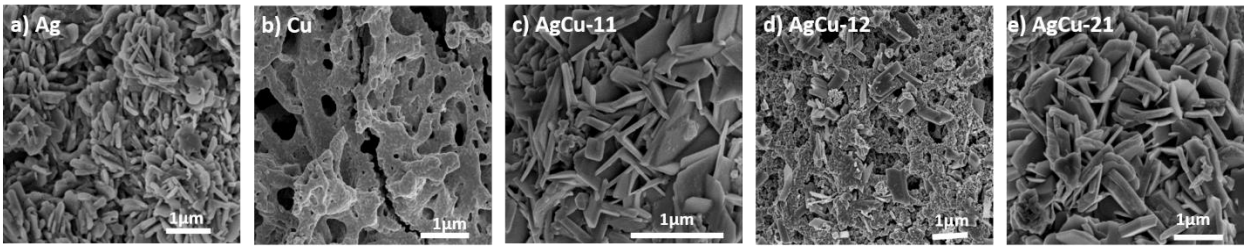

Figure 57. SEM Micrograph of synthesized nanoparticles using different modes of solution combustion synthesis

Figure 58 shows the TEM images of AgCu-11 and AgCu-21indicates the particles of Ag along with some continuous copper structure. Silver particles looks to be brighter than copper because of the higher atomic number (Z) of Ag (Z=47) when compared to Cu (Z=29). In AgCu-11 the Ag particles with average particle diameter of 10-12 nm are embedded over copper structure and its elemental composition is very well clear from Figure 58.a(ii-iv). Figure 58.b shows the TEM image of AgCu-21 where most of the silver is on the surface of the catalysts along with some small clusters of silver with spherical morphology that in the size range of 6-8 nm surrounded it.

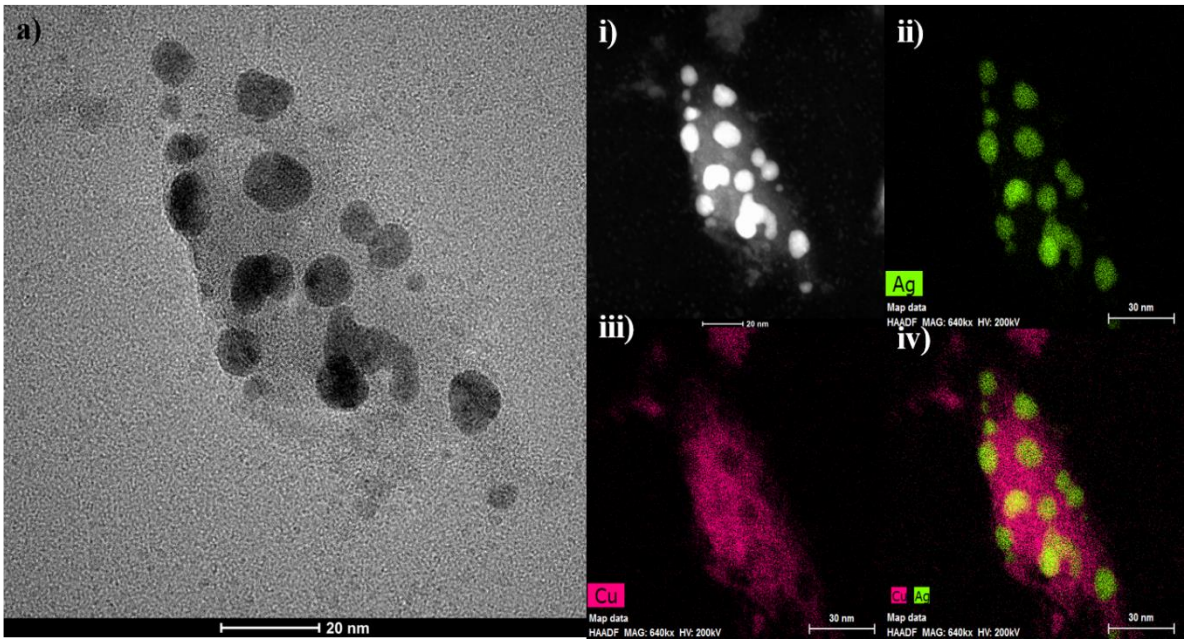
a)
20 nm
i)
20 nm
ii)
Ag
Map data
HAADF MAG: 640kx HV: 200kV
30 nm
iii)
Cu
Map data
HAADF MAG: 640kx HV: 200kV
30 nm
iv)
Cu Ag
Map data
HAADF MAG: 640kx HV: 200kV
30 nm

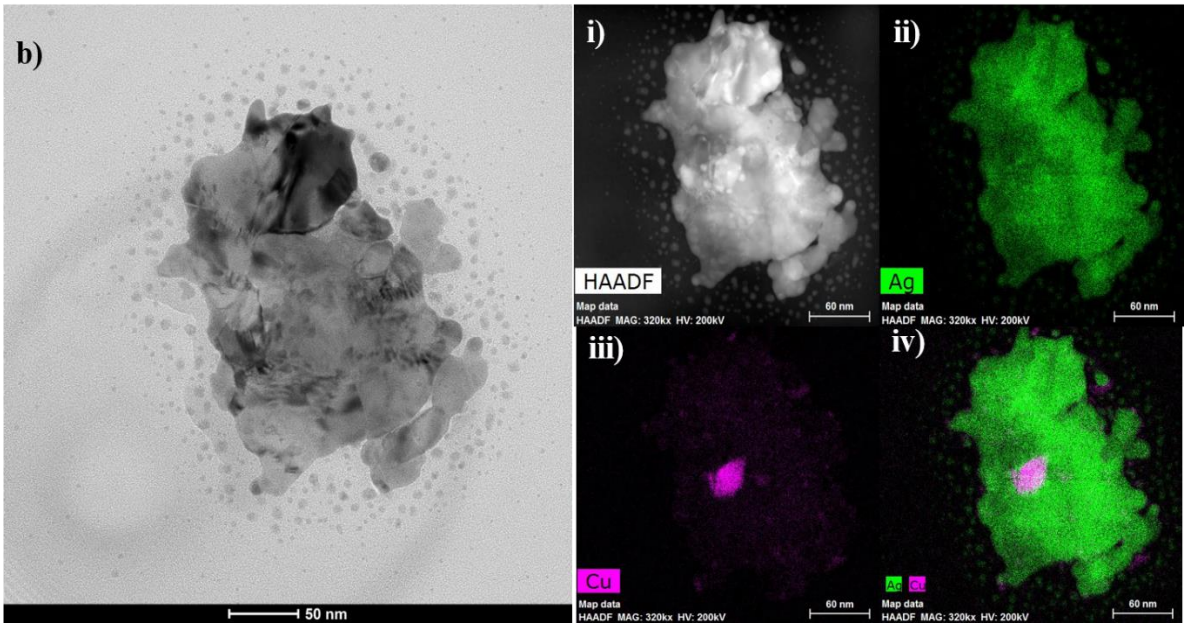

Figure 58. a) TEM image (i) and its corresponding HAADF-STEM (ii-iv) elemental mapping of Ag,Cu and AgCu in SCS AgCu-11 catalysts b) TEM image (i) and its corresponding HAADF-STEM (ii-iv) elemental mapping of Ag,Cu and AgCu in SCS AgCu-21 catalyst.

The XPS peaks of Ag 3d are shown in Figure 59.a and the fitted peaks of Ag $3d_{5/2}$ and Ag $3d_{3/2}$ are assigned to the binding energies of 368.4 eV and 374.4 eV, respectively, agreeing with the literature reported values [312,325]. Ag 3d spectra of bimetallic Ag-Cu shown in Figure 59.b indicate a clear shifting of peaks toward lower binding energy (BE). Ag 3d peaks shift towards lower BE at 365.9 eV might be due to the charge transfer between Ag and Cu, and thus a strong interaction in Ag-Cu. The XPS of Cu(2p) spectrum shown in Figure 59.c indicates the presence of two peaks of Cu $2p_{3/2}$ and Cu $2p_{1/2}$ where the position of each peak determines the oxidation state of Cu on the surface [326,327].

The monometallic Cu_2O nanoparticle show the maximum of Cu $2p_{3/2}$ at 933.6 eV and the sharp shake-up satellite in the region of 940.9 eV was identified to be the oxidized Cu surface of CuO species. Moreover, the strong Cu $2p_{3/2}$ and Cu $2p_{1/2}$ peaks of AgCu-11 and AgCu-21, centered at 932.8 eV and 953 eV with a splitting of 20.2 eV, are attributed to the presence of Cu^0 on the surface along with some oxides as evident from the intense shake-up satellites in the range of 940 – 945 eV (Cu $2p_{3/2}$) and 958 – 965 eV. The presence of metallic Cu in AgCu-21 is also evident from the XRD analysis as discussed earlier. Based on the XPS peaks, Ag-content on the surface is higher in the sample AgCu-21 as compared to AgCu-11, whereas the Cu amount on the surface of both the samples are almost similar (AgCu-11 ≈ AgCu-21). This trend in elemental composition is consistent with the EDX results.

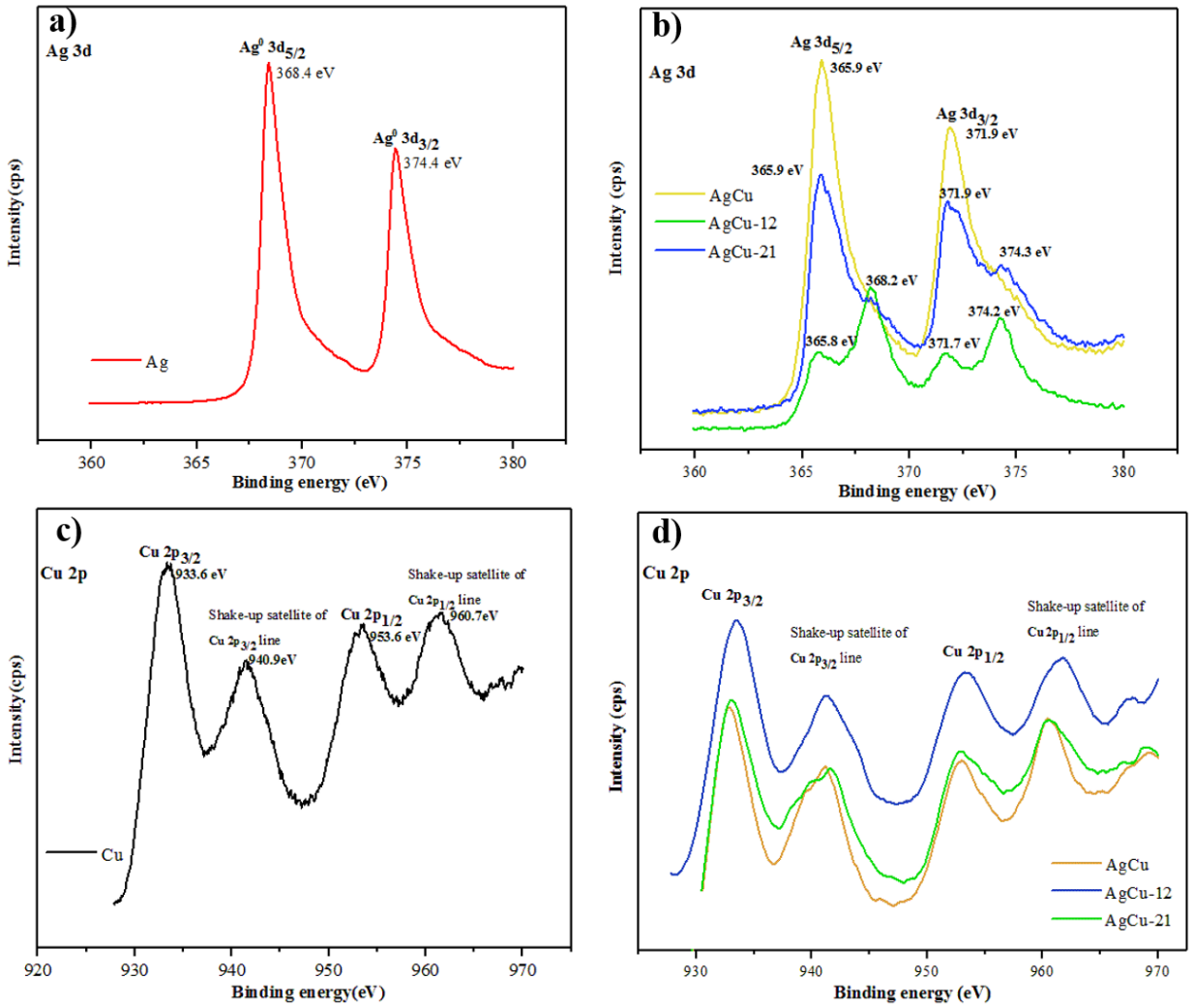

Figure 59. XPS spectrum of Ag 3d of (a) mono-metal- Ag (b) bimetal Ag-Cu; and Cu 2p of (c) mono-metal copper (d) bimetal Ag-Cu.

The O 1s spectra and their deconvoluted fittings are shown in Figure 60.a-f. The presence of O 1s peak at 532 eV shown in Figure 60.a is due to adsorbed oxygen on the metal surface [328]. A less intense shoulder peak of O 1s at 534.1 eV mostly could be due to physically adsorbed or trapped water [293,329]. The O 1s peak in Cu_2O in Figure 60.b shows a sharp intense peak at 529.7 eV and two shoulder peaks at 527.1 eV and 531.6

eV. The lower BE peak at 527.1 eV are due to the differential charging of oxides and the peak at 529.7 eV corresponds to the oxygen bonded with CuO [330,331]. Also, the shoulder peak observed at higher BE could be correlated with the oxygen species on the surface of the nanostructured oxides or small impurities of adsorbed water [332,333]. The O 1s XPS spectrum of AgCu-11 contains lower BE peaks at 529.8 eV that is attributed to the presence of Cu-O bond on the surface with a decrease in peak intensity when compared to pure CuO 1s peak. The reason is due to the presence of Ag on the surface decreasing the elemental composition of Cu. The other oxygen signal at 530.9 eV is the evidence of the presence of adsorbed OH group or chemisorbed H_2O. Another noticeable peak at higher BE of 538.1 eV belongs to the molecular O_2 that are commonly seen in the range of 538-543 eV. A similar trend of O 1s XPS spectra can be seen in Figure 60.f for AgCu-21. The significant similarity of AgCu-11 and AgCu-21 in structure and morphology has been explained in the previous sections and could be attributed to the order in which combustion synthesis takes place in the bimetallic systems. The surface elemental analysis of oxygen shows an overall trend in the sequence of Cu > AgCu-12 > AgCu-11 ≈ AgCu-21 > Ag, indicating the metallic nature of Ag.

A presence of carbon on the surface is expected to be because of using a carbon-containing fuel in combustion synthesis. A quantitative analysis on the surface shows a carbon content of 30.16%, 21.15%, 16.32%, 16.95%, and 17.22 % for SCS Ag, Cu, AgCu-11, AgCu-12 and AgCu-21, respectively. The reason for high carbon content on the surface of Ag is the use of high fuel ratio (φ=1) whereas a smaller fuel ratio of φ=0.5 was used for Cu, thus decreasing the carbon-content on the surface. The different ratios of φ were used in order to maximize the yield of nanoparticles synthesized. Using a high

value of $\varphi = 1$ for Cu resulted in low Cu yield as a large quantity of Cu nanoparticles dispersed in air as fumes during combustion synthesis, making it difficult to collect. In the second wave combustion synthesis (SWCS), a decrease in the carbon content could be due to further combustion of carbon that formed in the initial synthesis and the subsequent arrangement of atoms on the surface.

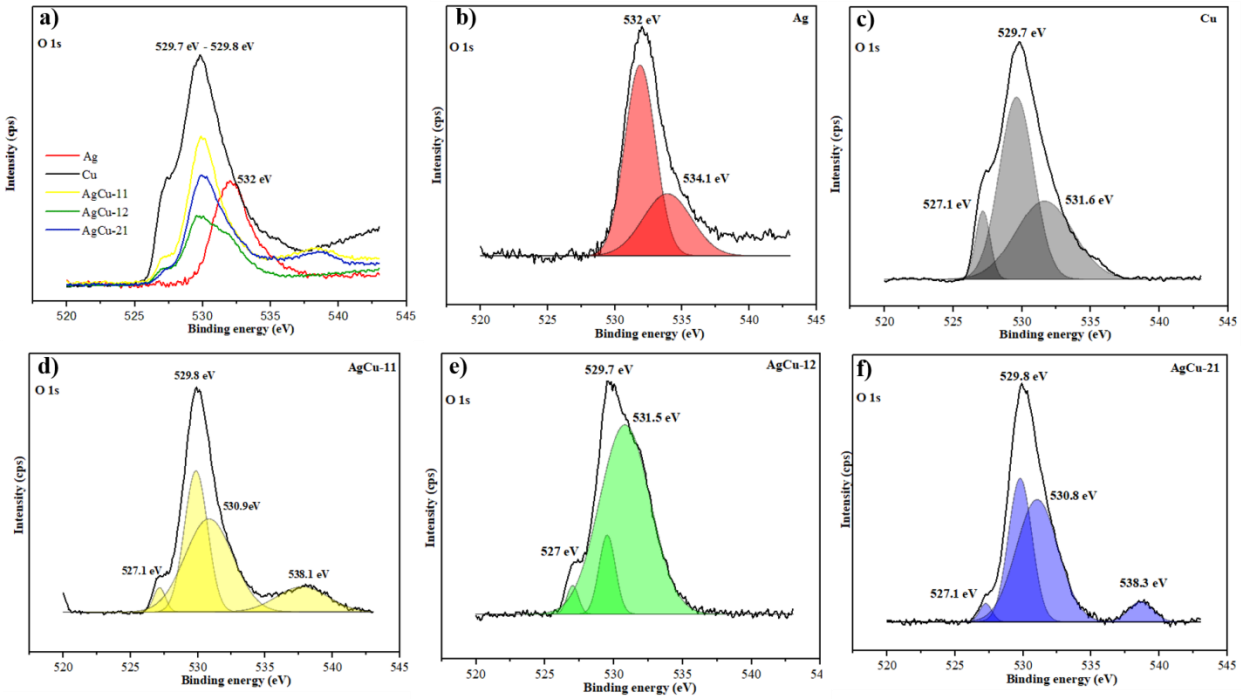

Figure 60. (a) The overall O1s spectrum of synthesized nanostructures (b-f) deconvolution of O 1s of individual nanoparticles of Ag, Cu, and AgCu compounds.

Previous studies reported that bimetallic particles show a significantly enhanced ORR activity compared to monometallic ones [13,112,288,334,335]. This could be due to two electronic effects namely ligand effect from the charge transfer between the metals involved and the strain effect due to the lattice strain resulting from the difference in

atomic radii of two different metals. In ligand effect mechanism on two metals, there will be a charge transfer from the metal with low work function to those with higher work function. Based on this finding, it is obvious that charge transfers from Ag with a work function of 4.4 eV to Cu that has higher work function of 4.53 eV [336]. Due to this charge transfer, the xps Ag peak on AgCu-21 shifted towards the lower binding energy. The ORR activity in alkaline medium is depending on the d band center of the metals that in turn governs the adsorption and desorption strength of O_2 [337]. Metals such as Ru, Rh, Ir and Pd with high d-band center possess low ORR activity owing to its strong adsorption strength of O_2 that fails to desorption of the oxygen intermediates. In case of metals with low d-band center (Au, Ag), the slow kinetic of O-O bond breaking limits the acitivy towards ORR. Therefore, raising the d-band center through adding another metal in Ag improves the kinetic of O-O bond breaking. The xps analysis shows the shift in the peak position attributed to the change in d-band center from Ag to Cu that favors the O-O bond breaking during ORR.

5.5.2. Electrochemical analysis and characterization

The electrochemical studies on all electrocatalysts synthesized via different schemes were performed with CV in N_2-saturated 1M KOH electrolyte as shown in Figure 61.(i)**,** and O_2-saturated 1M KOH electrolyte as shown in Figure 61.(ii) at a scan rate of 50 mVs^{-1}. The CV of Ag nanoparticles shown in Figure 61.(i) indicates 3 anodic peaks named as A_1, A_2, and A_3 in the forward scan and one cathodic peak C_1 in the reverse scan. Generally, the first anodic peak is related to the dissolution of silver as complex ion [338-340] of AgO^- as represented in equation

$$Ag + 2OH^- \rightarrow AgO^- + H_2O + e^-$$

The anodic peak A_2 is related to the formation of Ag_2O monolayer [341] as follows:

$$Ag + AgO^- \rightarrow Ag_2O + e^-$$

The further nucleation corresponds to the formation of multilayer Ag_2O is indicated by peak A_3.

In the negative scan, the cathodic peak C_1 represents the electro-reduction of Ag_2O to Ag that agrees with the reported scheme [322].

$$Ag_2O + H_2O + 2e^- \rightarrow 2Ag + 2OH^-$$

The CV of Cu is characterized by 3 anodic peaks A_4, A_5, and A_6 prior to oxygen evolution reaction (OER) and two cathodic peaks of C_2 and C_3. The electro oxidation peak at A_4 is related to the formation of porous Cu_2O layer [342] as follows:

$$2Cu + 2OH^- \rightarrow Cu_2O + H_2O + 2e^-$$

The peak A_5 is related to the adsorption of OH^- ions on the active sites of electrode assists the formation of $Cu(OH)_2$ and route to Cu_2O solid phase [343] according to the reaction

$$Cu + nOH^- \rightarrow Cu(OH)_n^{2-n} + 2e^-$$

When the potential reaches to the A_6 peak, $Cu(OH)_2$ and Cu_2O is converted to its thermodynamically stable form of CuO. In the reverse scan, the electro-reduction peak C_2 indicates the reduction of $Cu(OH)_2$ and CuO to Cu_2O, respectively, and C_3 is related to the further reduction of Cu_2O to Cu^0.

CVs of bimetallic Ag-Cu are the superimposition of the metallic Ag and metallic Cu. The peak intensity of C_1 decreases in AgCu-12 (Figure 61.(i)d), when compared to AgCu-11 and AgCu-21 and could be due to the decrease in Ag content on the surface of AgCu-12.

Similarly, the electrooxidation peak of silver (A_7), found in bimetallic Ag-Cu, is related to peak A_3 in Ag that shows an increase in peak current density for AgCu-21 and AgCu-11 in comparison with AgCu-12. This is due to the increase in the presence of Ag on the surface. Moreover, the electrooxidation peak at A_4 has its maximum intensity on AgCu-12 confirming the increase in the content of Cu. From the visual inspection, it is clear that the voltammetry profile of AgCu-12 is close to Cu excluding the peaks of Ag. The Figure 61.(ii) represents the cyclic voltammogram in O_2 saturated 1M KOH at a scan rate of 50 mV s^{-1}. The oxidation and reduction peaks are similar to Figure 61.(i), except the electro-reduction peak C_4 that corresponds to the reduction of oxides to metallic form (reverse process of A_1) that is the key process of oxygen reduction reaction (ORR). The reduction peak in shows a clear shift of reduction potential towards a positive direction that indicates the activity of the catalysts in the increasing order of Cu < Ag < AgCu-12 < AgCu-12 < AgCu-21. The enhanced activity of AgCu-21 could be due to the strong coupling of Ag and Cu as explained in XPS studies.

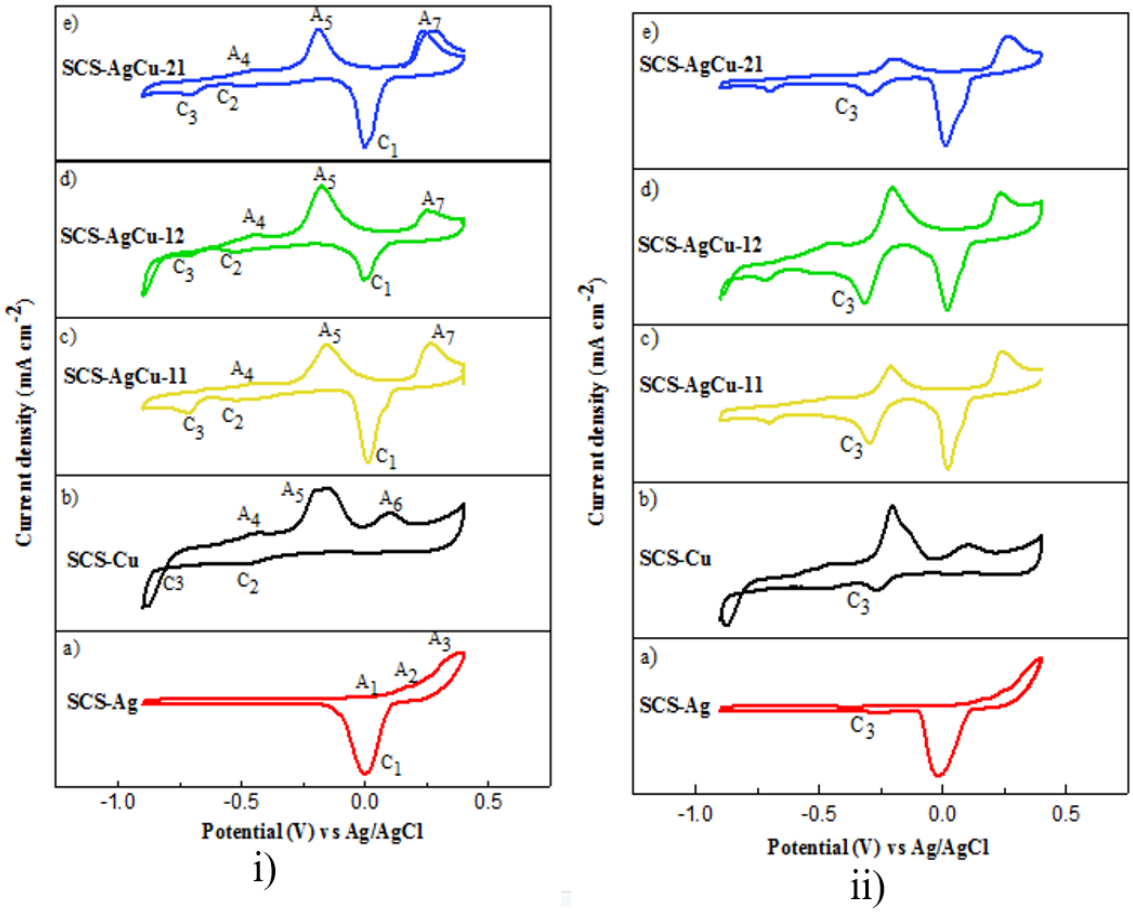

Figure 61. Cyclic voltammetry (CV) of (a) SCS Ag, (b) SCS Cu, (c) SCS AgCu-11, (d) SCS AgCu-11, (e) SCS AgCu-12 in the potential range of -0.9 V to 0.4 V at the scan rate of 50 mVs^{-1}; panel (i) N_2 saturated (ii) O_2 saturated.

The RDE curves on Ag, Cu, AgCu-11, AgCu-12 and AgCu-21 are shown in Figure 62.a. I-V plot characterized with negative reduction current and positive evolution current correspond to ORR and OER respectively. These results show the bifunctional effectiveness of the catalysts that can work for fuel cells and battery applications. The diffusion limiting current is higher for AgCu-21 than other catalysts. The activity of the catalyst is determined by the positive shift in the halfwave potential and the onset

potentials. Figure 62.b presents the onset potential of all the catalysts. The positive shift is maximum for AgCu-21 and decreases in the order of AgCu-21>AgCu-11>AgCu-12 >Ag>Cu. Similarly, the performance of each catalyst towards OER is shown in Figure 62.c. The current density starts to increase rapidly for AgCu-21 due to rapid transfer of electrons in AgCu-21 than other catalysts. OER catalyst shows the same trend as ORR, except AgCu-12 has lower activity towards evolution reaction than Ag nanoparticles. The reason could be the presence of more Cu on the surface and low effectiveness of copper towards OER as compared to Ag [109]. The improvement in electrocatalytic performance by alloying Ag and Cu has been reported by other authors as well [23-25], with slightly different values for limiting currents for Ag and Cu. This difference could be due to the synthesis method resulting in different surface composition and presence of some excess carbon on the surface as discussed in the XPS analysis of the samples. The synergistic coupling of Cu and Ag in the bimetal accelerates charge transfer and thus the activity of the catalyst in OER. In AgCu-21 and AgCu-11, there is a precatalytic oxidation peak centered at 0.15 V and 0.193 V that may be attributed to the lower oxidation of the silver species occurred during the initial sweep, respectively, but AgCu-12 and Cu do not show such a trend of pre-oxidation. This pre-oxidation peak clearly indicates the presence of Cu to be the reason for a decrease in performance of AgCu-12 for OER. The bifunctionality of the oxygen catalyst is shown by the potential difference between ORR and OER and could be reduced to as low as 0.415 V for AgCu-21 making it a suitable candidate for metal-air batteries and fuel cells. Figure 62.d shows an increase in limiting current density in the disk with an increase in the rotor rotation speed. The reason behind this behavior is the shortened diffusion distance at high speed, which reduces the barrier

for the electron passage. This is reflected in both, the reduction and oxidation peaks.

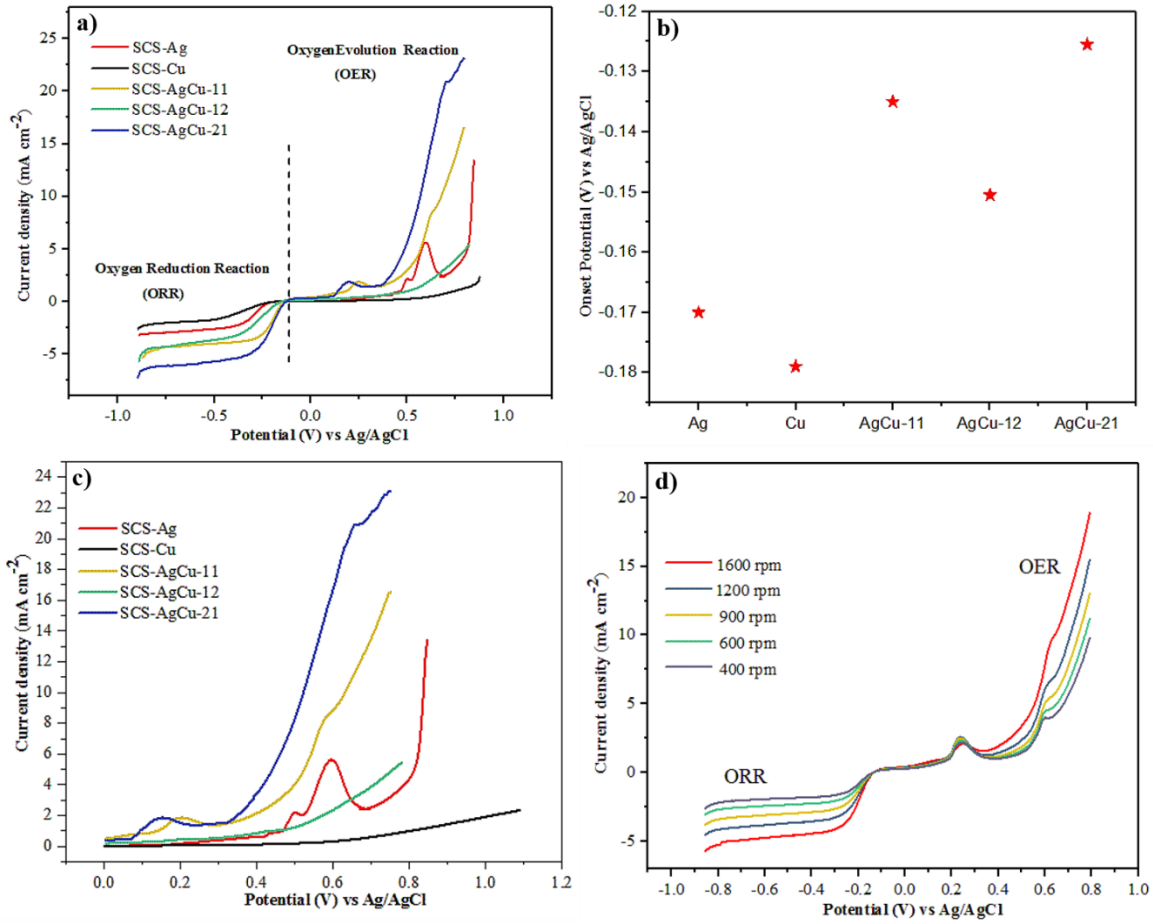

Figure 62. The electrochemical characterization of Ag-Cu catalyst a) RDE polarization curve of Ag-Cu catalyst in O_2 saturated 1 M KOH solution at a scan rate of 50 mVs^{-1} (-0.9 V to 0.8 V vs Ag/AgCl) b) onset potential of all SCS synthesized catalysts c) OER curve d) LSV curves at different rotation speed.

Figure 63.a represents the K-L plot at different rotor speed. The linearity of the K-L plot indicates the first order kinetics of the reaction towards the concentration of the dissolved oxygen. The number of electron transfer in the reduction reaction can be obtained from

the K-L plot based on Equ (3.10). The overall electron transfer is independent of the rotor speed but highly influenced by the catalyst loaded. The bar plot presented in Figure 63.b shows that the calculated electron transfer number is 3.9 for AgCu-21 favoring a 4-electron transfer mechanism. Other values also suggest that the bimetallic Ag-Cu catalyzes the ORR mechanism predominantly through the 4-electron transfer process. The kinetic current density, calculated by taking the inverse of the Y-intercept of the corresponding K-L plots, is also presented as bar charts in Figure 63.b. The kinetic current density carries the maximum value of 14.8 mA cm^{-2} for AgCu-21, 12.5 mA cm^{-2} for AgCu-11, 9.01 mA cm^{-2} for AgCu-12, 6.23 mA cm^{-2} for Ag and 5.21 mA cm^{-2} for Cu respectively.

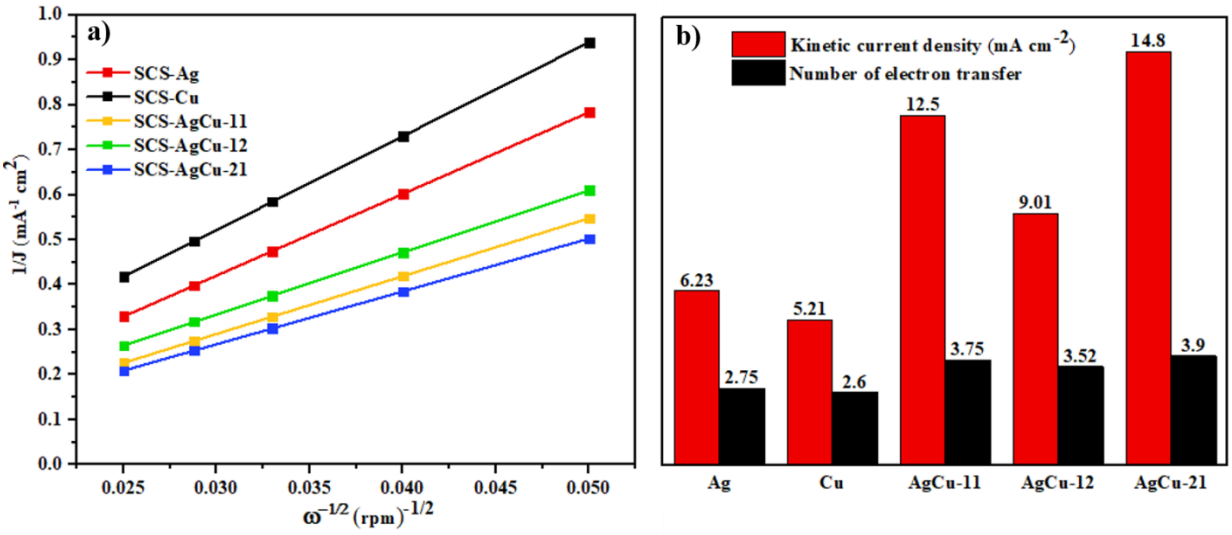

Figure 63. a) Koutecky-Levich plot for different catalysts at different rotation speeds b)

bar plot represents the kinetic current density and the number of electron transfer in an overall reaction for SCS based catalysts.

The rate determining step in ORR and OER is the O_2 adsorption that can be identified using tafel plot. It analyses the fundamental electrokinetics of anodic and cathodic reactions on the catalysts. Tafel plot is obtained by plotting the log (J_k) versus potential where J_k is the kinetic current density calculated from the KL equation (8). Tafel plot shown in Figure 64.a represents two tafel plots at low and high potentials for all the catalysts. These slopes correspond to the Temkin isotherm with a lower slope value at lower potential and an expected high slope value at a higher potential for Langmuir isotherm [290]. The overall tafel slopes for each catalyst for ORR and OER are shown in Figure 64. Tafel plot for a) ORR, and b) OER for all catalysts in O2 saturated 1 M KOH aqueous solution for 1600 rpm rotation; c) chronoamperometric response obtained at -0.5 V in O2 saturated 1 M KOH for 8000 sec., and d) cathodic current stability of different catalyst at O2 saturated 1 M KOH at -0.5 V.. It is clear from Table 3. Tafel Slopes for ORR and OER and the Exchange Current Density Obtained from Tafel Plot., that the ORR tafel slope is minimum (for low potential) for AgCu-21 and maximum for Cu. The lower tafel slope at a lower potential and the higher slope at a higher potential for AgCu-21 is an indication of the fast transport of electrons between electrode and catalysts. The intercept of the tafel plot is the logarithm of exchange current density (J_{ex}) which indicates the electronic activity and electron transfer that are the key parameters to determine the catalytic efficiency. The exchange current density calculated for the catalyst at low and high over potentials [344,345] ($J_{ex,low}$ and $J_{ex,high}$) are also presented in Table 3. AgCu-21

possesses the highest kinetics activity of about 1.6 times and 2.7 times more than AgCu-11 and AgCu-12 respectively. The OER tafel plots shown in Figure 64.b for all the catalysts indicate the minimum slope for AgCu-21 that is 41 mV dec^{-1} and maximum for Cu that holds the slope value of 67 mV dec^{-1}. Moreover, the smallest tafel slope for AgCu-21 indicates its enhanced ability for water electrolysis reaction. Tafel plots examined for both of OER and ORR promise the better catalytic performance for AgCu-21 due to the strong coupling of the metals in the nano-compound.

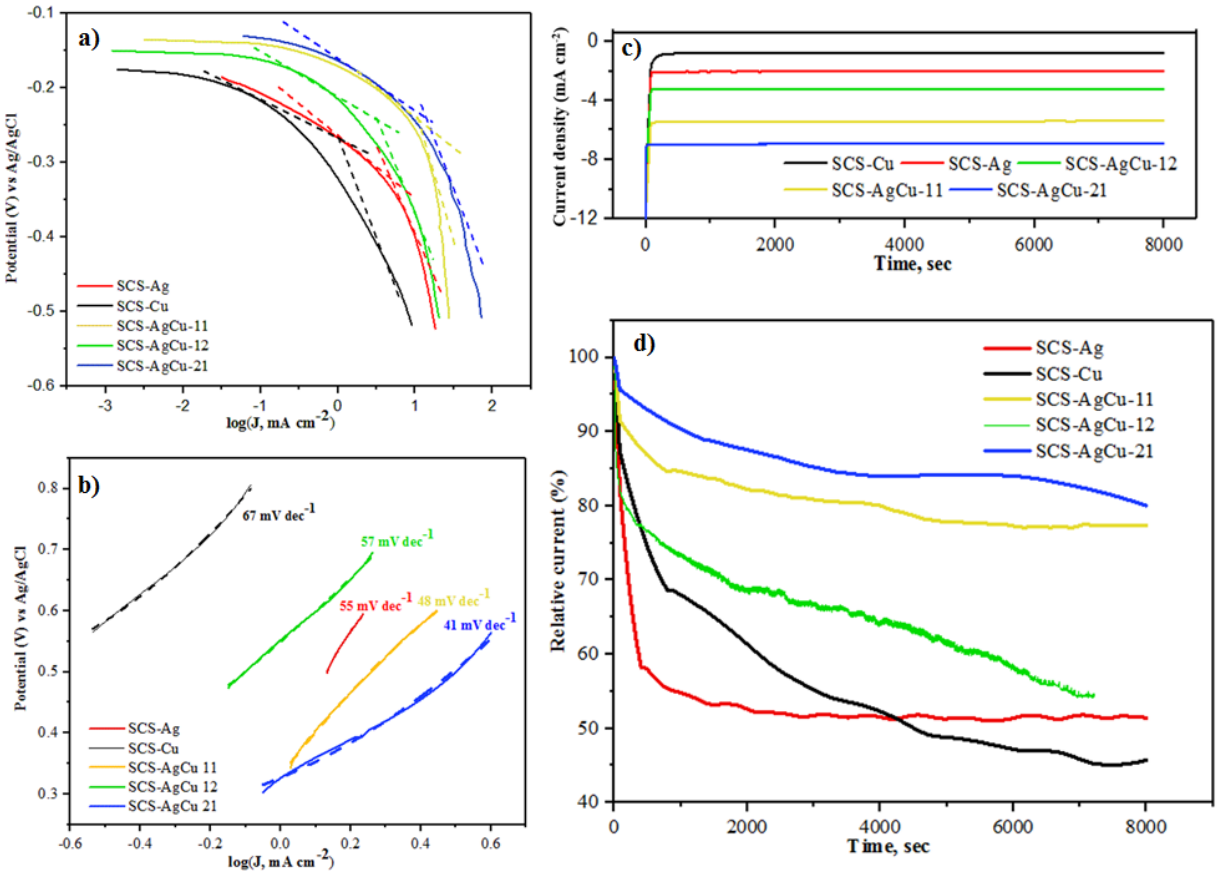

Figure 64. Tafel plot for a) ORR, and b) OER for all catalysts in O_2 saturated 1 M KOH aqueous solution for 1600 rpm rotation; c) chronoamperometric response obtained at -

0.5 V in O_2 saturated 1 M KOH for 8000 sec., and d) cathodic current stability of different catalyst at O_2 saturated 1 M KOH at -0.5 V.

Table 3. Tafel Slopes for ORR and OER and the Exchange Current Density Obtained from Tafel Plot.

Catalyst	ORR Tafel slope		OER Tafel slope	Exchange current density, (10^{-4} A cm^{-2})	
	b_{low} (mV dec^{-1})	b_{high} (mV dec^{-1})	(mV dec^{-1})	$J_{ex,low}$	$J_{ex,high}$
SCS- Ag	63	157	55	6.65	79.7×10^{-5}
SCS- Cu	71	135	67	1.02	12.1×10^{-5}
SCS-AgCu-11	57	172	48	21.58	10.1×10^{-3}
SCS-AgCu-12	68	163	57	12.76	12.5×10^{-4}
SCS-AgCu-21	51	179	42	35.4	15.1×10^{-3}

The long-term stability of the catalysts was evaluated using current-time chronoamperometric response at -0.5 V in 1M KOH aqueous solution and are presented in Figure 64.c-d. Due to the formation of double layer capacitance, there is a sharp decrease in current density for all the catalysts in Figure 64.c. Moreover, the current density for AgCu-21 is higher when compared to all other catalysts. In Figure 64.d, the AgCu-21 shows excellent stability and retention of more than 80 % of its initial current

even after 8000 sec. AgCu-11 also exhibits similar stability but the AgCu-12 lost its initial current over 60 % and tends to decrease more and more over the time. There is a sharp loss of current for 100 seconds in Ag and then it has become constant for the rest of time. AgCu-12 and Cu show the tendency of current drop even after the period of analysis. Notably, AgCu-21 exhibits higher current density and superior stability for ORR in the entire process. The stability and activity of the catalyst over 24 hr was analyzed as shown in Figure 65. It is clear from Figure 65.a that the activity of the catalyst is reduced to 25 % of its initial value after 30000 sec., which is stable after that till 24 hr. The TEM analysis of the catalyst after the stability indicates that the Ag undergoes some degradation over the Cu surface and the amount of Ag on Cu surface is reduced. After 30000 sec, the activity of the catalyst could be mainly from the Cu surface as the Ag involved in the reaction reduced. The cyclic voltammogram in Figure 65.b shows that the oxygen reduction peak (C_4) shift to the negative direction for the CV after stability test. This indicates that the activity of AgCu-21 after the continuous run over 24 hr degraded the activity for ORR.

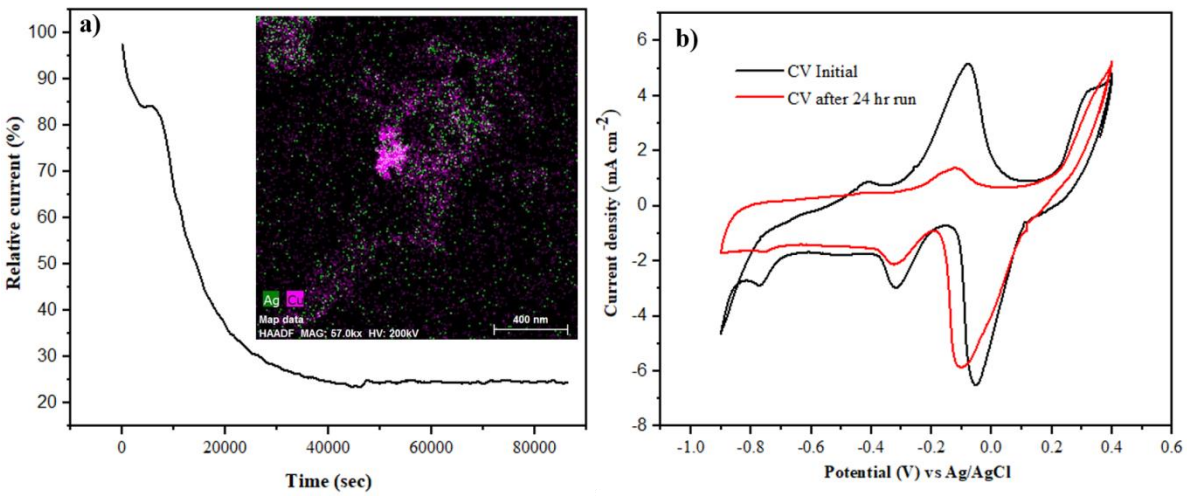

Figure 65. a) Relative current (%) of AgCu-21 for 24 hr. Inset: TEM elemental mapping of Ag and Cu after stability. b) cyclic voltammogram of AgCu-21 before and after stability.

AgCu-21 is found to be the best catalyst for ORR and OER among all the tested electrocatalysts, and the activity of the catalysts can be expressed in the increasing order as Cu<Ag<AgCu-12<AgCu-11<AgCu-21. This can be ascribed to the following reasons (1) a good coupling of Ag and Cu in SCS-AgCu-21, (2) synergistic effect between Ag and Cu atoms [38,109,283], (3) unique structure of Ag and Cu in AgCu-21, (4) metallic phase of Ag-Cu in AgCu-21. The AgCu-21 promotes the adsorption energy of oxygen molecules and enhances the activation energy of oxygen dissociation which is considered to be the rate determining step of ORR. Based on XPS results, the enhanced performance of AgCu bimetals could also be correlated with the shift in the binding energy of Ag (in AgCu bimetals) as AgCu-12<AgCu-11~AgCu-21.

5.6. Conclusion

Ag-Co catalysts with three different compositions were synthesized by combustion-based techniques. These NPs were applied for oxygen reduction and oxygen evolution reactions in alkaline medium. Among the three catalysts, the catalyst with high-content of Co in AgCo-12/C displayed better performance for electrocatalytic ORR and OER reactions. In general, the presence of Co-oxide on the surface of the AgCo-12/C catalyst is anticipated to enhance the adsorption and transport of oxygen involved in ORR reaction. The Ag atoms in the catalyst activate the O–O bond splitting and increase the reaction kinetics of ORR. All the three catalysts were found to follow the four-electron transfer mechanism for ORR reaction.

Bimetallic Ag-Cu were synthesized using different modes of solution combustion synthesis and characterized to study the morphology and composition. The electrochemical activity was measured for each catalyst and compared with Ag and Cu nanoparticles. XRD results show the presence of metallic copper in AgCu-21 and SEM/EDX indicate the presence of more silver on the surface of AgCu-21 compared to other bimetallic AgCu catalysts. The shifting of binding energy towards left (lower energy) in the XPS spectrum is an evidence of strong coupling of Ag and Cu in AgCu-21 than other three catalysts. All the catalysts synthesized were active for ORR and OER in the increasing order of AgCu-12<AgCu-11<AgCu-21. The AgCu-21 delivers a much better electrochemical performance towards ORR in terms of onset potential, limiting current density, kinetic current density, and stability. Also, the AgCu-21 catalyst exhibits a maximum kinetic current density of 14.5 mA cm^{-2} and at the overall ORR electron transfer number of approximately 3.9, indicating a four-electron transfer pathway.

The TEM analysis of the catalyst after the stability indicates that the Ag undergoes some

degradation over the Cu surface and the amount of Ag on Cu surface is reduced. Dissolution of catalyst surface during the ORR/OER shows major challenge for long term stability. In Ag-based alloys, there is a selective dealloying on ORR/OER activity and it is required to find better catalyst that remain same as single phase even after the long-term run.

Outcome of the chapter published in Journal:

- Ashok, A., Kumar, A., Matin, M. A., & Tarlochan, F. (2018). Synthesis of Highly Efficient Bifunctional Ag/Co_3O_4 Catalyst for Oxygen Reduction and Oxygen Evolution Reactions in Alkaline Medium. *ACS Omega*, 3(7), 7745-7756.
- Ashok, A., Kumar, A., & Tarlochan, F. (2018). Surface Alloying in Silver-Cobalt through a Second Wave Solution Combustion Synthesis Technique. *Nanomaterials*, 8(8), 604.
- Ashok, A., Kumar, A., & Tarlochan, F. "Probing the effect of combustion controlled surface alloying in silver and copper towards ORR and OER in alkaline medium" *Journal of Electroanalytical Chemistry* –Under Review

CHAPTER 6: SYNTHESIS OF PEROVSKITES USING SOLUTION COMBUSTION SYNTHESIS AND ITS PERFORMANCE AS AN OXYGEN ELECTROCATALYST.

6.1. Introduction

Recently perovskite oxides received wide attention due to the flexibility and tunability of its physio-chemical and catalytic properties. These classes of materials possess exceptional thermochemical stability, ionic conductivity and electrochemical behavior to make them promising candidates for industrial and academic research. In this chapter we followed the solution combustion synthesis technique to prepare the perovskite structures and tested its electrochemical characteristics towards ORR and OER bifunctionality.

6.2. Synthesis of $LaMnO_3$ perovskites

Different forms of lanthanum perovskites La-M (where M=Co, Mn, Fe, Ni, Cr) were prepared using a single step solution combustion synthesis (SCS) technique. The precursors of Lanthanum nitrate ($La(NO_3)_2 \cdot 6H_2O$), transition metal nitrates, and glycine ($C_2H_5NO_2$) with different fuel ratios (φ=0.5, 1, 1.5, 2.5) were measured based on the calculation to obtain 1.5 g of nanoparticles after the combustion reaction. The measured precursors where dissolved in 25 ml of de-ionized (DI) water and stirred for an hour to obtain homogenous solutions. The beaker containing this solution was placed over the hot plate heater of 300°C to evaporate the excess water and initiate the combustion synthesis generating desired nanopowders. The synthesized particles were hand ground and sieved using 75 µm sieve to obtain uniform nanoparticles of size <75 µm. The prepared nanoparticles were dispersed in water along with addition of carbon black to

ensure the electrical conductivity in the electrochemical reaction. A 30 mg of synthesized perovskite powder was dispersed well in 0.2 ml DI water and sonicated well for 1 hr and slowly 70 mg of carbon black was added into the well-dispersed solution. The prepared perovskite/carbon solution was heated over a hot plate at 110°C until the sample is dried, then ground to obtain uniform size La-M/C particles.

6.3. Results and discussion

6.3.1. Catalysts characterization

Figure 66 shows the adiabatic combustion temperature of different La-M based perovskites in relation to fuel ratio to metal-nitrate ratio (φ). The combustion temperature shows a maximum value at the stoichiometric condition (φ =1) for all the materials investigated. Also, at other φ values (φ = 0.5, 1.5 and 2) the combustion temperature is much smaller compared to the value at φ=1. Due to lower combustion temperature, it is anticipated that the crystallization of the synthesized powder may get affected and the particles could be synthesized in amorphous form [346].

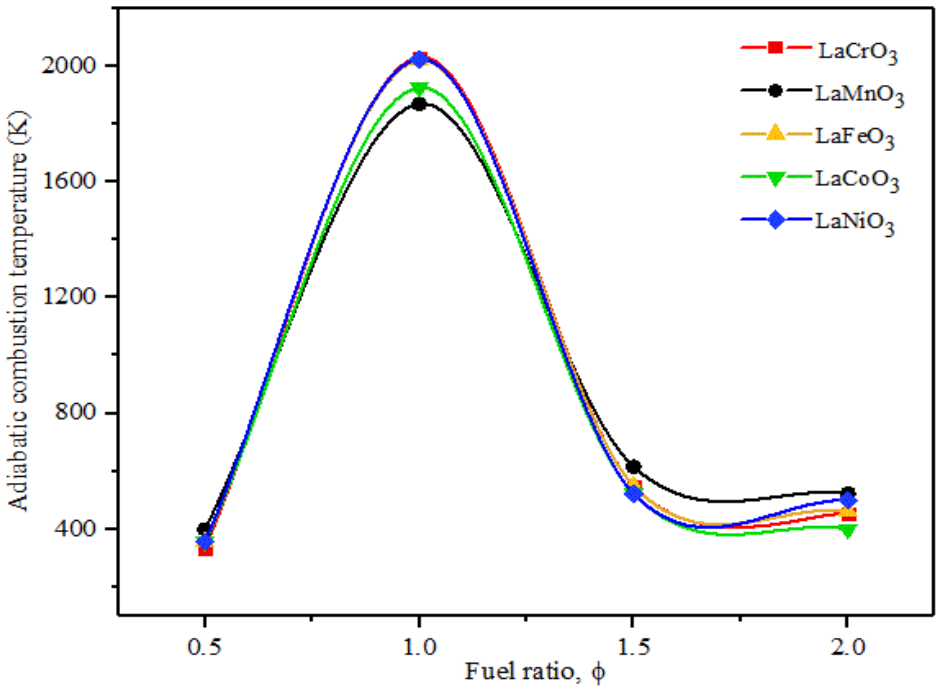

Figure 66. Combustion temperature for different perovskites in relation to fuel ratio(ϕ).

XRD pattern of the synthesized particles in Figure 67.a show the formation of crystallites with ABO_3 structure. $LaNiO_3$ particularly contain two different phases, $LaNiO_3$ and NiO, while all other compounds are completely in the perovskite form. Figure 67.b showing the XRD results of $LaCrO_3$ for different values of fuel to oxidizer ratio (φ), indicates the amorphous structure for φ=0.5 and φ = 2.5 as no peaks can be identified on the XRD pattern. However, for φ =1 and φ =1.5; well-defined crystallite peaks are observed. The combustion temperature obtained at φ =0.5 and φ = 2.5 does not provide enough energy for the crystallite structure formation.

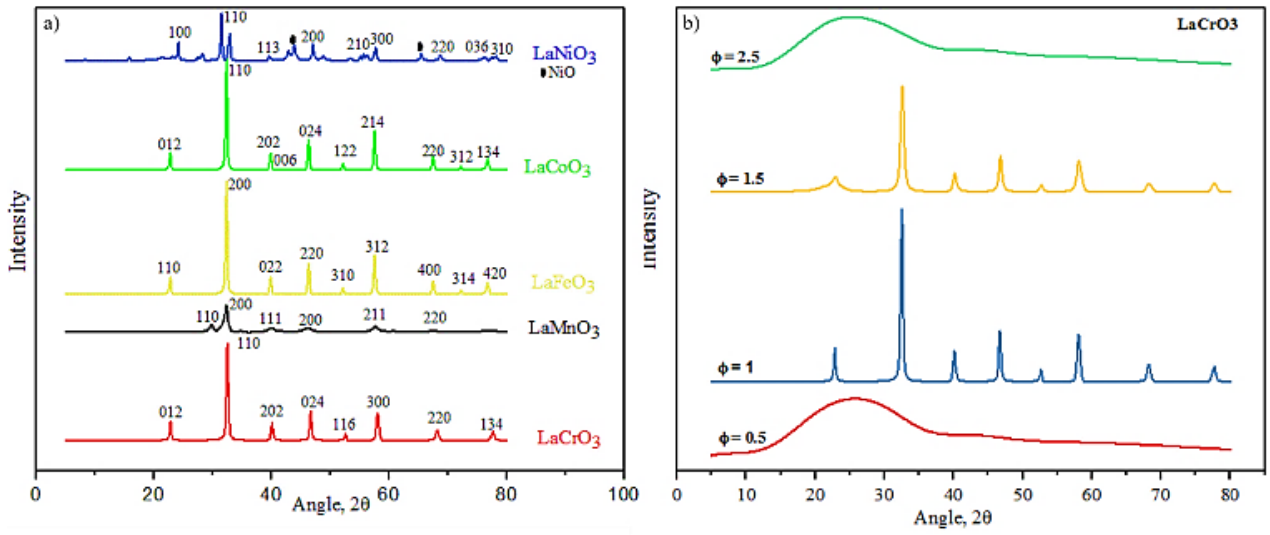

Figure 67. X-ray diffraction pattern of a) $LaMO_3$ (M=Cr,Fe,Mn,Co,Ni) at φ=1 b)$LaCrO_3$ synthesized for different fuel ratio ϕ=0.5, 1, 1.5, 2.5.

The morphologies of synthesized perovskite structures are shown in Figure 68. All the combustion synthesized nanopowder were found to be porous though it is difficult to identify individual particles, nonetheless large irregular shaped pores can be observed. The surface morphology of LaMnO3 and LaCoO3 look similar with smaller grain size when compared to other perovskite structures. The EDX analysis of the perovskites indicates the presence of atomic ratio of 1:1 for all La:M (Cr, Mn, Fe, Co, Ni) catalysts.

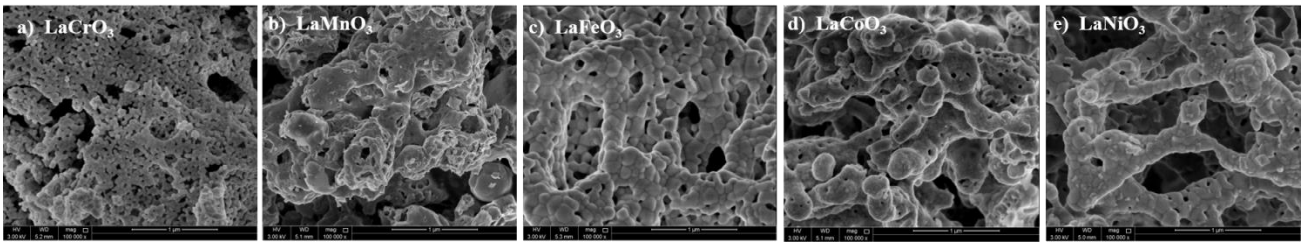

Figure 68. SEM micrograph for synthesized perovskites a) $LaCrO_3$, b) $LaMnO_3$, c) $LaFeO_3$, d) $LaCoO_3$, e) $LaNiO_3$ at a fuel ratio φ= 1. (scale bar- 1 µm).

The synthesized particles of $LaMnO_3$ were also characterized using HR-TEM as shown in Figure 69. The high magnification image in Figure 69.b shows lighter areas indicating the porous nature of the nanoparticles. The pores could have been created during the synthesis process because of the gases generated during the combustion reaction [263,307,308]. The average diameter of the pores was found to be 2.5 nm, that possibly could be affected by the fuel to oxidizer ratio along with the total pore volume. The SAED pattern in Figure 69.c shows the crystalline nature of the particles where the spot pattern designates the crystalline structure. Each bright point in SAED pattern for the set of planes with d_{hkl} measured are 0.187 nm, 0.27 nm and 0.38 nm corresponds to (200), (110) and (002) planes. EDX elemental mapping shown in Figure 69.d-g indicates the presence of La and Mn in equal ratio everywhere on the catalyst.

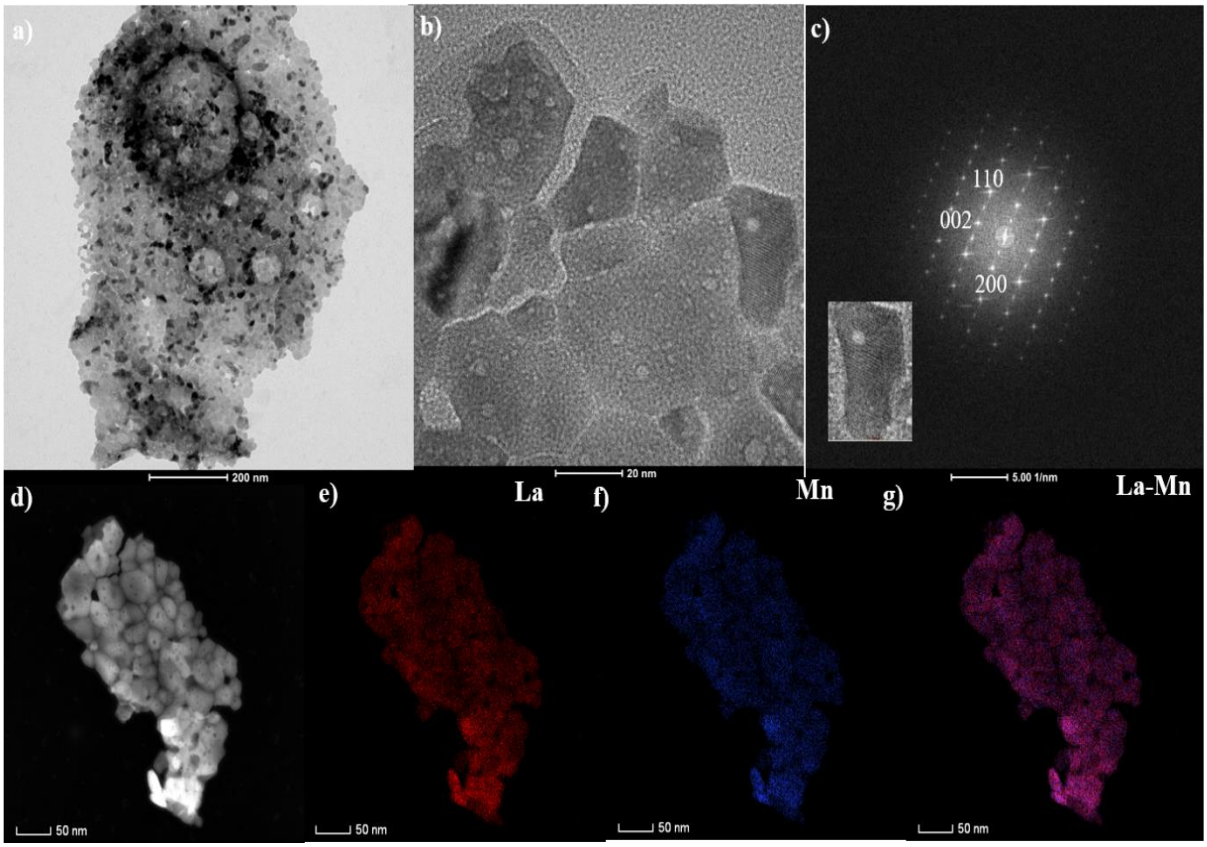

Figure 69. (a-b) HRTEM image and c) SAED pattern of $LaMnO_3$ (d-g) EDX elemental mapping of La, Mn and overlapped La-Mn.

The elemental analysis and mapping of $LaCoO_3$ shown in Figure 70 represents the high crystalline particles with primarily square shaped structure. However, the porosity that was clear in $LaMnO_3$ is not visible in $LaCoO_3$ nanoparticles. The particle distribution over selected region on $LaMnO_3$ and $LaCoO_3$ suggests the presence of particles in the range between 8 -20 nm along with some level of agglomeration. The particle distribution profile for these two samples is represented in Figure 71.

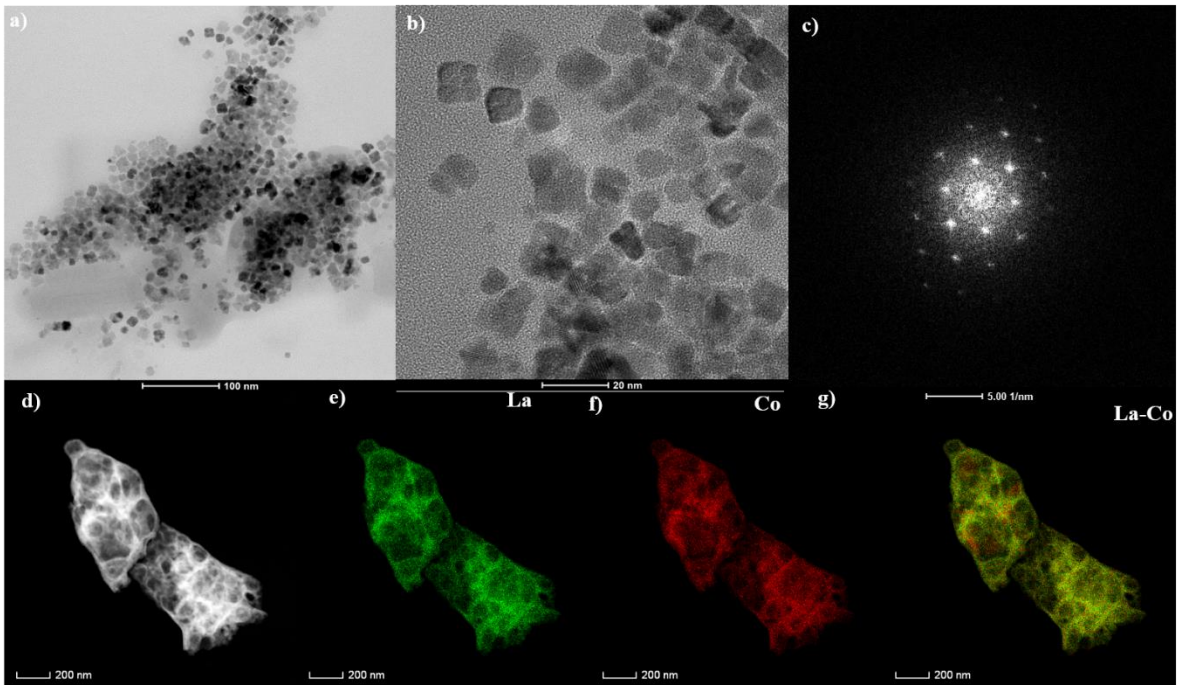

Figure 70. (a-b) HRTEM image and c) SAED pattern of $LaCoO_3$ (d-g) EDX elemental mapping of La, Mn and overlapped La-Mn.

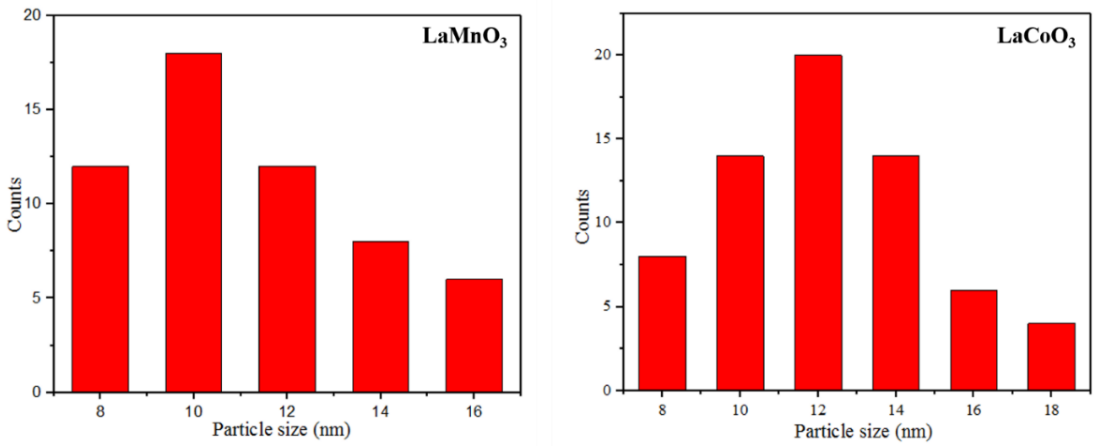

Figure 71. Particle size distribution histogram of a) $LaMnO_3$ b) $LaCoO_3$.

6.3.2. Electrochemical analysis and characterization

Figure 72 shows the cyclic voltammogram at different potentials for all the synthesized catalysts to represent both the ORR and OER activities. The oxygen reduction peaks for La-M (Co, Fe, Cr and Ni) are nearly similar except for $LaMnO_3$ a positive peak shifting to a higher potential is visible in Figure 72.(i). The CV graph in Figure 72.(ii) indicates the OER current density in the decreasing order of $LaCoO_3$ > $LaNiO_3$ > $LaCrO_3$ > $LaMnO_3$ > $LaFeO_3$.

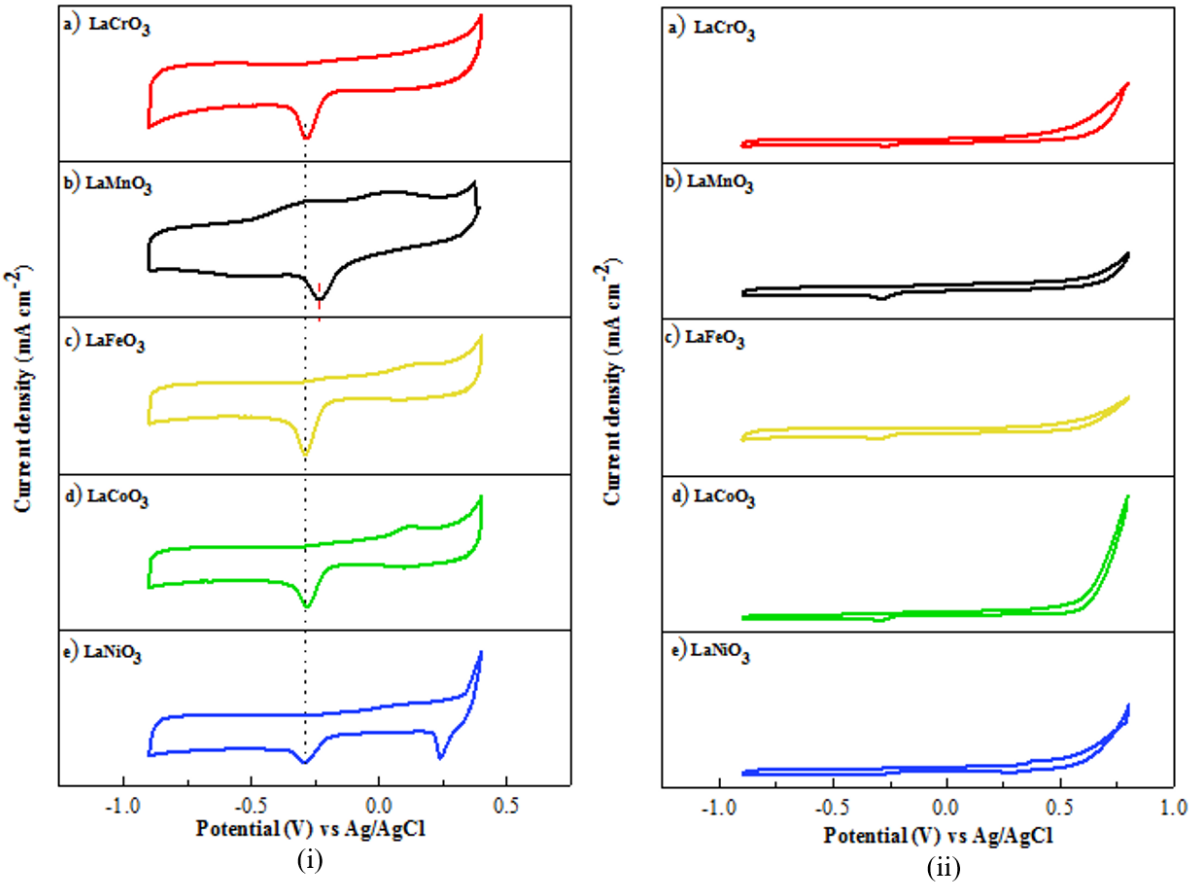

Figure 72. Cyclic voltammogram for Lanthanum based perovskites in 1 M KOH electrolyte in the potential window (i) -0.8V to 0.4V (ii) -0.8V to 0.8V.

LSV shown in Figure 73.a represents the oxygen reduction and evolution reaction (ORR and OER) of La-based metal perovskites in the potential range of -0.9V to 0.8V. ORR in oxygen saturated 1 M KOH solution shown in Figure 73.b indicates maximum diffusion limited current density for $LaMnO_3$ that decreases in the order of $LaMnO_3$>$LaCoO_3$>$LaNiO_3$>$LaFeO_3$>$LaCrO_3$. The onset potential of $LaMnO_3$ is -0.12 V and for all other catalysts the potential remains same as - 0.2 V. Figure 73.c shows the OER response of each catalyst in the potential window of 0.3V to 0.8V. At 0.55V the kinetics of $LaNiO_3$ is sharper than $LaCoO_3$ that diminishes by the time potential reaches a value of 0.68 V along with a subsequent decrease in current density at high potentials. The evolution current density is maximum for $LaCoO_3$ and decreases in the following order as $LaNiO_3$>$LaMnO_3$,>$LaCrO_3$>$LaFeO_3$. As proposed by Suntivich *et al*, the reason for maximum activity for $LaMnO_3$ and $LaCoO_3$ could be the unity e_g orbital filling to facilitate a strong adsorption of oxygenated intermediates participating in the rate determining steps in ORR and OER respectively. Voltammetry curve recorded on RDE at different speeds of rotation is shown in Figure 73.d. The current density increases with an increase in the rotation speed that could be due to a rapid transport of dissolved oxygen on the electrode surface.

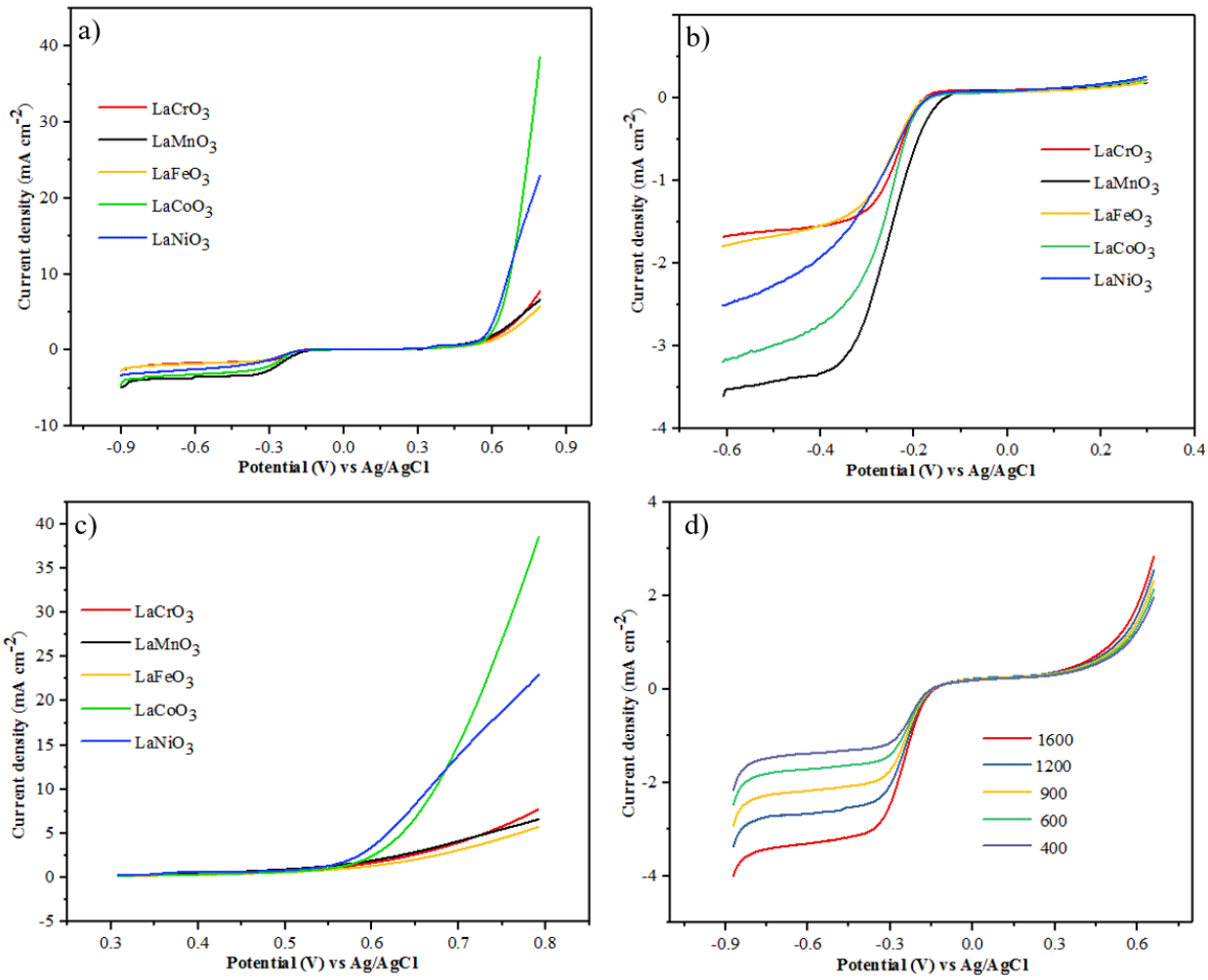

Figure 73. (a) Linear sweep voltammetry of all La-perovskites in O_2 saturated 1 M KOH electrolyte at 50 mVs^{-1} at 1600 rpm in the potential range of -0.9V to 0.8V, (b) oxygen reduction reaction (ORR) current densities at 1600 rpm (-0.6V to 0.3V), (c) oxygen reaction (OER) current densities in the potential between 0.3V to 0.8V, d) ORR current density of $LaMnO_3$ at different rotation speed (400 to 1600rpm).

The KL plot shown in

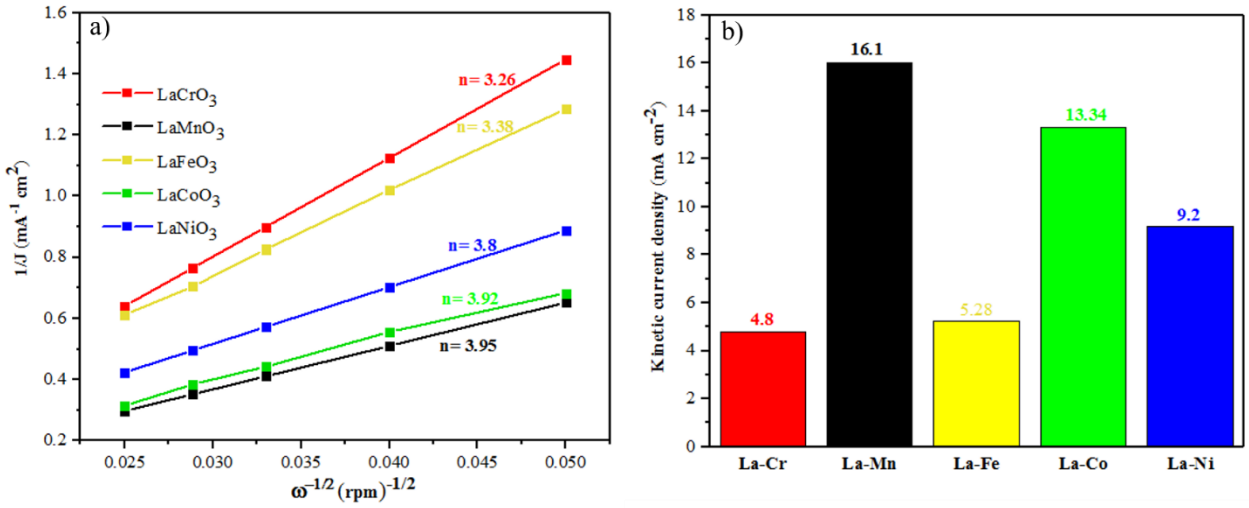

Figure 74.a follows a linear feature implying a first-order kinetics for the oxygen reduction reaction. The overall electron transfer in the reduction reaction is calculated from the equation (4) that are marked over each plot. The number of electrons involved is a function of catalysts, showing maximum for $LaMnO_3$ (3.95) followed by $LaCrO_3$ (3.26). Another parameter to determine the activity of the catalyst is its kinetic current density represented as bar plot in

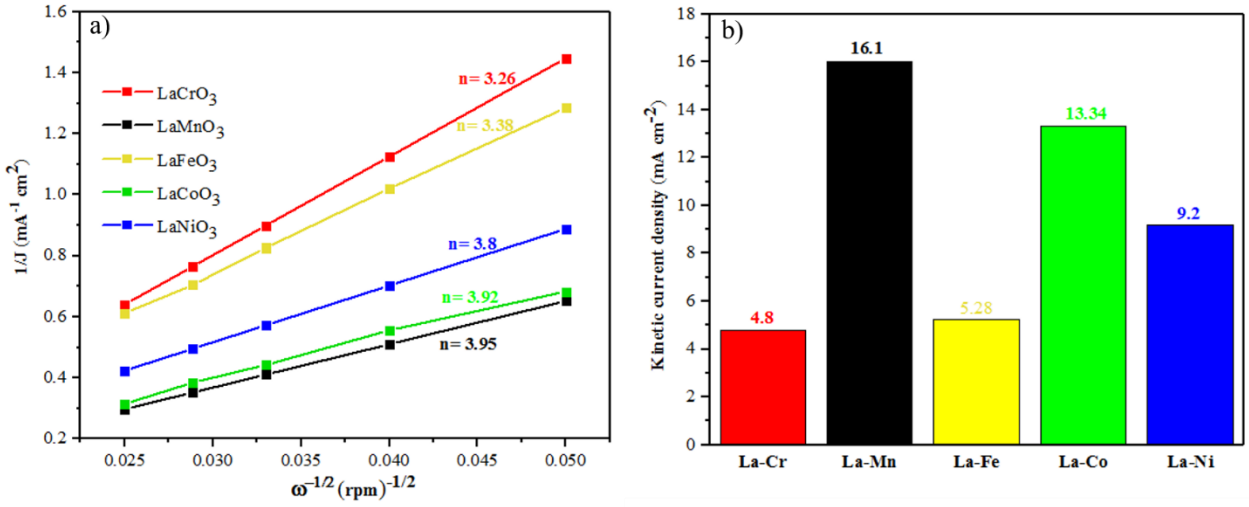

Figure 74.b. The kinetic current density decreases in the order of $LaMnO_3$ > $LaCoO_3$ >

$LaNiO_3$ > $LaFeO_3$ > $LaCrO_3$ that holds corresponding values of 16.1 $mAcm^{-2}$, 13. 34 $mAcm^{-2}$, 9.2 $mAcm^{-2}$, 5.28 $mAcm^{-2}$, and 4.8 $mAcm^{-2}$ respectively.

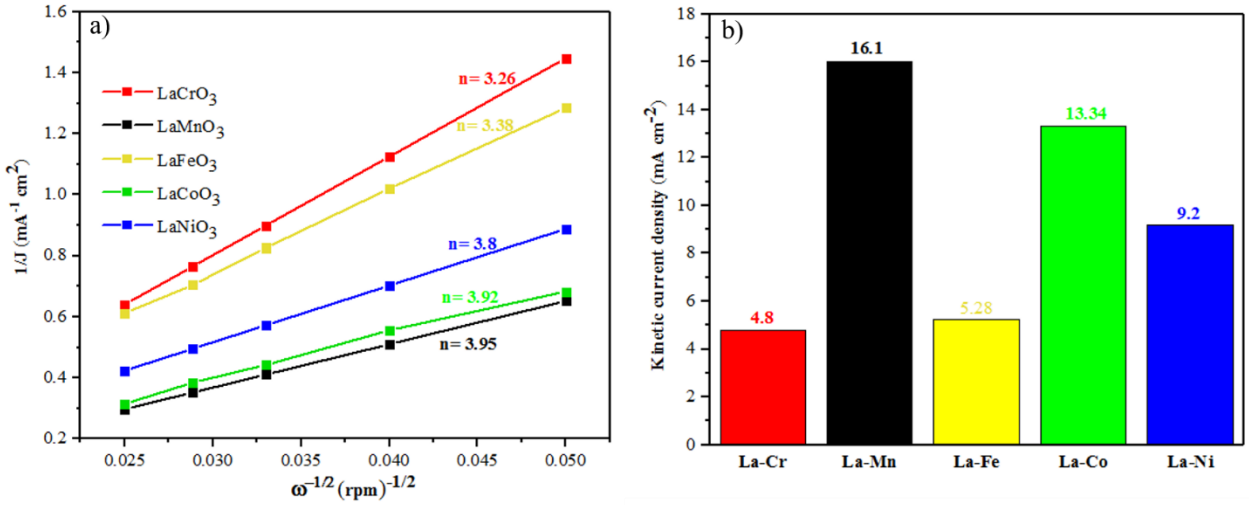

Figure 74. (a) Koutecky-Levich plot for ORR current densities at different rotation and represented the overall electron transfer in the reaction (b) kinetic current densities of La-based perovskite catalysts prepared using solution combustion synthesis.

Tafel plot is used to identify the O_2 adsorption rate on the catalysts for ORR and OER. This electro kinetic analysis can be performed by plotting the log(J_K) on the x-axis and potential over the y-axis. The consolidated data from Tafel plot is presented in Table 4. Tafel plot shown in Figure 75 indicates the presence of two linear regions at low and high potential values corresponding to Temkin and Langmuir isotherms respectively. A good ORR electro catalyst is expected to have high slope at Temkin and low slope at Langmuir isotherm [290]. While considering this statement, it is clear from Table 4 that $LaMnO_3$ with slope of 53/217 mV/dec^{-1} at low/high potential is the best active perovskites for

ORR. In $LaMnO_3$ the electron transfer between electrode and the catalyst will be faster when compared to other and this could be the reason for attaining more number of overall electron transfer to Mn coupled La perovskites. In Figure 75.b the tafel slope for OER is minimum for $LaNiO_3$ (~$LaCoO_3$) and maximum for $LaFeO_3$. The highly active $LaMnO_3$ for reduction reaction (ORR) shows poor performance in the oxygen evolution reaction (OER).

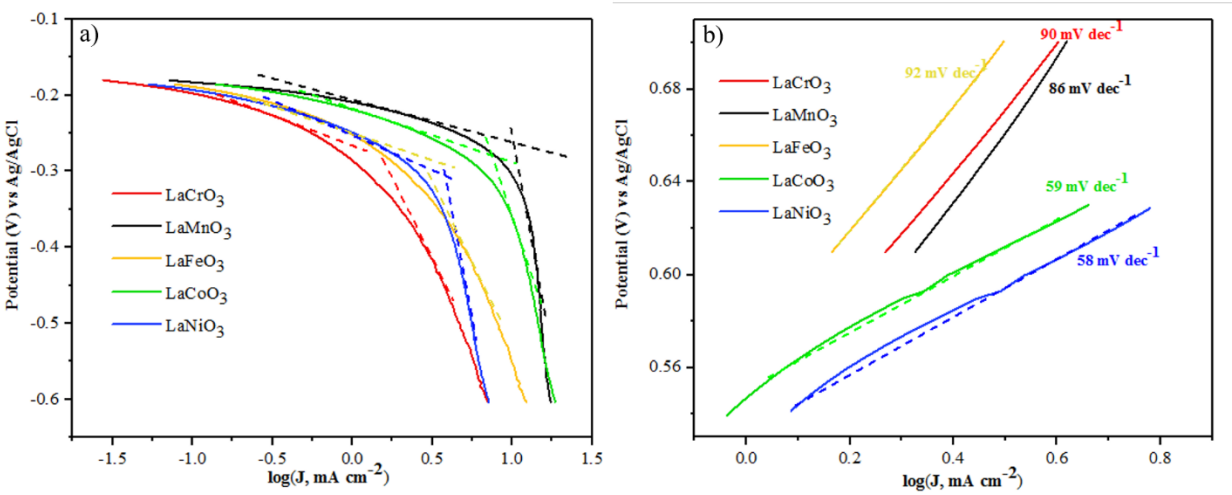

Figure 75. Tafel plot comparing the activity of perovskite catalyst for (a) ORR and (b) OER in O_2 saturated 1 M KOH electrolyte at room temperature at 1600 rpm rotation speed.

Table 4. Tafel Performance Parameters for ORR and OER

ORR Tafel slope		OER Tafel slope
b_{low} (mV dec^{-1})	b_{high} (mV dec^{-1})	(mV dec^{-1})
67	160	90
53	217	86
62	174	92
57	204	59
60	192	58

Alkalinity tolerance and catalytic activity are the main issues facing cathode electrocatalysts in alkaline media. Moreover, catalysts for ORR suffer from stability issues due to the deposition of intermediates on the surface of the catalyst during reduction reaction. Chronoamperometry was used to find the long-term stability of the catalysts at -0.5 V in O_2 saturated 1 M KOH solution at room temperature and the results are shown in Figure 76. After 150 sec, the current density decreases sharply in both catalysts possibly due to the formation of double layer capacitance [347] . Figure 76.a show the higher current density for $LaMnO_3$ when compared to $LaCoO_3$ at -0.5 V potential. The stability of catalyst over time was measured using the relative current shown in Figure 76.b. In $LaCoO_3$, 72% of the initial current drops after 2.25 hr and the trend looks to remain constant thereafter. There is a sharp decrease in the relative current for $LaMnO_3$ indicating the relative instability of catalyst after 2.25 hr. It is clear from the results that even if the current density of $LaMnO_3$ is higher, the stability could be an issue.

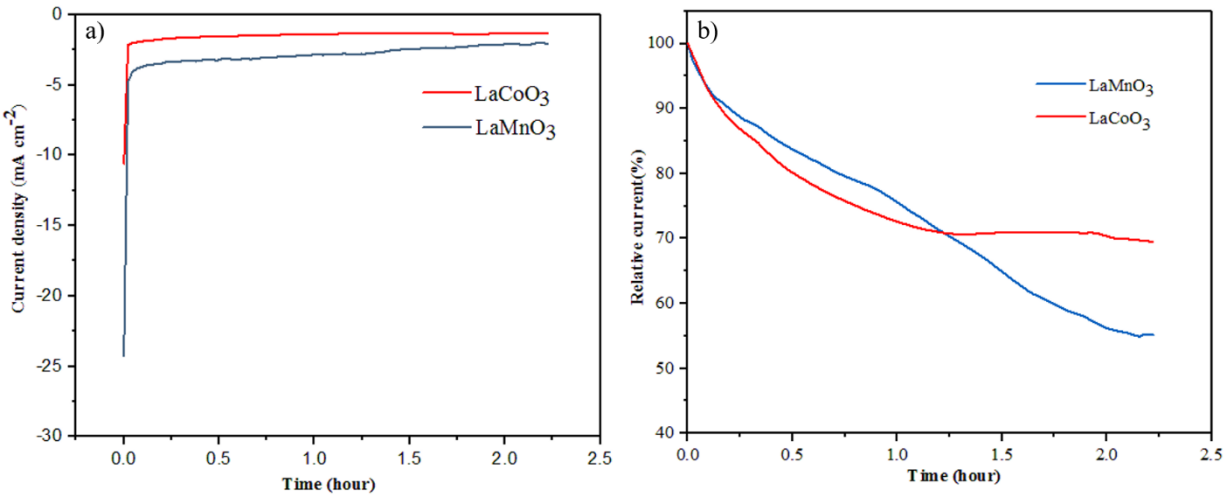

Figure 76. (a) Chronoamperometric current-time (I-t) curve obtained at -0.5 V in O_2 saturated 1 M KOH solution (b) Relative current to measure the cathodic stability of $LaMnO_3$ and $LaCoO_3$.

The electrochemical stability of $LaCoO_3$ was further evaluated using the continuous cyclic run between -0.3 to 0.6 V for 2000 cycles at a scan rate of 50 mVs^{-1}. The ORR and OER curves were recorded before and after cycling with a scan speed of 5 mVs^{-1} in O_2 saturated 1M KOH solution. After 2000 cycles, ORR curve in Figure 77.a show a 33 mV negative shift of half-wave potential. The OER curve for stability test shows a slight decay in the activity of catalyst towards evolution reaction as observed in Figure 77.b after 2000 cycles.

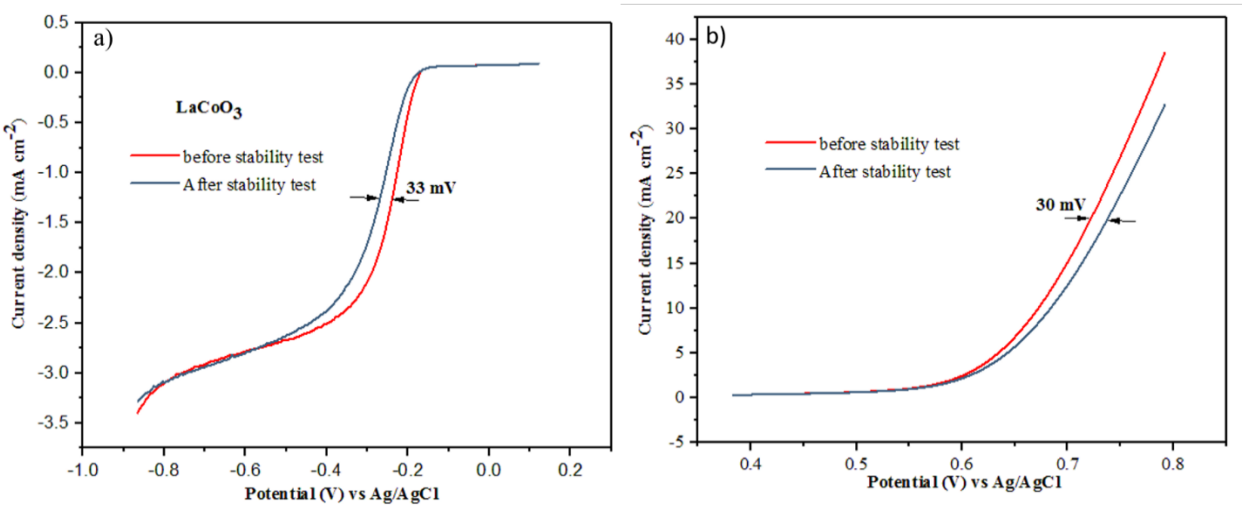

Figure 77. Electrochemical stability of $LaCoO_3$ in (a) ORR and (b) OER curves before and after 2000 CV cycle.

The TEM analysis of the catalyst after the stability test in Figure 78 indicates the existence of perovskites in their original form even after the stability. The elemental mapping of each elements and its composition shows that perovskites are relatively stable and there is no phase separation of the elements with respect to time.

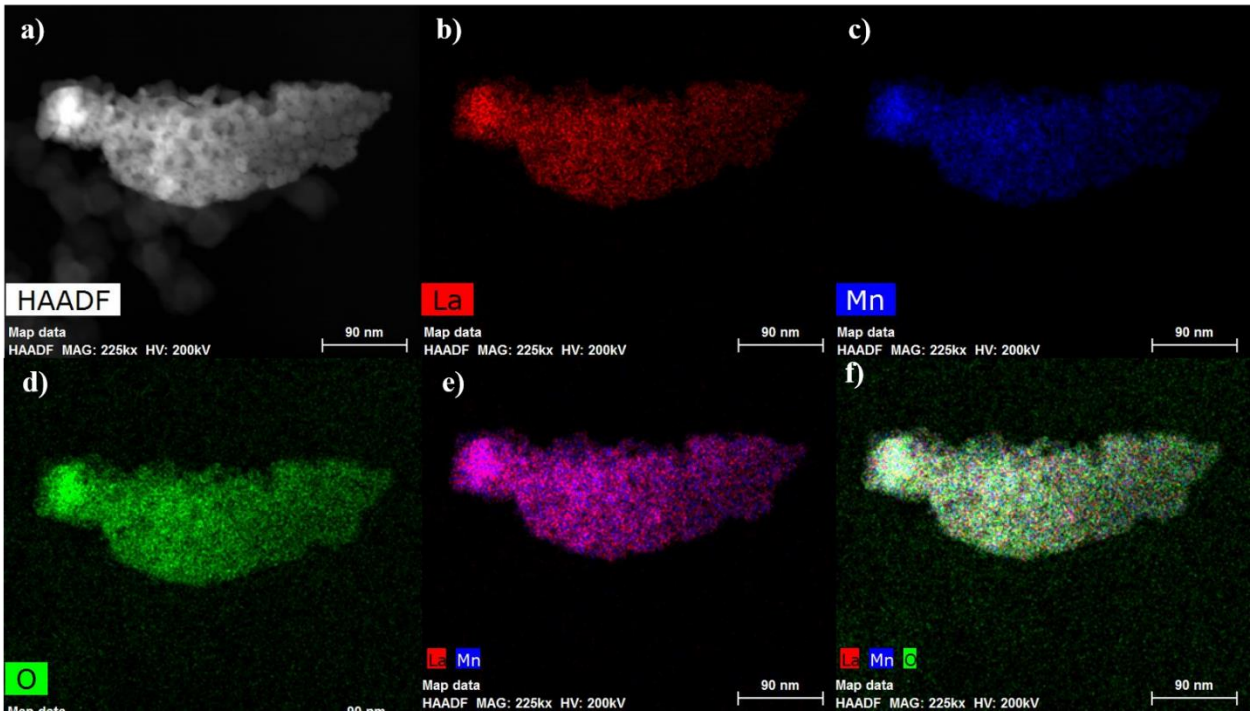

Figure 78. TEM elemental mapping of each elements in $LaMnO_3$ after the stability run.

The overall performance parameters are compiled in Table 5.

Table 5. Summary of Electrochemical Parameters of ORR and OER for Each Catalyst.

Catalyst	E_{onset} (V)	E_{OER} (V)	ΔE (V)	J_L (mA cm^{-2})	J_k (mA cm^{-2})	$n_{electron}$
$LaCrO_3$	-0.2	0.61	0.81	-1.6	4.8	3.26
$LaMnO_3$	-0.12	0.6	0.72	-3.5	16.1	3.95
$LaFeO_3$	-0.2	0.61	0.81	-1.75	5.25	3.38
$LaCoO_3$	-0.2	0.58	0.78	-3.2	13.34	3.92
$LaNiO_3$	-0.2	0.55	0.75	-2.6	9.2	3.8

** all voltages (V) are with respect to Ag/AgCl.

E_{onset} - Onset potential

ΔE – ORR-OER potential difference

J_L - Limiting current density

J_k - Kinetic current density

$n_{electron}$ - Number of electron Transfer

6.4. Conclusion

LaMO3 (M = Cr, Mn, Fe, Co, Ni) were synthesized using solution combustion method for different value of fuel to metal nitrate ratios. Experimental results indicate the nanomaterials crystallinity can be controlled by varying the amount of fuel during combustion synthesis and only appropriate fuel ratio (~φ=1) generates crystalline structure whereas a too-low or too-high fuel content would result in an amorphous structure. All the synthesized perovskites were evaluated for their performance towards

oxygen reduction and oxygen evolution reactions. Based on LSV results, LaMnO3 shows the maximum current density for oxygen reduction reaction, whereas LaCoO3 shows better performance for oxygen evolution reaction. The ORR kinetics was improved in the order of LaCrO3 < LaFeO3 < LaNiO3 < LaCoO3 < LaMnO3. Chronoamperometric results show that at -0.5V LaMnO3 holds the maximum current density with poor stability. The LaCoO3 catalyst showed better stability for oxygen reduction and oxygen evolution reactions with continuous cycling for 2000 cycles between -0.3V to 0.6V. A comparison of the LaCoO3 catalytic performance before and after the stability tests indicates a shifting in LSV curve at the half wave potential of 33mV for oxygen reduction towards negative potential, and 30mV for oxygen evolution towards positive potential. The elemental mapping of each elements and its composition shows that perovskites are relatively stable and there is no phase separation of the elements with respect to time.

Outcome of the chapter published in Journal:

- Ashok, A., Kumar, A., Bhosale, R. R., Tarlochan, F. (2018). Combustion synthesis of bifunctional $LaMO_3$ (M= Cr, Mn, Fe, Co, Ni) perovskites for oxygen reduction and oxygen evolution reaction in alkaline media. *Journal of Electroanalytical Chemistry*, 809, 22-30.

CHAPTER 7: EFFECT OF SALT ASSISTED COMBUSTION SYNTHESIS ON ELECTROCHEMICAL PERFORMANCE OF PEROVSKITES.

7.1. Introduction

CS is reported to be a fast, simple and economical mode of preparing nanoparticles that do not require any post combustion treatment [114,226,251,263,307,348-358]. Nonetheless, agglomeration of nanoparticles is seen as a major drawback in these materials. The research so far in the direction of agglomeration and nanoparticle morphology control (e.g. crystalline size, surface area and pores distribution) has mainly focused on the choice of fuels and adjusting the fuel to oxidizer ratio [254-257], which resulted in only limited success. In 2006, Weifang Chen and co-workers reported an alternative strategy to inhibiting agglomeration in SCS by introducing a soluble inert salt to the redox mixture of metal nitrate and fuel [258]. While using these diluents (KCl or NaCl) adiabatic temperature can be decreased to reduce sinter and further growth of particles. The salt inclusion acts as a template to inhibit the agglomeration by binding the particles from growing further and breaking up the three-dimensional porous structure. X. Zhang *et al*. proposed a possible mechanism of formation of well-dispersed $CoFe_2O_4$ nanoparticle using salt assisted solution combustion synthesis [259]. It is well established that the hardness, abrasive wear resistance and binding strength of the particles increase with a decrease in particle size and thereby influencing the other performance characteristics of these materials [260]. These inorganic salts are much cheaper, highly soluble in water, thermally stable at high temperature, unreactive to the redox mixture that can easily be removed from the product mixture through washing. In this work, we

follow the salt assisted solution combustion synthesis for the preparation of $LaMnO_3$ perovskites to understand the change in physical and material characterization when compared to conventional SCS synthesized $LaMnO_3$. Moreover, we investigate the improvement in the electrochemical properties of the salt assisted $LaMnO_3$ perovskite structures towards ORR and OER applications.

7.2. Experimental

Initially, the perovskites nanoparticles were prepared by mixing a measured quantity of metal nitrate and glycine with a known fuel to oxidizer ratio (φ). The quantity of metal nitrates and glycine was calculated based on a stoichiometric equation (1) reported elsewhere [263,307]. The precursors were dissolved in 25 ml of deionized water (DIW) and stirred continuously for 1 h to obtain a homogeneous mixture. Secondly, the KCl to metal ion ratio of 2/3 was used to measure the amount of KCl added to the solution and the mixture was placed on a heater at 300°C until all the water evaporates. Once the combustion takes place, the product was dispersed in DI water and boiled to dissolve and remove the extra salt residuals. This process was repeated several times to ensure no salt is left with the nanoparticles. The sequence of salt-assisted solution combustion synthesis is shown in Figure 79.

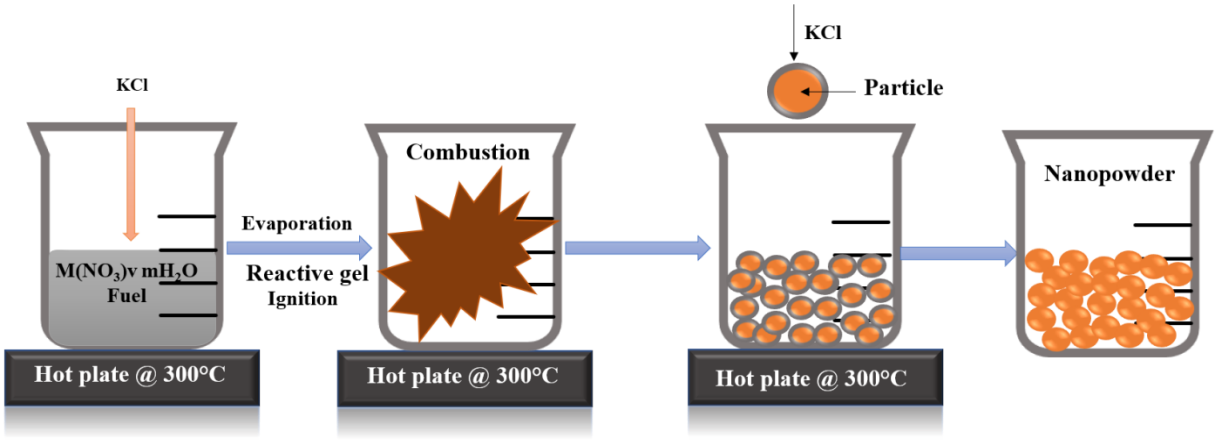

Figure 25

Figure 79. Stepwise synthesis of salt-assisted solution combustion synthesis (SCS)

7.3. Results and discussion

7.3.1. Catalysts characterization

The crystalline nature of the synthesized samples is represented in XRD profile in Figure 80. The XRD peaks of $LaMnO_3$ and $LaMnO_3$-SA shows some clear differences that could be due to the change in the crystalline structure as reported before [359]. $LaMnO_3$ synthesized without salt shows the peaks of rhombohedral phase in reference with JCPDS No. 72-0841 and no other impure phase were detected. While in presence of inert salt, there exists a phase transformation of crystal structure from rhombohedral to cubic phase as evident from JCPDS No. 75-0440. The triggering force of this phase transformation is attributed to the reduction in the reaction temperature after the addition of inert salt in the reactive system [258]. Wang *et al* studied the formation of cubic crystal phase {100} through the influence in controlling the growth of [100] to [111] ratio, in which the planes with faster growth rate disappear quickly[360]. In presence of salt, it is assumed that the O^{2-} and La^{3+} ions are bounded with K^{+} and Cl^{-} ions that block the growth of the

corresponding planes of [100]. The growth block of [100] reduced the ratio of [100] to [111] slowing down the growth of [100] to favor cubic crystal structure.

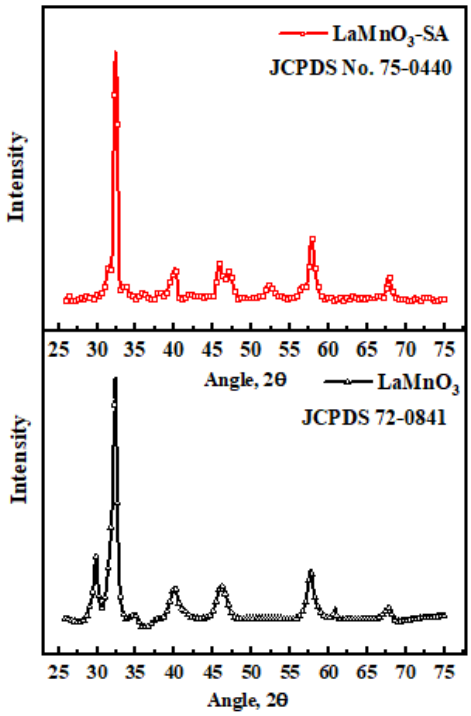

Figure 80. XRD profile of $LaMnO_3$ and $LaMnO_3$-SA sample

SEM image of the conventional solution combustion ($LaMnO_3$) and salt assisted $LaMnO_3$ ($LaMnO_3$-SA) in Figure 81 shows clear morphological differences. $LaMnO_3$ synthesized using normal SCS shows continuous foam like morphology where the presence of individual particles was not possible to identify due to the high level of agglomeration. While the $LaMnO_3$ synthesized using salt assisted solution combustion synthesis ($LaMnO_3$-SA) in Figure 81.b shows the presence of individual particles with clear boundaries throughout the inspected area. During the synthesis, when the reactive mixture

exceeds the melting temperature of the salt, the molten KCl act as a solvent and promote the mass transfer in the reactive medium. The molten KCl covers the newly formed crystallite sites and thus reduces its free enthalpy that in turn reduces the agglomeration of particles. The salt ions act as a matrix that inhibit the formation of three-dimensional agglomerates and reduces the particle growth rate promoting particles dispersion. The EDX analysis shows the existence of La and Mn in 1:1 ratio for both cases, whereas the carbon content is comparatively higher in conventional SCS that is reduced to half in the salt assisted combustion. The presence of nitrogen is likely to come from the un-combusted nitrate in $LaMnO_3$, which is completely absent in $LaMnO_3$-SA. This indicates that introduced salt not only reduces the level of agglomeration, also promotes the complete combustion of the redox mixture. A proper cleaning and filtration of the synthesized samples allows the complete removal of the salts from the catalyst surface that is indicated by a very low percentage of atomic concentration of K and Cl.

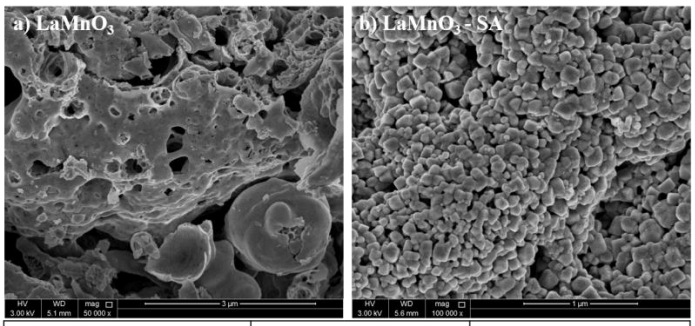

Element	$LaMnO_3$ Atomic conc (%)	$LaMnO_3$- SA Atomic conc (%)
Lanthanum (La)	17.44	18.76
Manganese (Mn)	16.79	18.02
Oxygen (O)	44.44	54.67
Carbon (C)	16.97	8.36
Nitrogen (N)	4.36	0
Potassium (K)	-	0.08
Chlorine (Cl)	-	0.11

Figure 81. SEM micrograph of a) combustion synthesized (CS) $LaMnO_3$ and b) salt assisted CS $LaMnO_3$ ($LaMnO_3$-SA) and their corresponding EDX elemental composition.

The TEM images in Figure 82 display the particle size, shape and agglomeration of $LaMnO_3$ in the two samples. The particle synthesized in absence of KCl in Figure 82.a show the three-dimensional structure with high level of agglomeration where individual particle analysis is not possible. The introduction of inert salts in the redox mixture breaks the three-dimensional network leading to an improvement in the dispersion that limits the growth of abnormal grain size. The particles prepared using salt assisted SCS in Figure 82.b show less agglomerated spherical nanoparticles in the size range of 10-20 nm. Selected-area electron diffraction (SAED) in inset Figure 82.b(i) shows spot pattern that confirm the existence of single crystalline $LaMnO_3$. The double lattice fringes in inset Figure 82.b(ii) contribute due to Mn^{3+} and Mn^{4+} species as previously reported [361].

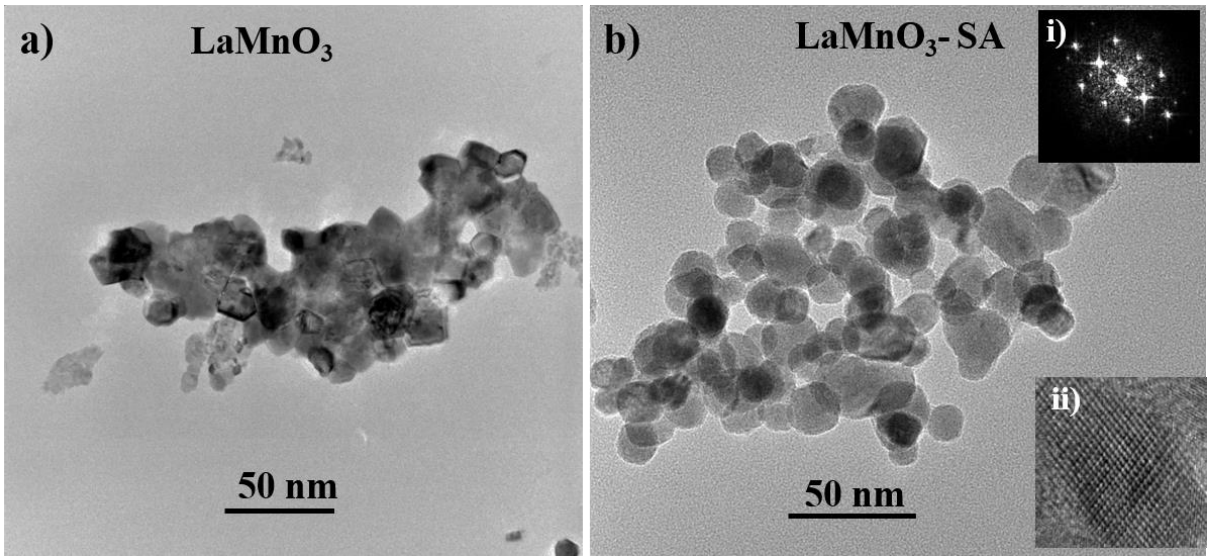

Figure 82. TEM image of $LaMnO_3$ synthesized using a) simple solution combustion synthesis b) salt-assisted solution combustion synthesis ($LaMnO_3$-SA). Inset of (b) shows i) selected area electron diffusion (SAED) pattern and ii) HRTEM image of $LaMnO_3$-SA particle.

The elemental distribution in the catalyst can be verified using HRTEM-STEM analysis coupled with EDS elemental mapping as in Figure 83**.** The elemental mapping Figure 83.b-f corresponding to the area on Figure 83.a. La, Mn and O was incorporated homogeneously throughout the entire structure. While overlapping the La and Mn (Figure 83.e), the entire color changes from red/yellow to orange color. In addition, with the overlapping of oxygen (Figure 83.f) the color changed again indicating a perfect matching of La, Mn and O over the entire selected area of $LaMnO_3$-SA.

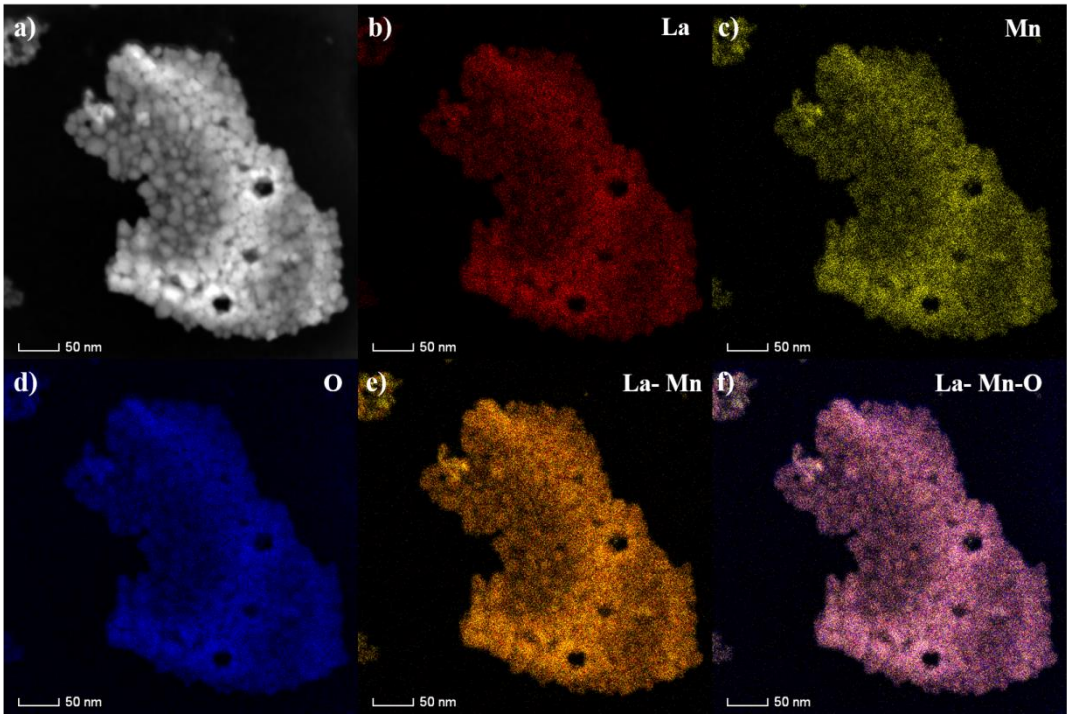

Figure 83. a) HAADF- STEM phase mapping of $LaMnO_3$-SA particles. EDS elemental mapping of b) La c) Mn d) O e) La-Mn and f) La-Mn-O performed on the area of the selected region of STEM image.

The XPS profile of the synthesized samples is shown in Figure 84**.** The deconvoluted La-3d spectrum in Figure 84.a shows four distinct peaks with two peaks at 834.3±0.5 eV and 851.1±0.4 eV with spin orbitals splitting of 16.8 eV corresponding to $3d_{5/2}$ and $3d_{3/2}$ respectively. The other two peaks are the shake up lines pointed at higher binding energies (838.1 eV and 855.188 eV) that are related to La^{3+} ions in the oxide form [362,363]. The XPS deconvolution spectrum of manganese in $LaMnO_3$ shows two asymmetric doublets of Mn $2p_{3/2}$ and Mn $2p_{1/2}$ centered at 641.7±0.5 eV and 633.58 eV with spin orbital splitting 11.6 eV. The peak fitting of Mn $2p_{3/2}$ shows the presence of two peaks at 641.9

±0.4 eV and 645 ± 0.2 eV that indicate the existence of Mn in mixed valence state. From literatures, it was found that the peak at 641.9 eV is due to Mn^{3+} and the peak at 645.15 eV is attributed to Mn^{4+} state [364,365]. The ratio of Mn^{4+} / Mn^{3+} is higher for $LaMnO_3$-SA than that of $LaMnO_3$ perovskites. This means a better surface enrichment of Mn^{4+} species in $LaMnO_3$-SA than the La-Mn perovskite synthesized using conventional SCS method. Larger amount of Mn^{4+} ions are related to a greater accessibility of oxygen that can act as a promising candidate for oxygen electrocatalysis [366].

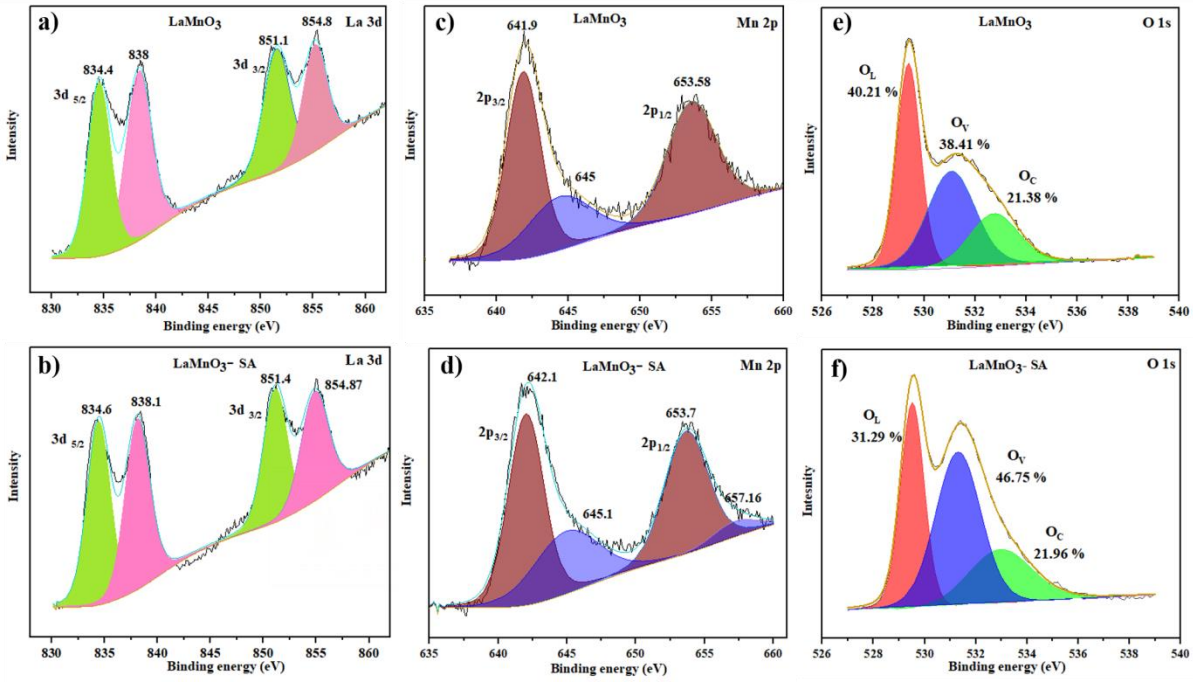

Figure 84. XPS spectrum for (a-b) La 3d (c-d) Mn 2p (e-f) O 1s of $LaMnO_3$ and $LaMnO_3$-SA respectively.

The deconvoluted O 1s spectrum (Figure 84.e-f) shows three characteristic peaks O_L, O_V and O_c centered at 529.6±0.7 eV, 531.6±0.2 eV and 532.5±0.3 eV respectively. The peak

O_L corresponds to lattice oxygen species and is related to La-O and Mn-O bonding on the perovskite surface. O_v represents the surface oxygen species such as O^- and OH^- groups attributed to surface defect sites or hydroxyl group. The peak corresponds to O_c represents the existence of moisture/oxygen from the surrounded air (molecular H_2O). The relative percentage of surface oxygen can be calculated based on $O_v/(O_v+O_c)$, which gives a higher value for $LaMnO_3$-SA than $LaMnO_3$. These results are consistent with the Mn^{4+} / Mn^{3+} ratio described earlier, where $LaMnO_3$-SA contain more surface oxygen than $LaMnO_3$.The presence of more oxygen defects in perovskites based on salt assisted combustion synthesis have highest energy state that provide more active sites for ORR and OER performance [367,368].

The textural properties such as specific surface area, pore volume and pore size of the synthesized catalyst were measured using nitrogen adsorption/desorption experiments. $LaMnO_3$-SA shows higher BET surface area of 12.3 m^2/g, where $LaMnO_3$ shows 6.089 m^2/g that is almost half of the area of $LaMnO_3$-SA. This increment in surface area correlates well with the reduction in the level of agglomeration using salt assisted synthesis. The pore volume and average pore size of $LaMnO_3$ was measured to be 0.003 cm^3/g and 50.6 nm and that for $LaMnO_3$-SA is 0.055 cm^3/g and 24.5 nm respectively. Moreover, these properties show an improvement in the surface characterization of the salt assisted synthesis that could help in enhancing the electrocatalytic activity of the perovskites. The increase in pore size and pore volume makes more available sites for the absorption of the oxygen species for reduction reaction.

7.3.2. Electrochemical analysis and characterization

The bifunctional electrocatalytic performance of $LaMnO_3$ and $LaMnO_3$-SA as oxygen electrode was tested using cyclic voltammogram (CV) and linear sweep voltammetry (LSV) in O_2 saturated 1M KOH electrolyte. Cyclic voltammogram (CV) of the catalyst at a scan rate of 50 mVs^{-1} saturated with N_2 and O_2 electrolyte is shown in Figure 85.a. Both the catalyst shows a well-defined prominent cathodic peak in O_2 purged electrolyte which belongs to oxygen reduction reaction (ORR) that was not detected in N_2 saturated solution (blue dotted line). The peak cathodic potential of $LaMnO_3$ is at -0.24 V and for $LaMnO_3$-SA the peak potential shifts to positive direction at -0.2 V under same condition. This positive shift of $LaMnO_3$-SA indicates a better interaction of perovskites synthesized after salt assisted mode and the adsorbed oxygenated species that are involved in the electrocatalytic reactions. ORR performance of the catalyst was further investigated using linear sweep voltammetry (LSV) in O_2 saturated electrolyte at a scan rate of 5 mVs^{-1} in the potential window of -0.8 V to +0.8 V at 1600 rpm as shown in Figure 85.b. $LaMnO_3$-SA shows higher limiting current density when compared to $LaMnO_3$. Moreover, the control in particle morphology and agglomeration improves the electrocatalytic performance of $LaMnO_3$ with a positive shift in half wave potential and onset potential as shown in inset figure. The half wave potential shifts a 75 mV towards right and 20 mV shift in the onset potential for $LaMnO_3$-SA when compared to $LaMnO_3$. The OER in the potential range of 0.2 V to 0.8 V shows an improved current density and faster OER response for $LaMnO_3$-SA compared to $LaMnO_3$. The faster anodic current response indicates the shorter potential difference between E_{onset} and potential at which anodic current starts to increase and that is indicated as ΔE. The prominent reversible oxygen electrode shows smaller ΔE value and higher bifunctionality of the catalyst. At 0.6 V, the

current density of $LaMnO_3$ is 2.06 $mAcm^{-1}$ and for $LaMnO_3$-SA the value reach to 7.1 $mAcm^{-1}$ at same potential that is more than thrice the value of $LaMnO_3$. The other two electrochemical parameter that need to be considered are the kinetic current density and the mass activity that govern the superior quality of the oxygen electrode as shown in Figure 85.c. The kinetic current density (J_k) calculated at -0.25 V based on Equ (2.8) is found to be ~ 3 times higher and the mass activity at the same potential is almost twice in $LaMnO_3$-SA electrode compared to $LaMnO_3$. The polarization curve of $LaMnO_3$-SA at different rotor speed (1600 rpm to 400 rpm) in Figure 85.d shows an increase in current density with increase in rotor speed and could be due to the rapid transport of dissolved oxygen between the electrolyte- catalyst interfaces. The inset of Figure 85.d shows KL plot with linear feature indicating the first order kinetics of oxygen reduction reaction. The number of electrons exchanged per oxygen molecule in the ORR is calculated from the KL equation (8) and found to be 3.98 that confirms a direct four-electron transfer mechanism where the oxygen is directly converted to water molecule on $LaMnO_3$-SA electrode

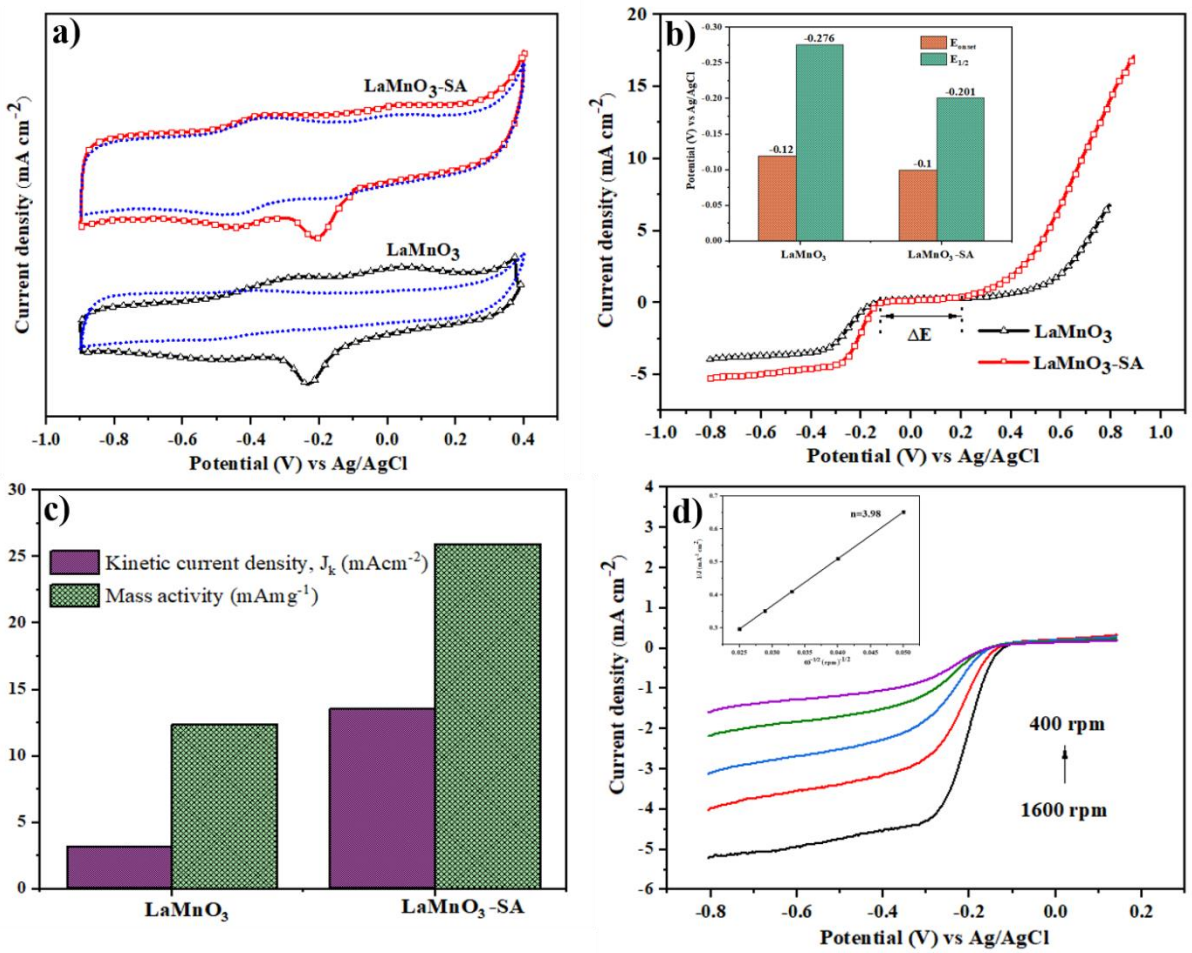

Figure 85. a) Cyclic voltammogram of $LaMnO_3$ and $LaMnO_3$-SA electrodes in O_2 and N_2 saturated 1 M KOH electrolyte at a scan rate of 50 mVs^{-1} b) Linear sweep voltammogram (LSV) of electrodes at a scan rate of 5 mVs^{-1} in the potential window of -0.8 V to +0.8 V at 1600 rpm that shows the ORR and OER performance. Inset. Bar plot comparison of half wave potential ($E_{1/2}$) and onset potential (E_{onset}) of both catalyst c) comparative analysis of kinetic current density and mass activity of the perovskite samples at 0.25 V. d) LSV of $LaMnO_3$-SA at different rotator speed (1600 rpm to 400 rpm). Inset. K-L plot of $LaMnO_3$-SA for ORR current densities at different rotation and the overall electron transfer in the reaction.

In a fuel cell application, the direct four electron transfer is preferred to the two-step electron transfer process. The ORR pathway (direct four electrons or two electron transfer) can be further evaluated using a rotating ring disc electrode (RRDE) measurement by monitoring the H_2O^- yield and number of electron transfer during ORR. The polarization curve in Figure 86.a exhibits higher disc current (I_D) and lower ring current (I_R) for $LaMnO_3$-SA when compared to $LaMnO_3$. The number of electron transfer and peroxide species formation are calculated and plotted in Figure 86.b to indicate that the formation of water molecule from oxygen reduction is through a four-electron transfer, in well agreement with the KL plot discussed earlier. Notably, the generation rate of peroxide species is lower in $LaMnO_3$-SA which indicates the faster ORR reaction rate through direct electron transfer that would speed up the overall reaction.

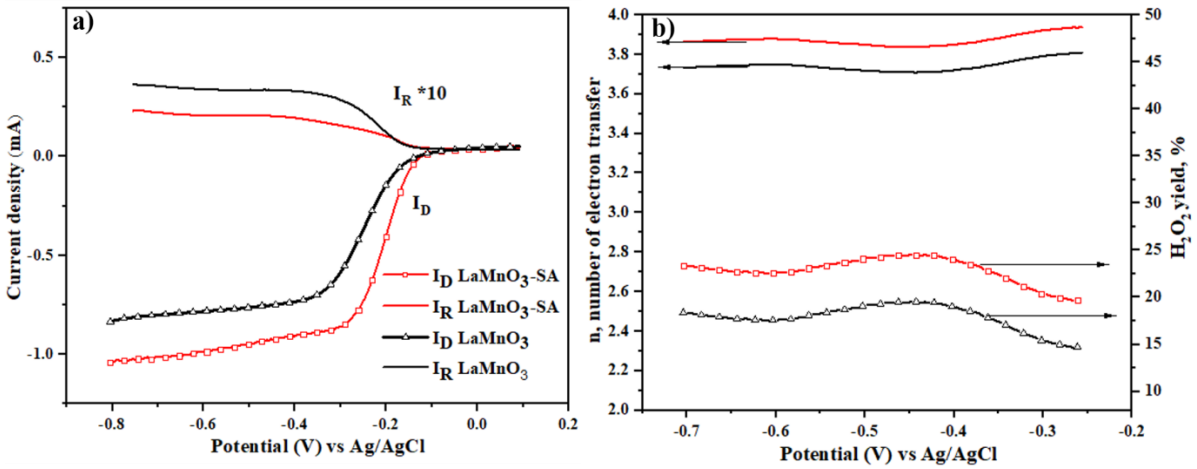

Figure 86. a) RRDE disc current (ID) and ring current (IR-multiplied by 10) of $LaMnO_3$ and $LaMnO_3$-SA at 1600 rpm in O_2 saturated 1 M electrolyte b) the calculated overall

electron transfer and hydrogen peroxide yield (%).

The kinetics and mechanism of ORR and OER reactions can be further investigated using Tafel plots obtained from the LSV curve and their corresponding kinetically controlled region. The Tafel plot can be obtained by plotting log (J_K) on the x-axis and potential over the y-axis. The Tafel plot obtained for $LaMnO_3$ and $LaMnO_3$-SA in Figure 87**.**a show two clear linear regions: one at lower potential and other at higher potential that are corresponding to Temkin and Langmuir isotherms respectively. It is evident that the excellent ORR activity is obtained with low slope at higher potential and higher value of slope at lower potential. While considering this perspective, $LaMnO_3$-SA with slope values of 51/245 $mVdec^{-1}$ shows faster ORR kinetics than that of $LaMnO_3$ with values 53/217 $mVdec^{-1}$. Similarly, the current response of OER is plotted in Figure 87.b displaying the higher slope for $LaMnO_3$-SA (97 $mVdec^{-1}$) compared to $LaMnO_3$ (114 $mVdec^{-1}$). These results suggest a better kinetics for salt assisted perovskite structure for ORR and OER electrochemical reactions.

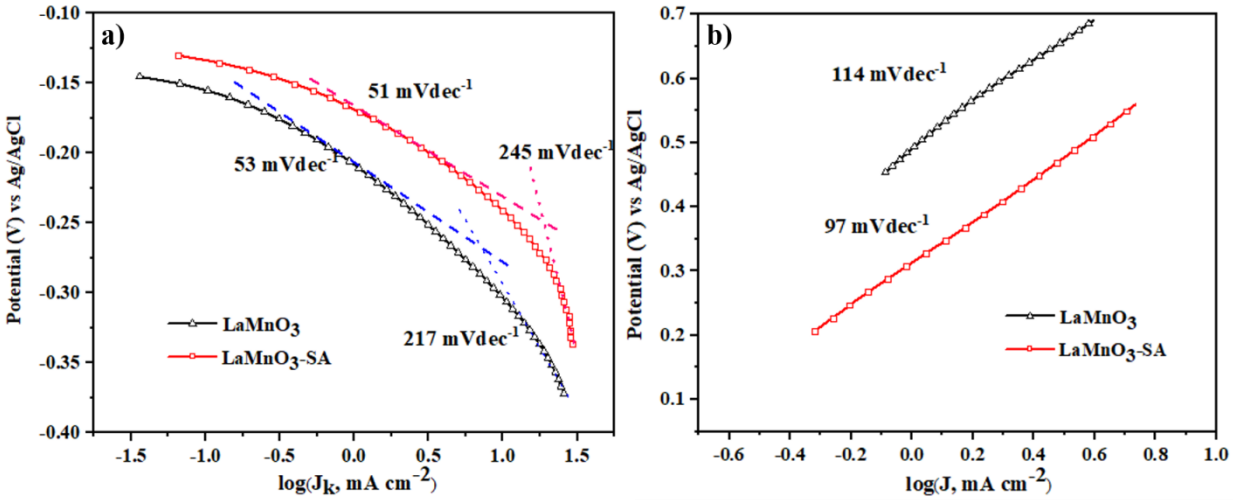

Figure 87. Tafel plot for a) ORR and b) OER measured from LSV that shows the activity comparison of $LaMnO_3$ and $LaMnO_3$-SA in 1 M KOH saturated with O_2 with a rotor speed of 1600 rpm and scan rate 5 mVs^{-1}.

Based on the above results and discussion, salt assisted mode of synthesis renders improvement in the bifunctionality of oxygen electrocatalyst through modifications in physical, chemical and electronic structure of the perovskites. The material characterizations show notable changes in the phase transformation from rhombohedral structure to cubic phase, reduction in the agglomeration and provide well dispersion of the particles. Zhou and Jaka, studied the phase transformation of $LaNiO_3$ perovskite during heat treatment and its influence into ORR/OER activity in alkaline medium [369]. This enhancement in the activity could originate from two factors; bond length and crystal structure. The dramatic improvement in the activity of cubic structure towards ORR and OER can be correlated to Fermi surface in the perovskite. Cubic structure has large fermi surface with hole inside and for orthorhombic large fermi surface combine into small

fermi surfaces of electrons and holes. The structure with larger number of holes exhibits greater conductivity that reduced the internal structural resistance [370]. In liquid phase heterogeneous catalysis, the electron transfer from the adsorbent bonding level to the conduction band of the solid material (catalyst) is considered as the rate determining factor. Owing to the higher electronic conductivity in cubic perovskite, there is an ease in the charge transfer that in turn enhances performance for ORR and OER in alkaline medium. The ORR/OER reaction likely to take place on the B site transition metal ions of the perovskites [185,371]. Hence the bond length of metal-oxygen bond is highly significant. In terms of bond length, the activity can be correlated as; cubic structure has comparatively higher Mn-O bond length when compared to rhombohedral one. If the bond length is too small, oxygen will strongly be bonded and the rate determining step is the removal of surface oxide and its intermediates. Moreover, the structure with very large bond length, the reaction is limited with the transfer of charge carriers (electron and proton) to the adsorbed O_2 [142]. The cubic structures with moderate Mn-O bond length that mediates the adsorption and removal of oxygenated species and its intermediates. This signifies the bifunctional activity of $LaMnO_3$ synthesized using salt assisted solution combustion synthesis.

Furthermore, on basis of the oxidation state of the transition metal, the advancement in the catalytic activity can be explained. The XPS profile of the synthesized samples shows the presence of high ratio of Mn^{4+} / Mn^{3+} for $LaMnO_3$-SA than that of $LaMnO_3$ perovskites. The adsorption and desorption of oxygen molecule governs the kinetics of ORR. If more oxygen vacancies are available, more active sites for oxygen adsorption is possible. The existence of Mn with unstable higher oxidation state (+4) on the surface

promote the filling of the oxygen vacancies with the dissolved oxygen from electrolyte. The formation of oxygen vacancies modifies the metal- oxygen bonding. During ORR on metal-oxide surface in presence of alkaline medium, there exist mainly four reactions including hydrogen replacement, oxide and peroxide formation and regeneration of hydroxide. The oxygen thus filled over the oxygen vacancies are found to be loosely bounded when compared to the lattice oxygen and resulted with easy desorption after the reaction [366]. So, an increase in the oxygen vacancies and the presence of higher Mn^{4+} / Mn^{3+} ratio on the structures of $LaMnO_3$-SA are more prominent, and facilitate the adsorption of oxygenated species, rendering more active sites for the electrochemical performance. An increase in the oxygen vacancies on the structures of $LaMnO_3$-SA are more prominent, and facilitate the adsorption of oxygenated species, rendering more active sites for the electrochemical performance.

7.4. Conclusion

Well-dispersed $LaMnO_3$ nanoparticles were successfully synthesized using a salt-assisted solution combustion synthesis ($LaMnO_3$-SA) that shows a cubic $LaMnO_3$ structure as compared to rhombohedral crystal structure obtained using conventional SCS. An improvement in surface area, pore volume and pore size are seen after the incorporation of the salt in the solution combustion synthesis. TEM results indicate that the presence of salt during combustion breaks down the three-dimensional crystalline structure and improves the dispersion of the particles during synthesis. In addition, an improvement in the oxygen vacancies is also observed on the surface that in turn facilitates the electronic conductivity to enhance the catalytic activity for ORR and OER. Based on the CV and LSV analysis, it is clear that the electrochemical properties of $LaMnO_3$-SA perovskite

exhibit outstanding performance owing to the aforementioned improvement in the structure.

CHAPTER 8: CONCLUSION AND FUTURE WORK

In this study, we focused on the synthesis of highly active, durable, cost effective bifunctional electrocatalyst for ORR/OER in alkaline medium using solution combustion synthesis based techniques. First, we studied the effect of different fuel ratio (φ = 0.5, 1, and 1.75) in SCS on the structural and physio-chemical properties of the synthesized cobalt nanoparticle and evaluated their electrocatalytic performance for ORR/OER. We found that increasing the fuel ratio (φ value) from 0.5 to 1.75 increases the crystallite size and lowers the surface area. The fuel rich condition provides a reducing atmosphere limiting further oxidation of synthesized nanoparticles but produces more carbon residue on the catalyst surface compared to fuel lean conditions. The LSV results obtained between a potential of −1.2 V and 0.75 V shows all the three cobalt oxide catalysts to have bifunctional properties of being active for both ORR and OER, with Co synthesized at lower fuel ratio (φ = 0.5) displaying the highest current density. The onset potential for Co (φ = 0.5) is more positive than Co (φ = 1) and Co (φ = 1.75). The kinetic current density for Co (φ = 0.5) is found to be highest and decreases with an increase in fuel ratio. The OER current starts at same potential for all the catalysts with a maximum density for Co (φ = 0.5) and gradually decreases with an increase in fuel ratio. The fuel lean condition (φ = 0.5) is associated with the synthesis of smaller nanoparticles with higher surface area, possibly being the dominant factor in improving the activity for ORR and OER reaction.

Later we synthesized bimetallic Ag-M (M=Cu and Co) using three different mode of combustion synthesis and studied the influence of each mode on the electrochemical

property. In this section we introduced, second wave solution combustion (SWSC) to synthesize bimetallic nanoparticle by changing the sequence in which each metal precursor is added. A better degree of mixing and alloying through the SWCS was evident. Based on the discussions, it is speculated that the sequence of combustion has a great role in controlling the surface/bulk elemental composition and structural characteristics of the synthesized nanopowder. SWCS reduces the amount of carbon content, as compared to the single-stage combustion; in addition, it is followed by a rearrangement of atoms. The nanoparticles synthesized using this modified technique can be used as bifunctional catalysts, owing to the enhanced surface phase distribution and structural properties. However, the catalysts were not durable as dealloying of Ag was noticed after certain stability analysis. Therefore, it is identified that in order to have long-term stability, it is essential to have a catalyst with uniform composition that does not undergo any dealloying or elemental rearrangement under the influence of sustained electrocatalytic operations. A quick literature survey indicates that special mixed metal oxides, such as perovskites, though difficult to synthesize are known for their stability and tunable properties, providing us a suitable system to investigate further for ORR and OER.

Consequently, lanthanum perovskites with $LaMO_3$ structure were synthesized with different fuel ratio and various transition metals (M= Cr, Mn, Fe, Co, Ni) on the B sites. The synthesis conditions were found to have a significant effect on the nature of the nanoparticles and can be tuned to synthesize amorphous or crystalline mixed metal oxides. The perovskites showed exceptional performance for ORR and OER in alkaline medium, where $LaMnO_3$ was found to be the most active for ORR, and $LaCoO_3$ for OER.

The ORR kinetics was improved in the order of $LaCrO_3 < LaFeO_3 < LaNiO_3 < LaCoO_3 < LaMnO_3$. The onset potential of $LaMnO_3$ is − 0.12 V, and for other La-transition metals is nearly − 0.2 V. A detailed analysis based on Koutechy-Levich plots obtained from rotating disk electrode shows a higher number of electron transfer for $LaMnO_3$ catalyst and the least for $LaCrO_3$, whereas the stability results indicate the $LaCoO_3$ to be more stable as compared to $LaMnO_3$. The TEM elemental phase analysis of $LaMnO_3$ after the stability test indicates the existence of single phase containing $LaMnO_3$ composition throughout the structure without any phase segregation, which demonstrates the development of highly durable perovskite structures using solution combustion synthesis as efficient bi-functional catalysts in alkaline medium.

At last, we followed a salt assisted SCS route for synthesizing $LaMnO_3$ perovskites ($LaMnO_3$-SA) with lower level of agglomeration and investigated its application as oxygen electrocatalyst. Through the effective incorporation of a KCl salt in the redox combustion mixture, the surface area of the particle doubled along with an improved pore size and pore volume distribution. The surface analysis by x-ray photoelectron spectroscopy indicates the formation of more surface oxygen defects with the introduction of the inert salt that helps the absorption of oxygenated species during electrochemical process. Remarkably, $LaMnO_3$-SA shows superior characteristics in terms of limiting current density, onset potential and half wave potential presentation enhanced bifunctionality towards ORR and OER. The mass activity of $LaMnO_3$-SA is almost double and kinetic current density shows thrice the value at -0.25 V in comparison to the traditional SCS $LaMnO_3$. This work demonstrates that active sites accessible for

oxygen electrocatalysis in SCS can be enhanced through the introduction of an inert salt during the synthesis. The bifunctional ORR/OER electrochemical performance with high activity and durability of the perovskites make them ideal candidates in the area of metal air batteries and fuel cells.

Major contribution and novelties of this study are as follows:

The comparison of the metal alloy for example Ag-M (M= Cu, Co) and metal oxide structure (ABO3) in terms of durability and phase dealloying in ORR/OER electrochemical reaction is reported for the first time.

The effect of synthesis sequence in solution combustion synthesis on the surface composition and final structure of the nano-compounds, and their impact on electrocatalytic ORR/OER performance have been investigated for first time in this work. This study significantly helps in the design of improved electrocatalysts for ORR and OER and explains the influence of synthesis parameters on the bifunctional electrochemical behavior.

The structural changes associated with the salt assisted combustion synthesis was studied using various characterization tools such as XRD, SEM, HR-TEM, EXD and XPS, which was helpful in understanding the structural changes and identifying active sites involved in ORR/OER catalysis.

In the light of the development so far, the following points are suggested for further enhancing the ORR/OER performance:

1. To incorporate graphene or any other highly conductive material with the synthesized catalysts to enhance the bifunctional performance of the catalyst.

2. A DFT calculation to understand the surface energy and formation of lattice oxygen vacancies on the synthesized catalysts would provide valuable information that can be used to further enhance the catalysts surface by fine-tuning the synthesis parameters to expose more active sites on the surface.
3. More detailed understanding of SWCS is required to identify the pathway of surface alloying process.
4. A scale-up and economic evaluation can be performed to understand the feasibility of commercial applications.

PUBLICATIONS

- Ashok, A., Kumar, A., Bhosale, R. R., Almomani, F., Saad, M. A. H. S., Suslov, S., & Tarlochan, F. (2019). Influence of fuel ratio on the performance of combustion synthesized bifunctional cobalt oxide catalysts for fuel cell application. *International Journal of Hydrogen Energy*, 44(1), 436-445.
- Ashok, A., Kumar, A., Matin, M. A., & Tarlochan, F. (2018). Synthesis of Highly Efficient Bifunctional Ag/Co_3O_4 Catalyst for Oxygen Reduction and Oxygen Evolution Reactions in Alkaline Medium. *ACS Omega*, 3(7), 7745-7756.
- Ashok, A., Kumar, A., & Tarlochan, F. (2018). Surface Alloying in Silver-Cobalt through a Second Wave Solution Combustion Synthesis Technique. *Nanomaterials*, 8(8), 604.
- Ashok, A., Kumar, A., & Tarlochan, F. "Probing the effect of combustion-

controlled surface alloying in silver and copper towards ORR and OER in alkaline medium" *Journal of Electroanalytical Chemistry* –Accepted

- Ashok, A., Kumar, A., Bhosale, R. R., Tarlochan, F. (2018). Combustion synthesis of bifunctional $LaMO_3$ (M= Cr, Mn, Fe, Co, Ni) perovskites for oxygen reduction and oxygen evolution reaction in alkaline media. *Journal of Electroanalytical Chemistry*, 809, 22-30.
- Ashok, A., Kumar, A., & Tarlochan, F. Improvement on the electrochemical performance of LaMnO3 as oxygen electrocatalyst through salt assisted solution combustion synthesis- *International Journal of Hydrogen Energy* –Under Review

REFERENCES

[1] A. Haines, A.J. McMichael, K.R. Smith, I. Roberts, J. Woodcock, A. Markandya, B.G. Armstrong, D. Campbell-Lendrum, A.D. Dangour, M. Davies, Public health benefits of strategies to reduce greenhouse-gas emissions: overview and implications for policy makers, The Lancet. 374 (2009) 2104-2114.

[2] M.I. Hoffert, K. Caldeira, G. Benford, D.R. Criswell, C. Green, H. Herzog, A.K. Jain, H.S. Kheshgi, K.S. Lackner, J.S. Lewis, H.D. Lightfoot, W. Manheimer, J.C. Mankins, M.E. Mauel, L.J. Perkins, M.E. Schlesinger, T. Volk, T.M. Wigley, Advanced technology paths to global climate stability: energy for a greenhouse planet, Science. 298 (2002) 981-987.

[3] J.G. Olivier, J.A. Peters, G. Janssens-Maenhout, Trends in global CO_2 emissions 2012 report, (2012).

[4] A.E. Outlook, with Projections to 2050, Energy Information Administration (EIA). (2017).

[5] D. Larcher, J. Tarascon, Towards greener and more sustainable batteries for electrical energy storage, Nature chemistry. 7 (2015) 19.

[6] F. Yilmaz, M.T. Balta, R. Selbaş, A review of solar based hydrogen production methods, Renewable and Sustainable Energy Reviews. 56 (2016) 171-178.

[7] L. Carrette, K. Friedrich, U. Stimming, Fuel cells–fundamentals and applications, Fuel cells. 1 (2001) 5-39.

[8] J. Salminen, D. Steingart, T. Kallio, Fuel cells and batteries, in: Anonymous Future Energy, Elsevier, 2008, pp. 259-276.

[9] C.K. Dyer, Fuel cells for portable applications, J. Power Sources. 106 (2002) 31-34.

[10] S. Park, Y. Shao, J. Liu, Y. Wang, Oxygen electrocatalysts for water electrolyzers and reversible fuel cells: status and perspective, Energy & Environmental Science. 5 (2012) 9331-9344.

[11] Y. Gorlin, T.F. Jaramillo, A bifunctional nonprecious metal catalyst for oxygen reduction and water oxidation, J. Am. Chem. Soc. 132 (2010) 13612-13614.

[12] N. Sasikala, K. Ramya, K. Dhathathreyan, Bifunctional electrocatalyst for oxygen/air electrodes, Energy Conversion and Management. 77 (2014) 545-549.

[13] S.A. Park, E.K. Lee, H. Song, Y.T. Kim, Bifunctional enhancement of oxygen reduction reaction activity on Ag catalysts due to water activation on $LaMnO_3$ supports in alkaline media, Sci. Rep. 5 (2015) 13552.

[14] L. Jörissen, Bifunctional oxygen/air electrodes, J. Power Sources. 155 (2006) 23-32.

[15] V. Nikolova, P. Iliev, K. Petrov, T. Vitanov, E. Zhecheva, R. Stoyanova, I. Valov, D. Stoychev, Electrocatalysts for bifunctional oxygen/air electrodes, J. Power Sources. 185 (2008) 727-733.

[16] S.M. Haile, Fuel cell materials and components, Acta Materialia. 51 (2003) 5981-6000.

[17] J. Lee, B. Jeong, J.D. Ocon, Oxygen electrocatalysis in chemical energy conversion and storage technologies, Current Applied Physics. 13 (2013) 309-321.

[18] R.R. Adzic, J. Zhang, K. Sasaki, M.B. Vukmirovic, M. Shao, J. Wang, A.U. Nilekar, M. Mavrikakis, J. Valerio, F. Uribe, Platinum monolayer fuel cell electrocatalysts, Topics in Catalysis. 46 (2007) 249-262.

[19] Y. Lu, Z. Xu, H.A. Gasteiger, S. Chen, K. Hamad-Schifferli, Y. Shao-Horn, Platinum− gold nanoparticles: a highly active bifunctional electrocatalyst for rechargeable lithium− air batteries, J. Am. Chem. Soc. 132 (2010) 12170-12171.

[20] V. Pfeifer, T.E. Jones, S. Wrabetz, C. Massué, J.J.V. Vélez, R. Arrigo, M. Scherzer, S. Piccinin, M. Hävecker, A. Knop-Gericke, Reactive oxygen species in iridium-based OER catalysts, Chemical science. 7 (2016) 6791-6795.

[21] T. Reier, M. Oezaslan, P. Strasser, Electrocatalytic oxygen evolution reaction (OER) on Ru, Ir, and Pt catalysts: a comparative study of nanoparticles and bulk materials, ACS Catalysis. 2 (2012) 1765-1772.

[22] H.G. Sanchez Casalongue, M.L. Ng, S. Kaya, D. Friebel, H. Ogasawara, A. Nilsson, In situ observation of surface species on iridium oxide nanoparticles during the oxygen evolution reaction, Angewandte Chemie International Edition. 53 (2014) 7169-7172.

[23] J. Zhang, K. Sasaki, E. Sutter, R.R. Adzic, Stabilization of platinum oxygen-reduction electrocatalysts using gold clusters, Science. 315 (2007) 220-222.

[24] C. Sealy, The problem with platinum, Materials Today. 11 (2008) 65-68.

[25] E. Antolini, Iridium as catalyst and cocatalyst for oxygen evolution/reduction in acidic polymer electrolyte membrane electrolyzers and fuel cells, ACS Catalysis. 4 (2014) 1426-1440.

[26] Y. Gorlin, T.F. Jaramillo, A bifunctional nonprecious metal catalyst for oxygen reduction and water oxidation, J. Am. Chem. Soc. 132 (2010) 13612-13614.

[27] Y. Bing, H. Liu, L. Zhang, D. Ghosh, J. Zhang, Nanostructured Pt-alloy electrocatalysts for PEM fuel cell oxygen reduction reaction, Chem. Soc. Rev. 39 (2010) 2184-2202.

[28] M. Jahan, Z. Liu, K.P. Loh, A Graphene oxide and copper-centered metal organic framework composite as a tri-functional catalyst for HER, OER, and ORR, Advanced Functional Materials. 23 (2013) 5363-5372.

[29] T. Toda, H. Igarashi, H. Uchida, M. Watanabe, Enhancement of the electroreduction of oxygen on Pt alloys with Fe, Ni, and Co, J. Electrochem. Soc. 146 (1999) 3750-3756.

[30] J. Suntivich, K.J. May, H.A. Gasteiger, J.B. Goodenough, Y. Shao-Horn, A perovskite oxide optimized for oxygen evolution catalysis from molecular orbital principles, Science. 334 (2011) 1383-1385.

[31] M. Pena, J. Fierro, Chemical structures and performance of perovskite oxides, Chem. Rev. 101 (2001) 1981-2018.

[32] J. Suntivich, H.A. Gasteiger, N. Yabuuchi, H. Nakanishi, J.B. Goodenough, Y. Shao-Horn, Design principles for oxygen-reduction activity on perovskite oxide catalysts for

fuel cells and metal–air batteries, Nature chemistry. 3 (2011) 546-550.

[33] W.S. Kim, G. Anoop, H.J. Lee, S.S. Lee, J.H. Kwak, H.J. Lee, J.Y. Jo, Facile synthesis of perovskite $LaMnO_{3-\delta}$ nanoparticles for the oxygen reduction reaction, Journal of Catalysis. 344 (2016) 578-582.

[34] F. Lu, J. Sui, J. Su, C. Jin, M. Shen, R. Yang, Hollow spherical $La_{0.8}Sr_{0.2}MnO_3$ perovskite oxide with enhanced catalytic activities for the oxygen reduction reaction, J. Power Sources. 271 (2014) 55-59.

[35] F.G. Baddour, L. Snowden-Swan, J.D. Super, K.M. Van Allsburg, Estimating Precommercial Heterogeneous Catalyst Price: A Simple Step-Based Method, Organic Process Research & Development. 22 (2018) 1599-1605.

[36] D.U. Lee, P. Xu, Z.P. Cano, A.G. Kashkooli, M.G. Park, Z. Chen, Recent progress and perspectives on bi-functional oxygen electrocatalysts for advanced rechargeable metal–air batteries, Journal of Materials Chemistry A. 4 (2016) 7107-7134.

[37] T. Takeguchi, T. Yamanaka, H. Takahashi, H. Watanabe, T. Kuroki, H. Nakanishi, Y. Orikasa, Y. Uchimoto, H. Takano, N. Ohguri, Layered perovskite oxide: a reversible air electrode for oxygen evolution/reduction in rechargeable metal-air batteries, J. Am. Chem. Soc. 135 (2013) 11125-11130.

[38] X. Wu, F. Chen, N. Zhang, A. Qaseem, R.L. Johnston, A silver-copper metallic glass electrocatalyst with high activity and stability comparable to Pt/C for zinc-air batteries, Journal of Materials Chemistry A. 4 (2016) 3527-3537.

[39] Y. Li, M. Gong, Y. Liang, J. Feng, J. Kim, H. Wang, G. Hong, B. Zhang, H. Dai, Advanced zinc-air batteries based on high-performance hybrid electrocatalysts, Nature communications. 4 (2013) 1805.

[40] Z. Jian, P. Liu, F. Li, P. He, X. Guo, M. Chen, H. Zhou, Core–shell-structured CNT@ RuO_2 composite as a high-performance cathode catalyst for rechargeable Li–O_2 batteries, Angewandte Chemie International Edition. 53 (2014) 442-446.

[41] C. Sun, F. Li, C. Ma, Y. Wang, Y. Ren, W. Yang, Z. Ma, J. Li, Y. Chen, Y. Kim, Graphene–Co_3O_4 nanocomposite as an efficient bifunctional catalyst for lithium–air batteries, Journal of Materials Chemistry A. 2 (2014) 7188-7196.

[42] K. Kwak, D.W. Kim, Y. Kang, J. Suk, Hierarchical Ru-and RuO_2-foams as high performance electrocatalysts for rechargeable lithium–oxygen batteries, Journal of Materials Chemistry A. 4 (2016) 16356-16367.

[43] F. Cheng, J. Chen, Metal–air batteries: from oxygen reduction electrochemistry to cathode catalysts, Chem. Soc. Rev. 41 (2012) 2172-2192.

[44] S. Mekhilef, R. Saidur, A. Safari, Comparative study of different fuel cell technologies, Renewable and Sustainable Energy Reviews. 16 (2012) 981-989.

[45] A.B. Stambouli, Fuel cells: The expectations for an environmental-friendly and sustainable source of energy, Renewable and Sustainable Energy Reviews. 15 (2011) 4507-4520.

[46] G. McLean, T. Niet, S. Prince-Richard, N. Djilali, An assessment of alkaline fuel cell technology, Int J Hydrogen Energy. 27 (2002) 507-526.

[47] Y. Gorlin, T.F. Jaramillo, A bifunctional nonprecious metal catalyst for oxygen reduction and water oxidation, J. Am. Chem. Soc. 132 (2010) 13612-13614.

[48] Y. Liang, Y. Li, H. Wang, J. Zhou, J. Wang, T. Regier, H. Dai, Co_3O_4 nanocrystals on graphene as a synergistic catalyst for oxygen reduction reaction, Nature materials. 10 (2011) 780.

[49] M. Wang, J. Huang, M. Wang, D. Zhang, W. Zhang, W. Li, J. Chen, Co_3O_4 nanorods decorated reduced graphene oxide composite for oxygen reduction reaction in alkaline electrolyte, Electrochemistry Communications. 34 (2013) 299-303.

[50] J. Wang, G. Yin, Y. Shao, S. Zhang, Z. Wang, Y. Gao, Effect of carbon black support corrosion on the durability of Pt/C catalyst, J. Power Sources. 171 (2007) 331-339.

[51] K.A. Stoerzinger, W. Lü, C. Li, T. Venkatesan, Y. Shao-Horn, Highly Active Epitaxial $La_{(1-x)}$ Sr_xMnO_3 Surfaces for the Oxygen Reduction Reaction: Role of Charge Transfer, The journal of physical chemistry letters. 6 (2015) 1435-1440.

[52] R. Cao, J. Lee, M. Liu, J. Cho, Recent progress in non-precious catalysts for metal-air batteries, Advanced Energy Materials. 2 (2012) 816-829.

[53] P. Christensen, A. Hamnett, D. Linares-Moya, Oxygen reduction and fuel oxidation in alkaline solution, Physical Chemistry Chemical Physics. 13 (2011) 5206-5214.

[54] C. Zinola, A. Arvia, G. Estiu, E. Castro, A quantum chemical approach to the influence of platinum surface structure on the oxygen electroreduction reaction, J. Phys. Chem. 98 (1994) 7566-7576.

[55] J.S. Spendelow, A. Wieckowski, Electrocatalysis of oxygen reduction and small alcohol oxidation in alkaline media, Physical Chemistry Chemical Physics. 9 (2007) 2654-2675.

[56] N. Ramaswamy, S. Mukerjee, Fundamental mechanistic understanding of electrocatalysis of oxygen reduction on Pt and non-Pt surfaces: acid versus alkaline media, Advances in Physical Chemistry. 2012 (2012).

[57] N. Ramaswamy, S. Mukerjee, Influence of inner-and outer-sphere electron transfer mechanisms during electrocatalysis of oxygen reduction in alkaline media, The Journal

of Physical Chemistry C. 115 (2011) 18015-18026.

[58] D.J. Davis, T.N. Lambert, J.A. Vigil, M.A. Rodriguez, M.T. Brumbach, E.N. Coker, S.J. Limmer, Role of Cu-ion doping in Cu-$_{\alpha}$-MnO_2 nanowire electrocatalysts for the oxygen reduction reaction, The Journal of Physical Chemistry C. 118 (2014) 17342-17350.

[59] Y. Wang, J. Li, Z. Wei, Transition-metal-oxide-based catalysts for the oxygen reduction reaction, Journal of Materials Chemistry A. 6 (2018) 8194-8209.

[60] R. Zhao, Y. Liu, C. Liu, G. Xu, Y. Chen, Y. Tang, T. Lu, Pd@ Pt core–shell tetrapods as highly active and stable electrocatalysts for the oxygen reduction reaction, Journal of Materials Chemistry A. 2 (2014) 20855-20860.

[61] S. Fu, G. Yang, Y. Zhou, H. Pan, C.M. Wai, D. Du, Y. Lin, Ultrasonic enhanced synthesis of multi-walled carbon nanotube supported Pt–Co bimetallic nanoparticles as catalysts for the oxygen reduction reaction, RSC Advances. 5 (2015) 32685-32689.

[62] K. Jayasayee, J.R. Van Veen, T.G. Manivasagam, S. Celebi, E.J. Hensen, F.A. De Bruijn, Oxygen reduction reaction (ORR) activity and durability of carbon supported PtM (Co, Ni, Cu) alloys: Influence of particle size and non-noble metals, Applied Catalysis B: Environmental. 111 (2012) 515-526.

[63] D. Sebastián, A.G. Ruíz, I. Suelves, R. Moliner, M.J. Lázaro, V. Baglio, A. Stassi, A.S. Aricò, Enhanced oxygen reduction activity and durability of Pt catalysts supported on carbon nanofibers, Applied Catalysis B: Environmental. 115 (2012) 269-275.

[64] K. Tiido, N. Alexeyeva, M. Couillard, C. Bock, B.R. MacDougall, K. Tammeveski, Graphene–TiO=$_2$ composite supported Pt electrocatalyst for oxygen reduction reaction, Electrochim. Acta. 107 (2013) 509-517.

[65] K. Eid, V. Malgras, P. He, K. Wang, A. Aldalbahi, S.M. Alshehri, Y. Yamauchi, L. Wang, One-step synthesis of trimetallic Pt–Pd–Ru nanodendrites as highly active electrocatalysts, RSC Advances. 5 (2015) 31147-31152.

[66] N. Marković, T. Schmidt, V. Stamenković, P. Ross, Oxygen reduction reaction on Pt and Pt bimetallic surfaces: a selective review, Fuel cells. 1 (2001) 105-116.

[67] A.M. Gómez-Marín, R. Rizo, J.M. Feliu, Some reflections on the understanding of the oxygen reduction reaction at Pt (111), Beilstein journal of nanotechnology. 4 (2013) 956-967.

[68] M. Macia, J. Campina, E. Herrero, J. Feliu, On the kinetics of oxygen reduction on platinum stepped surfaces in acidic media, J Electroanal Chem. 564 (2004) 141-150.

[69] K. Sasaki, H. Naohara, Y. Cai, Y.M. Choi, P. Liu, M.B. Vukmirovic, J.X. Wang, R.R. Adzic, Core-protected platinum monolayer shell high-stability electrocatalysts for fuel-cell cathodes, Angewandte Chemie International Edition. 49 (2010) 8602-8607.

[70] X. Zeng, R. Huang, G. Shao, Y. Wen, S. Sun, High-index-faceted platinum nanoparticles: insights into structural and thermal stabilities and shape evolution from atomistic simulations, Journal of Materials Chemistry A. 2 (2014) 11480-11489.

[71] G.J. Leong, M.C. Schulze, M.B. Strand, D. Maloney, S.L. Frisco, H.N. Dinh, B. Pivovar, R.M. Richards, Shape-directed platinum nanoparticle synthesis: nanoscale design of novel catalysts, Applied Organometallic Chemistry. 28 (2014) 1-17.

[72] Q. Chen, F.J. Vidal-Iglesias, J. Solla-Gullón, S. Sun, J.M. Feliu, Role of surface defect sites: from Pt model surfaces to shape-controlled nanoparticles, Chemical Science. 3 (2012) 136-147.

[73] D. Li, C. Wang, D.S. Strmcnik, D.V. Tripkovic, X. Sun, Y. Kang, M. Chi, J.D.

Snyder, D. van der Vliet, Y. Tsai, Functional links between Pt single crystal morphology and nanoparticles with different size and shape: the oxygen reduction reaction case, Energy & Environmental Science. 7 (2014) 4061-4069.

[74] M. Shao, A. Peles, K. Shoemaker, Electrocatalysis on platinum nanoparticles: particle size effect on oxygen reduction reaction activity, Nano letters. 11 (2011) 3714-3719.

[75] Y. Kawamura, R. Jinnouchi, Theoretical study of particle size effect on oxygen reduction reaction on Pt catalyst, ECS Transactions. 50 (2013) 1321-1331.

[76] E. Fabbri, S. Taylor, A. Rabis, P. Levecque, O. Conrad, R. Kötz, T.J. Schmidt, The effect of platinum nanoparticle distribution on oxygen electroreduction activity and selectivity, ChemCatChem. 6 (2014) 1410-1418.

[77] S.J. Hwang, S. Kim, J. Lee, S. Lee, J.H. Jang, P. Kim, T. Lim, Y. Sung, S.J. Yoo, Role of electronic perturbation in stability and activity of Pt-based alloy nanocatalysts for oxygen reduction, J. Am. Chem. Soc. 134 (2012) 19508-19511.

[78] V.R. Stamenkovic, B.S. Mun, M. Arenz, K.J. Mayrhofer, C.A. Lucas, G. Wang, P.N. Ross, N.M. Markovic, Trends in electrocatalysis on extended and nanoscale Pt-bimetallic alloy surfaces, Nature materials. 6 (2007) 241.

[79] B. Han, C.E. Carlton, J. Suntivich, Z. Xu, Y. Shao-Horn, Oxygen reduction activity and stability trends of bimetallic $Pt_{0.5}M_{0.5}$ nanoparticle in acid, The Journal of Physical Chemistry C. 119 (2015) 3971-3978.

[80] V.R. Stamenkovic, B.S. Mun, K.J. Mayrhofer, P.N. Ross, N.M. Markovic, Effect of surface composition on electronic structure, stability, and electrocatalytic properties of Pt-transition metal alloys: Pt-skin versus Pt-skeleton surfaces, J. Am. Chem. Soc. 128

(2006) 8813-8819.

[81] V.R. Stamenkovic, B. Fowler, B.S. Mun, G. Wang, P.N. Ross, C.A. Lucas, N.M. Markovic, Improved oxygen reduction activity on $Pt_3Ni(111)$ via increased surface site availability, Science. 315 (2007) 493-497.

[82] S. Choi, S. Xie, M. Shao, N. Lu, S. Guerrero, J.H. Odell, J. Park, J. Wang, M.J. Kim, Y. Xia, Controlling the size and composition of nanosized Pt–Ni octahedra to optimize their catalytic activities toward the oxygen reduction reaction, ChemSusChem. 7 (2014) 1476-1483.

[83] S. Kondo, M. Nakamura, N. Maki, N. Hoshi, Active sites for the oxygen reduction reaction on the low and high index planes of palladium, The Journal of Physical Chemistry C. 113 (2009) 12625-12628.

[84] M. Shao, T. Yu, J.H. Odell, M. Jin, Y. Xia, Structural dependence of oxygen reduction reaction on palladium nanocrystals, Chemical Communications. 47 (2011) 6566-6568.

[85] M. Shao, G. He, A. Peles, J.H. Odell, J. Zeng, D. Su, J. Tao, T. Yu, Y. Zhu, Y. Xia, Manipulating the oxygen reduction activity of platinum shells with shape-controlled palladium nanocrystal cores, Chemical Communications. 49 (2013) 9030-9032.

[86] H. Erikson, A. Sarapuu, K. Tammeveski, J. Solla-Gullón, J.M. Feliu, Enhanced electrocatalytic activity of cubic Pd nanoparticles towards the oxygen reduction reaction in acid media, Electrochemistry Communications. 13 (2011) 734-737.

[87] S. Choi, H. Jeong, K. Choi, J.Y. Song, J. Kim, Electrodeposition of triangular Pd rod nanostructures and their electrocatalytic and SERS activities, ACS applied materials & interfaces. 6 (2014) 3002-3007.

[88] W. Zhou, X. Yang, M.B. Vukmirovic, B.E. Koel, J. Jiao, G. Peng, M. Mavrikakis, R.R. Adzic, Improving electrocatalysts for O_2 reduction by fine-tuning the Pt− support interaction: Pt monolayer on the surfaces of a $Pd_3Fe(111)$ single-crystal alloy, J. Am. Chem. Soc. 131 (2009) 12755-12762.

[89] J. Son, S. Cho, C. Lee, Y. Lee, J.H. Shim, Spongelike nanoporous Pd and Pd/Au structures: facile synthesis and enhanced electrocatalytic activity, Langmuir. 30 (2014) 3579-3588.

[90] Y. Qi, J. Wu, H. Zhang, Y. Jiang, C. Jin, M. Fu, H. Yang, D. Yang, Facile synthesis of Rh–Pd alloy nanodendrites as highly active and durable electrocatalysts for oxygen reduction reaction, Nanoscale. 6 (2014) 7012-7018.

[91] M. Nie, P.K. Shen, Z. Wei, Nanocrystaline tungsten carbide supported Au–Pd electrocatalyst for oxygen reduction, J. Power Sources. 167 (2007) 69-73.

[92] K. Kwon, K.H. Lee, S. Jin, D.J. You, C. Pak, Ceria-promoted oxygen reduction reaction in Pd-based electrocatalysts, Electrochemistry Communications. 13 (2011) 1067-1069.

[93] J. Rossmeisl, Z. Qu, H. Zhu, G. Kroes, J.K. Nørskov, Electrolysis of water on oxide surfaces, J Electroanal Chem. 607 (2007) 83-89.

[94] K. Neyerlin, G. Bugosh, R. Forgie, Z. Liu, P. Strasser, Combinatorial study of high-surface-area binary and ternary electrocatalysts for the oxygen evolution reaction, J. Electrochem. Soc. 156 (2009) B363-B369.

[95] M. Wohlfahrt-Mehrens, J. Heitbaum, Oxygen evolution on Ru and RuO2 electrodes studied using isotope labelling and on-line mass spectrometry, Journal of electroanalytical chemistry and interfacial electrochemistry. 237 (1987) 251-260.

[96] B. Sun, P. Munroe, G. Wang, Ruthenium nanocrystals as cathode catalysts for lithium-oxygen batteries with a superior performance, Scientific reports. 3 (2013) 2247.

[97] K. Guo, Y. Li, J. Yang, Z. Zou, X. Xue, X. Li, H. Yang, Nanosized Mn–Ru binary oxides as effective bifunctional cathode electrocatalysts for rechargeable Li–O_2 batteries, Journal of Materials Chemistry A. 2 (2014) 1509-1514.

[98] J. Ding, Q. Shao, Y. Feng, X. Huang, Ruthenium-nickel sandwiched nanoplates for efficient water splitting electrocatalysis, Nano Energy. 47 (2018) 1-7.

[99] T. Reier, M. Oezaslan, P. Strasser, Electrocatalytic oxygen evolution reaction (OER) on Ru, Ir, and Pt catalysts: a comparative study of nanoparticles and bulk materials, Acs Catalysis. 2 (2012) 1765-1772.

[100] A.T.N. Nguyen, J.H. Shim, Facile one-step synthesis of Ir-Pd bimetallic alloy networks as efficient bifunctional catalysts for oxygen reduction and oxygen evolution reactions, J Electroanal Chem. 827 (2018) 120-127.

[101] Y. Zhao, M. Luo, S. Chu, M. Peng, B. Liu, Q. Wu, P. Liu, F.M. de Groot, Y. Tan, 3D Nanoporous Iridium-Based Alloy Microwires for Efficient Oxygen Evolution in Acidic Media, Nano Energy. (2019).

[102] L. Yuan, L. Jiang, T. Zhang, G. Wang, S. Wang, X. Bao, G. Sun, Electrochemically synthesized freestanding 3D nanoporous silver electrode with high electrocatalytic activity, Catalysis Science & Technology. 6 (2016) 7163-7171.

[103] A. Qaseem, F. Chen, X. Wu, R.L. Johnston, Pt-free silver nanoalloy electrocatalysts for oxygen reduction reaction in alkaline media, Catalysis Science & Technology. 6 (2016) 3317-3340.

[104] B. Liu, M. Wang, Preparation and characterization of size-controlled silver

nanoparticles decorated multi-walled carbon nanotubes and their electrocatalytic reduction properties for hydrogen peroxide, Russian J. Electrochem. 50 (2014) 476-481.

[105] Q. Yi, F. Niu, L. Li, R. Du, Z. Zhou, X. Liu, Novel nanoporous silver particles for electro-reduction of hydrogen peroxide in alkaline media, J Electroanal Chem. 654 (2011) 60-65.

[106] B. Blizanac, P.N. Ross, N. Marković, Oxygen Reduction on Silver Low-Index Single-Crystal Surfaces in Alkaline Solution: Rotating Ring DiskAg (h kl) Studies, The Journal of Physical Chemistry B. 110 (2006) 4735-4741.

[107] J. Han, N. Li, T. Zhang, Ag/C nanoparticles as an cathode catalyst for a zinc-air battery with a flowing alkaline electrolyte, J. Power Sources. 193 (2009) 885-889.

[108] P. Singh, D.A. Buttry, Comparison of oxygen reduction reaction at silver nanoparticles and polycrystalline silver electrodes in alkaline solution, The Journal of Physical Chemistry C. 116 (2012) 10656-10663.

[109] X. Huang, M. Xie, Y. Chen, Q. Zong, Z. Liu, Y. Jin, Copper–silver oxide nanowires grown on an alloy electrode as an efficient electrocatalyst for water oxidation, RSC Advances. 5 (2015) 26150-26156.

[110] C. Lee, C. Syu, C. Huang, H. Chiou, Y. Chao, C. Yang, Cornered silver and silver platinum nanodisks: Preparation and promising activity for alkaline oxygen reduction catalysis, Applied Catalysis B: Environmental. 132 (2013) 229-236.

[111] H. Lin, W. Tang, A. Kleiman-Shwarsctein, E.W. McFarland, Oxygen electroreduction on gold-cobalt oxide binary nanocluster catalysts, J. Electrochem. Soc. 155 (2008) B200-B206.

[112] Y. Wang, X. Lu, Y. Liu, Y. Deng, Silver supported on Co_3O_4 modified carbon as

electrocatalyst for oxygen reduction reaction in alkaline media, Electrochemistry Communications. 31 (2013) 108-111.

[113] A. Holewinski, J. Idrobo, S. Linic, High-performance Ag–Co alloy catalysts for electrochemical oxygen reduction, Nature chemistry. 6 (2014) 828-834.

[114] A. Ashok, A. Kumar, M.A. Matin, F. Tarlochan, Synthesis of Highly Efficient Bifunctional Ag/Co_3O_4 Catalyst for Oxygen Reduction and Oxygen Evolution Reactions in Alkaline Medium, ACS Omega. 3 (2018) 7745-7756.

[115] F. Berthier, B. Legrand, J. Creuze, R. Tétot, Ag/Cu (001) electrodeposition: beyond the classical nucleation theory, J Electroanal Chem. 562 (2004) 127-134.

[116] X. Wu, F. Chen, Y. Jin, N. Zhang, R.L. Johnston, Silver–Copper Nanoalloy Catalyst Layer for Bifunctional Air Electrodes in Alkaline Media, ACS applied materials & interfaces. 7 (2015) 17782-17791.

[117] K. Shin, D.H. Kim, S.C. Yeo, H.M. Lee, Structural stability of AgCu bimetallic nanoparticles and their application as a catalyst: a DFT study, Catalysis today. 185 (2012) 94-98.

[118] A. Fazil, R. Chetty, Synthesis and evaluation of carbon nanotubes supported silver catalyst for alkaline fuel cell, Electroanalysis. 26 (2014) 2380-2387.

[119] S. Jin, M. Chen, H. Dong, B. He, H. Lu, L. Su, W. Dai, Q. Zhang, X. Zhang, Stable silver nanoclusters electrochemically deposited on nitrogen-doped graphene as efficient electrocatalyst for oxygen reduction reaction, J. Power Sources. 274 (2015) 1173-1179.

[120] K. Lee, M.S. Ahmed, S. Jeon, Various carbon chain containing linkages grafted graphene with silver nanoparticles electrocatalysts for oxygen reduction reaction, J. Electrochem. Soc. 162 (2015) F1-F8.

[121] L. Yuan, L. Jiang, J. Liu, Z. Xia, S. Wang, G. Sun, Facile synthesis of silver nanoparticles supported on three dimensional graphene oxide/carbon black composite and its application for oxygen reduction reaction, Electrochim. Acta. 135 (2014) 168-174.

[122] R. Adžić, S. Strbac, N. Anastasijević, Electrocatalysis of oxygen on single crystal gold electrodes, Mater. Chem. Phys. 22 (1989) 349-375.

[123] N. Marković, R. Adžić, B. Cahan, E. Yeager, Structural effects in electrocatalysis: oxygen reduction on platinum low index single-crystal surfaces in perchloric acid solutions, J Electroanal Chem. 377 (1994) 249-259.

[124] P. Hu, Y. Song, L. Chen, S. Chen, Electrocatalytic activity of alkyne-functionalized AgAu alloy nanoparticles for oxygen reduction in alkaline media, Nanoscale. 7 (2015) 9627-9636.

[125] Y. Song, K. Liu, S. Chen, AgAu bimetallic Janus nanoparticles and their electrocatalytic activity for oxygen reduction in alkaline media, Langmuir. 28 (2012) 17143-17152.

[126] G. Fu, X. Jiang, Y. Chen, L. Xu, D. Sun, J. Lee, Y. Tang, Robust bifunctional oxygen electrocatalyst with a “rigid and flexible” structure for air-cathodes, NPG Asia Materials. 10 (2018) 618.

[127] L. Yuan, Z. Yan, L. Jiang, E. Wang, S. Wang, G. Sun, Gold-iridium bifunctional electrocatalyst for oxygen reduction and oxygen evolution reactions, Journal of energy chemistry. 25 (2016) 805-810.

[128] Y. Wang, W. Huang, C. Si, J. Zhang, X. Yan, C. Jin, Y. Ding, Z. Zhang, Self-supporting nanoporous gold-palladium overlayer bifunctional catalysts toward oxygen reduction and evolution reactions, Nano Research. 9 (2016) 3781-3794.

[129] P. Zhang, X. Lu, Y. Huang, J. Deng, L. Zhang, F. Ding, Z. Su, G. Wei, O.G. Schmidt, MoS2 nanosheets decorated with gold nanoparticles for rechargeable Li–O_2 batteries, Journal of Materials Chemistry A. 3 (2015) 14562-14566.

[130] S. Xu, P. Wu, Facile and green synthesis of a surfactant-free Au clusters/reduced graphene oxide composite as an efficient electrocatalyst for the oxygen reduction reaction, Journal of Materials Chemistry A. 2 (2014) 13682-13690.

[131] M. Govindhan, A. Chen, Simultaneous synthesis of gold nanoparticle/graphene nanocomposite for enhanced oxygen reduction reaction, J. Power Sources. 274 (2015) 928-936.

[132] Z. Chen, D. Higgins, A. Yu, L. Zhang, J. Zhang, A review on non-precious metal electrocatalysts for PEM fuel cells, Energy & Environmental Science. 4 (2011) 3167-3192.

[133] P. Żółtowski, D. Dražić, L. Vorkapić, Carbon-air electrode with regenerative short time overload capacity: Part 1. Effect of manganese dioxide, J. Appl. Electrochem. 3 (1973) 271-283.

[134] L. Mao, T. Sotomura, K. Nakatsu, N. Koshiba, D. Zhang, T. Ohsaka, Electrochemical characterization of catalytic activities of manganese oxides to oxygen reduction in alkaline aqueous solution, J. Electrochem. Soc. 149 (2002) A504-A507.

[135] F. Cheng, Y. Su, J. Liang, Z. Tao, J. Chen, MnO_2-based nanostructures as catalysts for electrochemical oxygen reduction in alkaline media†, Chemistry of Materials. 22 (2009) 898-905.

[136] Y. Meng, W. Song, H. Huang, Z. Ren, S. Chen, S.L. Suib, Structure–property relationship of bifunctional MnO_2 nanostructures: highly efficient, ultra-stable

electrochemical water oxidation and oxygen reduction reaction catalysts identified in alkaline media, J. Am. Chem. Soc. 136 (2014) 11452-11464.

[137] I. Roche, K. Scott, Carbon-supported manganese oxide nanoparticles as electrocatalysts for oxygen reduction reaction (orr) in neutral solution, J. Appl. Electrochem. 39 (2009) 197-204.

[138] I. Roche, E. Chaînet, M. Chatenet, J. Vondrák, Durability of carbon-supported manganese oxide nanoparticles for the oxygen reduction reaction (ORR) in alkaline medium, J. Appl. Electrochem. 38 (2008) 1195-1201.

[139] J. Du, Y. Pan, T. Zhang, X. Han, F. Cheng, J. Chen, Facile solvothermal synthesis of $CaMn_2O_4$ nanorods for electrochemical oxygen reduction, Journal of Materials Chemistry. 22 (2012) 15812-15818.

[140] H. Wang, Y. Yang, Y. Liang, G. Zheng, Y. Li, Y. Cui, H. Dai, Rechargeable Li–O_2 batteries with a covalently coupled MnCo 2 O 4–graphene hybrid as an oxygen cathode catalyst, Energy & Environmental Science. 5 (2012) 7931-7935.

[141] H. Zhu, S. Zhang, Y. Huang, L. Wu, S. Sun, Monodisperse $M_xFe_{3-x}O_4$ (M= Fe, Cu, Co, Mn) Nanoparticles and Their Electrocatalysis for Oxygen Reduction Reaction, Nano letters. 13 (2013) 2947-2951.

[142] J. Suntivich, H.A. Gasteiger, N. Yabuuchi, H. Nakanishi, J.B. Goodenough, Y. Shao-Horn, Design principles for oxygen-reduction activity on perovskite oxide catalysts for fuel cells and metal–air batteries, Nature chemistry. 3 (2011) 546-550.

[143] N.H. Chou, P.N. Ross, A.T. Bell, T.D. Tilley, Comparison of Cobalt-based Nanoparticles as Electrocatalysts for Water Oxidation, ChemSusChem. 4 (2011) 1566-1569.

[144] J. Rosen, G.S. Hutchings, F. Jiao, Ordered mesoporous cobalt oxide as highly efficient oxygen evolution catalyst, J. Am. Chem. Soc. 135 (2013) 4516-4521.

[145] J. Xiao, Q. Kuang, S. Yang, F. Xiao, S. Wang, L. Guo, Surface structure dependent electrocatalytic activity of Co_3O_4 anchored on graphene sheets toward oxygen reduction reaction, Scientific reports. 3 (2013) 2300.

[146] M. De Koninck, B. Marsan, $Mn_xCu_{1-x}Co_2O_4$ used as bifunctional electrocatalyst in alkaline medium, Electrochim. Acta. 53 (2008) 7012-7021.

[147] P.W. Menezes, A. Indra, N.R. Sahraie, A. Bergmann, P. Strasser, M. Driess, Cobalt–manganese-based spinels as multifunctional materials that unify catalytic water oxidation and oxygen reduction reactions, ChemSusChem. 8 (2015) 164-171.

[148] S. Trasatti, Electrocatalysis in the anodic evolution of oxygen and chlorine, Electrochim. Acta. 29 (1984) 1503-1512.

[149] P.W. Menezes, A. Indra, D. González-Flores, N.R. Sahraie, I. Zaharieva, M. Schwarze, P. Strasser, H. Dau, M. Driess, High-performance oxygen redox catalysis with multifunctional cobalt oxide nanochains: morphology-dependent activity, ACS Catalysis. 5 (2015) 2017-2027.

[150] Y. Li, P. Hasin, Y. Wu, $Ni_xCo_{3-x}O_4$ nanowire arrays for electrocatalytic oxygen evolution, Adv Mater. 22 (2010) 1926-1929.

[151] M. Prabu, K. Ketpang, S. Shanmugam, Hierarchical nanostructured $NiCo_2O_4$ as an efficient bifunctional non-precious metal catalyst for rechargeable zinc–air batteries, Nanoscale. 6 (2014) 3173-3181.

[152] X. Wu, K. Scott, A non-precious metal bifunctional oxygen electrode for alkaline anion exchange membrane cells, J. Power Sources. 206 (2012) 14-19.

[153] M. Pena, J. Fierro, Chemical structures and performance of perovskite oxides, Chem. Rev. 101 (2001) 1981-2018.

[154] S. Royer, D. Duprez, F. Can, X. Courtois, C. Batiot-Dupeyrat, S. Laassiri, H. Alamdari, Perovskites as substitutes of noble metals for heterogeneous catalysis: dream or reality, Chem. Rev. 114 (2014) 10292-10368.

[155] S.B. Adler, Mechanism and kinetics of oxygen reduction on porous $La_{1-x}Sr_xCoO_{3-\delta}$ electrodes, Solid State Ionics. 111 (1998) 125-134.

[156] J. Sunarso, A.A. Torriero, W. Zhou, P.C. Howlett, M. Forsyth, Oxygen reduction reaction activity of La-based perovskite oxides in alkaline medium: a thin-film rotating ring-disk electrode study, The Journal of Physical Chemistry C. 116 (2012) 5827-5834.

[157] Y. Ohno, S. Nagata, H. Sato, Effect of electrode materials on the properties of high-temperature solid electrolyte fuel cells, Solid State Ionics. 3 (1981) 439-442.

[158] J.O. Bockris, T. Otagawa, The electrocatalysis of oxygen evolution on perovskites, J. Electrochem. Soc. 131 (1984) 290-302.

[159] J. Bockris, T. Otagawa, V. Young, Solid state surface studies of the electrocatalysis of oxygen evolution on perovskites, Journal of Electroanalytical Chemistry and Interfacial Electrochemistry. 150 (1983) 633-643.

[160] J. Griffith, L. Orgel, Ligand-field theory, Quarterly Reviews, Chemical Society. 11 (1957) 381-393.

[161] O. Malta, A simple overlap model in lanthanide crystal-field theory, Chemical Physics Letters. 87 (1982) 27-29.

[162] W.T. Hong, M. Risch, K.A. Stoerzinger, A. Grimaud, J. Suntivich, Y. Shao-Horn, Toward the rational design of non-precious transition metal oxides for oxygen

electrocatalysis, Energy & Environmental Science. 8 (2015) 1404-1427.

[163] A. Dinger, R. Martin, X. Mosquet, M. Rabl, D. Rizoulis, M. Russo, G. Sticher, Batteries for electric cars: Challenges, opportunities, and the outlook to 2020, The Boston Consulting Group. 7 (2010) 2017.

[164] J.B. Goodenough, An interpretation of the magnetic properties of the perovskite-type mixed crystals $La_{1-x}Sr_xCoO_{3-\lambda}$, Journal of Physics and Chemistry of Solids. 6 (1958) 287-297.

[165] G. Maris, Y. Ren, V. Volotchaev, C. Zobel, T. Lorenz, T. Palstra, Evidence for orbital ordering in $LaCoO_3$, Physical Review B. 67 (2003) 224423.

[166] M.L. Medarde, Structural, magnetic and electronic properties of perovskites (R= rare earth), Journal of Physics: Condensed Matter. 9 (1997) 1679.

[167] J. Yan, J. Zhou, J. Goodenough, Ferromagnetism in $LaCoO_3$, Physical Review B. 70 (2004) 014402.

[168] C. Ritter, M. Ibarra, J. De Teresa, P. Algarabel, C. Marquina, J. Blasco, J. Garcia, S. Oseroff, S. Cheong, Influence of oxygen content on the structural, magnetotransport, and magnetic properties of $LaMnO_{3-\delta}$, Physical Review B. 56 (1997) 8902.

[169] J. Zhou, J. Goodenough, B. Dabrowski, P. Klamut, Z. Bukowski, Enhanced Susceptibility in L NiO $_3$ Perovskites (L= L a, P r, N d, N d 0.5 Sm 0.5), Phys. Rev. Lett. 84 (2000) 526.

[170] J. Suntivich, H.A. Gasteiger, N. Yabuuchi, H. Nakanishi, J.B. Goodenough, Y. Shao-Horn, Design principles for oxygen-reduction activity on perovskite oxide catalysts for fuel cells and metal–air batteries, Nature chemistry. 3 (2011) 546-550.

[171] J. Suntivich, K.J. May, H.A. Gasteiger, J.B. Goodenough, Y. Shao-Horn, A

perovskite oxide optimized for oxygen evolution catalysis from molecular orbital principles, Science. 334 (2011) 1383-1385.

[172] Y. Matsumoto, H. Yoneyama, H. Tamura, Electrochemical properties of lanthanum nickel oxide, Journal of Electroanalytical Chemistry and Interfacial Electrochemistry. 80 (1977) 115-121.

[173] Y. Matumoto, H. Yoneyama, H. Tamura, A new catalyst for cathodic reduction of oxygen: lanthanum nickel oxide, Chem. Lett. 4 (1975) 661-662.

[174] J.O. Bockris, T. Otagawa, The electrocatalysis of oxygen evolution on perovskites, J. Electrochem. Soc. 131 (1984) 290-302.

[175] T. Hyodo, M. Hayashi, N. Miura, N. Yamazoe, Catalytic activities of rare-earth manganites for cathodic reduction of oxygen in alkaline solution, J. Electrochem. Soc. 143 (1996) L266-L267.

[176] J. Sunarso, A.A. Torriero, W. Zhou, P.C. Howlett, M. Forsyth, Oxygen reduction reaction activity of La-based perovskite oxides in alkaline medium: a thin-film rotating ring-disk electrode study, The Journal of Physical Chemistry C. 116 (2012) 5827-5834.

[177] J. Suntivich, H.A. Gasteiger, N. Yabuuchi, Y. Shao-Horn, Electrocatalytic measurement methodology of oxide catalysts using a thin-film rotating disk electrode, J. Electrochem. Soc. 157 (2010) B1263-B1268.

[178] J. Suntivich, H.A. Gasteiger, N. Yabuuchi, H. Nakanishi, J.B. Goodenough, Y. Shao-Horn, Design principles for oxygen-reduction activity on perovskite oxide catalysts for fuel cells and metal–air batteries, Nature chemistry. 3 (2011) 546-550.

[179] T. Poux, A. Bonnefont, G. Kéranguéven, G.A. Tsirlina, E.R. Savinova, Electrocatalytic oxygen reduction reaction on perovskite oxides: series versus direct

pathway, ChemPhysChem. 15 (2014) 2108-2120.

[180] X. Li, W. Qu, J. Zhang, H. Wang, Electrocatalytic activities of $La_{0.6}Ca_{0.4}CoO_3$ and $La_{0.6}Ca_{0.4}CoO_3$-carbon composites toward the oxygen reduction reaction in concentrated alkaline electrolytes, J. Electrochem. Soc. 158 (2011) A597-A604.

[181] E. Fabbri, R. Mohamed, P. Levecque, O. Conrad, R. Kötz, T.J. Schmidt, Composite electrode boosts the activity of $Ba_{0.5}Sr_{0.5}Co_{0.8}Fe_{0.2}O_{3-\delta}$ perovskite and carbon toward oxygen reduction in alkaline media, ACS Catalysis. 4 (2014) 1061-1070.

[182] V. Hermann, D. Dutriat, S. Müller, C. Comninellis, Mechanistic studies of oxygen reduction at $La_{0.6}Ca_{0.4}CoO_3$-activated carbon electrodes in a channel flow cell, Electrochim. Acta. 46 (2000) 365-372.

[183] Y. Zhu, W. Zhou, Y. Chen, J. Yu, X. Xu, C. Su, M.O. Tadé, Z. Shao, Boosting oxygen reduction reaction activity of palladium by stabilizing its unusual oxidation states in perovskite, Chemistry of Materials. 27 (2015) 3048-3054.

[184] T. Otagawa, J. Bockris, Lanthanum nickelate as electrocatalyst: oxygen evolution, J. Electrochem. Soc. 129 (1982) 2391-2392.

[185] J. Suntivich, K.J. May, H.A. Gasteiger, J.B. Goodenough, Y. Shao-Horn, A perovskite oxide optimized for oxygen evolution catalysis from molecular orbital principles, Science. 334 (2011) 1383-1385.

[186] Y. Zhao, L. Xu, L. Mai, C. Han, Q. An, X. Xu, X. Liu, Q. Zhang, Hierarchical mesoporous perovskite La0.5Sr0.5CoO2.91 nanowires with ultrahigh capacity for Li-air batteries, Proc. Natl. Acad. Sci. U. S. A. 109 (2012) 19569-19574.

[187] C. Jin, X. Cao, F. Lu, Z. Yang, R. Yang, Electrochemical study of $Ba_{0.5}Sr_{0.5}Co_{0.8}Fe_{0.2}O_3$ perovskite as bifunctional catalyst in alkaline media, Int J Hydrogen Energy. 38

(2013) 10389-10393.

[188] D. Wang, Q. Zhang, K. Zhou, W. Yang, Y. Hu, X. Gong, The influence of manganese–cobalt oxide/graphene on reducing fire hazards of poly (butylene terephthalate), J. Hazard. Mater. 278 (2014) 391-400.

[189] Y. Liang, H. Wang, P. Diao, W. Chang, G. Hong, Y. Li, M. Gong, L. Xie, J. Zhou, J. Wang, Oxygen reduction electrocatalyst based on strongly coupled cobalt oxide nanocrystals and carbon nanotubes, J. Am. Chem. Soc. 134 (2012) 15849-15857.

[190] S. Yang, G. Cui, S. Pang, Q. Cao, U. Kolb, X. Feng, J. Maier, K. Müllen, Fabrication of Cobalt and Cobalt Oxide/Graphene Composites: Towards High-Performance Anode Materials for Lithium Ion Batteries, ChemSusChem. 3 (2010) 236-239.

[191] S. Eigler, A. Hirsch, Chemistry with graphene and graphene oxide—challenges for synthetic chemists, Angewandte Chemie International Edition. 53 (2014) 7720-7738.

[192] J. Xu, J. Wu, L. Luo, X. Chen, H. Qin, V. Dravid, S. Mi, C. Jia, Co_3O_4 nanocubes homogeneously assembled on few-layer graphene for high energy density lithium-ion batteries, J. Power Sources. 274 (2015) 816-822.

[193] Y. Wang, X. Ma, L. Lu, Y. He, X. Qi, Y. Deng, Carbon supported MnO_x–Co_3O_4 as cathode catalyst for oxygen reduction reaction in alkaline media, Int J Hydrogen Energy. 38 (2013) 13611-13616.

[194] D.U. Lee, B.J. Kim, Z. Chen, One-pot synthesis of a mesoporous $NiCo_2O_4$ nanoplatelet and graphene hybrid and its oxygen reduction and evolution activities as an efficient bi-functional electrocatalyst, Journal of Materials Chemistry A. 1 (2013) 4754-4762.

[195] W. Yan, Z. Yang, W. Bian, R. Yang, $FeCo_2O_4$/hollow graphene spheres hybrid with enhanced electrocatalytic activities for oxygen reduction and oxygen evolution reaction, Carbon. 92 (2015) 74-83.

[196] Y. Liang, H. Wang, J. Zhou, Y. Li, J. Wang, T. Regier, H. Dai, Covalent hybrid of spinel manganese–cobalt oxide and graphene as advanced oxygen reduction electrocatalysts, J. Am. Chem. Soc. 134 (2012) 3517-3523.

[197] Y. Yang, H. Fei, G. Ruan, C. Xiang, J.M. Tour, Efficient Electrocatalytic Oxygen Evolution on Amorphous Nickel–Cobalt Binary Oxide Nanoporous Layers, ACS nano. 8 (2014) 9518-9523.

[198] M. Fu, Q. Jiao, Y. Zhao, In situ fabrication and characterization of cobalt ferrite nanorods/graphene composites, Mater Charact. 86 (2013) 303-315.

[199] A. Pendashteh, J. Palma, M. Anderson, R. Marcilla, NiCoMnO 4 nanoparticles on N-doped graphene: Highly efficient bifunctional electrocatalyst for oxygen reduction/evolution reactions, Applied Catalysis B: Environmental. 201 (2017) 241-252.

[200] S. Guo, S. Zhang, L. Wu, S. Sun, Co/CoO nanoparticles assembled on graphene for electrochemical reduction of oxygen, Angewandte Chemie. 124 (2012) 11940-11943.

[201] J. Wu, Y. Xue, X. Yan, W. Yan, Q. Cheng, Y. Xie, Co_3O_4 nanocrystals on single-walled carbon nanotubes as a highly efficient oxygen-evolving catalyst, Nano Research. 5 (2012) 521-530.

[202] C. Alegre, A. Stassi, E. Modica, C.L. Vecchio, A. Aricò, V. Baglio, Investigation of the activity and stability of Pd-based catalysts towards the oxygen reduction (ORR) and evolution reactions (OER) in iron–air batteries, RSC Advances. 5 (2015) 25424-25427.

[203] Z. Chen, A. Yu, R. Ahmed, H. Wang, H. Li, Z. Chen, Manganese dioxide nanotube and nitrogen-doped carbon nanotube based composite bifunctional catalyst for rechargeable zinc-air battery, Electrochim. Acta. 69 (2012) 295-300.

[204] X. Li, Y. Fang, X. Lin, M. Tian, X. An, Y. Fu, R. Li, J. Jin, J. Ma, MOF derived Co_3O_4 nanoparticles embedded in N-doped mesoporous carbon layer/MWCNT hybrids: extraordinary bi-functional electrocatalysts for OER and ORR, Journal of Materials Chemistry A. 3 (2015) 17392-17402.

[205] Y. Li, L. Zou, J. Li, K. Guo, X. Dong, X. Li, X. Xue, H. Zhang, H. Yang, Synthesis of ordered mesoporous $NiCo_2O_4$ via hard template and its application as bifunctional electrocatalyst for Li-O 2 batteries, Electrochim. Acta. 129 (2014) 14-20.

[206] W. Yang, J. Salim, S. Li, C. Sun, L. Chen, J.B. Goodenough, Y. Kim, Perovskite $Sr_{0.95}Ce_{0.05}CoO_{3-\delta}$ loaded with copper nanoparticles as a bifunctional catalyst for lithium-air batteries, Journal of Materials Chemistry. 22 (2012) 18902-18907.

[207] Y. Yang, H. Fei, G. Ruan, L. Li, G. Wang, N.D. Kim, J.M. Tour, Carbon-free electrocatalyst for oxygen reduction and oxygen evolution reactions, ACS applied materials & interfaces. 7 (2015) 20607-20611.

[208] H. Yuan, L. Deng, X. Cai, S. Zhou, Y. Chen, Y. Yuan, Nitrogen-doped carbon sheets derived from chitin as non-metal bifunctional electrocatalysts for oxygen reduction and evolution, RSC Advances. 5 (2015) 56121-56129.

[209] J. Zhang, M.B. Vukmirovic, Y. Xu, M. Mavrikakis, R.R. Adzic, Controlling the Catalytic Activity of Platinum-Monolayer Electrocatalysts for Oxygen Reduction with Different Substrates, Angewandte Chemie International Edition. 44 (2005) 2132-2135.

[210] S.G. Peera, A. Sahu, S. Bhat, S. Lee, Nitrogen functionalized graphite nanofibers/Ir

nanoparticles for enhanced oxygen reduction reaction in polymer electrolyte fuel cells (PEFCs), RSC Advances. 4 (2014) 11080-11088.

[211] T. Reier, M. Oezaslan, P. Strasser, Electrocatalytic oxygen evolution reaction (OER) on Ru, Ir, and Pt catalysts: a comparative study of nanoparticles and bulk materials, Acs Catalysis. 2 (2012) 1765-1772.

[212] S. Siracusano, N. Van Dijk, E. Payne-Johnson, V. Baglio, A. Aricò, Nanosized IrOx and IrRuOx electrocatalysts for the O_2 evolution reaction in PEM water electrolysers, Applied Catalysis B: Environmental. 164 (2015) 488-495.

[213] F. Mattos-Costa, P. de Lima-Neto, S. Machado, L. Avaca, Characterisation of surfaces modified by sol-gel derived $Ru_xIr_{1-x}O_2$ coatings for oxygen evolution in acid medium, Electrochim. Acta. 44 (1998) 1515-1523.

[214] C. Wang, Y. Sui, G. Xiao, X. Yang, Y. Wei, G. Zou, B. Zou, Synthesis of Cu–Ir nanocages with enhanced electrocatalytic activity for the oxygen evolution reaction, Journal of Materials Chemistry A. 3 (2015) 19669-19673.

[215] Q. Wang, F. Wu, N. Wang, L. Wang, X. Zhang, Electrochemical behavior of $Ir_xRu_{1-x}O_2$ oxides as anodic electrocatalyst for electrosynthesis of dinitrogen pentoxide, Electrochim. Acta. 74 (2012) 227-234.

[216] M. Wu, J.Y. Jo, S.J. Kim, Y. Kang, H. Jung, H. Jung, Hydrous amorphous RuO_2 nanoparticles supported on reduced graphene oxide for non-aqueous Li–O_2 batteries, RSC Advances. 6 (2016) 23467-23470.

[217] R. Cao, J. Lee, M. Liu, J. Cho, Recent progress in non-precious catalysts for metal-air batteries, Advanced Energy Materials. 2 (2012) 816-829.

[218] Z. Xiao, A. Laplante, Characterizing and recovering the platinum group minerals–

–a review, Minerals Eng. 17 (2004) 961-979.

[219] Q. Zhang, E. Uchaker, S.L. Candelaria, G. Cao, Nanomaterials for energy conversion and storage, Chem. Soc. Rev. 42 (2013) 3127-3171.

[220] S.J. Klaine, P.J. Alvarez, G.E. Batley, T.F. Fernandes, R.D. Handy, D.Y. Lyon, S. Mahendra, M.J. McLaughlin, J.R. Lead, Nanomaterials in the environment: behavior, fate, bioavailability, and effects, Environmental toxicology and chemistry. 27 (2008) 1825-1851.

[221] G. Adlakha-Hutcheon, R. Khaydarov, R. Korenstein, R. Varma, A. Vaseashta, H. Stamm, M. Abdel-Mottaleb, Nanomaterials, nanotechnology, in: Anonymous Nanomaterials: Risks and Benefits, Springer, 2009, pp. 195-207.

[222] D. Vollath, Nanoparticles-Nanocomposites Nanomaterials: An Introduction for Beginners, John Wiley & Sons, 2013.

[223] B. Bhushan, D. Luo, S.R. Schricker, W. Sigmund, S. Zauscher, Handbook of Nanomaterials Properties, Springer Science & Business Media, 2014.

[224] A.S. Edelstein, R. Cammaratra, Nanomaterials: Synthesis, Properties and Applications, CRC press, 1998.

[225] W. Wen, J. Wu, J. Tu, A novel solution combustion synthesis of cobalt oxide nanoparticles as negative-electrode materials for lithium ion batteries, J. Alloys Compounds. 513 (2012) 592-596.

[226] A.S. Mukasyan, K.S. Martirosyan, Combustion of Heterogeneous Systems: Fundamentals and Applications for Materials Synthesis 2007, Transworld Research Network, 2007.

[227] W. Chen, F. Li, J. Yu, Combustion synthesis and characterization of nanocrystalline

CeO_2-based powders via ethylene glycol–nitrate process, Mater Lett. 60 (2006) 57-62.

[228] S.T. Aruna, A.S. Mukasyan, Combustion synthesis and nanomaterials, Current Opinion in Solid State and Materials Science. 12 (2008) 44-50.

[229] N.L. de Freitas, E. Fagury-Neto, H.L. Lira, L. Gama, Kiminami, Ruth Herta Goldsmith Aliaga, de Melo Costa, Ana Cristina Figueiredo, Combustion synthesis of α-Al_2O_3 powders, 530 (2006) 631-636.

[230] K.C. Patil, S. Aruna, T. Mimani, Combustion synthesis: an update, Current Opinion in Solid State and Materials Science. 6 (2002) 507-512.

[231] L.A. Chick, L. Pederson, G. Maupin, J. Bates, L. Thomas, G. Exarhos, Glycine-nitrate combustion synthesis of oxide ceramic powders, Mater Lett. 10 (1990) 6-12.

[232] I.S. Altman, I.E. Agranovski, M. Choi, Mechanism of nanoparticle agglomeration during the combustion synthesis, Appl. Phys. Lett. 87 (2005) 053104.

[233] A. Varma, A.S. Mukasyan, A.S. Rogachev, K.V. Manukyan, Solution combustion synthesis of nanoscale materials, Chem. Rev. 116 (2016) 14493-14586.

[234] F. Maglia, U. Anselmi-Tamburini, G. Spinolo, Z.A. Munir, Zirconia-Based Metastable Solid Solutions through Self-Propagating High-Temperature Synthesis: Synthesis, Characterization, and Mechanistic Investigations, J Am Ceram Soc. 83 (2000) 1935-1941.

[235] A. Makino, C.K. Law, SHS combustion characteristics of several ceramics and intermetallic compounds, J Am Ceram Soc. 77 (1994) 778-786.

[236] A.G. Merzhanov, The chemistry of self-propagating high-temperature synthesis, Journal of Materials Chemistry. 14 (2004) 1779-1786.

[237] B. Akgün, H.E. Çamurlu, Y. Topkaya, N. Sevinç, Mechanochemical and volume

combustion synthesis of ZrB2, International Journal of Refractory Metals and Hard Materials. 29 (2011) 601-607.

[238] A.S. Mukasyan, C. Costello, K.P. Sherlock, D. Lafarga, A. Varma, Perovskite membranes by aqueous combustion synthesis: synthesis and properties, Separation and Purification Technology. 25 (2001) 117-126.

[239] K. Patil, M. Hegde, T. Rattan, S. Aruna, Chemistry of nanocrystalline oxide materials-Combustion synthesis, properties and applications, (2008).

[240] A. Mukasyan, P. Dinka, Novel approaches to solution-combustion synthesis of nanomaterials, International Journal of Self-Propagating High-Temperature Synthesis. 16 (2007) 23-35.

[241] R. Lenka, T. Mahata, P. Sinha, A. Tyagi, Combustion synthesis of gadolinia-doped ceria using glycine and urea fuels, J. Alloys Compounds. 466 (2008) 326-329.

[242] M.T. Makhlouf, B. Abu-Zied, T. Mansoure, Direct fabrication of cobalt oxide nano-particles employing glycine as a combustion fuel, Physical Chemistry. 2 (2012) 86-93.

[243] T. Takeda, K. Kato, S. Kikkawa, Gel combustion synthesis of rare earth aluminate using glycine or urea, Journal of the Ceramic Society of Japan. 115 (2007) 588-591.

[244] N. Kasapoğlu, A. Baykal, Y. Köseoğlu, M. Toprak, Microwave-assisted combustion synthesis of $CoFe_2O_4$ with urea, and its magnetic characterization, Scr. Mater. 57 (2007) 441-444.

[245] V. Zhuravlev, V. Bamburov, A. Beketov, L. Perelyaeva, I. Baklanova, O. Sivtsova, V. Vasil'ev, E. Vladimirova, V. Shevchenko, I. Grigorov, Solution combustion synthesis of α-Al 2 O_3 using urea, Ceram. Int. 39 (2013) 1379-1384.

[246] Y. Han, S. Li, X. Wang, X. Chen, Synthesis and sintering of nanocrystalline

hydroxyapatite powders by citric acid sol–gel combustion method, Mater. Res. Bull. 39 (2004) 25-32.

[247] R. Ianoş, A. Tăculescu, C. Păcurariu, I. Lazău, Solution combustion synthesis and characterization of magnetite, Fe_3O_4, nanopowders, J Am Ceram Soc. 95 (2012) 2236-2240.

[248] M. Qin, X. Du, Z. Li, I.S. Humail, X. Qu, Synthesis of aluminum nitride powder by carbothermal reduction of a combustion synthesis precursor, Mater. Res. Bull. 43 (2008) 2954-2960.

[249] R. Garcia, G. Hirata, J. McKittrick, New combustion synthesis technique for the production of $(In_xGa_{1-x})_2O_3$ powders: Hydrazine/metal nitrate method, J. Mater. Res. 16 (2001) 1059-1065.

[250] N. Thorat, K. Shinde, S. Pawar, K. Barick, C. Betty, R. Ningthoujam, Polyvinyl alcohol: an efficient fuel for synthesis of superparamagnetic LSMO nanoparticles for biomedical application, Dalton Transactions. 41 (2012) 3060-3071.

[251] A. Kumar, A. Cross, K. Manukyan, R. Bhosale, L. Van den Broeke, J. Miller, A. Mukasyan, E. Wolf, Combustion synthesis of copper–nickel catalysts for hydrogen production from ethanol, Chem. Eng. J. 278 (2015) 46-54.

[252] A. Kumar, A. Mukasyan, E. Wolf, Combustion synthesis of Ni, Fe and Cu multi-component catalysts for hydrogen production from ethanol reforming, Applied Catalysis A: General. 401 (2011) 20-28.

[253] A. Kumar, E. Wolf, A. Mukasyan, Solution combustion synthesis of metal nanopowders: Nickel—Reaction pathways, AIChE J. 57 (2011) 2207-2214.

[254] L. Ge, W. Zhou, R. Ran, Z. Shao, S. Liu, Facile autocombustion synthesis of $La_{0.}$

$_{6}Sr_{0.4}Co_{0.2}Fe_{0.8}O_{3-\delta}$ (LSCF) perovskite via a modified complexing sol–gel process with NH4NO3 as combustion aid, J. Alloys Compounds. 450 (2008) 338-347.

[255] A.F. Junior, de Oliveira Lima, Emília Celma, M.A. Novak, P.R. Wells Jr, Synthesis of nanoparticles of $Co_xFe_{(3-x)}O_4$ by combustion reaction method, J Magn Magn Mater. 308 (2007) 198-202.

[256] R. Lenka, T. Mahata, P. Sinha, A. Tyagi, Combustion synthesis of gadolinia-doped ceria using glycine and urea fuels, J. Alloys Compounds. 466 (2008) 326-329.

[257] C. Yan, Z. Xu, F. Cheng, Z. Wang, L. Sun, C. Liao, J. Jia, Nanophased $CoFe_2O_4$ prepared by combustion method, Solid State Commun. 111 (1999) 287-291.

[258] W. Chen, F. Li, J. Yu, L. Liu, A facile and novel route to high surface area ceria-based nanopowders by salt-assisted solution combustion synthesis, Materials Science and Engineering: B. 133 (2006) 151-156.

[259] X. Zhang, W. Jiang, D. Song, H. Sun, Z. Sun, F. Li, Salt-assisted combustion synthesis of highly dispersed superparamagnetic $CoFe_2O_4$ nanoparticles, J. Alloys Compounds. 475 (2009) L34-L37.

[260] J. Niu, X. Yi, I. Nakatsugawa, T. Akiyama, Salt-assisted combustion synthesis of β-SiAlON fine powders, Intermetallics. 35 (2013) 53-59.

[261] A.J. Bard, L.R. Faulkner, J. Leddy, C.G. Zoski, Electrochemical Methods: Fundamentals and Applications, wiley New York, 1980.

[262] A. Patterson, The Scherrer formula for X-ray particle size determination, Physical review. 56 (1939) 978.

[263] A. Ashok, A. Kumar, R.R. Bhosale, M.A.H. Saleh, U.K. Ghosh, M. Al-Marri, F.A. Almomani, M.M. Khader, F. Tarlochan, Cobalt oxide nanopowder synthesis using

cellulose assisted combustion technique, Ceram. Int. 42 (2016) 12771-12777.

[264] Z. Wang, W. Wang, L. Zhang, D. Jiang, Surface oxygen vacancies on Co_3O_4 mediated catalytic formaldehyde oxidation at room temperature, Catalysis Science & Technology. 6 (2016) 3845-3853.

[265] D. Zhang, J. Zhu, N. Zhang, T. Liu, L. Chen, X. Liu, R. Ma, H. Zhang, G. Qiu, Controllable fabrication and magnetic properties of double-shell cobalt oxides hollow particles, Sci. Rep. 5 (2015) 8737.

[266] S.K. Meher, P. Justin, G.R. Rao, Nanoscale morphology dependent pseudocapacitance of NiO: Influence of intercalating anions during synthesis, Nanoscale. 3 (2011) 683-692.

[267] X. Wang, X. Chen, L. Gao, H. Zheng, Z. Zhang, Y. Qian, One-dimensional arrays of Co_3O_4 nanoparticles: synthesis, characterization, and optical and electrochemical properties, The Journal of Physical Chemistry B. 108 (2004) 16401-16404.

[268] R. Xu, H.C. Zeng, Self-generation of tiered surfactant superstructures for one-pot synthesis of Co_3O_4 nanocubes and their close-and non-close-packed organizations, Langmuir. 20 (2004) 9780-9790.

[269] S.K. Meher, G.R. Rao, Effect of microwave on the nanowire morphology, optical, magnetic, and pseudocapacitance behavior of Co_3O_4, The Journal of Physical Chemistry C. 115 (2011) 25543-25556.

[270] S.K. Meher, G.R. Rao, Ultralayered Co_3O_4 for high-performance supercapacitor applications, The Journal of Physical Chemistry C. 115 (2011) 15646-15654.

[271] D. Ferrer, A. Torres-Castro, X. Gao, S. Sepulveda-Guzman, U. Ortiz-Mendez, M. Jose-Yacaman, Three-layer core/shell structure in Au− Pd bimetallic nanoparticles, Nano

letters. 7 (2007) 1701-1705.

[272] D. Kim, J. Resasco, Y. Yu, A.M. Asiri, P. Yang, Synergistic geometric and electronic effects for electrochemical reduction of carbon dioxide using gold–copper bimetallic nanoparticles, Nature communications. 5 (2014) 4948.

[273] N. Toshima, T. Yonezawa, Bimetallic nanoparticles—novel materials for chemical and physical applications, New Journal of Chemistry. 22 (1998) 1179-1201.

[274] M. Zhong, C. Huang, G. Wang, Hydrogen storage of Al-Li bimetal alloy nanostructures, J. Alloys Compounds. 725 (2017) 388-392.

[275] T. Yang, L. Zhang, X. Li, D. Xia, Structural and morphological characterization of gold–nickel electrocatalyst synthesized by taking advantage of the AuNi phase separation mechanism, J. Alloys Compounds. 492 (2010) 83-87.

[276] J. Rick, M. Tsai, B.J. Hwang, Biosensors incorporating bimetallic nanoparticles, Nanomaterials. 6 (2015) 5.

[277] Y. Gou, X. Liang, B. Chen, Porous Ni–Co bimetal oxides nanosheets and catalytic properties for CO oxidation, J. Alloys Compounds. 574 (2013) 181-187.

[278] D. Lu, L. Yuan, Z. Chen, R. Zeng, Y. Cai, Co-precipitation preparation of $LiNi_{0.5}Mn_{1.5}O_4$ hollow hierarchical microspheres with superior electrochemical performance for 5 V Li-ion batteries, J. Alloys Compounds. 730 (2018) 509-515.

[279] N.V. Long, T.D. Hien, T. Asaka, M. Ohtaki, M. Nogami, Synthesis and characterization of Pt–Pd nanoparticles with core-shell morphology: Nucleation and overgrowth of the Pd shells on the as-prepared and defined Pt seeds, J. Alloys Compounds. 509 (2011) 7702-7709.

[280] Y. Yang, Z. Zhao, R. Cui, H. Wu, D. Cheng, Structures, thermal stability, and

chemical activity of crown-jewel-structured Pd–Pt nanoalloys, The Journal of Physical Chemistry C. 119 (2014) 10888-10895.

[281] X. Wang, Y. Qu, Y. Zhao, H. Chu, Effect of the composition of lanthanide complexes on their luminescence enhancement by Ag@ SiO_2 core-shell nanoparticles, Nanomaterials. 8 (2018) 98.

[282] E. Iglesia, S.L. Soled, R.A. Fiato, G.H. Via, Bimetallic synergy in cobalt ruthenium Fischer-Tropsch synthesis catalysts, Journal of Catalysis. 143 (1993) 345-368.

[283] C. Zafferoni, G. Cioncoloni, M.L. Foresti, L. Dei, E. Carretti, F. Vizza, A. Lavacchi, M. Innocenti, Synergy of Cobalt and Silver Microparticles Electrodeposited on Glassy Carbon for the Electrocatalysis of the Oxygen Reduction Reaction: An Electrochemical Investigation, Molecules. 20 (2015) 14386-14401.

[284] A. Nairan, U. Khan, M. Iqbal, M. Khan, K. Javed, S. Riaz, S. Naseem, X. Han, Structural and magnetic response in bimetallic core/shell magnetic nanoparticles, Nanomaterials. 6 (2016) 72.

[285] A. Salker, M.F. Desai, Low-temperature nitric oxide reduction over silver-substituted cobalt oxide spinels, Catalysis Science & Technology. 6 (2016) 430-433.

[286] Q. Wang, C. Xu, M. Ming, Y. Yang, B. Xu, Y. Wang, Y. Zhang, J. Wu, G. Fan, In Situ Formation of AgCo Stabilized on Graphitic Carbon Nitride and Concomitant Hydrolysis of Ammonia Borane to Hydrogen, Nanomaterials (Basel). 8 (2018) 10.3390/nano8050280.

[287] A. Alonso, X. Munoz-Berbel, N. Vigués, J. Macanás, M. Munoz, J. Mas, D.N. Muraviev, Characterization of fibrous polymer silver/cobalt nanocomposite with enhanced bactericide activity, Langmuir. 28 (2011) 783-790.

[288] H.M. Amin, H. Baltruschat, D. Wittmaier, K.A. Friedrich, A highly efficient bifunctional catalyst for alkaline air-electrodes based on a Ag and Co_3O_4 hybrid: RRDE and online DEMS insights, Electrochim. Acta. 151 (2015) 332-339.

[289] A. Holewinski, J. Idrobo, S. Linic, High-performance Ag–Co alloy catalysts for electrochemical oxygen reduction, Nature chemistry. 6 (2014) 828-834.

[290] F. Lima, J. De Castro, E.A. Ticianelli, Silver-cobalt bimetallic particles for oxygen reduction in alkaline media, J. Power Sources. 161 (2006) 806-812.

[291] E. Gulari, Ç Güldür, S. Srivannavit, S. Osuwan, Co oxidation by silver cobalt composite oxide, Applied Catalysis A: General. 182 (1999) 147-163.

[292] B. Małecka, A. Łącz, E. Drożdż, A. Małecki, Thermal decomposition of d-metal nitrates supported on alumina, Journal of Thermal Analysis and Calorimetry. 119 (2015) 1053-1061.

[293] G.I. Waterhouse, G.A. Bowmaker, J.B. Metson, The thermal decomposition of silver (I, III) oxide: a combined XRD, FT-IR and Raman spectroscopic study, Physical Chemistry Chemical Physics. 3 (2001) 3838-3845.

[294] M. Hernández-Rodríguez, M. Goya, M. Arevalo, J. Rodríguez, E. Pastor, Carbon supported Ag and Ag–Co catalysts tolerant to methanol and ethanol for the oxygen reduction reaction in alkaline media, Int J Hydrogen Energy. 41 (2016) 19789-19798.

[295] Z. Zhang, L. Xin, K. Sun, W. Li, Pd–Ni electrocatalysts for efficient ethanol oxidation reaction in alkaline electrolyte, Int J Hydrogen Energy. 36 (2011) 12686-12697.

[296] Y. Joo, M.S. Ahmed, H.S. Han, S. Jeon, Preparation of electrochemically reduced graphene oxide-based silver-cobalt alloy nanocatalysts for efficient oxygen reduction reaction, Int J Hydrogen Energy. 42 (2017) 21751-21761.

[297] A.P. Jamale, S. Shanmugam, C. Bhosale, L. Jadhav, Physiochemical properties of combustion synthesized $La_{0.6}Sr_{0.4}Co_{0.8}$ $Fe_{0.2}O_{3-\delta}$ perovskite: A role of fuel to oxidant ratio, Materials Science in Semiconductor Processing. 40 (2015) 855-860.

[298] L. Jadhav, S. Patil, A. Jamale, A. Chavan, Solution Combustion Synthesis: Role of Oxidant to Fuel Ratio on Powder Properties, 757 (2013) 85-98.

[299] S. Farhadi, J. Safabakhsh, P. Zaringhadam, Synthesis, characterization, and investigation of optical and magnetic properties of cobalt oxide (Co_3O_4) nanoparticles, Journal of Nanostructure in Chemistry. 3 (2013) 69.

[300] W. Zhou, Z. Shao, R. Ran, H. Gu, W. Jin, N. Xu, LSCF Nanopowder from Cellulose–Glycine-Nitrate Process and its Application in Intermediate-Temperature Solid-Oxide Fuel Cells, J Am Ceram Soc. 91 (2008) 1155-1162.

[301] S.N. Mailu, T.T. Waryo, P.M. Ndangili, F.R. Ngece, A.A. Baleg, P.G. Baker, E.I. Iwuoha, Determination of anthracene on Ag-Au alloy nanoparticles/overoxidized-polypyrrole composite modified glassy carbon electrodes, Sensors. 10 (2010) 9449-9465.

[302] K. Lin, H. Cheng, H. Hsu, L. Lin, W. Hsieh, Band gap variation of size-controlled ZnO quantum dots synthesized by sol–gel method, Chemical Physics Letters. 409 (2005) 208-211.

[303] S.P. Lim, A. Pandikumar, N.M. Huang, H.N. Lim, Enhanced photovoltaic performance of silver@ titania plasmonic photoanode in dye-sensitized solar cells, RSC Advances. 4 (2014) 38111-38118.

[304] M. Srivastava, A.K. Ojha, S. Chaubey, A. Materny, Synthesis and optical characterization of nanocrystalline $NiFe_2O_4$ structures, J. Alloys Compounds. 481 (2009) 515-519.

[305] K.H. Mahmoud, Synthesis and spectroscopic investigation of cobalt oxide nanoparticles, Polymer Composites. 37 (2016) 1881-1885.

[306] C.R. Dhas, R. Venkatesh, K. Jothivenkatachalam, A. Nithya, B.S. Benjamin, A.M.E. Raj, K. Jeyadheepan, C. Sanjeeviraja, Visible light driven photocatalytic degradation of Rhodamine B and Direct Red using cobalt oxide nanoparticles, Ceram. Int. 41 (2015) 9301-9313.

[307] A. Ashok, A. Kumar, R.R. Bhosale, M.A.H. Saleh, van den Broeke, Leo JP, Cellulose assisted combustion synthesis of porous Cu–Ni nanopowders, RSC Advances. 5 (2015) 28703-28712.

[308] I.S. Altman, I.E. Agranovski, M. Choi, Mechanism of nanoparticle agglomeration during the combustion synthesis, Appl. Phys. Lett. 87 (2005) 053104.

[309] B. Li, X. Wen, R. Li, Z. Wang, P.G. Clem, H. Fan, Stress-induced phase transformation and optical coupling of silver nanoparticle superlattices into mechanically stable nanowires, Nature communications. 5 (2014).

[310] V. Ramakrishnan, H. Kim, J. Park, B. Yang, Cobalt oxide nanoparticles on TiO_2 nanorod/FTO as a photoanode with enhanced visible light sensitization, RSC Advances. 6 (2016) 9789-9795.

[311] J. Xiao, Q. Kuang, S. Yang, F. Xiao, S. Wang, L. Guo, Surface structure dependent electrocatalytic activity of Co_3O_4 anchored on graphene sheets toward oxygen reduction reaction, Scientific reports. 3 (2013).

[312] M. Pang, J. Hu, H.C. Zeng, Synthesis, morphological control, and antibacterial properties of hollow/solid Ag2S/Ag heterodimers, J. Am. Chem. Soc. 132 (2010) 10771-10785.

[313] W. Fan, S. Jewell, Y. She, M.K. Leung, In situ deposition of Ag–Ag 2 S hybrid nanoparticles onto TiO_2 nanotube arrays towards fabrication of photoelectrodes with high visible light photoelectrochemical properties, Physical Chemistry Chemical Physics. 16 (2014) 676-680.

[314] S. Agnihotri, S. Mukherji, S. Mukherji, Immobilized silver nanoparticles enhance contact killing and show highest efficacy: elucidation of the mechanism of bactericidal action of silver, Nanoscale. 5 (2013) 7328-7340.

[315] A.M. Ferraria, A.P. Carapeto, do Rego, Ana Maria Botelho, X-ray photoelectron spectroscopy: silver salts revisited, Vacuum. 86 (2012) 1988-1991.

[316] J. Liu, S. Zou, L. Xiao, J. Fan, Well-dispersed bimetallic nanoparticles confined in mesoporous metal oxides and their optimized catalytic activity for nitrobenzene hydrogenation, Catalysis Science & Technology. 4 (2014) 441-446.

[317] Z. Chen, J. Wang, D. Chao, T. Baikie, L. Bai, S. Chen, Y. Zhao, T.C. Sum, J. Lin, Z. Shen, Hierarchical porous $LiNi_{1/3}Co_{1/3}Mn_{1/3}O_2$ nano-/micro spherical cathode material: Minimized cation mixing and improved Li mobility for enhanced electrochemical performance, Scientific reports. 6 (2016) 25771.

[318] S. Xie, Y. Liu, J. Deng, J. Yang, X. Zhao, Z. Han, K. Zhang, H. Dai, Insights into the active sites of ordered mesoporous cobalt oxide catalysts for the total oxidation of o-xylene, Journal of Catalysis. 352 (2017) 282-292.

[319] S. Hashimoto, T. Sugie, Z. Zhang, K. Yamashita, M. Noda, Effects of final annealing in oxygen on characteristics of BaTiO3 thin films for resistance random access memory, Japanese Journal of Applied Physics. 54 (2015) 10NA12.

[320] J. Tian, H. Gao, H. Kong, P. Yang, W. Zhang, J. Chu, Influence of transition metal

doping on the structural, optical, and magnetic properties of TiO_2 films deposited on Si substrates by a sol–gel process, Nanoscale research letters. 8 (2013) 533.

[321] M. Innocenti, C. Zafferoni, A. Lavacchi, L. Becucci, F. Di Benedetto, E. Carretti, F. Vizza, M. Foresti, Electroactivation of Microparticles of Silver on Glassy Carbon for Oxygen Reduction and Oxidation Reactions, J. Electrochem. Soc. 161 (2014) D3018-D3024.

[322] J. Guo, A. Hsu, D. Chu, R. Chen, Improving oxygen reduction reaction activities on carbon-supported Ag nanoparticles in alkaline solutions, The Journal of Physical Chemistry C. 114 (2010) 4324-4330.

[323] A. Damjanovic, M.A. Genshaw, J.O. Bockris, M., Distinction between Intermediates Produced in Main and Side Electrodic Reactions, J. Chem. Phys. 45 (1966) 4057-4059.

[324] Y. Zhao, S. Chen, B. Sun, D. Su, X. Huang, H. Liu, Y. Yan, K. Sun, G. Wang, Graphene-Co_3O_4 nanocomposite as electrocatalyst with high performance for oxygen evolution reaction, Scientific reports. 5 (2015).

[325] C.D. Wagner, G. Muilenberg, Handbook of X-Ray Photoelectron Spectroscopy, Perkin-Elmer, 1979.

[326] D. Svintsitskiy, E. Slavinskaya, T.Y. Kardash, V. Avdeev, B. Senkovskiy, S. Koscheev, A. Boronin, Low-temperature catalytic CO oxidation over mixed silver–copper oxide $Ag_2Cu_2O_3$, Applied Catalysis A: General. 510 (2016) 64-73.

[327] D. Svintsitskiy, A. Stadnichenko, D. Demidov, S. Koscheev, A. Boronin, Investigation of oxygen states and reactivities on a nanostructured cupric oxide surface, Appl. Surf. Sci. 257 (2011) 8542-8549.

[328] G. Schön, J. Tummavuori, B. Lindström, C.R. Enzell, C. Swahn, ESCA studies of Ag, Ag_2O and AgO, Acta Chem. Scand. 27 (1973) 2623-2633.

[329] T. MORIMOTO, K. AOKI, Effect of adsorbed H_2O on the reaction of Ag_2O with CO_2, Langmuir. 2 (1986) 525-528.

[330] T. Robert, M. Bartel, G. Offergeld, Characterization of oxygen species adsorbed on copper and nickel oxides by X-ray photoelectron spectroscopy, Surf. Sci. 33 (1972) 123-130.

[331] J. Haber, T. Machej, L. Ungier, J. Ziólkowski, ESCA studies of copper oxides and copper molybdates, Journal of Solid State Chemistry. 25 (1978) 207-218.

[332] C. Wagner, D. Zatko, R. Raymond, Use of the oxygen KLL Auger lines in identification of surface chemical states by electron spectroscopy for chemical analysis, Anal. Chem. 52 (1980) 1445-1451.

[333] N. McIntyre, M. Cook, X-ray photoelectron studies on some oxides and hydroxides of cobalt, nickel, and copper, Anal. Chem. 47 (1975) 2208-2213.

[334] S.M. AlShehri, J. Ahmed, T. Ahamad, P. Arunachalam, T. Ahmad, A. Khan, Bifunctional electro-catalytic performances of $CoWO_4$ nanocubes for water redox reactions (OER/ORR), RSC Advances. 7 (2017) 45615-45623.

[335] N. Sánchez-Padilla, D. Morales-Acosta, M. Morales-Acosta, S. Montemayor, F. Rodríguez-Varela, Catalytic activity and selectivity for the ORR of rapidly synthesized M@ Pt (M= Pd, Fe_3O_4, Ru) core–shell nanostructures, Int J Hydrogen Energy. 39 (2014) 16706-16714.

[336] A. Dweydari, C. Mee, Work function measurements on (100) and (110) surfaces of silver, physica status solidi (a). 27 (1975) 223-230.

[337] F. Lima, J. Zhang, M. Shao, K. Sasaki, M. Vukmirovic, E. Ticianelli, R. Adzic, Catalytic activity− d-band center correlation for the O_2 reduction reaction on platinum in alkaline solutions, The Journal of Physical Chemistry C. 111 (2007) 404-410.

[338] R. Giles, J. Harrison, Potentiodynamic sweep measurements of the anodic oxidation of silver in alkaline solutions, Journal of Electroanalytical Chemistry and Interfacial Electrochemistry. 27 (1970) 161-163.

[339] B.G. Pound, D.D. Macdonald, J.W. Tomlinson, The electrochemistry of silver in KOH at elevated temperatures—II. Cyclic voltammetry and galvanostatic charging studies, Electrochim. Acta. 25 (1980) 563-573.

[340] A. Zaky, Electrochemical behaviour of copper–silver alloys in sodium carbonate aqueous solution, Br. Corros. J. 36 (2001) 59-64.

[341] G. Briggs, M. Fleischmann, D. Lax, H. Thirsk, Texture, growth and orientation of anodically formed silver oxides, Transactions of the Faraday Society. 64 (1968) 3120-3127.

[342] N. McIntyre, S. Sunder, D. Shoesmith, F. Stanchell, Chemical information from XPS—applications to the analysis of electrode surfaces, Journal of Vacuum Science and Technology. 18 (1981) 714-721.

[343] D. Shoesmith, S. Sunder, M. Bailey, G. Wallace, F. Stanchell, Anodic oxidation of copper in alkaline solutions: Part IV. Nature of the passivating film, Journal of Electroanalytical Chemistry and Interfacial Electrochemistry. 143 (1983) 153-165.

[344] A. Muthukrishnan, Y. Nabae, T. Hayakawa, T. Okajima, T. Ohsaka, Fe-containing polyimide-based high-performance ORR catalysts in acidic medium: a kinetic approach to study the durability of catalysts, Catalysis Science & Technology. 5 (2015) 475-483.

[345] B. Ge, K. Li, Z. Fu, L. Pu, X. Zhang, The addition of ortho-hexagon nano spinel Co_3O_4 to improve the performance of activated carbon air cathode microbial fuel cell, Bioresour. Technol. 195 (2015) 180-187.

[346] A.S. Mukasyan, C. Costello, K.P. Sherlock, D. Lafarga, A. Varma, Perovskite membranes by aqueous combustion synthesis: synthesis and properties, Separation and Purification Technology. 25 (2001) 117-126.

[347] B. Rezaei, E. Havakeshian, A.A. Ensafi, Fabrication of a porous Pd film on nanoporous stainless steel using galvanic replacement as a novel electrocatalyst/electrode design for glycerol oxidation, Electrochim. Acta. 136 (2014) 89-96.

[348] A. Kumar, A. Ashok, R.R. Bhosale, M.A.H. Saleh, F.A. Almomani, M. Al-Marri, M.M. Khader, F. Tarlochan, In situ DRIFTS Studies on Cu, Ni and CuNi catalysts for Ethanol Decomposition Reaction, Catalysis Letters. 146 (2016) 778-787.

[349] A. Ashok, A. Kumar, R.R. Bhosale, F. Almomani, Saad, Mohd Ali H Saleh, S. Suslov, F. Tarlochan, Influence of fuel ratio on the performance of combustion synthesized bifunctional cobalt oxide catalysts for fuel cell application, Int J Hydrogen Energy. 44 (2019) 436-445.

[350] A. Ashok, A. Kumar, F. Tarlochan, Preparation of Nanoparticles via Cellulose-Assisted Combustion Synthesis, International Journal of Self-Propagating High-Temperature Synthesis. 27 (2018) 141-153.

[351] A. Ashok, A. Kumar, J. Ponraj, S.A. Mansour, F. Tarlochan, Single Step Synthesis of Porous $NiCoO_2$ for Effective Electrooxidation of Glycerol in Alkaline Medium, J. Electrochem. Soc. 165 (2018) J3301-J3309.

[352] A. Ashok, A. Kumar, R. Bhosale, M.A.S. Saad, F. AlMomani, F. Tarlochan, Study

of ethanol dehydrogenation reaction mechanism for hydrogen production on combustion synthesized cobalt catalyst, Int J Hydrogen Energy. 42 (2017) 23464-23473.

[353] A. Ashok, A. Kumar, F. Tarlochan, Surface Alloying in Silver-Cobalt through a Second Wave Solution Combustion Synthesis Technique, Nanomaterials. 8 (2018) 604.

[354] A. Kumar, E. Wolf, A. Mukasyan, Solution combustion synthesis of metal nanopowders: Copper and copper/nickel alloys, AIChE J. 57 (2011) 3473-3479.

[355] A. Rogachev, A. Mukasyan, Combustion of heterogeneous nanostructural systems (Review), Combustion, Explosion, and Shock Waves. 46 (2010) 243-266.

[356] A. Varma, A.S. Mukasyan, K.T. Deshpande, P. Pranda, P.R. Erri, Combustion synthesis of nanoscale oxide powders: mechanism, characterization and properties, 800 (2003) AA4. 1.

[357] M. Hossain, G.F. Samu, K. Gandha, S. Santhanagopalan, J.P. Liu, C. Janáky, K. Rajeshwar, Solution combustion synthesis, characterization, and photocatalytic activity of CuBi2O4 and its nanocomposites with CuO and α-Bi_2O_3, The Journal of Physical Chemistry C. 121 (2017) 8252-8261.

[358] A. Kormányos, A. Thomas, M.N. Huda, P. Sarker, J.P. Liu, N. Poudyal, C. Janáky, K. Rajeshwar, Solution combustion synthesis, characterization, and photoelectrochemistry of $CuNb_2O_6$ and $ZnNb_2O_6$ nanoparticles, The Journal of Physical Chemistry C. 120 (2016) 16024-16034.

[359] W. Chen, J. Hong, Y. Li, Facile fabrication of perovskite single-crystalline LaMnO3 nanocubes via a salt-assisted solution combustion process, J. Alloys Compounds. 484 (2009) 846-850.

[360] Z.L. Wang, Transmission Electron Microscopy of Shape-Controlled Nanocrystals

and Their Assemblies, J Phys Chem B. 104 (2000) 1153-1175.

[361] Q. Chu, X. Wang, B. Li, F. Liu, X. Liu, High pressure flux synthesis of LaMnO 3 δ with charge ordering, RSC Advances. 3 (2013) 21311-21314.

[362] R. Dudric, A. Vladescu, V. Rednic, M. Neumann, I. Deac, R. Tetean, XPS study on La0. 67Ca0. 33Mn1− xCoxO3 compounds, J. Mol. Struct. 1073 (2014) 66-70.

[363] T. Vijayaraghavan, R. Sivasubramanian, S. Hussain, A. Ashok, A Facile Synthesis of LaFeO3-Based Perovskites and Their Application towards Sensing of Neurotransmitters, ChemistrySelect. 2 (2017) 5570-5577.

[364] N. Sethulakshmi, A. Unnimaya, I. Al-Omari, S. Al-Harthi, S. Sagar, S. Thomas, G. Srinivasan, M. Anantharaman, On magnetic ordering in heavily sodium substituted hole doped lanthanum manganites, J Magn Magn Mater. 391 (2015) 75-82.

[365] A. Santoni, G. Speranza, M. Mancini, F. Padella, L. Petrucci, S. Casadio, Core-level and valence band photoemission study of perovskite oxide powders synthesized by mechanically and thermally activated solid-state reaction, Journal of Physics: Condensed Matter. 11 (1999) 3387.

[366] A. Machocki, T. Ioannides, B. Stasinska, W. Gac, G. Avgouropoulos, D. Delimaris, W. Grzegorczyk, S. Pasieczna, Manganese–lanthanum oxides modified with silver for the catalytic combustion of methane, Journal of Catalysis. 227 (2004) 282-296.

[367] B. Hua, Y. Sun, M. Li, N. Yan, J. Chen, Y. Zhang, Y. Zeng, B. Shalchi Amirkhiz, J. Luo, Stabilizing double perovskite for effective bifunctional oxygen electrocatalysis in alkaline conditions, Chemistry of Materials. 29 (2017) 6228-6237.

[368] T.Y. Ma, Y. Zheng, S. Dai, M. Jaroniec, S.Z. Qiao, Mesoporous $MnCo_2O_4$ with abundant oxygen vacancy defects as high-performance oxygen reduction catalysts,

Journal of Materials Chemistry A. 2 (2014) 8676-8682.

[369] W. Zhou, J. Sunarso, Enhancing bi-functional electrocatalytic activity of perovskite by temperature shock: A case study of $LaNiO_{3-\delta}$, The journal of physical chemistry letters. 4 (2013) 2982-2988.

[370] N. Hamada, Electronic band structure of $LaNiO_3$, Journal of Physics and Chemistry of Solids. 54 (1993) 1157-1160.

[371] Y. Wang, H. Cheng, Oxygen reduction activity on perovskite oxide surfaces: a comparative first-principles study of $LaMnO_3$, $LaFeO_3$, and $LaCrO_3$, The Journal of Physical Chemistry C. 117 (2013) 2106-2112.